National Library
of Canada

Bibliothèque nationale
du Canada

Canadian Theses Service

Service des thèses canadiennes

Ottawa, Canada
K1A 0N4

NOTICE

The quality of this microform is heavily dependent upon the quality of the original thesis submitted for microfilming. Every effort has been made to ensure the highest quality of reproduction possible.

If pages are missing, contact the university which granted the degree.

Some pages may have indistinct print especially if the original pages were typed with a poor typewriter ribbon or if the university sent us an inferior photocopy.

Reproduction in full or in part of this microform is governed by the Canadian Copyright Act, R.S.C. 1970, c. C-30, and subsequent amendments.

AVIS

La qualité de cette microforme dépend grandement de la qualité de la thèse soumise au microfilmage. Nous avons tout fait pour assurer une qualité supérieure de reproduction.

S'il manque des pages, veuillez communiquer avec l'université qui a conféré le grade.

La qualité d'impression de certaines pages peut laisser à désirer, surtout si les pages originales ont été dactylographiées à l'aide d'un ruban usé ou si l'université nous a fait parvenir une photocopie de qualité inférieure.

La reproduction, même partielle, de cette microforme est soumise à la Loi canadienne sur le droit d'auteur, SRC 1970, c. C-30, et ses amendements subséquents.

NL-339 (r. 88/04) c

Canada

UNIVERSITY OF ALBERTA

ENERGETICS OF SELECTED GAS PHASE ION-MOLECULE REACTIONS

BY

GARY JOHN CHARLES PAUL

A THESIS SUBMITTED TO
THE FACULTY OF GRADUATE STUDIES AND RESEARCH
IN PARTIAL FULFILLMENT OF THE REQUIREMENTS FOR THE
DEGREE OF DOCTOR OF PHILOSOPHY

DEPARTMENT OF CHEMISTRY
EDMONTON,ALBERTA
FALL 1990

National Library of Canada
Bibliothèque nationale du Canada

Canadian Theses Service
Service des thèses canadiennes

Ottawa, Canada
K1A 0N4

The author has granted an irrevocable non-exclusive licence allowing the National Library of Canada to reproduce, loan, distribute or sell copies of his/her thesis by any means and in any form or format, making this thesis available to interested persons.

The author retains ownership of the copyright in his/her thesis. Neither the thesis nor substantial extracts from it may be printed or otherwise reproduced without his/her permission.

L'auteur a accordé une licence irrévocable et non exclusive permettant à la Bibliothèque nationale du Canada de reproduire, prêter, distribuer ou vendre des copies de sa thèse de quelque manière et sous quelque forme que ce soit pour mettre des exemplaires de cette thèse à la disposition des personnes intéressées.

L'auteur conserve la propriété du droit d'auteur qui protège sa thèse. Ni la thèse ni des extraits substantiels de celle-ci ne doivent être imprimés ou autrement reproduits sans son autorisation.

ISBN 0-315-64774-4

Canada

UNIVERSITY OF ALBERTA

RELEASE FORM

NAME OF AUTHOR: **GARY JOHN CHARLES PAUL**

TITLE OF THESIS: **ENERGETICS OF SELECTED GAS PHASE ION-MOLECULE REACTIONS**

DEGREE FOR WHICH THESIS WAS PRESENTED: **Ph.D.**

YEAR THIS DEGREE GRANTED: **1990**

PERMISSION IS HEREBY GRANTED TO THE UNIVERSITY OF ALBERTA LIBRARY TO REPRODUCE SINGLE COPIES OF THIS THESIS AND TO LEND OR SELL SUCH COPIES FOR PRIVATE, SCHOLARLY OR SCIENTIFIC RESEARCH PURPOSES ONLY.

THE AUTHOR RESERVES OTHER PUBLICATION RIGHTS, AND NEITHER THE THESIS NOR EXTENSIVE EXTRACTS FROM IT MAY BE PRINTED OR OTHERWISE REPRODUCED WITHOUT THE AUTHOR'S WRITTEN PERMISSION.

SIGNED: Gary Paul

PERMANENT ADDRESS: 309, Dorchester Road,
Weymouth, Dorset,
England.

DATED: Sept. 6 1990

THE UNIVERSITY OF ALBERTA

FACULTY OF GRADUATE STUDIES AND RESEARCH

THE UNDERSIGNED CERTIFY THAT THEY HAVE READ, AND RECOMMENDED TO THE FACULTY OF GRADUATE STUDIES AND RESEARCH FOR ACCEPTANCE, A THESIS ENTITLED **ENERGETICS OF SELECTED GAS PHASE ION-MOLECULE REACTIONS** SUBMITTED BY **GARY JOHN CHARLES PAUL** IN PARTIAL FULFILLMENT OF THE REQUIREMENTS FOR THE DEGREE OF **DOCTOR OF PHILOSOPHY.**

SUPERVISOR ____________________

____

____

J. S. Martin

____

EXTERNAL EXAMINER ____________________

DATED: ____________

TO MUM AND DAD

ABSTRACT

The energetics of the gas phase negative ion-molecule association reactions $M + X^- = M{\cdot}X^-$, where M are substituted benzenes, quinones and ethylenes and X^- are the halide ions (F^-, Cl^-, Br^- and I^-), were determined by equilibrium measurements with the pulsed electron high pressure mass spectrometer (PHPMS). Evaluation of the equilibrium constants for the halide association (XA) reactions leads directly to absolute bond free energy determinations, $-\Delta G^o_{XA}$, in $M{\cdot}X^-$. Under conditions where halide association equilibria could not be measured directly, relative bond free energies, $-\Delta\Delta G^o_{XA}$, were obtained by measurements of the transfer equilibria $M{\cdot}X^- + M' = M + M'{\cdot}X^-$. Combining $-\Delta\Delta G^o_{XA}$ values with directly determined $-\Delta G^o_{XA}$ values leads to further absolute bond free energy determinations.

The hydrogen bond free energies in the singly substituted phenol complexes $YPhOH{\cdot}Br^-$, combined with previous data for $X^- = Cl^-$ and I^- from this laboratory, are used to examine the substituent effects on hydrogen bonding. The dominant contribution to $YPhOH{\cdot}Br^-$ stabilization, where the extent of proton transfer from YPhOH to Br^- is small, is due to the field effects of the substituents with π delocalization playing only a small part. Thus, the correlation with the acidity of YPhOH, where π delocalization is important, is not very close.

Substituent effect analysis of experimentally determined bond free energies and quantum mechanical calculations are used to gain structural information on the complexes $M{\cdot}X^-$ where M does not possess substituents with protic hydrogens. The results indicate the complexes $M{\cdot}X^-$ have a variety of structures, depending on X^- and the nature of the substituents.

The temperature dependence of the equilibrium constants for the gas phase reactions $HO^- + HOH = HO^-{\cdot}HOH$ and $CH_3O^- + HOCH_3 = CH_3O^-{\cdot}HOCH_3$

was measured with the PHPMS. The enthalpy and entropy changes were obtained from van't Hoff plots of the equilibrium constants. The enthalpy changes were found to be in good agreement with experimentally determined values reported by Meot-Ner and Sieck and recent theoretical results. The agreement for the entropy changes is found not to be as good.

The electron affinities of 20 cyclic diones, mostly substituted maleic and phthalic anhydrides and maleimides and phthalimides, were determined with the PHPMS by measuring gas phase electron transfer equilibria $A^- + B = A + B^-$ involving these compounds and reference compounds whose electron affinities were determined previously. The effects of substituents on electron affinities are similar to those observed previously for other groups of organic compounds.

ACKNOWLEDGEMENTS

I would like to express my sincere gratitude to Professor Paul Kebarle for all his help and encouragement throughout the course of my studies.

Many thanks to the members of the mass spectrometry group for both their assistance and their friendship: Gordon Nicol, Paul Sharpe, Glen Dillow, Swapan Chowdhury, Thomas Heinis, Arthur Blades, Francis Wampler and Liang Tang. Special thanks to Louis Crocker for proof reading this dissertation and Michael Ikonomou for his invaluable help and support in times of desperation.

I would like to thank the members of the glass blowing, electronics and and machine shops for their much needed help. In particular I would like to thank Hubert Hoffman, Randy Benson, Henry Stolk, Cornelius Brusselers and Gerald Streefkerk for both their skill and friendship.

Special thanks to the lovely ladies of the Chemistry Department: Corrinne Treit, Marie Labbe, Pat Campbell, Jeanette Loiselle, Mary Waters, Marion Brady and Selina, for all the help and kindness they have shown me.

Many thanks to all the wonderful people whom I have met during my stay in Edmonton: Bruce Todd, Andrew Graham, Lisa Ross, Danielle McLoughlin, Rob McLaren, Bo Singh, Bobby McDonald, Karen McLeod, Jim Jenkins, Keith Lepla, Steve Astley, Paul and Meenu Glavina, the Mullin Clan, Hank Herr, John Drover, Danny Barson, Allen Ball, Mike McGibbon, Calvin Coleman, Derek Cole, Kingsley Donkor, Mr. Demoz, Andrew Bennet and Xizhong Li. I'll miss you all.

Love as always to the family back in Weymouth without whose encouragement none of this would have been possible. Especially Mum and Grandma because I know how much this means to you.

Finally to the person who had to put up with me while I was going nuts. Natasha, I love you.

TABLE OF CONTENTS

CHAPTER PAGE

1 INTRODUCTION 1

1.1 The Present Study 1

1.2 The Pulsed Electron High Pressure Mass Spectrometer (PHPMS) 8

1.2a PHPMS: The Method 8

1.2b PHPMS: The Apparatus 10

References 23

2 STABILITIES IN THE GAS PHASE OF HYDROGEN BONDED COMPLEXES, $YC_6H_4OH{\cdot}X^-$, OF SUBSTITUTED PHENOLS, YC_6H_4OH, WITH HALIDE ANIONS X^- (Cl^-, Br^- and I^-) 27

2.1 Introduction 27

2.2 Experimental 30

2.3 Results and Discussion 36

2.3a Results 36

2.3b Hydrogen Bond Energy in $YPhOH{\cdot}X^-$. Gas Phase Acidities and Substituent Effect Analysis 40

2.3c Hydrogen Bonding in $MH{\cdot}B^-$ 54

References 56

3 STABILITIES OF COMPLEXES OF Br^- WITH SUBSTITUTED BENZENES, SB, BASED ON DETERMINATIONS OF THE GAS PHASE EQUILIBRIA $Br^- + SB = SB{\cdot}Br^-$ 58

3.1 Introduction 58

3.2 Experimental 64

3.3 Results and Discussion 75
3.3a Results 75
3.3b Singly Substituted Benzenes 82
3.3c Multiply Substituted Benzenes 93
References 99
4 STABILITIES OF σ BONDED AND ELECTROSTATIC COMPLEXES, $C_6F_5Y{\cdot}X^-$, OF PERFLUOROBENZENES, C_6F_5Y, WITH HALIDE ANIONS X^- (F^-, Cl^-, Br^- and I^-) 102
4.1 Introduction 102
4.2 Experimental 106
4.2a Experimental Conditions Used in Equilibrium Measurements 106
4.2b $C_6F_5Y{\cdot}F^-$ and $YC_6F_4O^-$ Production in the Ion Source 113
4.3 Results and Discussion 130
4.3a Results 130
4.3b σ Bonding in the Complexes $C_6F_5Y{\cdot}F^-$ 138
4.3c Electrostatic Bonding in the Complexes $C_6F_5Y{\cdot}X^-$ (X^- = Cl^-, Br^- and I^-) 154
References 160
5 STABILITIES OF COMPLEXES OF SUBSTITUTED QUINONES (SQ) AND ETHYLENES (SE) WITH HALIDE ANIONS X^- (F^-, Cl^- AND Br^-) 162
5.1 Introduction 162
5.2 Experimental 163
5.3 Results and Discussion 166
5.3a Results 166

5.3b Bonding in the Complexes SQ·X$^-$ where SQ = Substituted Quinones and X$^-$ = F$^-$, Cl$^-$ and Br$^-$ 169

5.3c Bonding in the Complexes SE·X$^-$ where SE = Substituted Ethylenes and X$^-$ = F$^-$, Cl$^-$ and Br$^-$ 184

References 194

6 THE THERMODYNAMICS OF THE ASSOCIATION REACTIONS $HO^- + H_2O = HO^-{\cdot}HOH$ AND $CH_3O^- + CH_3OH = CH_3O^-{\cdot}HOCH_3$ IN THE GAS PHASE 196

6.1 Introduction 196

6.2 Experimental 199

6.2a Apparatus and Temperature Measurements 199

6.2b Experimental Conditions Used in Equilibrium Measurements 203

6.3 Results and Discussion 209

6.3a Experimental Results from Ion Equilibrium Measurements 209

6.3b Comparison of ΔH° Values with Other Work 217

6.3c The Entropy Changes ΔS_1° and ΔS_2° 220

References 225

7 ELECTRON AFFINITIES OF CYCLIC UNSATURATED DICARBONYLS: MALEIC ANHYDRIDES, MALEIMIDES AND CYCLOPENTENEDIONE 228

7.1 Introduction 228

7.2 Experimental 230

7.3 Results and Discussion 230

7.3a Thermochemical Data for Electron Attachment 230

7.3b Effects of Substituents on the Electron Affinities 239

7.3c Comparison with Reduction Potentials in Solution

Solvation Energy of the Radical Anions 244

References 249

8 CONCLUDING SUMMARY 251

References 255

LIST OF TABLES

TABLE PAGE

2.1 Bond free energies (423 K) corresponding to reaction $Br^- + YPhOH = YPhOH{\cdot}Br^-$ 38

2.2 Bond free energies (423 K) corresponding to reaction $X^- + YPhOH = YPhOH{\cdot}X^-$ ($X^- = Cl^-$, Br^- and I^-) 39

2.3 Values for resonance ρ_R, field ρ_F and polarizability ρ_α parameters from linear regression analysis of Taft eqn. (2.6) 45

2.4 Resonance R and field F contributions of substituents to $-\delta\Delta G^o$ 53

3.1 Bond free energies (423 K) corresponding to reaction $Br^- + SB = SB{\cdot}Br^-$ involving singly substituted benzenes 80

3.2 Bond free energies (423 K) corresponding to reaction $Br^- + SB = SB{\cdot}Br^-$ involving singly and doubly substituted nitrobenzenes 81

3.3 Values for resonance ρ_R, field ρ_F and polarizability ρ_α parameters from linear regression analysis of Taft eqn. (3.7) 86

3.4 Resonance R and field F contributions of substituents to $-\delta\Delta G^o$ 87

4.1 Bond free energies (423 K) corresponding to reaction $C_6F_5Y + X^- = C_6F_5Y{\cdot}X^-$ ($X^- = F^-$, Cl^-, Br^- and I^-) 134

4.2 Thermochemical data for bromide attachment to C_6F_6, C_6F_5CN and 1,4-diCNC_6F_4 obtained via van't Hoff plots 137

4.3 Values for resonance ρ_R and field ρ_F parameters from linear regression analysis of Taft eqns. (4.11) and (4.12) 148

4.4 Resonance R and field F contributions of substituents to $-\delta\Delta G^o$ 150

5.1 Bond free energies (423 K) corresponding to reactions: SQ + X^- = SQ·X^- and SE + X^- = SE·X^-, where SQ, SE are substituted quinones and ethylenes and X^- = F^-, Cl^-, Br^- and I^- 168

5.2 Thermochemical data for reactions: TCNE + X^- = TCNE·X^- and F_4-p-BQ + X^- = F_4-p-BQ·X^- (X^- = Cl^- and Br^-), obtained via van't Hoff plots 170

5.3 Bond strength determinations corresponding to reactions: F_4-p-BQ + X^- = F_4-p-BQ·X^- (X^- = Cl^- and Br^-) and TCNE + X^- = TCNE·X^- (X^- = F^-, Cl^- and Br^-) 177

6.1 Thermochemical and theoretical data for reactions (6.1) and (6.2): OH^- + HOH = HO^-·HOH and CH_3O^- + CH_3OH = CH_3O^-·$HOCH_3$ 215

6.2 Theoretical ΔS° for reaction (6.1): OH^- + HOH = HO^-·HOH 222

6.3 Theoretical ΔS° for reaction (6.2): CH_3O^- + CH_3OH = CH_3O^-·$HOCH_3$ 223

7.1 Thermochemical data for electron attachment: e + B = B^- where B = cyclic unsaturated dicarbonyls 234

LIST OF FIGURES

FIGURE PAGE

1.1 Simplified diagram of the ion source of the pulsed electron high pressure mass spectrometer (PHPMS) 9

1.2 Schematic diagram of the gas handling plant (GHP). 11

1.3 Schematic of the PHPMS apparatus 15

1.4 Pulsing sequence with typical voltages and durations. 18

2.1 Time dependence of ion intensities observed after ionizing pulse to ion source containing PhOH, CH_2Br_2 and methane. 32

2.2 Equilibrium constants for reaction (2.1) involving Br^- and different phenols (YPhOH) 34

2.3 Time dependence of ion intensities observed after ionizing pulse to ion source containing $3\text{-}NO_2PhOH$, 3-CNPhOH, CH_2Br_2 and methane 35

2.4 Scale of $-\Delta G^{o}_{BrA,423K}$ for reaction (2.1): $Br^- + YPhOH = YPhOH{\cdot}Br^-$ 37

2.5 Plot of $-\delta\Delta G^{o}_{BrA,423K}$ for Br^- hydrogen bonding to p-YPhOH versus relative gas phase acidities of phenols 41

2.6 Plot of $-\delta\Delta G^{o}_{BrA,423K}$ for Br^- hydrogen bonding to p-YPhOH versus relative gas phase acidities of benzoic acids 42

2.7 $-\delta\Delta G^{o}_{BrA,423K}$ for Br^- and p-YPhOH versus $-\delta\Delta G^{o}_{Calc}$ calculated with Taft σ parameters 44

2.8 $-\delta\Delta G^{o}_{BrA,423K}$ for Br^- and m-YPhOH versus $-\delta\Delta G^{o}_{Calc}$ calculated with Taft σ parameters 47

2.9 $-\delta\Delta G^{o}_{ClA,423K}$ for Cl^- and restricted number of p-YPhOH versus $-\delta\Delta G^{o}_{Calc}$ calculated with Taft σ parameters 48

2.10 $-\delta\Delta G^o_{BrA,423K}$ for Br^- and restricted number of p-YPhOH versus $-\delta\Delta G^o_{Calc}$ calculated with Taft σ parameters 49

2.11 $-\delta\Delta G^o_{IA,423K}$ for I^- and restricted number of p-YPhOH versus $-\delta\Delta G^o_{Calc}$ calculated with Taft σ parameters 50

3.1 Time dependence of ion intensities observed after ionizing pulse to ion source containing m-CNNB, CH_2Br_2 and methane 66

3.2 Equilibrium constants for reaction (3.1) involving Br^- and different singly substituted benzenes (C_6H_5Y) 67

3.3 Equilibrium constants for reaction (3.1) involving Br^- and different singly substituted nitrobenzenes (YNB) 68

3.4 K_{BrA} for reaction (3.1) involving singly substituted benzenes versus total ion source pressure 70

3.5 Equilibrium constants for reaction (3.1): NB + Br^- = NB·Br^-, where NB is nitrobenzene, versus ion source voltage 72

3.6 K_{BrTr} for reaction (3.2) involving singly substituted benzenes versus total ion source pressure 73

3.7 van't Hoff plots of equilibrium constants for bromide attachment to NB and m-CF_3NB 76

3.8 Scale of $-\Delta G^o_{BrA,423K}$ for reaction (3.1): SB + Br^- = SB·Br^- where SB are singly substituted benzenes 78

3.9 Scale of $-\Delta G^o_{BrA,423K}$ for reaction (3.1): SB + Br^- = SB·Br^- where SB are singly and doubly substituted nitrobenzenes 79

3.10 Plot of $-\delta\Delta G^o_{BrA,423K}$ for Br^- bonding to singly substituted benzenes versus dipole moment 83

3.11 $-\delta\Delta G^o_{BrA,423K}$ for Br^- bonding to singly substituted benzenes versus $-\delta\Delta G^o_{Calc}$ calculated with Taft σ parameters 85

3.12 Plot of $-\delta\Delta G^{o}_{ClA,423K}$ for Cl^- bonding to singly substituted benzenes versus $-\delta\Delta G^{o}_{Calc}$ calculated with Taft σ parameters 88
3.13 Plot of $-\delta\Delta G^{o}_{BrA,423K}$ for Br^- bonding to singly substituted benzenes versus relative gas phase acidities of benzoic acids 90
3.14 Plot of $-\delta\Delta G^{o}_{BrA,423K}$ for Br^- bonding to singly substituted benzenes versus relative gas phase acidities of phenols 91
3.15 $-\Delta G^{o}_{BrA,423K}$ versus $-\Delta G^{o}_{NO_2A,423K}$ for Br^- and NO_2^- bonding to ortho and meta-substituted nitrobenzenes 96
4.1 Time dependence of ion intensities observed after ionizing pulse to ion source containing $C_6F_5CF_3$, CH_2Br_2 and methane 107
4.2 Equilibrium constants for reaction (4.1) involving Cl^- and different perfluorobenzenes (C_6F_5Y) 109
4.3 Equilibrium constants for reaction (4.1) involving Br^- and different perfluorobenzenes (C_6F_5Y) 110
4.4 Time dependence of ion intensities observed after ionizing pulse to ion source containing C_6F_5CN, $C_6F_5NO_2$ and methane 112
4.5 Negative ion mass spectra of CH_4/C_6F_5CN and $CH_4/C_6F_5NO_2$ 115
4.6 Negative ion mass spectra of CH_4/C_6F_5Cl and $CH_4/C_6F_5Cl/O_2$ 120
4.7 Negative ion mass spectra of CH_4/C_6F_5CN and $CH_4/C_6F_5CN/O_2$ 121
4.8 Proposed S_NAr reaction pathway for the attack of $C_6F_5NO_2$ by $C_6F_5NO_2^-$ 123
4.9 Negative ion mass spectra of CH_4/C_6F_5CN and $CH_4/C_6F_5CN/C_6F_5NO_2$ 125
4.10 Proposed S_NAr reaction pathways for attack of C_6F_5Y ($Y = CN, NO_2$) by $NO_2C_6F_4O^-$ 127
4.11 Negative ion mass spectrum of $CH_4/C_6F_5CN/C_6F_5NO_2$ 129

4.12 Scale of $-\Delta G^{o}_{ClA,423K}$ for reaction (4.1): $C_6F_5Y + Cl^- = C_6F_5Y{\cdot}Cl^-$ 131

4.13 Scale of $-\Delta G^{o}_{BrA,423K}$ for reaction (4.1): $C_6F_5Y + Br^- = C_6F_5Y{\cdot}Br^-$ 132

4.14 Ladder of interconnecting $-\Delta G^{o}_{FTr,423K}$ for reaction (4.2): $C_6F_5Y{\cdot}F^- + C_6F_5Y' = C_6F_5Y + C_6F_5Y'{\cdot}F^-$ 135

4.15 van't Hoff plots of equilibrium constants for bromide attachment to C_6F_6, C_6F_5CN and 1,4-diCNC_6F_4 136

4.16 Optimized geometry of $C_6F_6{\cdot}F^-$ 140

4.17 Intrinsic Reaction Coordinates (IRC) of the reaction $F^- + C_6F_6$ 141

4.18 Potential energy diagram for the reaction $F^- + C_6F_6$ 142

4.19 Optimized geometries of $C_6F_6{\cdot}F^-$ where the attacking fluorine is in positions A, B and C of the IRC 145

4.20 $-\delta\Delta G^{o}_{FA,423K}$ for F^- bonding to the perfluorobenzenes versus $-\delta\Delta G^{o}_{Calc}$ calculated with Taft σ parameters 147

4.21 Plot of fluoride attachment free energies versus electron attachment free energies for the perfluorobenzenes 152

4.22 $-\delta\Delta G^{o}_{ClA,423K}$ for Cl^- bonding to the perfluorobenzenes versus $-\delta\Delta G^{o}_{Calc}$ calculated with Taft σ parameters 156

4.23 $-\delta\Delta G^{o}_{BrA,423K}$ for Br^- bonding to the perfluorobenzenes versus $-\delta\Delta G^{o}_{Calc}$ calculated with Taft σ parameters 157

5.1 Time dependence of ion intensities observed after ionizing pulse to ion source containing F_4-p-BQ, CH_2Br_2 and methane 165

5.2 van't Hoff plots of K_{XA} for reactions: TCNE + X^- = TCNE$\cdot X^-$ and F_4-p-BQ + X^- = F_4-p-BQ$\cdot X^-$ where X^- = Cl^- and Br^- 167

5.3 Optimized geometry of F_4-p-BQ 171

5.4 Optimized geometry of the F_4-p-BQ$\cdot$Br$^-$ partial charge transfer complex 172

5.5 Optimized geometry of the F_4-p-BQ$\cdot$Br$^-$ Meisenheimer complex 173

5.6 Optimized geometry of the F_4-p-BQ·Br^- electrostatic complex 174

5.7 Optimized geometry of the F_4-p-BQ·Cl^- partial charge transfer complex 175

5.8 Optimized geometry of the F_4-p-BQ·Cl^- electrostatic complex 176

5.9 Optimized geometry of TCNE 185

5.10 Optimized geometry of the TCNE·F^- Meisenheimer complex 186

5.11 Optimized geometry of the TCNE·Cl^- Meisenheimer complex 187

5.12 Optimized geometry of the TCNE·Cl^- electrostatic complex 188

5.13 Optimized geometry of the TCNE·Br^- Meisenheimer complex 189

5.14 Optimized geometry of the TCNE·Br^- electrostatic complex 190

6.1 Modifications of ion source for temperature measurement 201

6.2 Ion source temperatures measured by thermocouples Tc 2 and Tc 3 (Figure 6.1) 202

6.3 Time dependence of ion intensities observed after ionizing pulse to ion source containing D_2O, N_2O and methane 205

6.4 Independence of equilibrium constants for reaction (6.1): $DO^- + DOD = DO^- \cdot DOD$, of N_2O pressure 207

6.5 Independence of equilibrium constants for reaction (6.2): $CH_3O^- + CH_3OH = CH_3O^- \cdot HOCH_3$, of N_2O pressure 208

6.6 Independence of K_1 of D_2O pressure 210

6.7 Independence of K_2 of CH_3OH pressure 211

6.8 van't Hoff plots of K_1 for reaction (6.1): $DO^- + DOD = DO^- \cdot DOD$ 212

6.9 van't Hoff plots of K_2 for reaction (6.2): $CH_3O^- + CH_3OH = CH_3O^- \cdot HOCH_3$ 213

7.1 Ladder of interconnecting $\Delta G^o_{et,423K}$ for reaction (7.1): $A^- + B = A + B^-$ involving cyclic unsaturated dicarbonyls 231

7.2 van't Hoff plots of electron transfer equilibrium constants K_{et} 235

7.3 Scale of electron transfer enthalpies, ΔH_{et}^{o}, for reaction (7.1):
$A^{-} + B = A + B^{-}$ involving cyclic unsaturated dicarbonyls 236
7.4 Entropy changes, ΔS_{et}^{o}, for electron transfer reaction (7.1) 237
7.5 Electron attachment free energies, $-\Delta G_{a}^{o}$, for the maleic and phthalic anhydrides 240
7.6 Plot of polarographic halfwave potentials in dimethylformamide versus electron attachment free energies for certain cyclic unsaturated dicarbonyls 245
7.7 Plot of solvation energies, $\Delta\Delta G_{sol}^{o}$, in dimethylformamide versus electron attachment free energies 247

CHAPTER 1

INTRODUCTION

1.1 The Present Study

Gas phase determinations of the energetics of ion-molecule interactions coupled with structural information from quantum mechanical calculations has led to an understanding of the chemical bonding present in a variety of ion-molecule complexes [1-15]. Accurate structural and thermodynamic information on gas phase ion-solvent pairs has also helped provide a basis for the understanding of solvent effects on the energetics of chemical reactions; this information has been used to construct intermolecular potential functions describing ion-molecule interactions in solution [16-19]. Ion-molecule association energetics are also of significance in analytical mass spectrometric methods such as Chemical Ionization (CI), Atmospheric Pressure Ionization (API) and Fast Atom Bombardment (FAB) since the stabilities of the ion-molecule complexes are often reflected in the abundances of the respective ion-molecule complexes observed with these methods [20-22].

Absolute and relative bond strength determinations for simple anions (B^-) with a large number of organic and inorganic molecules (M, M') are available from measurements of ion-molecule association (1.1) and transfer (1.2) equilibria

$$M + B^- = M{\cdot}B^- \tag{1.1}$$

$$M{\cdot}B^- + M' = M + M'{\cdot}B^- \tag{1.2}$$

performed mostly with the pulsed electron high pressure mass spectrometer (PHPMS) [23] and ion cyclotron resonance mass spectrometer (ICR) [24]. The pulsed electron high pressure mass spectrometer is the apparatus used in the present investigation and, with working pressures of 1-5 torr, is suitable for measurements of both association and transfer equilibria; see Section 1.2. With the ICR working at much lower pressures, 10^{-6} torr, only transfer equilibria (1.2) can be measured as association reactions (1.1) require third body stabilization and generally have too slow a rate to be measured at these pressures. Combining relative bond strengths from equilibrium (1.2) measurements with absolute bond strengths from equilibrium (1.1) measurements leads to further absolute bond strength determinations. A recent compilation of the thermodynamic data corresponding to reaction (1.1) has been provided by Keesee and Castleman [25].

The majority of gas phase ion-molecule bond strength determinations to date involve hydrogen bonded ion-solvent molecule complexes as these data provide the start point for the construction of solvation models. Kebarle et al. [26-31] initiated work in this area measuring the bond strengths for a variety of simple anions (B^-) with compounds MH containing protic hydrogens such as the oxygen acids (alcohols, carboxylic acids, phenols). In these studies the hydrogen bond strengths of the complexes $MH{\cdot}B^-$ ($B^- = O_2^-, Cl^-$) were observed to increase with increasing gas phase acidity of MH [29, 30]. Further investigation of this relationship was performed by McMahon and Larson [32, 33] who measured the bond strengths of the halide ions F^- and Cl^- to a large variety of compounds MH. Stronger hydrogen bonding was determined in the fluoride adducts $MH{\cdot}F^-$ with a linear dependence on the gas phase acidity of MH while only a rough correlation with gas phase acidity was observed for the $MH{\cdot}Cl^-$ bond strengths. The contrast in behavior of F^- and Cl^- was explained in terms of the different gas phase basicities of the two anions [33]. A larger degree of proton transfer to the halide ion occurs in the complexes $MH{\cdot}F^-$ as a result of the stronger basicity of the smaller F^- anion and the hydrogen bonds formed have considerable covalent character. The degree of proton transfer in the complexes $MH{\cdot}Cl^-$ is smaller and the hydrogen bonds are of a more electrostatic character [33]. The increased exothermicity of the $MH{\cdot}F^-$ forming reaction derives largely from the exothermicity of the proton transfer and, thus, the increase in the hydrogen bond energy directly follows the acidity of MH. In the absence of substantial proton transfer in the complexes $MH{\cdot}Cl^-$ a less pronounced relationship between bond strength and gas phase acidity is observed. A simple relationship between hydrogen bond strength and gas phase acidity was not observed for the complexes $MH{\cdot}Cl^-$ where MH are the carbon acids [3]. The acidity of many carbon acids is due not only to the presence of inductively electron withdrawing groups but also to π delocalization of the negative charge in the anion. Cyclopentadiene is an extreme example of this. The poor correlation between MH gas phase acidities and $MH{\cdot}Cl^-$ bond strengths is not surprising as the π delocalization in M^- should only be a small effect in the $MH{\cdot}Cl^-$ complexes.

In Chapter 2 of the present work determinations of the hydrogen bond free energies, $-\Delta G^o$, corresponding to the gas phase bromide association (BrA) reactions $YPhOH + Br^- = YPhOH{\cdot}Br^-$, from equilibrium measurements with the PHPMS, are described. Very little proton transfer is anticipated in the singly subtituted phenol complexes due to the high gas phase acidity of HBr [34]. Taft substituent effect analysis [35] of the hydrogen bond free energies in $YPhOH{\cdot}Br^-$ is used to evaluate the substituent contributions to stability as well as investigate the relationship between hydrogen bond strength and gas phase acidity. The same treatment was performed for the complexes $YPhOH{\cdot}Cl^-$ and $YPhOH{\cdot}I^-$ whose bond free energies were determined previously in this laboratory [3, 36]. The findings for the YPhOH·X$^-$ systems (X$^-$ = Cl$^-$, Br$^-$ and I$^-$) can be generalized to MH·B$^-$ hydrogen bonded complexes.

Hydrogen bond strength determinations, -ΔH°, corresponding to gas phase reactions (1.3) and (1.4),

$$HO^- + HOH = HO^-{\cdot}HOH \qquad (1.3)$$

$$CH_3O^- + CH_3OH = CH_3O^-{\cdot}HOCH_3 \qquad (1.4)$$

from measurement of the temperature dependence of the equilibrium constants with the PHPMS, are also described in the present work (Chapter 6). Reactions (1.3) and (1.4) are of fundamental interest (see below) and a previous hydrogen bond strength determination for $CH_3O^-{\cdot}HOCH_3$, obtained directly with a PHPMS, has been used to anchor a scale of relative bond strengths from ICR equilibrium measurements [37]. The energetics of reactions (1.3) and (1.4) were re-determined in the present work due to differences in previous experimentally determined -ΔH° values for these reactions [26, 28, 37-39]. Because of the conflicting results, some possible sources of error such as temperature measurement and side reactions were re-examined.

Gas phase information on the stabilities of ion-molecule pairs is of importance in determining the role of solvation in fundamental molecular properties such as relative acidities, basicities and nucleophilicities [2, 40-43]. Bond strength determinations for ion-molecule complexes such as $HO^-{\cdot}HOH$ and $CH_3O^-{\cdot}HOCH_3$ can be used to evaluate the effect of a solvent molecule on relative acidity and this number can then be compared to known gas phase and solution phase data. For example, from experimentally determined enthalpy changes methanol is observed to be more acidic than water in the gas phase [38] while the acidities of both are similar in aqueous solution [40].

$$HO^- + CH_3OH = H_2O + CH_3O^- \qquad (1.5)$$
$$\Delta H^\circ = -9.5 \text{ kcal/mol}$$

$$HO^- (aq) + CH_3OH (aq) = H_2O (aq) + CH_3O^- (aq) \qquad (1.6)$$
$$\Delta H^\circ \approx -1 \text{ kcal/mol}$$

The change in relative acidity is due to the better solvation of the hydroxide ion in water. The effect of one solvent molecule on the relative acidity of water and methanol has been determined by Ikuta [44] with ab initio MO calculations using a high level basis set (6-31G* + diffuse functions + electron correlation).

$$HO^- \cdot HOH + CH_3OH = H_2O + CH_3O^- \cdot HOH \qquad (1.7)$$
$$\Delta H^\circ = -3.8 \text{ kcal/mol}$$

The enthalpy change of -3.8 kcal/mol shows that the addition of one solvent molecule accounts for over half the difference in gas phase versus aqueous phase acidity. Accurate gas phase determinations of ion-solvent pair bond strengths combined with gas phase acidity data can also be used to investigate such trends, i.e., ΔH° for reaction (1.7) = $D(HO^- \cdot HOH) - D(CH_3O^- \cdot HOH) + D(CH_3O^- - H^+) - D(HO^- - H^+)$.

Accurate bond strength determinations for $HO^- \cdot HOH$ and $CH_3O^- \cdot HOCH_3$ and the structures for these complexes [18, 19, 44-48] are required to construct intermolecular potential functions describing ion-molecule interactions involving HO^- and CH_3O^- in water and methanol respectively [18, 19]. As methanol and particularly water are common solvents for chemical reactions, many experimental and theoretical studies involving the interaction of a variety of simple anions with single water and methanol molecules have been performed [2, 3, 5, 6, 9, 10, 12, 16-19, 25-30, 32, 33, 37-39, 44-48].

As previously mentioned, the quantitative study of ion-molecule interactions in the gas phase can provide important characterization of the chemical bonding present in a variety of ion-molecule complexes. Chapters 3 and 4 of the present study involve equilibrium measurements of the reactions SB + X^- = SB·X^-, where SB are singly, doubly and triply substituted benzenes and X^- is Br^-, and C_6F_5Y + X^- = $YC_6F_5 \cdot X^-$, where C_6F_5Y are the perfluorobenzenes and X^- are F^-, Cl^-, Br^- and I^-. Previous work involving gas phase thermodynamic data for X^- (F^-, Cl^-, Br^- and I^-) and quantum mechanical calculations indicate the most stable substituted benzene complexes might have a variety of structures depending on X^- and the nature of the substituents [3, 7, 43, 49, 50]. Thus X^- may engage in hydrogen bonding to an aromatic proton or lead to a σ bonded complex or form a complex where X^- is on an axis perpendicular to the benzene plane. In the present work substituent effect analysis [35] of experimentally determined bond free energies for each class of substituted benzene complexes is employed to provide information on the bonding present in these adducts. Combining these results with structural information from previous calculations allows bonding assignments to be made.

In Chapter 5 the investigation of chemical bonding in ion-molecule complexes is extended to quinones and ethylenes, substituted with strong electron withdrawing groups (-F, -Cl and -CN), with the halide ions X^- (F^-, Cl^- and Br^-). These complexes have been observed both in solution and in the gas phase [51-55] and are of interest because the substituted quinones (SQ) and substituted ethylenes (SE) are strong electron acceptors, i.e., have large electron affinities [56, 57], and may stabilize σ bond formation on attack by the weaker halide nucleophiles (X^- = Cl^- and Br^-) [51]. In the present work discussion of the chemical bonding in the SQ·X^- and SE·X^- complexes is based on thermodynamic data corresponding to the gas phase reactions SQ + X^- =

$SQ{\cdot}X^-$ and $SE + X^- = SE{\cdot}X^-$ ($X^- = Cl^-$ and Br^-), obtained with the PHPMS, and ab initio MO calculations performed by Hirao et al. [58] determining stabilities and geometries for selected $SQ{\cdot}X^-$ and $SE{\cdot}X^-$ complexes ($X^- = F^-$, Cl^- and Br^-).

The final part of the present work describes a continuation of the extensive determinations of electron affinities of organic molecules (substitued benzenes, naphthalenes, anthracenes, quinones and perfluorobenzenes) performed in this laboratory with the PHPMS [56, 57, 59-64]. The electron affinity is one of the fundamental properties of a molecular negative ion and is defined as the difference in energy between the neutral molecule plus an electron at rest at infinity and the molecular negative ion, when both the negative ion and the neutral molecule are in their ground electronic, vibrational and rotational states. Typically, organic compounds with positive electron affinities have conjugated bonds resulting in a relatively low-lying unoccupied π^* molecular orbital (LUMO) which accepts the extra electron and becomes the singly occupied molecular orbital (SOMO). In addition to conjugation, the presence of electron withdrawing substituents, e.g., F, Cl, CN, NO_2, leads to a lowering of the LUMO energy and, thus, a higher electron affinity.

Chapter 7 describes determinations of the electron affinities of 20 cyclic diones, mostly substituted maleic and phthalic anhydrides and maleimides and phthalimides, by measurements with the PHPMS of the gas phase electron transfer equilibria (1.8)

$$A^- + B = A + B^- \qquad (1.8)$$

involving these compounds and reference compounds whose electron affinities were determined previously. From the results the effect of substituents on electron affinities for maleic and phthalic anhydrides are discussed and the magnitudes of these effects are compared to those observed earlier for substituted benzoquinones and naphthoquinones [56]. Comparison of the gas phase electron affinities with available solution phase reduction potential data [65-67] also permits evaluation of the solvation energies of the radical anions. This allows the relationship between electron affinities of the precursor neutral compounds and solvation exothermicities of the radical anions to be investigated.

1.2 The Pulsed Electron High Pressure Mass Spectrometer (PHPMS)

In the present work equilibrium measurements of the gas phase negative ion-molecule reactions of interest were achieved with the pulsed electron high pressure mass spectrometer (PHPMS). At working pressures of 1-5 torr the PHPMS fulfills the two major criteria for ion-molecule equilibrium measurements: 1) the reactants and products must be in thermal equilibrium with the surroundings, 2) sufficient time must be available for the system to reach chemical equilibrium. A brief description of the method and apparatus follows. For greater detail, see Kebarle [23].

1.2a PHPMS: The Method

A simplified diagram illustrating the ionization process in the PHPMS ion source is shown in Figure 1.1. The ion source typically contains 1-5 torr of the bath gas (usually methane) and millitorr concentrations of the reactants. A short 10-50 μs pulse of high energy (2.8 kV) electrons enters the ion source and ionizes the bath gas, creating secondary electrons. These electrons are slowed down on subsequent collisions with the bath gas molecules to near thermal energies. The slow electrons are then captured by reactant molecules with positive electron affinities and sufficient electron capture cross-sections, and the resultant excited ions are in turn thermalized by collisions with the bath gas. As

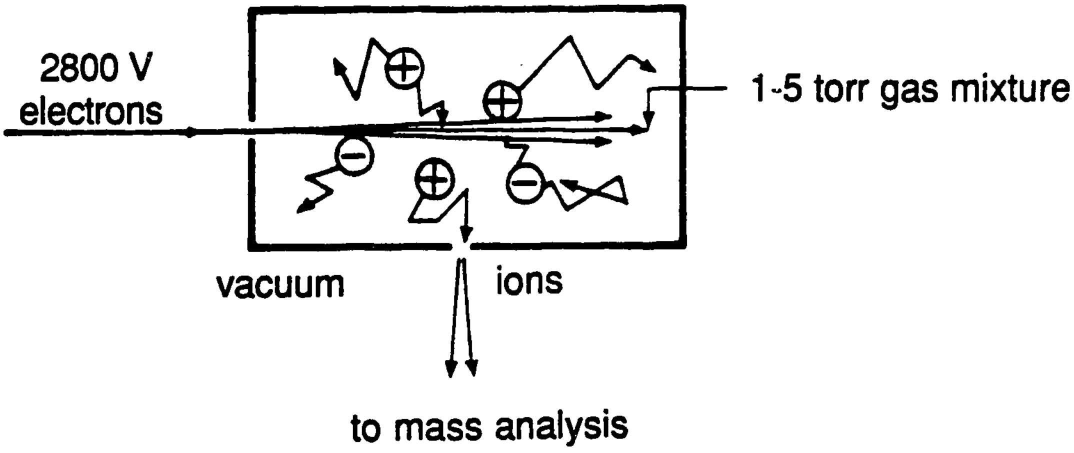
2800 V
electrons
1-5 torr gas mixture
vacuum
ions
to mass analysis

Figure 1.1 Ion source of pulsed electron high pressure mass spectrometer (PHPMS). Diffusion of ions to the wall is slow due to the relatively high bath gas pressure (1-5 torr). This leads to "ion trapping". Thermal conditions are also a consequence of high bath gas pressures.

the ions diffuse in the field free ion source they undergo thousands of collisions and under suitably selected conditions thermal ion-molecule equilibrium is achieved. The sequence of reactions which occur in the ion source for a typical ion-molecule association reaction (1.1) after the short electron pulse are shown below:

$$CH_4 + e^- \ (2.8\ \text{kV}) \longrightarrow CH_4^+,\ CH_3^+ \ldots\ldots \text{etc.} + 2e^- \qquad (1.9)$$

$$B + e^- \longrightarrow [B^-]^* \xrightarrow{CH_4} B^- + CH_4^* \qquad (1.10)$$

$$M + B^- \rightleftharpoons [M{\cdot}B^-]^* \xrightarrow{CH_4} M{\cdot}B^- + CH_4^* \qquad (1.11)$$

$$B^-,\ M{\cdot}B^- \longrightarrow \text{Diffuse to the walls} \qquad (1.12)$$

Ions diffusing into the vicinity of the very narrow ion exit slit in the ion source wall escape into the vacuum chamber where they are accelerated by an electric field, mass analyzed with a magnetic sector and detected with a secondary electron multiplier. The ions which arrive at the detector after the electron pulse are counted and the counts stored in a multiscaler as a function of time. Each ion intensity is accumulated over 5000-10000 pulses which leads to a better signal to noise ratio. The ion residence time in the ion source is typically in the millisecond range due to the absence of electric fields and slowness of ion diffusion to the wall at the pressures used. This is sufficient time for most ion-molecule reactions to reach chemical equilibrium.

1.2b PHPMS: The Apparatus

The gas handling plant (GHP), containing the 5 l bulb in which preparation of the desired gas mixtures takes place, is shown in Figure 1.2. The GHP consists of six VG ultra-high vacuum all metal valves (stainless steel with copper gaskets) mounted on a stainless steel manifold with the 5 l bulb and

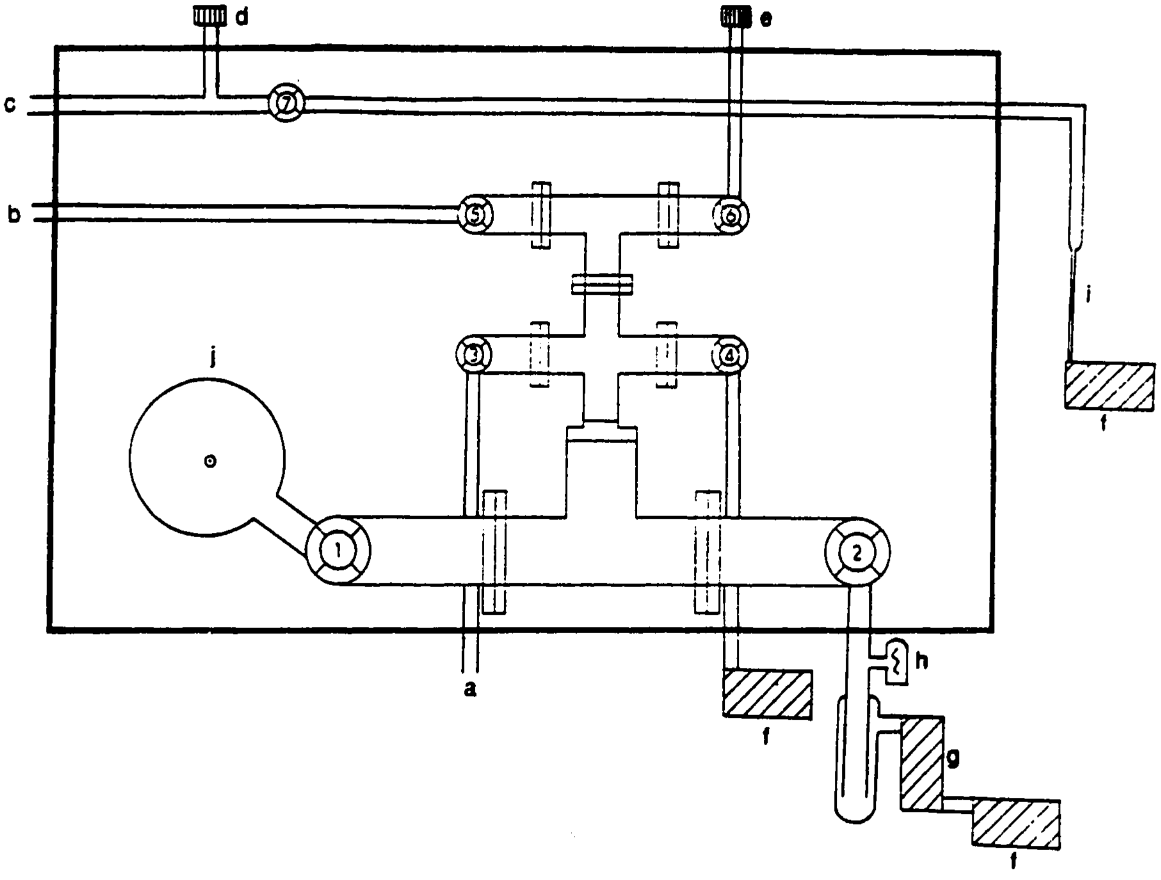

Figure 1.2 The Gas Handling Plant (GHP): (1) valve to 5 litre bulb; (2) valve to diffusion pump; (3) gas inlet valve; (4) valve to roughing pump; (5) valve to ion source; (6) valve to Validyne pressure gauge; (7) valve from ion source; (a) to gas cylinder; (b) to the ion source; (c) from the ion source; (d) Baratron manometer (0-10 torr); (e) Validyne manometer (0-1000 torr); (f) roughing pump; (g) diffusion pump; (h) ion gauge; (i) capillary; (j) 5 litre glass bulb.

other GHP components connected by borosilicate glass tubing. The whole system is contained in a box made of 2.5 cm thick asbestos boards which is heated by three GE 100 watt oven-type heaters covered with metal shields to ensure uniform heating. This arrangement allows the GHP to be baked at temperatures up to 250°C to remove any impurities present in the system. Typically, the GHP is operated at temperatures of ~150°C.

The bath gas (usually methane) is admitted to the evacuated stainless steel manifold and 5 l bulb from a high pressure gas cylinder attached to valve 3; see Figure 1.2. Typically, an atmosphere of the bath gas is admitted which is measured by a Validyne pressure gauge (reluctance manometer) attached to valve 6. After shutting off the 5 l bulb with valve 1, the reactants (commonly liquids or solids dissolved in an inert solvent) are injected directly into the bulb through a rubber septum. The septum is attached to a small glass tube extension on the bulb. It is important to replace the septum when introducing a new series of compounds. The pressures of the reactants in the bulb are calculated from the number of moles injected in and the GHP temperature. The GHP temperature of ~150°C ensures complete vaporization of the majority of the liquids and solids injected into the bulb.

After approximately 30 minutes of mixing, valve 1 (Figure 1.2), leading to the re-evacuated manifold, is opened and valve 5 is used to control the flow of gas to the ion source. The glass line leading from the GHP to the ion source is wrapped with heating tape and kept at ~100°C in order to prevent the condensation of the reactants on the glass wall. A slow gas flow through the ion source is achieved by having a gas outlet tube from the ion source connected to a rough pump through a capillary (via valve 7). Gas flow ensures the presence of a fresh gas mixture in the ion source at all times during an experiment. The slow nature of the flow means that the total pressure in the ion source can be kept nearly constant while collecting ion intensity profiles for the various ions present in the ion source. This is an especially important requirement when measuring ion-molecule association equilibria such as reaction (1.1) as the ion ratio, i.e., $M{\cdot}B^-/B^-$, is directly dependent on the ion source pressure; see Chapter 2. The ion source pressure is measured by a 0-10 torr Baratron pressure gauge (capacitance manometer) connected to the ion source gas outlet line prior to valve 7.

After the experiment, valve 5 (Figure 1.2) is shut and the GHP is pumped by rotary pump (valve 4) down to pressures in the millitorr range. Subsequent pumping by an oil diffusion pump (valve 2) with a liquid nitrogen cold trap lowers the pressure to $\sim 10^{-6}$ torr.

The body of the PHPMS is shown in Figure 1.3. The electron gun, ion source, ion acceleration tower and mass detection system are housed in a vacuum chamber which is pumped by high capacity diffusion pumps. While in operation, low pressures outside the ion source are essential in order to avoid the occurrence of ion-molecule collisions in the region between the ion source and the detector. If collisions occur in this region the detected ion intensities are not a true representation of the ion populations inside the ion source. To cope with the gas outflow from the ion source, a 6 inch water-cooled oil diffusion pump is positioned below the stainless steel manifold (28, Figure 1.3) which holds the major components of the PHPMS. The ion acceleration and mass analysis region is differentially pumped by a 4 inch diffusion pump (29). A low pressure in this region is desirable, especially for ion-molecule association equilibrium measurements; see Chap. 3. Under typical experimental conditions (1-5 torr pressure in the ion source), the manifold pressure is in the 10^{-4}-10^{-5} torr range while the pressure in the flight tube of the mass analyzer (27) is $\sim 10^{-6}$ torr. At these pressures the mean free path, i.e., the average distance between

Figure 1.3

A.	Electron Gun
1.	Filament
2.	Drawout
3.	Extractor
4-6.	Focusing and accelerating electrodes
7-8.	Electron deflection plates in X and Y directions
9.	Electric and magnetic shield
B.	Ion Source
10.	Ion source block with heaters
11.	Wire mesh electric shield
12.	Electron entrance slit
13.	Electron trap and ion repeller
14.	Ion exit slit flange
15.	Gas inlet and outlet tubes
16.	Ion source lid flange with kovar seal
17.	Support of ion source
18.	Insulator of support
C.	Ion Acceleration Tower
19-24.	Cylindrically symmetrical electrodes
25.	Collimating and ion deflecting slits
26.	Flange carrying entrance into mass analyzer slit
27.	Mass analyzer tube
D.	Vacuum System
28.	To 6 inch pump
29.	To 4 inch pump

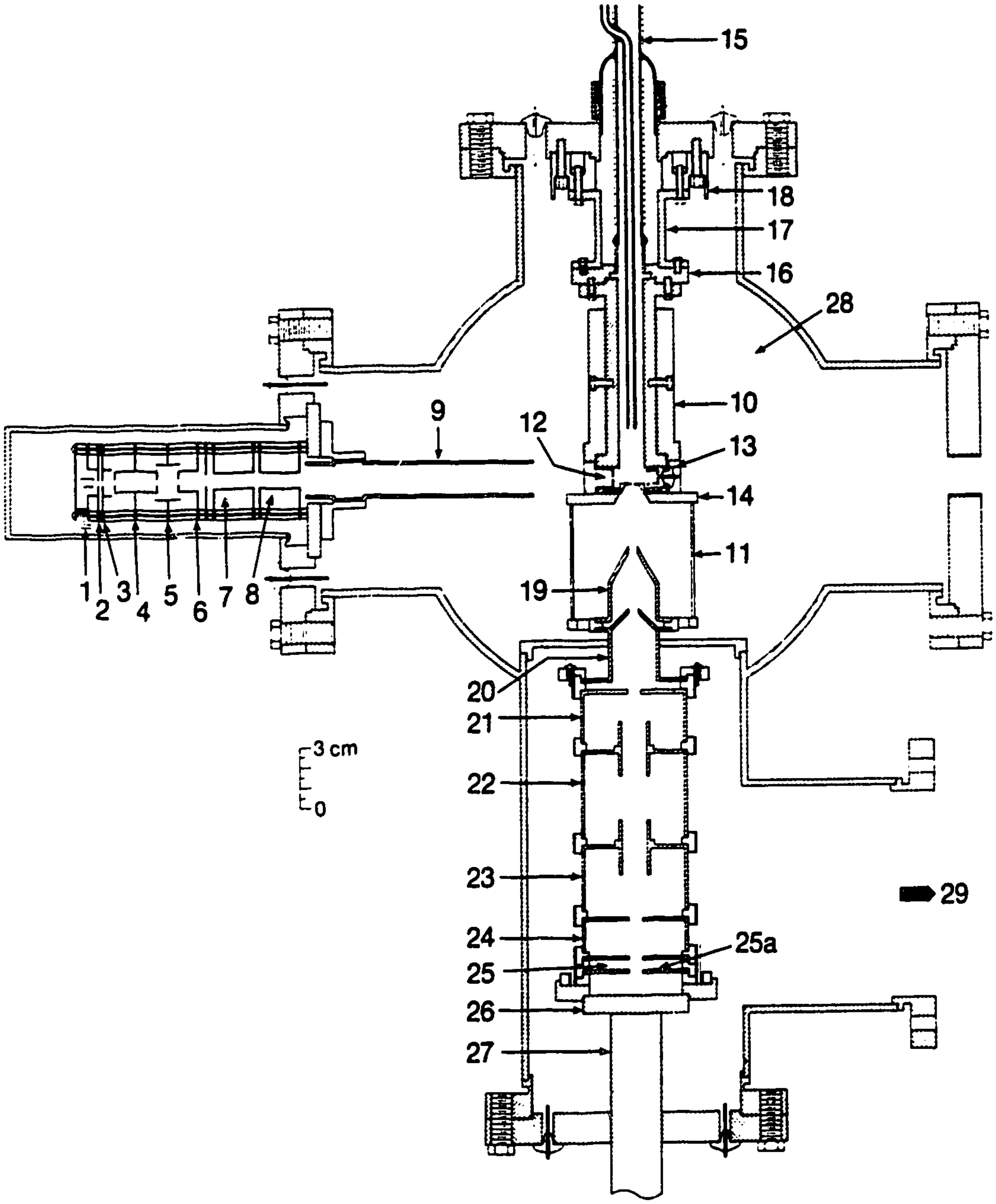
15
18
17
16
28
10
9
12
13
14
11
19
1
2
3
4
5
6
7
8
20
21
22
23
24
25a
25
26
27
29
3 cm
0

Figure 1.3 Main components of the pulsed electron high pressure mass spectrometer: ion source, electron gun and ion accelerating tower.

collisions, is greater than the distance travelled by the ion from the ion source to the detector.

The electron gun assembly is shown in detail in Figure 1.3. Electrons emitted from the heated filament (1, Figure 1.3) are accelerated and focused by a series of electrodes and plates (2-8) towards a narrow electron entrance slit in the ion source wall. By keeping the filament at -2800 V relative to the ion source potential (absolute potentials of filament and ion source are -4000 V and -1200 V respectively) high velocity electrons are generated which are necessary for penetration of the high pressure ion source. Focusing of the electron beam along the z axis is achieved by electrodes (2-6) with two pairs of deflection plates (7-8) positioning the beam in the x and y directions; see Figure 1.3. The final position of the electron beam is attained by adjusting the electrode voltages until a maximum current is read on a microammeter connected to the electron trap/ion repeller plate inside the ion source (13, Figure 1.3). Some minor adjustments to the focusing are usually required when gas is present in the ion source. The positioning of the filament at a considerable distance from the ion source in this arrangement (~20 cm) ensures a longer filament lifetime as exposure to the gas escaping from the ion source electron entrance slit is minimal. Thoriated iridium was the preferred filament material under the experimental conditions of the present work; this material has a superior operational lifetime compared to filaments made of 75/25 tungsten/rhenium. Another advantage of the distant positioning of the filament is that the hot filament does not effect the temperature of the ion source, which is solely controlled by the ion source heaters.

Due to the use of a magnetic sector for mass analysis in the PHPMS used in the present work, the electron gun has to be extensively shielded with multiple layers of high μ metal sheets. This is necessary because even weak stray magnetic fields can deflect the electron beam and change the ionizing electron current. This effect is mass dependent and results in x,y refocusing of the electron beam being required to obtain maximum intensity for ions of different masses. This, of course, is highly undesirable.

Pulsing of the electron gun is achieved by varying the potential of the drawout electrode (2, Figure 1.3) at regular intervals. A schematic diagram of the pulsing system is shown in Figure 1.4. The electron gun is switched off by applying a potential of -50 V to the drawout electrode relative to the filament potential. The gun is turned on by a short 10-50 μs positive pulse to the drawout plate (+50 V with respect to the filament), delivered by a floating pulse amplifier which is triggered by a master pulse generator. The triggering pulse from the master pulse generator simultaneously triggers the sweep of the multichannel scaler which allows a time dependence of the ion intensity after the ionizing pulse to be obtained. With the gun on electrons are allowed to penetrate the ion source for the duration of the pulse. Then the drawout electrode returns to its original negative potential with respect to the filament. The frequency of the cycle is controlled by the master pulse generator at ~5 ms/cycle.

A second pulse generator connected to the electron trap/ion repeller plate (13, Figure 1.3) is used to destroy the remaining negative ions in the ion source before repetition of the cycle. This is achieved by an ion repeller pulse of ~50 μs duration and -50 V relative to the ion source which is applied ~1 ms before repetition of the electron pulse; see Figure 1.4.

A schematic diagram of the ion source is shown in Figure 1.3. The gas mixture prepared in the GHP flows in and out of the ion source through concentric glass tubes (15, Figure 1.3). The inlet (outer) glass tube is joined to the metal ion source by a kovar seal (16).

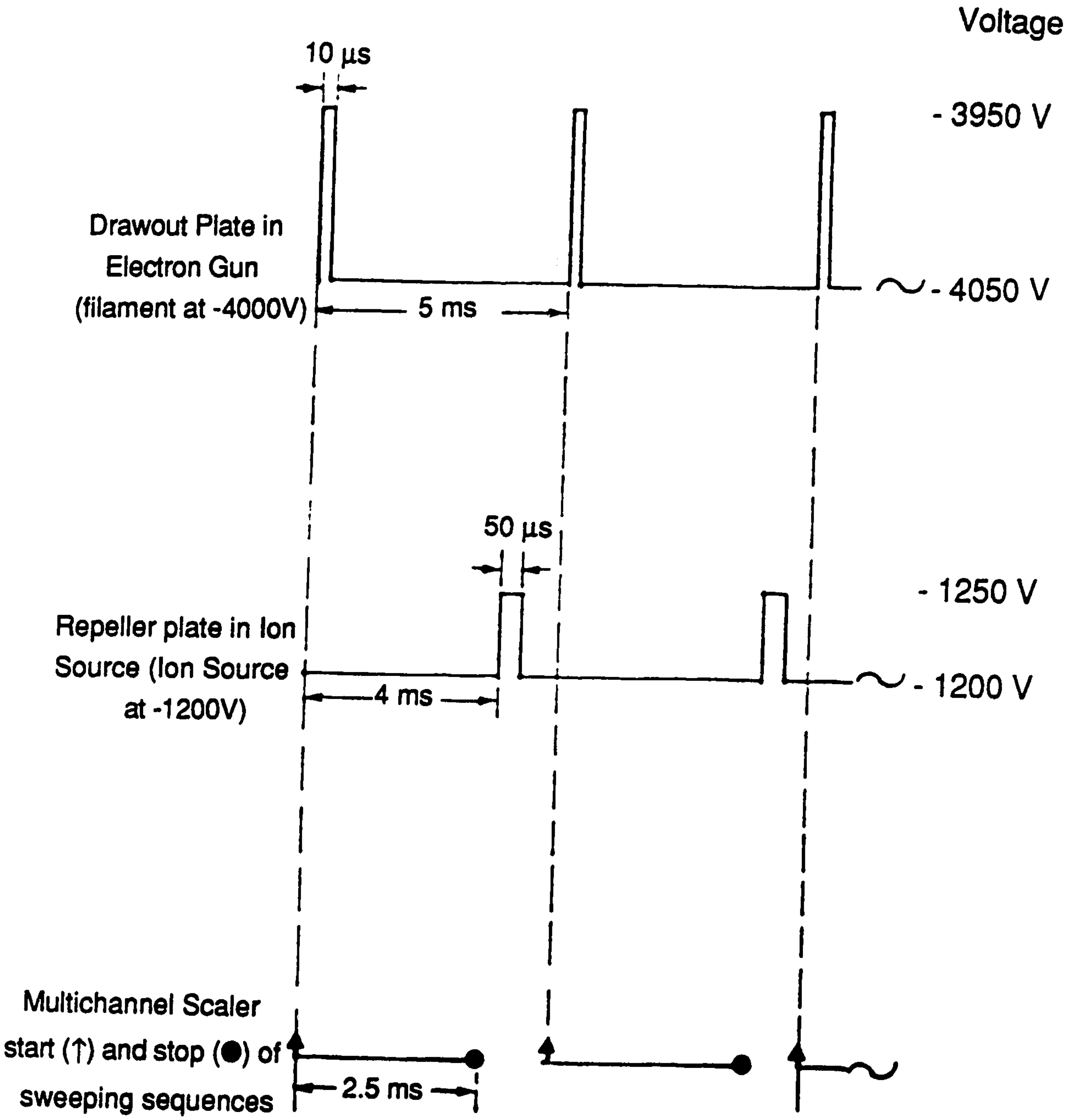
Voltage
10 µs
- 3950 V
Drawout Plate in Electron Gun (filament at -4000V)
5 ms
- 4050 V
50 µs
- 1250 V
Repeller plate in Ion Source (Ion Source at -1200V)
4 ms
- 1200 V
Multichannel Scaler start (↑) and stop (●) of sweeping sequences
2.5 ms

Figure 1.4 Pulsing sequence with typical voltages and durations.

The ion source consists of a 10 cm long cylindrical stainless steel block with a circular 1.3 cm diameter channel running through it. One end of the block is attached to a stainless steel cylindrical support (17, Figure 1.3) which, in turn, is supported, via an insulator (18), by the flange. At the other end of the ion source is a 1.3 cm diameter channel which runs perpendicular to the main axis channel. This channel is the reaction chamber. The exits of this channel are blocked off by two hat-like flanges which carry the electron entrance slit (12) and the electron trap/ion repeller plate (13). The central channel is sealed by a flange carrying the ion exit slit (14). Thin gold wire gaskets are used to tightly seal these flanges to the ion source. Both the electron entrance and ion exit slits are made by spot-welding two small stainless steel razor blade pieces across a 2 mm hole in the center of the flange. This tricky procedure is carried out under a microscope, using a specially designed jig to maneuver the razor blade pieces into the desired position. With this arrangement slit widths of 0.010-0.015 mm are achieved. These narrow slit dimensions are necessary in order to achieve near molecular flow of the gas from the ion source to the vacuum chamber. Under molecular flow conditions the ions do not undergo collisions while passing through the slits and, thus, no serious distortion of the ion populations present in the ion source occurs. In addition, molecular flow through the ion exit slit is required to avoid the effects of cooling due to adiabatic expansion of the gas into the vacuum. Under dynamic flow conditions this cooling effect promotes higher cluster formation.

Heating of the ion source is achieved by inserting 6 cartridge heaters into the circular channels of the stainless steel heating jacket that surrounds the ion source (10, Figure 1.3). The ion source heaters are held in place by two semi-circular shields which are screwed to the jacket. The heaters are supplied with ac power via a transformer (Variac). An isolation transformer has to be positioned between the Variac and the ion source heaters because the heaters are floating at the ion source potential while the machine is in operation.

The temperature of the gas in the ion source is determined indirectly by measuring the temperature of the inner wall of the reaction chamber. A small hole was drilled into the ion source which terminated near the inner wall. This hole is positioned in the plane of the electron entrance and ion exit slits. The thermocouple, which is contained within a hollow screw, is tightly screwed into the hole to ensure good thermal contact between the thermocouple tip and the ion source wall. Modifications of this method of ion source temperature measurement are described in Chapter 6.

A cylindrical wire mesh electric shield (11, Figure 1.3) is positioned outside the ion source below the ion exit slit. Its purpose is to ensure a uniform electric field for the ions to be accelerated from the ion exit slit to the first electrode in the ion acceleration tower. The supporting cage consists of eight posts held rigid by a solid base at one end and a ring at the other. The wire mesh is spot-welded to these posts and allows for a high pumping speed to be maintained.

The ion acceleration tower is shown in detail in Figure 1.3. Ions escaping the ion source (14) into the vacuum chamber are accelerated and focused by a series of electrodes (19-25a) onto the mass analyzer entrance slit (26). Ion focusing is relatively easy because of the small dimensions of the ion exit slit. An acceleration voltage of 1200 V is applied to the ions as the mass analyzer is at ground potential.

Mass analysis of the ions is performed with a 90°, 15 cm radius magnetic sector. Mass scanning is achieved by changing the magnetic field at a constant acceleration voltage. No correction for ion transmission is required for magnetic sector instruments.

After mass analysis the ions are detected by a secondary electron multiplier (Spiraltron 4219 EIC). The Spiraltron consists of a glass cone attached to a glass stem and is coated on the inside by a high resistance film. This electron multiplier has a gain of 3 x 10^8 when an acceleration voltage of 3.0 kV is placed across the two ends. Typical operational voltages for negative ion detection are: Cone +600 V (ion entrance); Bottom of stem (electron exit) +3600 V. The negative output pulses from the multiplier are collected and amplified before being counted. The amplifier (EG + G Quad Amplifier AN201/N) has sufficient sensitivity to detect secondary pulses which represent less than 10^6 electron charges and resolve electron pulses separated by as little as 10^{-8} s. The amplified pulses are fed into a discriminator where a gate level is set to allow only signal pulses to be transmitted while low level noise is rejected. The amplifier/discriminator arrangement allows for ion count rates up to 10^7 per second which is more than sufficient since typical ion intensities for the PHPMS are 10^3-10^5 cps The count rates are measured with an Ortec Model 441 ratemeter. The amplified pulses are collected by a multiscaler and dedicated computer (Le Croy 3500 computer with the Le Croy multiscaler interface MCS 3521A). The sweep of the multichannel scaler is synchronized with the triggering pulse of the electron gun; see Figure 1.4. In a typical experiment a dwell time of 4 µs per channel is set and 512 channels are used. The ions detected in the first 4 µs after the beginning of the electron pulse are stored in the first channel of the multiscaler. The ions detected from 4-8 µs are stored in the second channel and so on for 512 channels. Thus, the change in ion intensity over ~2.0 ms is followed. After ~5 ms the electron gun is pulsed again and the ions detected for each channel are added to those collected previously. The ion signal is typically collected over 5000-10000 pulses in order to achieve a good intensity ion profile. The duration of the ion profile can be adjusted by changing the dwell time per channel.

The various ion profiles collected in an experiment are stored in the Le Croy computer. Initial identification of the ions present in the ion source is achieved by recording a complete mass spectrum of the ionized gas mixture; see Chapter 4. The ion profiles collected can be displayed together on the screen of the Le Croy computer, which contains several programmes for data analysis.

REFERENCES

1. "Gas Phase Ion Chemistry". Editor M. T. Bowers. Academic Press. New York (1979). Vol. 1 and 2.
2. P. Kebarle, Annu. Rev. Phys. Chem., 28, 445 (1977).
3. M. A. French, S. Ikuta and P. Kebarle, Can. J. Chem., 60, 1907 (1982).
4. S. Chowdhury and P. Kebarle, J. Chem. Phys., 85, 4989 (1986).
5. T. D. Mark and A. W. Castleman, Jr., Adv. Atom. Molec. Phys., 20, 65 (1985).
6. K. Hiraoka, S. Misuze and S. Yamabe, J. Phys. Chem., 92, 3943 (1988).
7. K. Hiraoka, S. Misuze and S. Yamabe, J. Phys. Chem., 91, 5294 (1987).
8. K. Hiraoka, S. Misuze and S. Yamabe, J. Chem. Phys., 87, 3647 (1987).
9. M. Meot-Ner, J. Am. Chem. Soc., 110, 3854 (1988).
10. M. Meot-Ner, J. Am. Chem. Soc., 110, 3858 (1988).
11. J. W. Larson, J. E. Szulejko and T. B. McMahon, J. Am. Chem. Soc., 110, 7604 (1988).
12. J. W. Larson and T. B. McMahon, J. Am. Chem. Soc., 109, 6230 (1987).
13. J. W. Larson and T. B. McMahon, J. Am. Chem. Soc., 107, 766 (1985).
14. H. van der Wel and N. M. M. Nibbering, Recl. Trav. Chim. Pays-Bas, 107, 491 (1988).
15. J. C. Sheldon, G. J. Currie, J. Lahnstein, R. N. Hayes and J. Bowie, Nouv. J. Chim., 9, 205 (1985).
16. J. Chandrasekar, D. C. Spellmeyer and W. L. Jorgensen, J. Am. Chem. Soc., 106, 903 (1984).
17. J. Chandrasekar and W. L. Jorgensen, J. Am. Chem. Soc., 107, 2974 (1985).

18. J. Gao, D. S. Garner and W. L. Jorgensen, J. Am. Chem. Soc., 108, 4784 (1986).
19. W. L. Jorgensen and M. Ibrahim, J. Comput. Chem., 2, 7 (1981).
20. A. G. Harrison, "Chemical Ionization Mass Spectrometry". CRC Press. Boca Raton, Florida (1983).
21. G. W. Caldwell, J. A. Masucci and M. G. Ikonomou, Org. Mass Spectrom., 24, 8 (1989).
22. H. P. Tannenbaum, J. D. Roberts and R. C. Dougherty, Anal. Chem., 47, 49 (1975).
23. P. Kebarle, "Techniques of Chemistry: Techniques for the Study of Ion-Molecule Reactions". Editors J. M. Farrar and W. H. Saunders, Jr. Wiley-Interscience. New York (1988). Chapter 5.
24. P. R. Kemper and M. T. Bowers, "Techniques of Chemistry: Techniques for the Study of Ion-Molecule Reactions". Editors J. M. Farrar and W. H. Saunders, Jr. Wiley-Interscience. New York (1988). Chapter 1.
25. R. G. Keese and A. W. Castleman, Jr., J. Phys. Chem. Ref. Data, 15, 1011 (1986).
26. M. Arshadi and P. Kebarle, J. Phys. Chem., 74, 1483 (1970).
27. M. Arshadi, R. Yamdagni and P. Kebarle, J. Phys. Chem., 74, 1475 (1970).
28. J. D. Payzant, R. Yamdagni and P. Kebarle, Can. J. Chem., 49, 3308 (1971).
29. R. Yamdagni and P. Kebarle, J. Am. Chem. Soc., 93, 7139 (1971).
30. R. Yamdagni, J. D. Payzant and P. Kebarle, Can. J. Chem., 51, 2507 (1973).
31. J. B. Cumming, M. A. French and P. Kebarle, J. Am. Chem. Soc., 99, 6999 (1977).

32. J. W. Larson and T. B. McMahon, J. Am. Chem. Soc., 105, 2944 (1983).

33. J. W. Larson and T. B. McMahon, J. Am. Chem. Soc., 106, 517 (1984).

34. S. G. Lias, J. E. Bartmess, J. F. Liebman, J. L. Holmes, R. D. Levin and W. G. Mallard, J. Phys. Chem. Ref. Data, 17, Suppl. No. 1 (1988).

35. R. W. Taft and R. D. Topsom, Prog. Phys. Org. Chem., 16, 1 (1987).

36. G. Caldwell and P. Kebarle, unpublished work.

37. G. Caldwell, M. D. Rozeboom, J. P. Kiplinger and J. E. Bartmess, J. Am. Chem. Soc., 106, 4660 (1984).

38. M. Meot-Ner and L. W. Sieck, J. Phys. Chem., 90, 6687 (1986).

39. C. R. Moylan, J. A. Dodd, H. Chan-Chung and J. I. Brauman, J. Chem. Phys., 86, 5350 (1987).

40. J. E. Bartmess, J. A. Scott and R. T. McIver, Jr., J. Am. Chem. Soc., 101, 6056 (1979).

41. G. Caldwell, T. F. Magnera and P. Kebarle, J. Am. Chem. Soc., 106, 959 (1984).

42. W. N. Olmstead and J. I. Brauman, J. Am. Chem. Soc., 99, 4219 (1977).

43. G. W. Dillow and P. Kebarle, J. Am. Chem. Soc., 110, 4877 (1988).

44. S. Ikuta, J. Comput. Chem., 5, 374 (1984).

45. W. P. Kraemer and G. H. F. Diercksen, Theor. Chim. Acta, 23, 398 (1972).

46. M. D. Newton and S. Ehrenson, J. Am. Chem. Soc., 93, 4971 (1971).

47. B. O. Roos, W. P. Kraemer and G. H. F. Diercksen, Theor. Chim. Acta, 42, 77 (1976).

48. C. M. Rohlfing, L. C. Allen, C. M. Cook and H. B. Schlegel, J. Chem. Phys., 78, 2498 (1983).

49. K. Hiraoka, S. Mizuse, and S. Yamabe, Chem. Phys. Lett., 147, 174 (1988).

50. K. Hiraoka, S. Misuze and S. Yamabe, J. Chem. Phys., 86, 4102 (1987).

51. J. Bowie, Aust. J. Chem., 30, 2161 (1977).
52. G. Briegleb, W. Liptay and R. Fick, Z. Physik. Chem., 33, 181 (1962).
53. G. Heublein, S. Spange and P. Hallpap, J. Prakt. Chem., 321, 503 (1979).
54. J. A. A. de Boer, D. N. Reinhoudt, J. W. H. M. Uiterwijk and S. Harkema, J. Chem. Soc., Chem. Commun., 194 (1982).
55. S. Spange and G. Heublein, Z. Chem., 28, 218 (1988).
56. T. Heinis, S. Chowdhury, S. L. Scott and P. Kebarle, J. Am. Chem. Soc., 110, 400 (1988).
57. S. Chowdhury and P. Kebarle, J. Am. Chem. Soc., 108, 5453 (1986).
58. G. Paul, K. Hirao, S. Obata and P. Kebarle, in preparation.
59. S. Chowdhury, T. Heinis, E. P. Grimsrud and P. Kebarle, J. Phys. Chem., 90, 2747 (1986).
60. E. P. Grimsrud, G. Caldwell, S. Chowdhury and P. Kebarle, J. Am. Chem. Soc., 107, 4627 (1985).
61. S. Chowdhury, E. P. Grimsrud, T. Heinis and P. Kebarle, J. Am. Chem. Soc., 108, 3630 (1986).
62. S. Chowdhury, T. Heinis and P. Kebarle, J. Am. Chem. Soc., 108, 4662 (1986).
63. S. Chowdhury, H. Kishi, G. W. Dillow and P. Kebarle, Can. J. Chem., 67, 603 (1989).
64. G. W. Dillow and P. Kebarle, J. Am. Chem. Soc., 111, 5592 (1989).
65. M. E. Peover, Trans. Faraday Soc., 58, 2370 (1962).
66. J. B. Nagy, O. B. Nagy and A. Bruylants, J. Phys. Chem., 78, 980 (1974).
67. O. B. Nagy, H. Lion and J. B. Nagy, Bull. Soc. Chim. Belg., 84, 1053 (1975).

CHAPTER 2

STABILITIES IN THE GAS PHASE OF HYDROGEN BONDED COMPLEXES, $YC_6H_4OH{\cdot}X^-$, OF SUBSTITUTED PHENOLS, YC_6H_4OH, WITH HALIDE ANIONS X^- (Cl^-, Br^- and I^-)

2.1 Introduction

In the present work bond free energies, $-\Delta G^{o}_{XA}$, corresponding to the gas phase reaction (2.1) involving phenols with substituents Y were determined from measurements of halide association (XA) equilibria (2.1) with a pulsed electron high pressure mass spectrometer (PHPMS).

$$YPhOH + X^- = YPhOH{\cdot}X^- \qquad (2.1)$$

The bond free energies of 26 differently substituted phenol complexes (X^- = Br^-) are reported here. Data for a smaller set of 5 phenols and Cl^- was published earlier [1] and data for 5 phenols and I^- are available from previous unpublished work from this laboratory [2]. These combined results provide quite a complete set of data for the effect of substituents Y on the hydrogen bonding of the phenols to the halide ions. Hydrogen bonding is favored in these complexes because of the acidic nature of the protic hydrogen [3, 4]; see structure I.

---

1. A version of this chapter has been accepted for publication: G. J. C. Paul and P. Kebarle, Can. J. Chem., 1990.

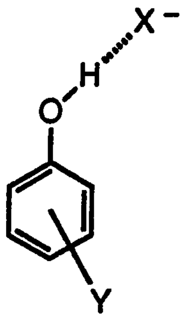

I

Clustering data are of interest in a number of areas [5]. For example, hydrogen bonded adduct ions MH·X$^-$, where MH are analytes with protic hydrogens, are observed in analytical mass spectrometric techniques such as Chemical Ionization, Atmospheric Pressure Ionization and Fast Atom Bombardment [5-8] and knowledge regarding the stabilities of such ions is useful in these areas. Thermochemical information on hydrogen bonded negative cluster ions is also of interest because these species are known to exist in the earth's atmosphere [9]. However, the principal interest in these data derives from previous work [1, 10-14] which attempted to establish some general principles concerning the stability of hydrogen bonded ion-molecule complexes involving ions B$^-$ with complete electron shells.

A very simple and useful systematization was the observation that for compounds MH with protic hydrogens such as the oxygen acids (alcohols, carboxylic acids, phenols) the strength of the hydrogen bond to a given negative ion B$^-$, in the complex MH·B$^-$, increases regularly with increase of the gas phase acidity of MH [1, 10-15]. Thus, a plot of the hydrogen bond energies in complexes to Cl$^-$, involving a series of MH as diverse as HOH, alcohols ROH, carboxylic acids RCO_2H and substituted phenols, shows a regular increase of bonding with increasing gas phase acidity of MH [13]. Similar relationships involving an even larger variety of compounds MH and F^- and Cl^- have been obtained by Larson and McMahon [16, 17].

In trying to understand the nature of this relationship it is useful to restrict the MH to a series of closely related compounds such as the substituted phenols. The first investigation of this series [1] involved Cl^-. The $YPhOH{\cdot}Cl^-$ series differs from the Br^- and I^- series in one important respect. The gas phase acidity of HCl is higher than that of unsubstituted phenol [3, 4]. However, strongly acidifying substituents such as CN and NO_2 lead to phenols whose acidity is higher than that of HCl [3, 4]. Therefore, in the $YPhOH{\cdot}Cl^-$ series there will be a significant increase of proton transfer from the phenols to Cl^- with increasing acidity of the phenols.

In a series of MH with X^- for which a large increase of the extent of proton transfer occurs, the increased exothermicity of the complex forming reaction may derive largely from the exothermicity of the proton transfer. In such a case the increase of the "hydrogen bond energy" $MH{\cdot}X^-$ as measured by $-\Delta G^o_{XA}$ will directly follow the acidity of MH. Of more interest is the question whether a relation of the bond energy with the acidity exists in the absence of substantially increased proton transfer. Due to the much higher gas phase acidity of HBr and HI, relative to HCl [3, 4], the formation of the complexes in reaction (2.1) involving Br^- and I^- is expected to involve at all times complexes corresponding largely to $MH{\cdot}X^-$, i.e., involving a much lower proton transfer increase. A comparison of the substituent effects on $-\Delta G^o_{XA}$ for these series with that for Cl^- should allow one to unravel the importance and nature of the effects in the absence of proton transfer.

Interesting theoretical studies of hydrogen bonded complexes to Cl^- have been reported by Hirao et al. [18]. Hydrogen bonded complexes of the type $ROH{\cdot}X^-$ form also in dipolar aprotic solvents. For a relevant study of $YPhOH{\cdot}Cl^-$, see Kolthoff [19], and for data on phenol phenoxide complexes, see Bordwell [20].

2.2 Experimental

The halide association equilibria (2.1), where $X^- = Br^-$, were measured using the pulsed electron high pressure mass spectrometer (PHPMS) described in Chapter 1.

The gas mixtures were prepared in the 5 litre glass bulb in the gas handling plant (GHP); see Figure 1.2. The 5 l bulb was initially filled with the bath gas methane to a pressure of ~700 torr. Known amounts of reactants were injected into the 5 l bulb either as pure liquids or solids dissolved in an inert solvent at room temperature. Two suitable solvents for the solid compounds were dimethylformamide (DMF) and toluene. These compounds have weak bromide association free energies ($\Delta G^o_{BrA,423K}$ (DMF) = -5.2 kcal/mol, $\Delta G^o_{BrA,303K}$ (Toluene) = -2.5 kcal/mol; determined in the present work) and therefore lead only to minor Br^- adduct formation. The GHP was kept at a temperature of ~150°C in order to completely vaporize all the reactants. After ~1 hour of mixing a constant gas flow through the ion source was established. The mixing time was longer than normal (~30 minutes) because phenols strongly adsorb on the glass wall of the 5 l bulb and time has to be allowed for the wall to saturate [13, 21]. The ion source was kept at 150°C (423 K) for all free energy determinations in the present work. Methane at ion source pressures of 2-4 torr was used as the major (bath) gas. Reactant, YPhOH, concentrations ranged from 0.1-15 mtorr.

Bromide ions were generated in the ion source by the dissociative electron capture of near thermal secondary electrons by dibromomethane, CH_2Br_2, present in 1.0-5.0 mtorr concentrations in the ion source. As the bromide ions diffused towards the walls of the ion source they collided with neutral YPhOH molecules and under suitably selected conditions equilibrium (2.1) was achieved. No higher order cluster ions, $(\mathrm{YPhOH})_{n>1}\cdot\mathrm{Br}^-$, or $\mathrm{CH_2Br_2\cdot Br^-}$ adducts [22] were observed under the experimental conditions described.

The electron beam was pulsed on for 10-50 µs every 5 ms in these experiments and each ion was observed over 6000-10000 pulses. The ions were counted and the counts stored in a multichannel scaler as a function of time after the electron pulse. The collection was typically for only 2-4 ms after the electron pulse. A typical intensity versus time profile of the ions involved in reaction (2.1), $X^- = \mathrm{Br}^-$, is shown in Figure 2.1. Thermodynamic equilibrium is assumed to be achieved between unsubstituted phenol and Br^- about ~0.5 ms after the electron pulse. Evidence for this is the constant vertical distance between the two ions which for the logarithmic intensity plot corresponds to a constant ion ratio. The decrease in the intensity of the two ions after ~0.7 ms is due to diffusion of the ions to the ion source wall. This occurs at nearly equal rates as the diffusion coefficient only has a small dependence on ion mass under PHPMS conditions [23].

$$K_{\mathrm{BrA}} = \frac{\mathrm{I(YPhOH\cdot Br^-)}}{\mathrm{I(Br^-)\,p(YPhOH)}} \qquad (2.2)$$

Substituting the ion intensity ratio of the adduct to bromide ion into expression (2.2) leads to the equilibrium constant, K_{BrA}. Accurate measurement of the ion source pressure with a capacitance manometer allows for accurate determination of the reactant pressure, p(YPhOH); see Chapter 1. The amount of YPhOH which is converted to $\mathrm{YPhOH\cdot Br^-}$ is negligible and, therefore, the concentration of YPhOH is constant throughout the experiment. From the

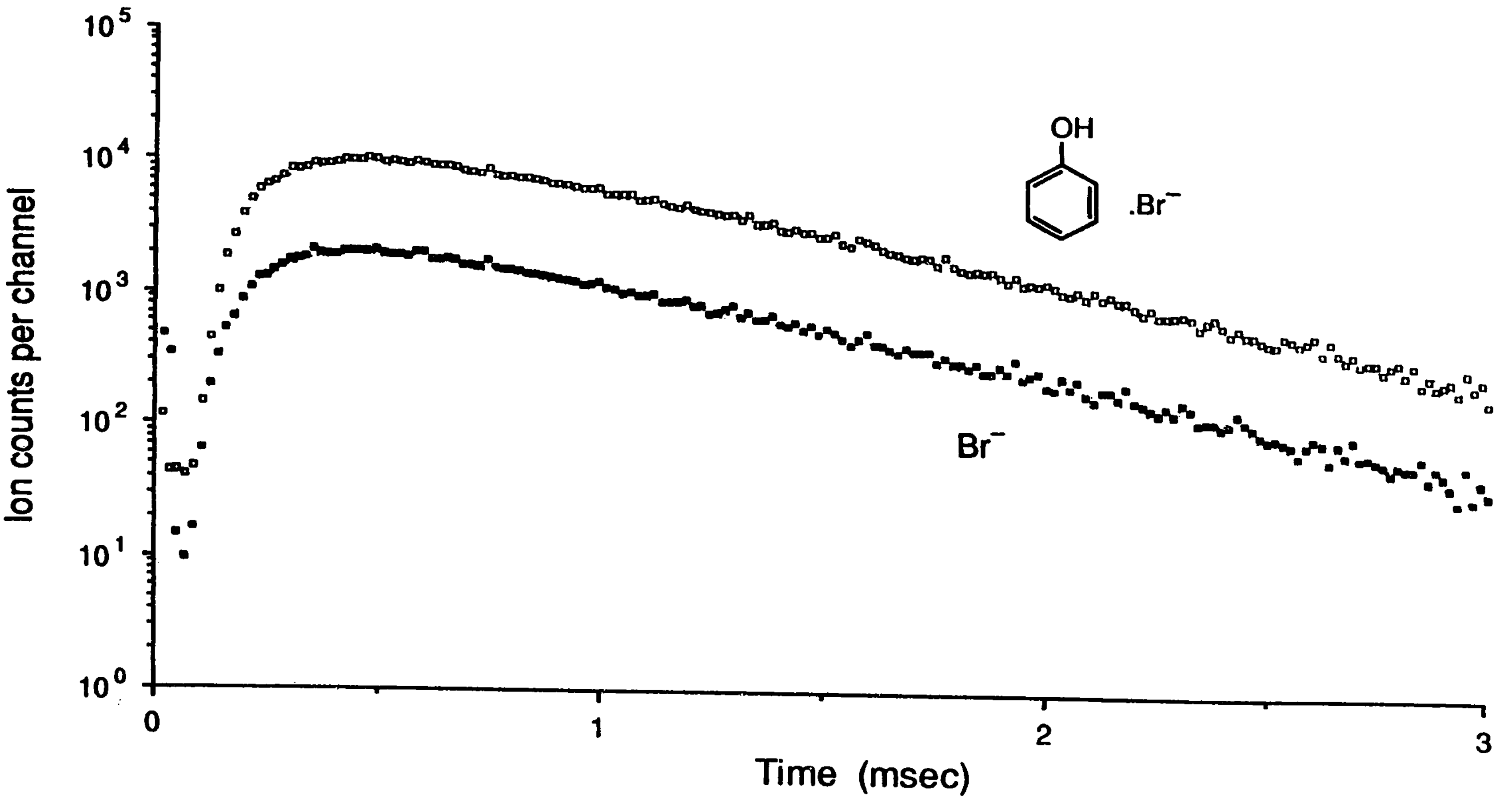

Figure 2.1 Raw data plot: ion intensity versus time after the 20 μs ionizing electron pulse. Obtained with a gas mixture of 2.8 torr CH_4, 10.0 mtorr PhOH and 3.4 mtorr CH_2Br_2 at 423K. Br^- ions result from dissociative electron capture by CH_2Br_2. The Br^- attachment equilibrium (2.1) becomes established some 0.5 ms after the electron pulse. The decrease of ion intensity after ~0.7 ms is due to diffusion of the ions to the wall.

equilibrium constant the bond free energy of YPhOH·Br$^-$, $-\Delta G^o_{BrA}$, can be obtained from expression (2.3).

$$-\Delta G^o_{BrA} = RT\ln K_{BrA} \tag{2.3}$$

For each experiment, where the partial pressure ratio of YPhOH to methane was constant, the equilibrium constant K_{BrA} was determined at three different ion source pressures between 2 and 4 torr in order to check its invariance. K_{BrA} was evaluated with two different YPhOH/methane partial pressure ratios where the ratio was changed by at least a factor of five.

The equilibrium constants for reaction (2.1) involving different partial pressures of YPhOH are shown in Figure 2.2. The K_{BrA} values are observed to be essentially invariant to the partial pressures of YPhOH.

Only values for $-\Delta G^o_{BrA}$ up to ~14 kcal/mol could be obtained by the direct measurements of equilibria (2.1). As $-\Delta G^o_{BrA}$ increases, K_{BrA} increases and beyond a given point the Br$^-$ intensity becomes too small for reliable measurements. The higher bond free energies were obtained indirectly by measurements of bromide transfer (BrTr) equilibria (2.4) which provided relative $-\Delta G^o_{BrA}$.

$$\text{YPhOH} + \text{Y'PhOH}\cdot\text{Br}^- = \text{YPhOH}\cdot\text{Br}^- + \text{Y'PhOH} \tag{2.4}$$

The time dependence of the ion intensities observed for one reaction (2.4), involving 3-CF_3 and 3-NO_2 phenol is shown in Figure 2.3. The establishment of equilibrium is observed ~0.7 ms after the short 20 µs electron pulse.

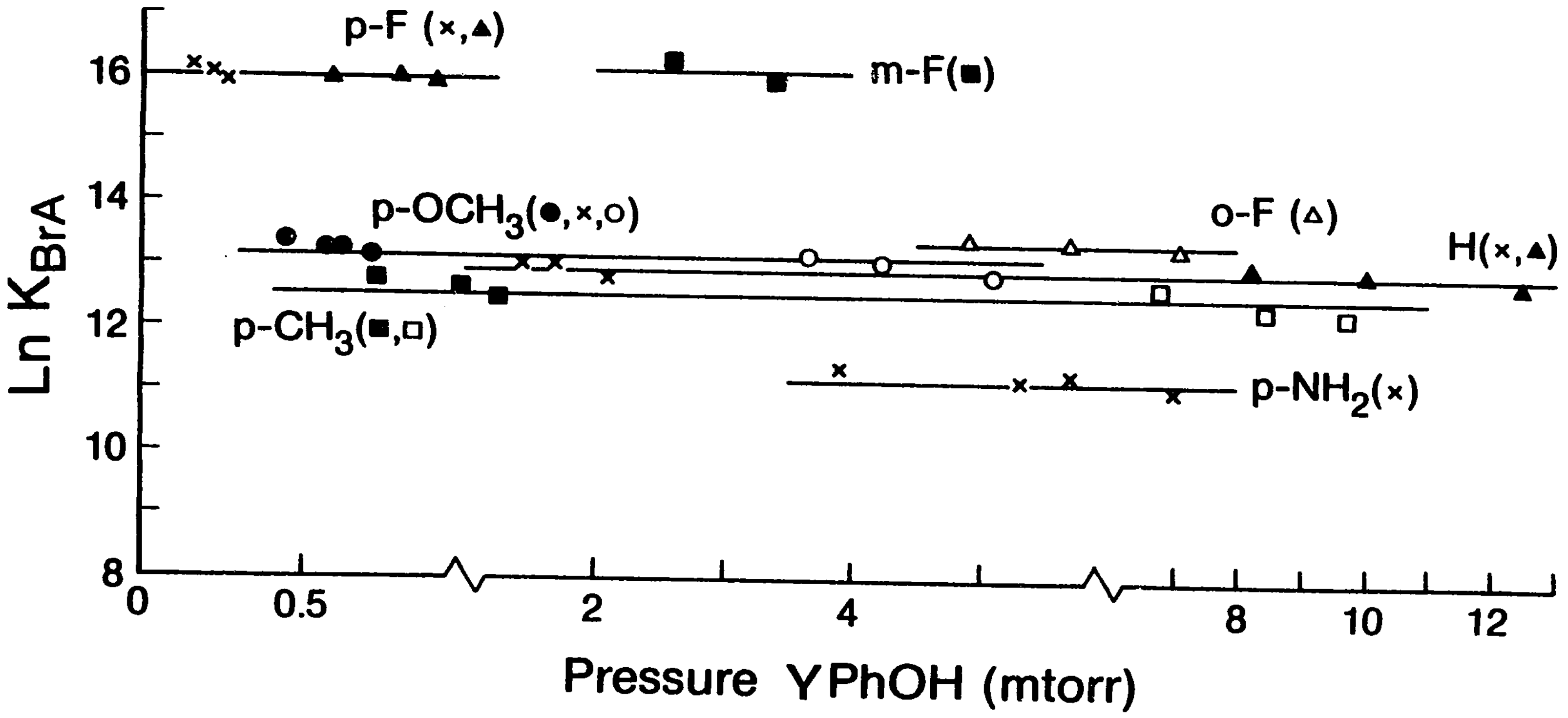

Figure 2.2 Equilibrium constants for reaction (2.1) involving Br^- and different YPhOH. Ion source temperature, 423 K. CH_4 pressures change from 2-4 torr in runs with the same symbol. In such runs, the CH_4 to YPhOH pressure ratio is constant.

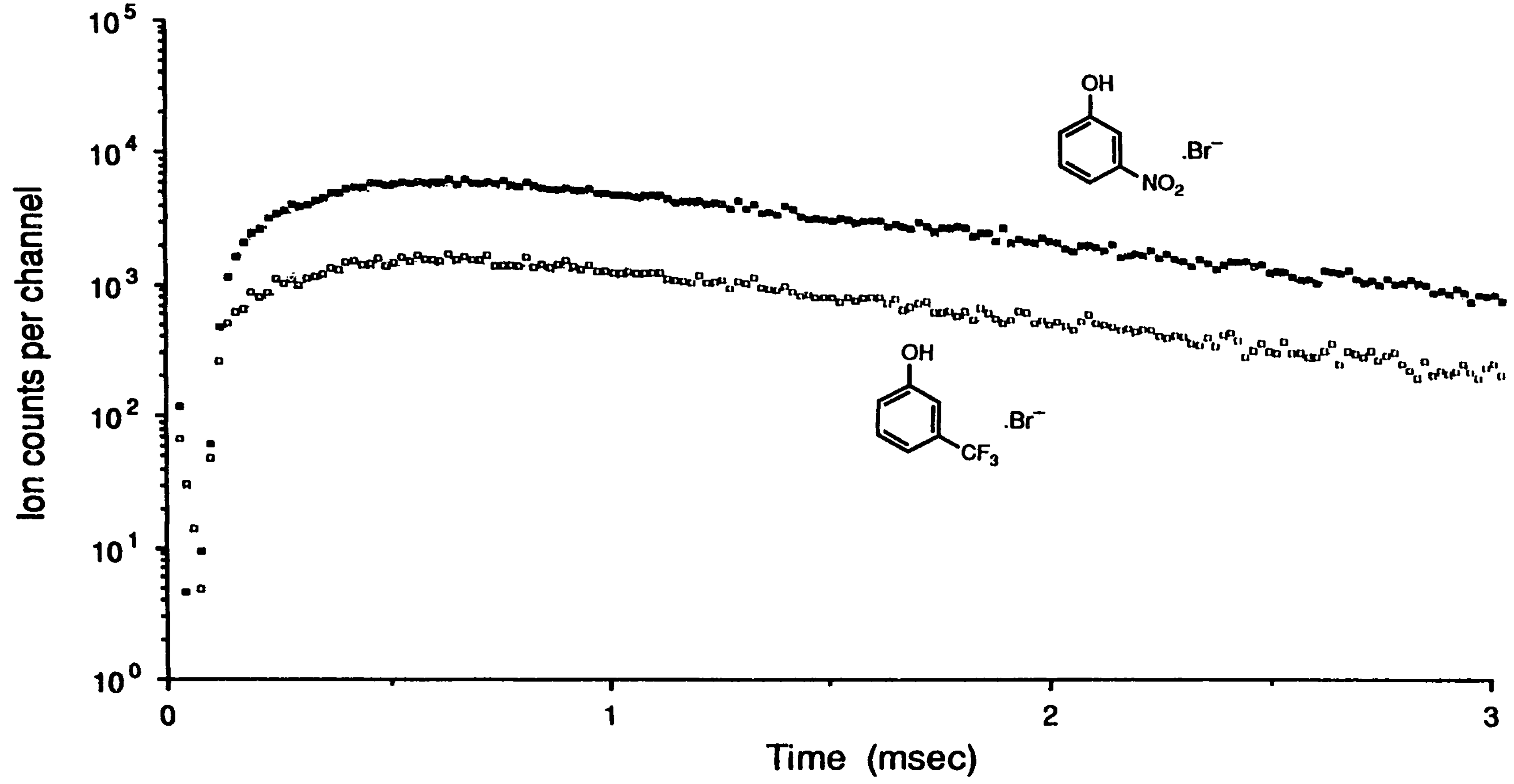

Figure 2.3 Raw data plot: ion intensity versus time after the 20 μs ionizing electron pulse. Obtained with a gas mixture of 2.6 torr CH_4, 0.9 mtorr 3-NO_2PhOH, 2.0 mtorr 3-CF_3PhOH and 3.4 mtorr CH_2Br_2 at 423K. The Br^- transfer equilibrium (2.4) becomes established some 0.7 ms after the electron pulse.

$$K_{BrTr} = \frac{I(YPhOH{\cdot}Br^-)\ p(Y'PhOH)}{I(Y'PhOH{\cdot}Br^-)\ p(YPhOH)} \qquad (2.5)$$

Substitution of the adduct ion intensity ratio into expression (2.5) leads to the equilibrium constant, K_{BrTr}. Similar checks to those performed for K_{BrA}, involving different partial pressure ratios of the two reacting phenols, were performed for K_{BrTr}.

The ΔG^o_{XA} for reaction (2.1) involving $X^- = Cl^-$ and I^- were determined in earlier work [1, 2] using similar techniques. For a description of equilibrium measurements involving I^- and ROH and RCO_2H molecules, see Caldwell and Kebarle [24].

2.3 Results and Discussion

2.3a Results

The $-\Delta G^o_{BrA,423K}$ values for YPhOH are shown on a scale of increasing $-\Delta G^o_{BrA,423K}$ in Figure 2.4. The absolute $-\Delta G^o_{BrA,423K}$ values (below ~14 kcal/mol) determined in the present work are probably accurate to ±1 kcal/mol. This was the error bar quoted for absolute bond free energy determinations of $ROH{\cdot}I^-$ and $RCO_2H{\cdot}I^-$ complexes performed in this laboratory [24]. The lengths of the arrows shown in Figure 2.4 correspond to $-\Delta G^o_{BrTr,423K}$ determinations. By combining $-\Delta G^o_{BrTr,423K}$ with absolute $-\Delta G^o_{BrA,423K}$ due to equilibria (2.1) a complete scale of $-\Delta G^o_{BrA,423K}$ extending up to 19 kcal/mol for the most acidic phenol, $4\text{-}NO_2C_6H_4OH$, was obtained. The $-\Delta G^o_{BrA,423K}$ values are summarized in Table 2.1. The more limited data for the $YPhOH{\cdot}I^-$ and $YPhOH{\cdot}Cl^-$ bond free energies [1, 2] are given in Table 2.2 which includes also the corresponding bromide determinations to facilitate an easy comparison of the three sets of data.

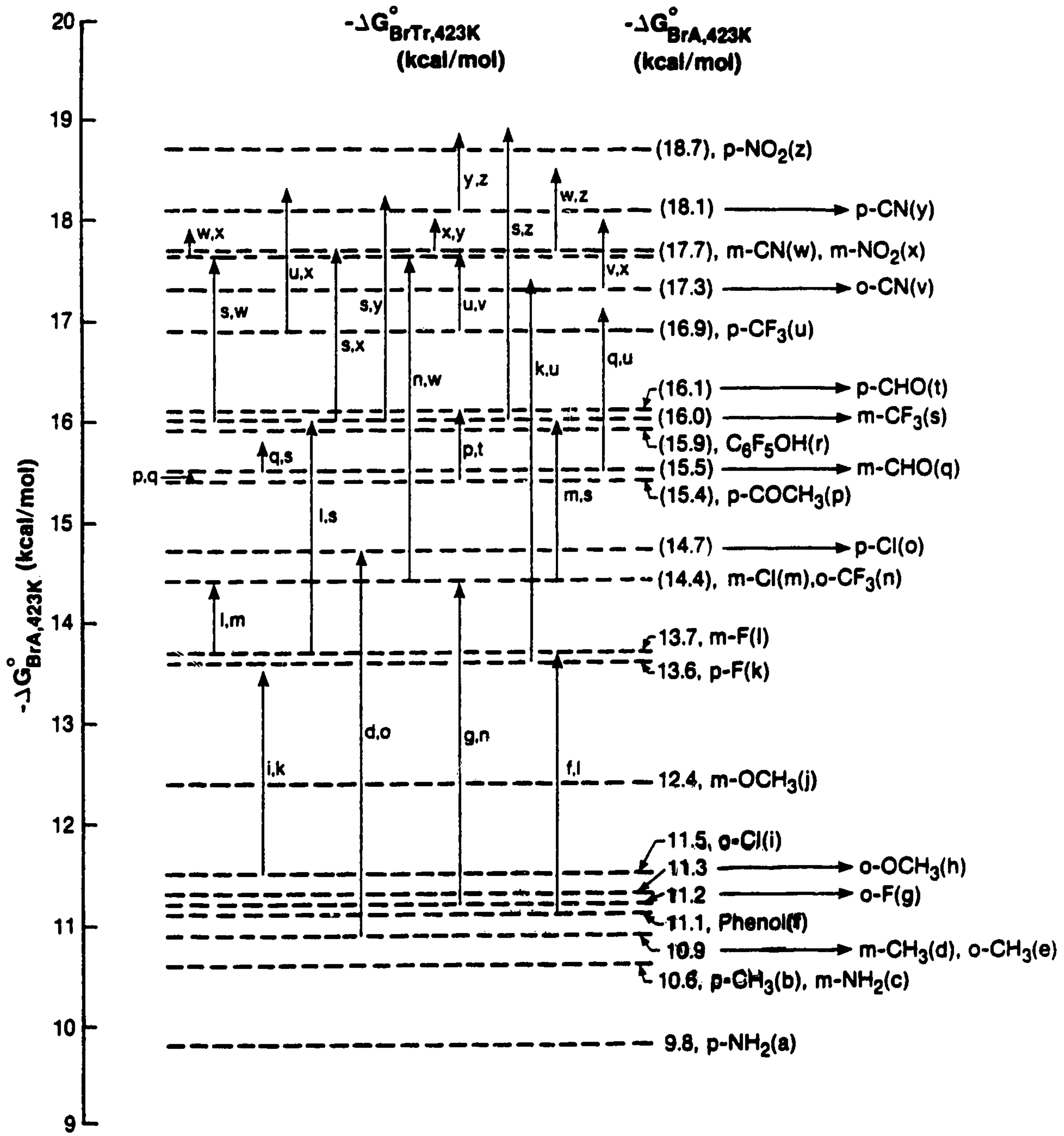
20
19
18
17
16
15
14
13
12
11
10
9
$-\Delta G^{o}_{BrA,423K}$ (kcal/mol)
$-\Delta G^{o}_{BrTr,423K}$ (kcal/mol)
$-\Delta G^{o}_{BrA,423K}$ (kcal/mol)
(18.7), p-NO_2(z)
(18.1) → p-CN(y)
(17.7), m-CN(w), m-NO_2(x)
(17.3) → o-CN(v)
(16.9), p-CF_3(u)
(16.1) → p-CHO(t)
(16.0) → m-CF_3(s)
(15.9), C_6F_5OH(r)
(15.5) → m-CHO(q)
(15.4), p-$COCH_3$(p)
(14.7) → p-Cl(o)
(14.4), m-Cl(m),o-CF_3(n)
13.7, m-F(l)
13.6, p-F(k)
12.4, m-OCH_3(j)
11.5, o-Cl(i)
11.3 → o-OCH_3(h)
11.2 → o-F(g)
11.1, Phenol(f)
10.9 → m-CH_3(d), o-CH_3(e)
10.6, p-CH_3(b), m-NH_2(c)
9.8, p-NH_2(a)
y,z
w,z
w,x
u,x
x,y
s,z
v,x
s,w
s,y
u,v
s,x
n,w
k,u
q,u
q,s
p,t
p,q
m,s
l,s
l,m
i,k
d,o
g,n
f,l

Figure 2.4 Scale of $-\Delta G^{o}_{BrA,423K}$ for reactions (2.1): $Br^- + YPhOH = YPhOH{\cdot}Br^-$. Standard state 1 atm. Values up to 14 kcal/mol were obtained by direct measurements of equilibria (2.1). Higher values were obtained from measurements of the Br^- transfer equilibria (2.4). Lengths of arrows shown correspond to $-\Delta G^{o}_{BrTr,423K}$. Letters beside arrows identify phenols involved in equilibrium (2.4).

Table 2.1 [a] Gibbs Free Energy Change $-\Delta G^{o}_{BrA,423K}$ for Reaction: $Br^{-} + YPhOH = YPhOH{\cdot}Br^{-}$

Position-Y	$-\Delta G^{o}_{BrA,423K}$ (kcal/mol)	Position-Y	$-\Delta G^{o}_{BrA,423K}$ (kcal/mol)
4-NH_2	9.8	2-CF_3	14.4
3-NH_2	10.6	3-CF_3	16.0
4-CH_3	10.6	4-CF_3	16.9
2-CH_3	10.9	4-CH_3CO	15.4
3-CH_3	10.9	3-CHO	15.5
H	11.1	4-CHO	16.1
4-OCH_3	11.3	2-CN	17.3
3-OCH_3	12.4	3-CN	17.7
2-F	11.2	4-CN	18.1
4-F	13.6	2-NO_2	-
3-F	13.7	3-NO_2	17.7
2-Cl	11.5	4-NO_2	18.7
4-Cl	14.7	F_5[b]	15.9
3-Cl	14.4		

a. Data from Figure 2.4. YPhOH are substituted phenols. Standard state 1 Atm.

b. perfluorophenol.

Table 2.2[a] Gibbs Free Energy Change $-\Delta G^{o}_{XA,423K}$ for Reaction: $YPhOH + X^{-} = YPhOH{\cdot}X^{-}$

Position -Y	$-\Delta G^{o}_{XA,423K}$ **(kcal/mol)**		
	Cl⁻	**Br⁻**	**I⁻**
4-Me	15.3	10.6	7.5
H[b]	15.9	11.1	8.4
4-Cl	19.5	14.7	11.6
3-Cl	-	14.4	12.2
3-F	-	13.7	10.7
4-F	18.0	13.6	10.5
3-CN	-	17.7	14.1
4-CN	24.7	18.1	14.9
$3-NO_2$	-	17.7	14.3
$4-NO_2$	-	18.7	-

a. Data for Br^{-}, present work, Cl^{-} [1, 13], I^{-} [2]. Standard state 1 Atm. ΔH^{o}_{XA} can be approximately evaluated from $\Delta H^{o}_{XA} = \Delta G^{o}_{XA,TK} + T\Delta S^{o}_{XA}$, where $-\Delta S^{o}_{XA} \approx 25$ (Cl^{-}); 23 (Br^{-}) and 21 (I^{-}) (cal deg^{-1} mol^{-1}). Entropy changes from: ref [13] Cl^{-}; estimated Br^{-}; [2] I^{-}. Furthermore, $-\Delta S^{o}_{XA}$ is approximately constant for whole substituent series and for given X^{-}, see [1].

2.3b Hydrogen Bond Energy in YPhOH·X$^-$. Gas Phase Acidities and Substituent Effect Analysis

A plot of the hydrogen bond free energies in YPhOH·Br$^-$ relative to the unsubstituted phenol versus the relative gas phase acidities of para substituted phenols [3, 4] is shown in Figure 2.5. A fairly good correlation (correlation coefficient $r = 0.956$) is observed. However, a much better correlation ($r = 0.998$) is obtained in Figure 2.6 where the plot is against the acidities of the para substituted benzoic acids.

This comparison shows when extensive proton transfer from MH to X$^-$ is not involved, as is the case for X$^-$ = Br$^-$, the relationship of bond energies with the acidity of the MH is only indirect, i.e., a consequence of a similarity of the substituent effects on the acidity and the hydrogen bonding ability. The much better correlation with the benzoic acids means a greater similarity with the substituent effects on the acidity of the benzoic acids. The causes for the better agreement with the benzoic acids can be deduced from a comparison of the deviations for specific substituents observed in Figures 2.5 and 2.6. However, a general examination of the substituent effects in the hydrogen bonded complexes, YPhOH·X$^-$, provides a more comprehensive view.

The two most important contributions to the substituent effect are the field/inductive (F) and resonance (R) effects [25]. The field/inductive effect is predominantly the attractive charge-dipole interaction between the reaction center and the substituent (+F) and is transmitted through polarizable bonds and space. This interaction is long range and involves no transfer of charge. The resonance effect involves interaction of the reaction center with a π electron system conjugated to that of the substituent. As π charge transfer to the substituent can either be positive or negative, i.e., π acceptor or π donor

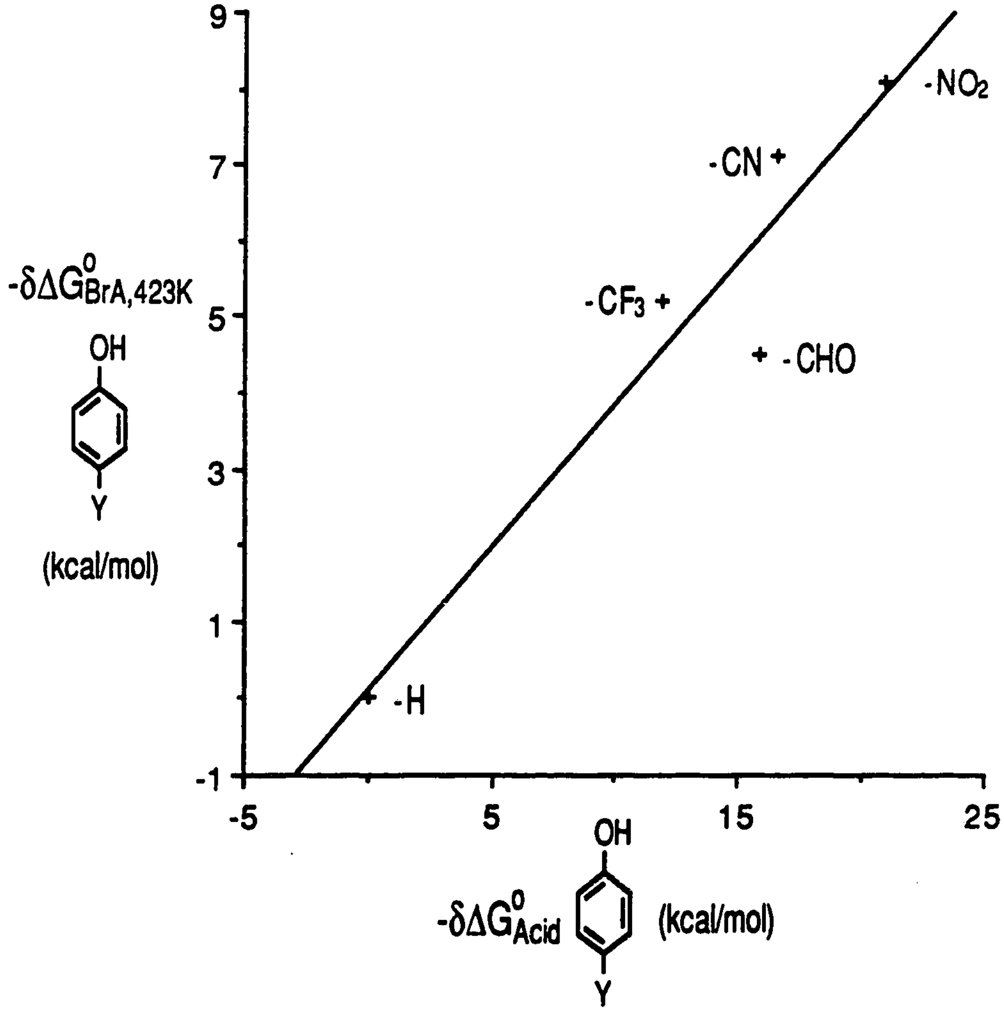

Figure 2.5 Plot of $-\delta\Delta G^{o}_{BrA,423K}$ for Br^{-} hydrogen bonding to phenols versus relative gas phase acidities of phenols. Substituents in para position.

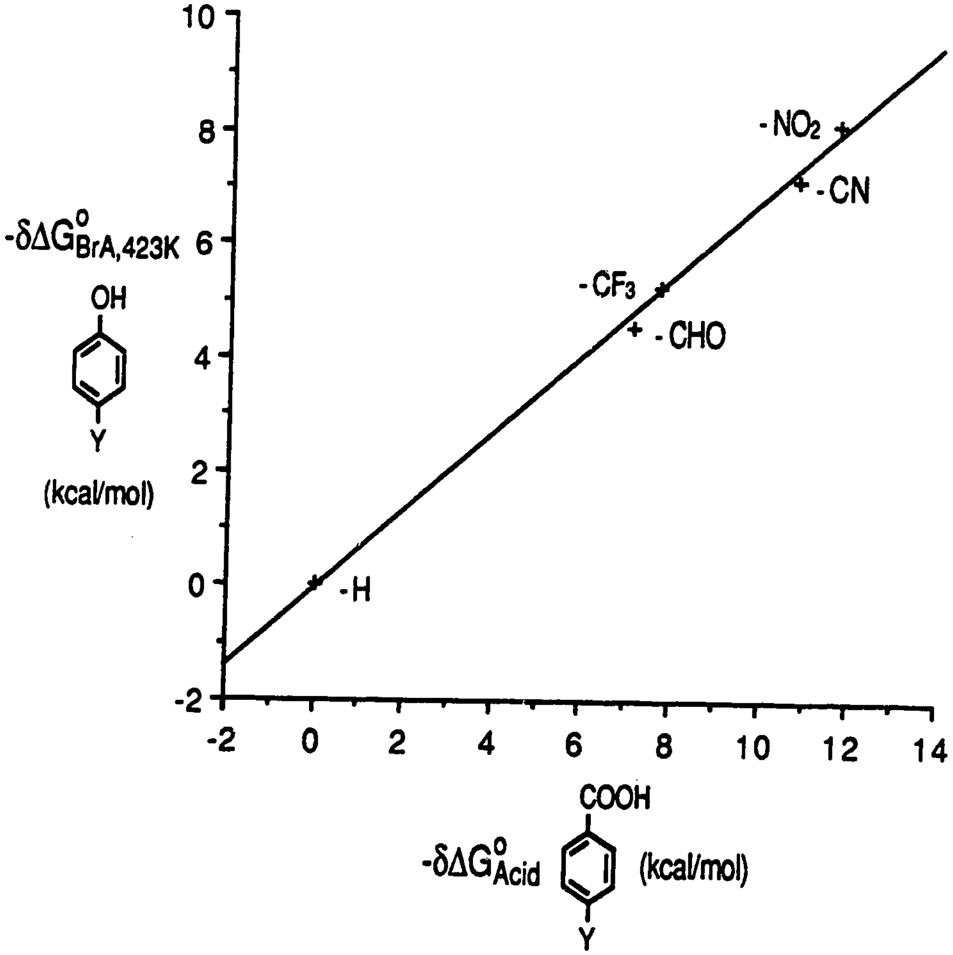

Figure 2.6 Plot of $-\delta\Delta G^{o}_{BrA,423K}$ for Br^- hydrogen bonding to phenols versus relative gas phase acidities of benzoic acids. Substituents in para position.

substituent, π stabilization (+R) or destabilization (-R) of the reaction center can occur.

Taft et al. [25-28] have developed and refined greatly the analysis of substituent effects. The present analysis is based on the work of Taft and Topsom [25]. The separation of the substituent effect, $\delta\Delta G^{o}$, into contributions due to π electron delocalization (resonance) and field/inductive effects for a substituent in a given position to the functional group, either p- or m-, is obtained from equation (2.6), which also includes polarizability, α, effects.

$$-\delta\Delta G^{o} = \rho_R\sigma_R + \rho_F\sigma_F + \rho_\alpha\sigma_\alpha \qquad (2.6)$$

σ_R, σ_F and σ_α are reaction system independent parameters that rank the resonance, field and polarizability capacity of the given substituent; these values are tabulated [25, 26]. The parameters ρ_R, ρ_F and ρ_α depend on the given reaction and their magnitude is determined by regression analysis for the best fit when the experimentally determined $\delta\Delta G^{o}$ for the given reaction system is substituted into equation (2.6).

The experimentally determined $-\delta\Delta G^{o}_{BrA,423K}$ for para substituents relative to Y = H plotted versus the $-\delta\Delta G^{o}_{BrA,423K}$ calculated from equation (2.6) with the best fit ρ parameters (labelled $-\delta\Delta G^{o}_{Calc}$) are shown in Figure 2.7. A very good correlation (correlation coefficient r = 0.991) is observed. The polarizability contributions were neglected in the fit shown. A somewhat better fit, r = 0.995, is obtained with inclusion of the polarizability. The ρ parameters for both fits are given in Table 2.3. Since the emphasis of the present discussion will deal with the changes of ρ_R and ρ_F for the different systems and the ρ_α values in all cases are very small (Table 2.3) the polarizability will not be considered in the further discussion. Small ρ_α values are anticipated for p- and m-YPhOH·X$^-$ complexes

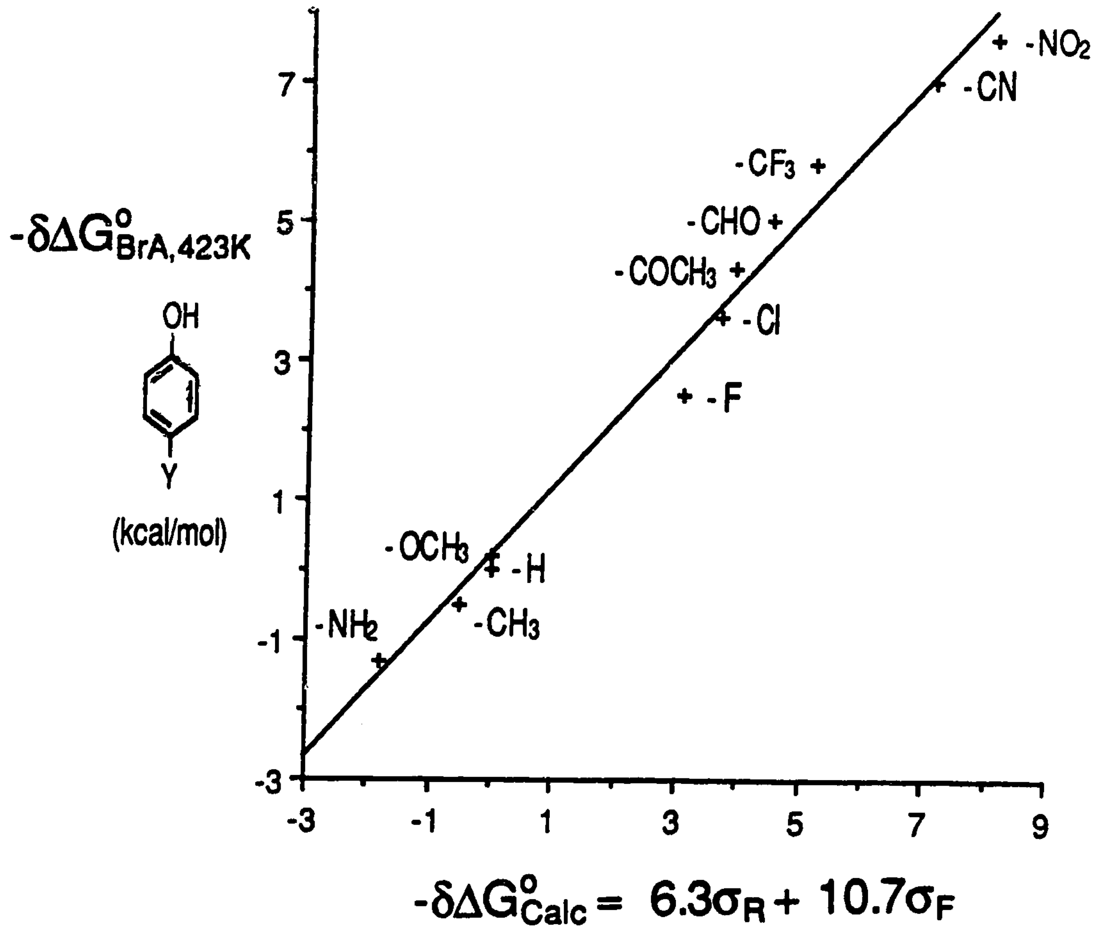

Figure 2.7 $-\delta\Delta G^o_{BrA,423K}$ for Br⁻ and substituted phenols versus $-\delta\Delta G^o_{Calc}$ calculated with Taft σ parameters, see equation (2.6). Substituents in para position.

Table 2.3 Values for Resonance ρ_R, Field ρ_F and Polarizability ρ_α Parameters, Taft Equation (2.6)^a

Substituents position	**Reaction**	ρ_R	ρ_F	ρ_α	r^b	**Origin of data**
meta^a	Br^-	4.1±0.6	9.7±0.4	-	0.988	Table 2.1
		4.0±0.5	8.9±0.5	-1.3±0.8	0.993	
para^a	Br^-	6.3±0.6	10.7±0.4	-	0.991	Table 2.1
		6.1±0.5	10.0±0.5	-1.2±0.5	0.995	
para^a	Br^-	7.6±0.7	10.4±0.3	-	0.999	Table 2.2
		7.4±0.5	10.1±0.2	-0.5±0.3	1.000	
para^a	Cl^-	12.7±1.2	12.5±0.4	-	0.998	Table 2.2
		12.2±0.4	11.9±0.2	-0.9±0.2	1.00	
para^a	I^-	8.1±0.9	9.7±0.3	-	0.998	Table 2.2
		8.1±1.3	9.7±0.7	0.1±0.7	0.998	
para^c	Benzoic acids	14.6±0.7	15.0±0.6	0.1±1.0	0.997	Taft [25]
meta^c	Benzoic acids	11.5±0.9	14.7±0.5	-	0.998	Taft [25]
para^c	Phenols π acceptors	49.0±1.5	18.6±0.5	0.6±0.8	0.999	Taft [25]
para^c	Phenols π donors	22.0±1.4	18.8±0.9	-3.1±0.5	0.993	Taft [25]
meta^c	Phenols	12.2±1.2	19.0±0.7	-	0.994	Taft [25]

---

a. ρ values obtained from linear regression analysis of eq. (2.6), where $\delta\Delta G^o_{XA,423K}$ corresponds to experimentally determined ΔG° for reaction $PhOH{\cdot}X^- + YPhOH = PhOH + YPhOH{\cdot}X^-$. Since $\delta\Delta S^o_{XA} \approx 0$, see [1], $\delta\Delta G^o_{XA}$, even though determined at 423K is also valid at 298K, i.e., $\delta\Delta G^o_{XA,298K} \approx \delta\Delta G^o_{XA,423K}$.

b. Correlation coefficient.

c. Gas phase acidities.

as polarizability is a short range effect and there is a relatively long distance between the reaction center (H-X$^-$) and substituent.

A plot of $-\delta\Delta G^o_{BrA,423K}$ for meta substituents and the best fit ρ parameters is shown in Figure 2.8. A very good fit is obtained also for this system.

Since a much more restricted number of substituents was used in the determinations [1, 2] involving Cl$^-$ and I$^-$ and since the ρ values depend somewhat on the number of substituents included in the fit, regression analyses for these three ions and the same restricted set of substituents, in para position, were obtained. The resulting plots for Cl$^-$, Br$^-$ and I$^-$ are shown in Figures 2.9-2.11. The ρ values and the correlation coefficients from the restricted fits for Cl$^-$, Br$^-$ and I$^-$ are given in Table 2.3. A comparison of the ρ_R and ρ_F values for Br$^-$ between the extended plot (Figure 2.7) and the restricted plot (Figure 2.10) shows that the ρ_F is essentially the same while ρ_R changes only a little, i.e., from 6.3 to 7.6; see also Table 2.3. This indicates that the restricted plots for results for Cl$^-$, Br$^-$ and I$^-$ provide ρ_F and ρ_R values which are still quite meaningful.

Also included in Table 2.3 are the ρ values for the substituent effect on the gas phase acidities of phenols and benzoic acids obtained by Taft [25]. Examining first the data for the para position, one finds that the ρ_F values decrease in the order: phenol acidity 18.6, benzoic acid acidity 15, YPhOH·X$^-$ bond free energy: Cl$^-$ 12.5, Br$^-$ 10.4, I$^-$ 9.7. This order agrees with expectation when one considers the gradually increasing delocalization of the negative charge (phenols to benzoic acids) and the increasing remoteness of the negative charge from the substituent, present for the whole series.

Considering the ρ_R values, it is significant to note that the $-\delta\Delta G^o_{XA,423K}$ plots for para substituents, which in all cases include both π donor and π acceptor substituents, give good linear relationships (Figures. 2.7, 2.9-2.11). The same is true for gas phase acidities of para substituted benzoic acids [25];

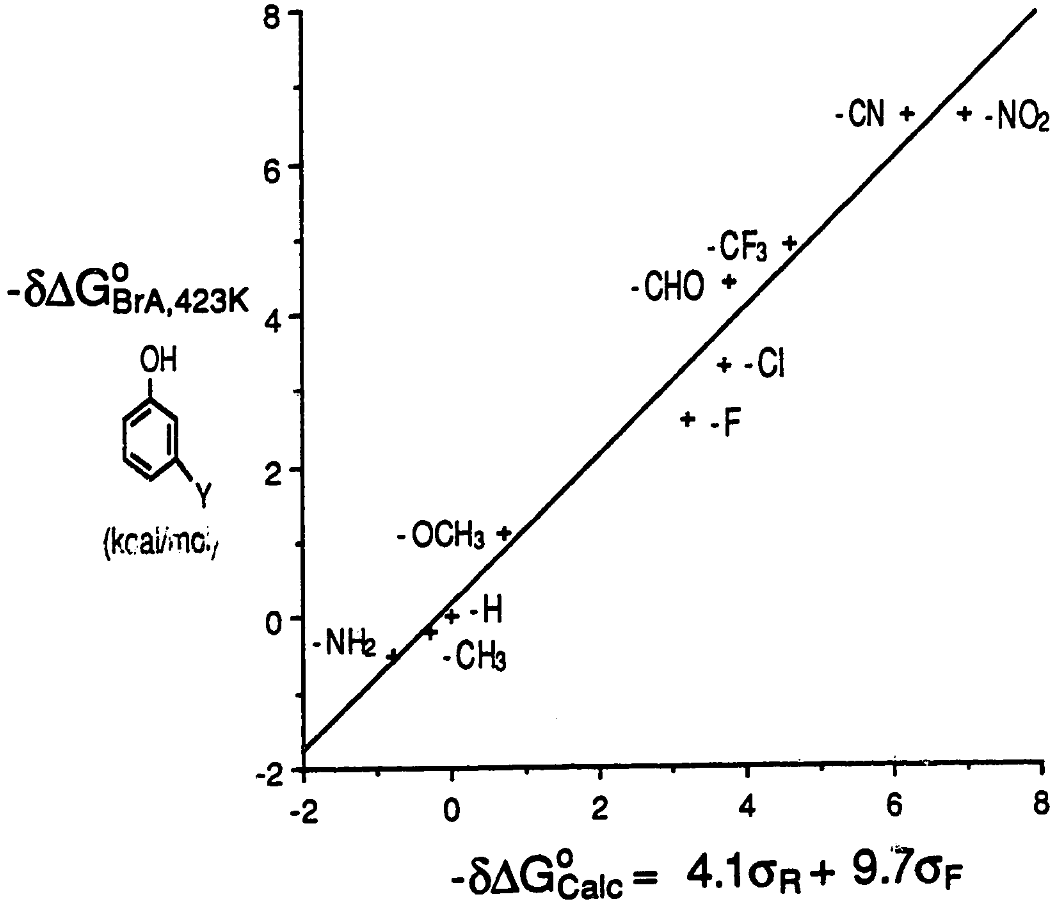

Figure 2.8 $-\delta\Delta G^o_{BrA,423K}$ for Br^- and substituted phenols versus $-\delta\Delta G^o_{Calc}$ calculated with Taft σ parameters, see equation (2.6). Substituents in meta position.

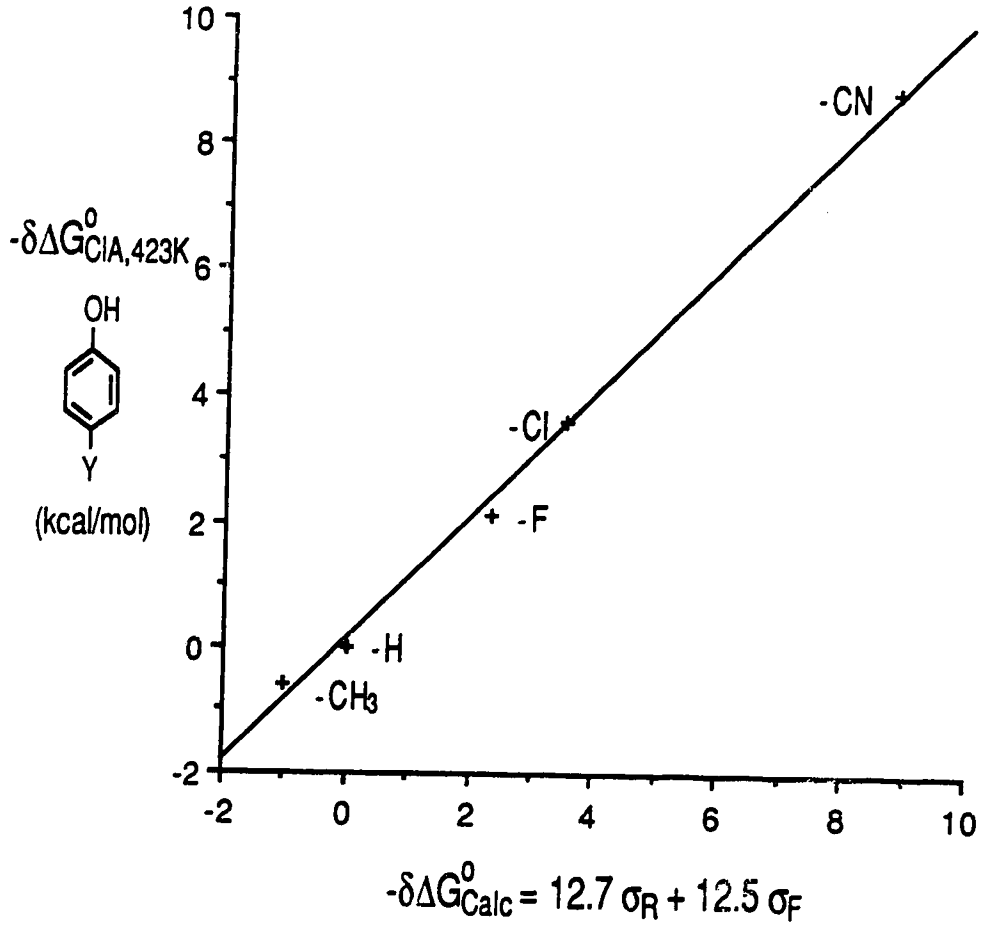

Figure 2.9 $-\delta\Delta G^o_{ClA,423K}$ for Cl^- and restricted number of substituted phenols versus $-\delta\Delta G^o_{Calc}$ calculated with Taft σ parameters, see equation (2.6). Substituents in para position.

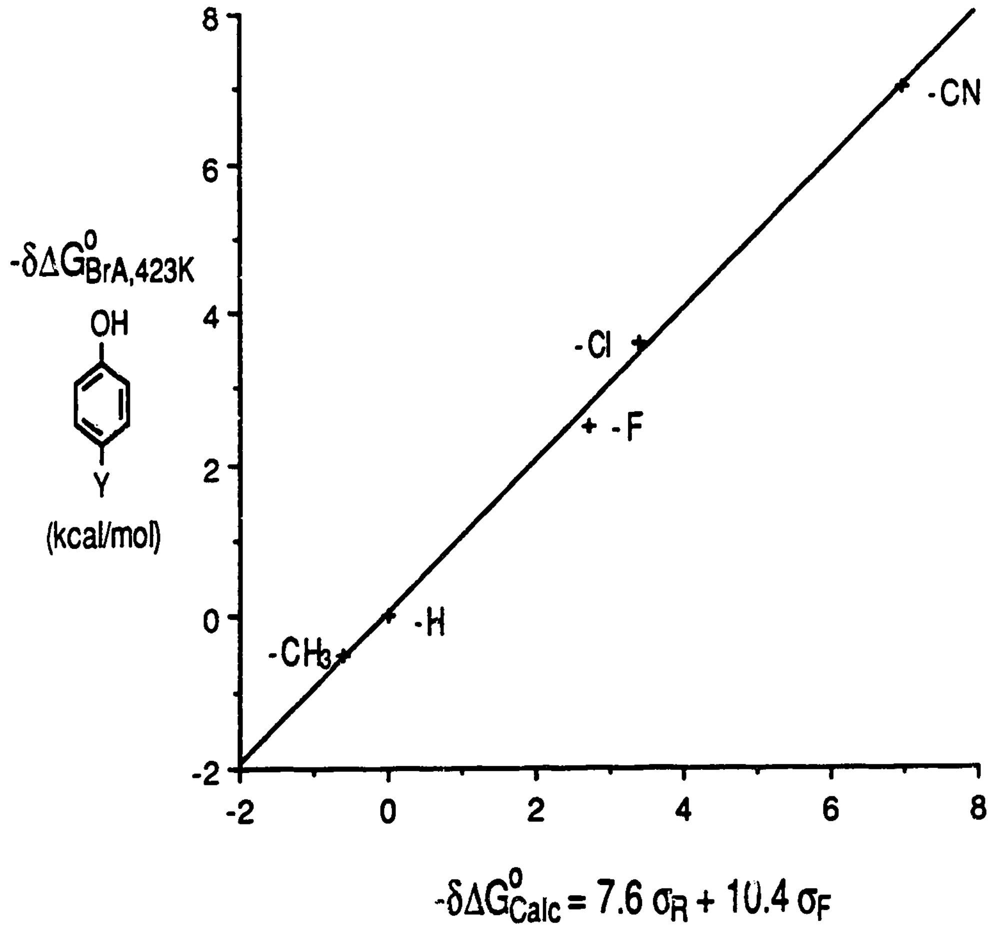

Figure 2.10 $-\delta\Delta G^{o}_{BrA,423K}$ for Br^{-} and restricted number of substituted phenols versus $-\delta\Delta G^{o}_{Calc}$ calculated with Taft σ parameters, see equation (2.6). Substituents in para position.

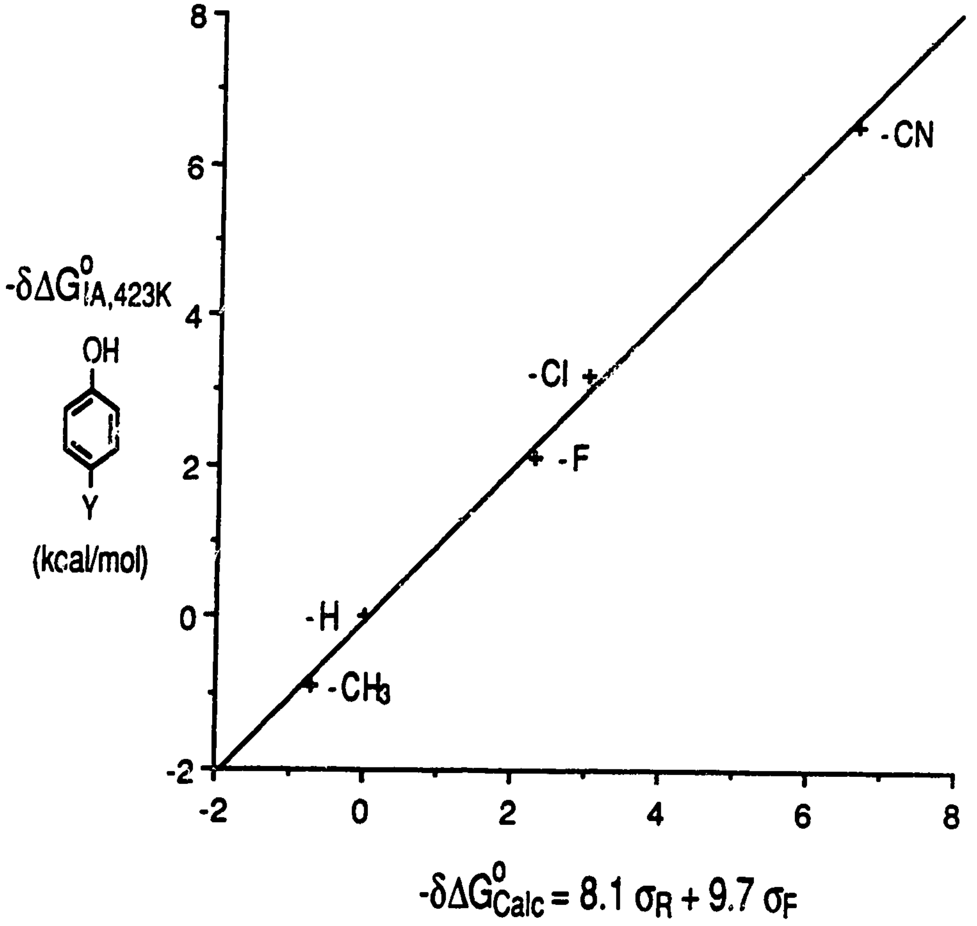

Figure 2.11 $-\delta\Delta G^{o}_{IA,423K}$ for I^- and restricted number of substituted phenols versus $-\delta\Delta G^{o}_{Calc}$ calculated with Taft σ parameters, see equation (2.6). Substituents in para position.

see Table 2.3. On the other hand, it is known [25] that for the para substituted phenol acidities a single straight line relationship cannot be obtained for both strong π donors, i.e., -OH, -OCH_3, -NH_2, and strong π acceptors, i.e., CN, NO_2,CHO, because the reaction center, O^-, is very strongly π donating to the benzene ring and thus suppresses π donation by π donor substituents [25]. The separated fits ρ_R values for the phenols [25], are π donor, $\rho_R = 22$, π acceptor $\rho_R = 49$; see Table 2.3. Comparing the π acceptor value with the ρ_R values for benzoic acids, $\rho_R = 14.6$ and YPhOH·X^- bond free energies: $\rho_R = 12.7$ (Cl^-); 7.6 (Br^-); 8.1 (I^-) one finds that the latter are very much smaller and fairly close together. This result could have been anticipated from the plots of YPhOH·Br^- bond free energies versus the acidities of phenols and benzoic acids; see Figures 2.5 and 2.6.

The similarity between the ρ_R values for benzoic acid acidities and the YPhOH·X^- bond free energies reflect the expected dominant stabilization for π accepting substituents in these systems; see resonance structures III and IV.

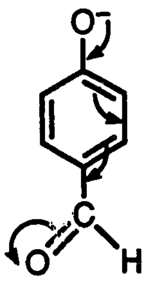

II

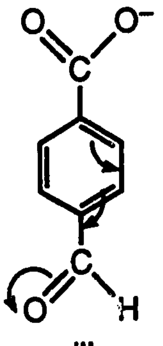

III

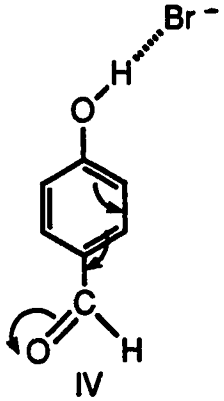

IV

The benzoate anion and the YPhOH·X^- complexes lack the direct, into the ring π donation by the negative functional group exhibited by the phenoxides, structure II. The stabilizing effect of π accepting substituents for the YPhOH·X^- systems thus derives from a π shift from the ring into the substituent which is induced by the negative charge on X^- and is similar to that occurring in the benzoate anions. On this basis one expects NO_2 and CHO, the most strongly π accepting substituents (σ_R: CHO 0.19; NO_2 0.18; CN 0.10; CF_3 0.07, from [25, 26]) to show the largest deviations in the YPhOH·X^- bond free energy-phenol acidity plot (Figure 2.5) and exactly this is found to be the case. This also suggests that charge stabilization in YPhOH·X^- systems through π delocalization involving the phenol oxygen electron pairs is only a small effect.

The ρ_R values for the p-YPhOH·X^- systems are: Cl^- 12.7; Br^- 7.6; I^- 8.1. On the basis of the increasing remoteness of X^- in the above series one would have expected the values to decrease monotonically, i.e., $\rho_R(Br^-) \geq \rho_R(I^-)$. The small reversal of the experimental result for this pair is probably due to experimental error. The observed much larger $\rho_R(Cl^-)$ probably includes also the effect of an actual partial proton transfer from YPhOH to Cl^- which occurs for this series.

In order to provide an illustration for the actual magnitudes of the resonance ($R = \rho_R\sigma_R$) and field ($F = \rho_F \sigma_F$) contributions to $-\delta\Delta G^o_{BrA,423K}$ (equation (2.6)), the R and F values evaluated from the ρ values in Table 2.3 and σ values of Taft [25, 26] for the substituent effect on the hydrogen bonded phenols to Br^- are shown in Table 2.4. The corresponding R and F terms for the gas phase acidities of para substituted phenols and benzoic acids are also provided for comparison. Examination of the values in Table 2.4 shows that the F effects are almost completely dominant for both the para and meta substituted YPhOH·Br^-. This explains the similarity between the $-\delta\Delta G^o_{BrA,423K}$ values for the meta and para YPhOH·X^- systems (Table 2.4 and Figures 2.6 and 2.7) and also the similarity of those with the substituent effects on benzoic acid acidities which are also dominated, but somewhat less so, by the F effects; see Table 2.4.

Table 2.4 Resonance R and Field F Contributions of Substituents[a]

Substituent	4-YPhOHBr^{-}[b]		3-YPhOHBr^{-}[b]		4-YPhOH[c]		4-YPhCO$_2$H[c]	
	R	F	R	F	R	F	R	F
-NO$_2$[e]	1.1	7.0	0.7	6.3	8.8	12.1	2.6	9.8
-CN[e]	0.7	6.4	0.4	5.8	4.9	11.2	1.5	9.0
-CHO[e]	1.2	3.3	0.8	3.0	9.3	5.8	2.8	4.7
-CF$_3$[e]	0.5	4.7	0.4	4.2	3.4	8.2	1.0	6.6
-H	0.0	0.0	0.0	0.0	0.0	0.0	0.0	0.0
-Cl[f]	-1.1	4.8	-0.6	4.3	d	d	-2.5	6.8
-F[f]	-1.6	4.7	-1.0	4.2	d	d	-3.7	6.6

a. Contribution $R = \rho_R\sigma_R$ and $F = \rho_F\sigma_F$ in kcal/mol to $-\delta\Delta G^{\circ}$, see eq. (2.6), for given substituent.

b. $-\delta\Delta G^{o}_{BrA,423K}$ for reaction (2.1).

c. $-\delta\Delta G^{o}_{Acid}$ for gas phase acidities of phenols and benzoic acids.

d. π donor substituents require a separate fit, see text.

e. π acceptor substituent.

f. π donor substituent.

The stabilizing effect of electron withdrawing substituents in YPhOH·Br$^-$ for ortho substituents is somewhat smaller than that for meta ≈ para; see Table 2.1. This holds for both small size substituents like F and large substituents like NO_2. Since the field effect is the dominant factor in all these systems the somewhat smaller stabilization for the ortho compounds should be due to the unfavorable orientation of the dipole, produced by the substituent, relative to the negative charge, i.e., Br$^-$.

2.3c Hydrogen Bonding in MH·B$^-$

The findings for the YPhOH·X$^-$ systems can be generalized to MH·B$^-$ hydrogen bonded complexes. For a given related series of MH with increasing gas phase acidity, the increased strength of the hydrogen bond as measured by the energy required for the dissociation to MH + B$^-$, consists of two contributions. One is the gradually increasing extent of actual proton transfer from MH to B$^-$ on formation of the complex. This effect is very important when the acidity of BH is close to and becomes smaller than that of MH. The second contribution can be best observed when the acidity of BH is much larger than that of MH for the whole MH series. This contribution is due to effects in MH which increase the dipole in M$^-$-H$^+$ and thus the hydrogen bond energy. The major effect in this case are field type effects in MH. The negative charge of the approaching B$^-$ induces also some π delocalization in MH. This R effect is less important. Since changes of the structure of MH that increase the acidity of MH increase also the favorable F and the less important R stabilization in MH·B$^-$, the hydrogen bonding in MH·B$^-$ tracks, but only partially so, the acidity of MH. The YPhOH·X$^-$ complexes are particularly useful since for these systems a convincing dissection of the above effects is possible. This is the case, because the contrast between the effects on acidity and hydrogen bonding is especially strong, due to the large R effect in the phenoxides; see structures II-IV. Somewhat similar and even larger differences between hydrogen bonding ability and acidity are observed for the carbon acids, where the acidity may be almost entirely due to resonance stabilization after deprotonation, as is the case for cyclopentadiene [13].

REFERENCES

1. J. B. Cumming, M. A. French and P. Kebarle, J. Am. Chem. Soc., 99, 6999 (1977).
2. G. Caldwell and P. Kebarle, unpublished work.
3. S. G. Lias, J. E. Bartmess, J. F. Liebman, J. L. Holmes, R. D. Levin and W. G. Mallard, J. Phys. Chem. Ref. Data, 17, Suppl. No. 1 (1988).
4. J. B. Cumming and P. Kebarle, Can. J. Chem., 56, 1 (1978).
5. T. D. Mark and A. W. Castleman, Jr., Adv. Atom. Molec. Phys., 20, 65 (1985).
6. A. G. Harrison, "Chemical Ionization Mass Spectrometry". CRC Press. Boca Raton, Florida (1983).
7. G. W. Caldwell, J. A. Masucci and M. G. Ikonomou, Org. Mass Spectrom., 24, 8 (1989).
8. H. P. Tannenbaum, J. D. Roberts and R. C. Dougherty, Anal. Chem., 47, 49 (1975).
9. E. E. Ferguson, F. C. Fehsenfeld and D. L. Albritton, "Gas Phase Ion Chemistry". Editor M. T. Bowers. Academic Press. New York (1979). Vol. 1, Chap. 2.
10. R. Yamdagni and P. Kebarle, J. Am. Chem. Soc., 93, 7139 (1971).
11. R. Yamdagni, J. D. Payzant and P. Kebarle, Can. J. Chem., 51, 2507 (1973).
12. P. Kebarle, Annu. Rev. Phys. Chem., 28, 445 (1977).
13. M. A. French, S. Ikuta and P. Kebarle, Can. J. Chem., 60, 1907 (1982).
14. G. Caldwell and P. Kebarle, Can. J. Chem., 63, 1399 (1985).
15. P. Kebarle, W. R. Davidson, M. A. French, J. B. Cummings and T. B. McMahon, Faraday Discuss. Chem. Soc., 64, 220 (1978).

16. J. W. Larson and T. B. McMahon, J. Am. Chem. Soc., 105, 2944 (1983).
17. J. W. Larson and T. B. McMahon, J. Am. Chem. Soc., 106, 517 (1984).
18. S. Yamabe, N. Ihiro and K. Hirao, Chem. Phys. Letts., 92, 172 (1982).
19. I. M. Kolthoff and M. K. Chantooni, Jr., J. Am. Chem. Soc., 91, 4621 (1969).
20. F. G. Bordwell, R. J. McCallum and W. N. Olmstead, J. Org. Chem., 49, 1424 (1984).
21. M. A. French, Ph. D. Thesis, University of Alberta (1977).
22. K. Hiraoka, S. Mizuse and S. Yamabe, J. Chem. Phys., 87, 3647 (1987).
23. P. Kebarle, "Techniques of Chemistry: Techniques for the Study of Ion-Molecule Reactions". Editors J. M. Farrar and W. H. Saunders, Jr. Wiley-Interscience. New York (1988). Chapter 5.
24. G. Caldwell and P. Kebarle, J. Am. Chem. Soc., 106, 967 (1984).
25. R. W. Taft and R. D. Topsom, Prog. Phys. Org. Chem., 16, 1 (1987).
26. R. W. Taft, J. L. M. Abboud, F. Anvia, M. Berthelot, M. Fujio, J.-F. Gal, A. D. Headley, W. G. Henderson, I. Koppel, J. H. Qian, M. Mishima, M. Taagepera and S. Uegi, J. Am. Chem. Soc., 110, 1797 (1988).
27. R. W. Taft and I. C. Lewis, J. Am. Chem. Soc., 80, 2436 (1958).
28. R. W. Taft and I. C. Lewis, J. Am. Chem. Soc., 81, 5343 (1959).

CHAPTER 3

STABILITIES OF COMPLEXES OF Br^- WITH SUBSTITUTED BENZENES, SB, BASED ON DETERMINATIONS OF THE GAS PHASE EQUILIBRIA $Br^- + SB = SB{\cdot}Br^-$

3.1 Introduction

The formation of complexes between X^- (CH_3O^-, F^-, Cl^-, Br^- and I^-) and substituted benzenes (SB) is of interest in gas phase ion chemistry [1, 2] and condensed phase organic chemistry [3, 4]. The $SB{\cdot}X^-$ adducts have been used for analytical purposes in Negative Ion Chemical Ionization [5-8] and knowledge of the stabilities of these complexes is of obvious use in this area.

The formation energies of complexes $SB{\cdot}X^-$ from SB and X^- can be obtained by measurements of equilibria (3.1) and (3.2) in the gas phase with a suitable mass spectrometric apparatus [9].

$$SB + X^- = SB{\cdot}X^- \qquad (3.1)$$

$$SB{\cdot}X^- + SB' = SB + SB'{\cdot}X^- \qquad (3.2)$$

Measurements involving X^- (particularly F^- and Cl^-) and a variety of compounds other than substituted benzenes have been reported by this [10-16] and other laboratories [17-20]. In the present work the discussion is restricted to substituted benzenes. Furthermore, substituents are excluded which have protic hydrogens, such as CO_2H, OH and NH_2, and engage in strong hydrogen

---

1. A version of this chapter has been submitted for publication: G. J. C. Paul and P. Kebarle, J. Am. Chem. Soc., 1990.

bonding to X^-. The stabilities of the hydrogen bonded complexes $YPhOH{\cdot}X^-$ were discussed in Chapter 2. The complexes dealt with here are those in which X^- bonds to the benzene moiety. Since equilibrium determinations provide information on the energetics but not on the structure of the complexes, quantum mechanical calculations have been essential for the understanding of the type of bonding and structures that are present. Depending on the nature of the substituents and X^- an interesting variety of most stable structures can occur. The most important ones, I-IV, are shown below. For simplicity the substituent(s) have been omitted from the structures.

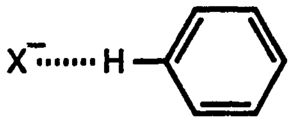

I

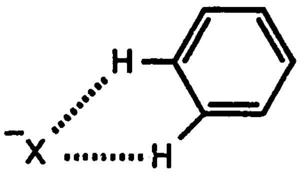

II

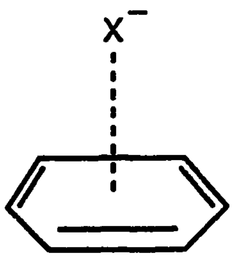

III

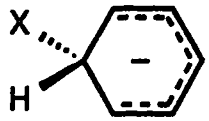

IV

Earlier work [13] on equilibria (3.1) involving Cl^- and a few substituted benzenes which also included minimal basis set (STO-3G) calculations, indicated that structure I is the most stable one for benzene and singly substituted benzenes. π donor, σ acceptor substituents lead to complexes I where Cl^- interacts with the C-H hydrogen in position meta to the substituent although the interaction with the para C-H is only slightly weaker. The predicted structure for $C_6H_5F{\cdot}Cl^-$ [13] follows (structure V).

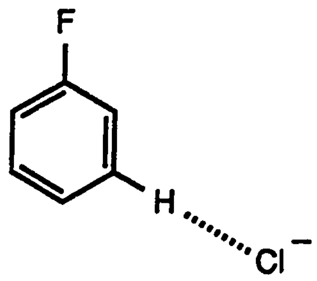

V

Bonding to the C-H hydrogen in position meta to the π donor F substituent is favored as the adjacent carbon atom possesses the lowest negative π electron density [21]. Theoretical calculations (AM1 method) by Meot-Ner et al. [22] predicted the aromatic proton meta to the F substituent in C_6H_5F to be most acidic and hence most favorable for hydrogen bonding. Recent calculations with larger basis sets (3-21G) by Hiraoka, Mizuse and Yamabe [23] for F^-, Cl^- and Br^- and unsubstituted benzene also predict structure I to be the most stable, while structure II is predicted to be most stable for the I^- complex with benzene.

Mulliken electron population analysis [23] indicates significant electron transfer from X^- to C_6H_6 only for $C_6H_6{\cdot}F^-$. The extent of electron transfer decreases rapidly for Cl^-, Br^- and I^-. The bonding structure I for F^-, Cl^- and Br^- can be considered as a $C\text{-}H{\cdots}X^-$ hydrogen bond, while that for I^- and structure II is a bifurcated H bond [23]. The bonds become progressively more electrostatic from F^- to I^- and the bifurcated H bond with I^- is a classical electrostatic structure.

Strongly π and σ electron accepting substituents like NO_2 can be expected to increase the $C\text{-}H{\cdots}X^-$ bond strength. However, in the presence of such substituents and for small X^- like F^- and CH_3O^-, which can form strong covalent bonds, the most stable structure may not be I but the σ bonded complex IV. σ bonded complexes like IV are well known. Multiple NO_2 substitution, as in 1,3,5-trinitrobenzene, and F^- and CH_3O^- leads to stable σ bonded complexes (Meisenheimer complexes) which are well characterized in solution [24, 25]. σ complexes of this type are of special interest in the gas phase [26-30] as well as in solution [24, 25] since they are probable intermediates in aromatic substitution reactions (S_NAr) involving nucleophiles X^-.

Recent calculations [31] dealing with the complex formed by F^- and nitrobenzene, using 3-21G plus diffuse functions basis sets, predict structure VI (analogous to structure I) to be most stable where the C-H involved in the hydrogen bond is in position para to the nitro group. The most stable σ complex, structure VII (analogous to structure IV), where F^- inserts in the para position to the nitro group is only somewhat less stable.

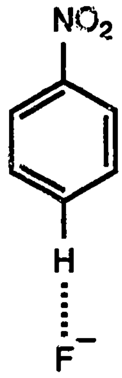

VI

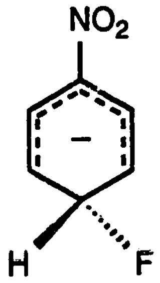

VII

The formation of the σ bond in position para to the NO_2 substituent (structure VII) is expected on qualitative grounds. The carbon in the para position of nitrobenzene has the lowest negative π electron density due to the +R (resonance) effect of the substituent [21] and may be expected to be the site of nucleophilic attack. Furthermore, the resulting σ bonded adduct is strongly substituted by the same +R effect of the substituent [21, 32]. The bond energies ($-\Delta E^{o}_{FA}$) in the two complexes are predicted as ~27 (structure VI) and ~22 kcal/mol (structure VII) [26]. This is much higher than $-\Delta E^{o}_{FA} \approx -\Delta H^{o}_{FA} \approx 14$ kcal/mol for the C-H-F^- bonded complex with unsubstituted benzene [23].

A low level theoretical study [33] using the MNDO basis set in which the principal interest involved the reaction coordinate of nucleophilic aromatic substitution of chloride by X^- (F^-, Cl^-, Br^- and CH_3O^-), also provided information of the stabilities of the σ bonded Meisenheimer complexes involving the nucleophile X^- and p-Cl nitrobenzene; see structure VIII.

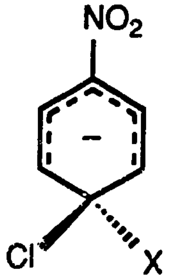

VIII

The predicted bonding energies (in kcal/mol) were 58.7 (F^-), 17.5 (Cl^-), 23.2 (Br^-), 57.3 (CH_3O^-). Bond energies of some of the ion X^--molecule dipole complexes were also provided but, unfortunately, the structures were not well described and it is unclear whether hydrogen bonded structures analogous to structure I were included in the geometry search. The bond energies of the ion-dipole complexes that were quoted were all smaller than those quoted for the corresponding Meisenheimer complexes.

The complex III, where X^- lies on an axis perpendicular to the benzene plane, is not a charge transfer complex. While electron transfer from X^- to the LUMO of benzene might appear to be a distinct possibility, the relatively high electron affinity of X and electrostatics [34] hinder the formation of a π complex. Thus, the negative quadrupole moment of benzene, $Q_{zz} = -8.7 \times 10^{-26}$ esu [35], perpendicular to the plane of benzene (due to π electron clouds above and below the molecular plane) leads to a significant electrostatic repulsion between X^- and benzene and a low stability of the axial complex III, when unsubstituted benzene is involved [34]. On the other hand, a relatively strong bond energy ($-\Delta H^{\circ}_{KA}$ = 18.3 kcal/mol) was measured for the axial complex $C_6H_6{\cdot}K^+$ (structure IX) where the ion-quadrupole moment interaction is attractive [34].

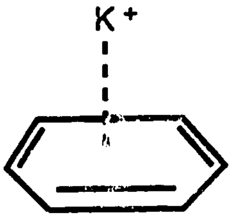

IX

π complex formation (analogous to structure IX) has also been proposed for the $C_6H_6{\cdot}Na^+$ [34] and $C_6H_6{\cdot}NO^+$ [36] adducts. Stronger electrophiles such as H^+ [37], $SiMe_3^+$ [38] and NO_2^+ [39] are proposed to form σ bonded adducts (Wheland intermediates) with benzene.

Structures III have been predicted by Hiraoka, Mizuse and Yamabe [40] to be the most stable complexes when the highly substituted benzene, C_6F_6, and X^- = Cl^-, Br^- and I^- are involved; see Chapter 4. The axial $C_6F_6{\cdot}X^-$ complex is described as being largely electrostatically bonded [40]. Other strong electron withdrawing substituents like CN, CF_3 and NO_2, when present in multiple substitution in benzene, also should promote the formation of the axial electrostatic complex III with the larger nucleophiles Cl^-, Br^- and I^-. The strong bases F^- and CH_3O^- are predicted to form a σ complex with C_6F_6 [27, 41, 42].

From the discussion presented above it becomes evident that structures I-IV could be occurring with different X^- and differently substituted benzenes and that some effort is required to arrive at a prediction for the most stable complex under certain given circumstances. In the present work experimentally determined bond energies based on determinations of equilibria (3.1) with $X^- =$ Br^- and singly, doubly and triply substituted benzenes are reported. The singly substituted benzene complexes are subjected to substituent effect analysis following Taft [43]. This analysis provides very useful supplementary information which, when combined with the structural information discussed above, permits bonding structural assignments to be made. These extend also over complexes involving Cl^- and NO_2^- whose equilibria were measured in previous work [27, 44-46]. Experimental data and theoretical calculations involving X^- (F^-, Cl^- and Br^-) with perfluorobenzenes and X^- (F^-, Cl^- and Br^-) with perfluoroquinones and tetracyanoethylene are reported in Chapters 4 and 5.

3.2 Experimental

Association equilibria (3.1), $X^- = Br^-$, were measured with the pulsed electron high pressure mass spectrometer (PHPMS) described in Chapter 1. The method of equilibrium measurement was as described in Chapter 2. In order to cover a large number of compounds the majority of the equilibrium constant determinations (K_{BrA}) were made at only one temperature, 423 K. The corresponding free energy changes were obtained with equation (3.3).

$$-\Delta G^{o}_{BrA} = RT\ln K_{BrA} \qquad (3.3)$$

The gas mixtures were prepared in the gas handling plant (GHP) which was kept at a temperature of ~150°C. For some of the singly substituted benzenes this temperature was lowered to 80°C to prevent their thermal decomposition. After 30 minutes of mixing a constant gas flow through the ion source was established. The ion source was kept predominantly at 150°C (423 K) except for association equilibrium (3.1) measurements involving weakly bound bromide adducts. For these experiments an ion source temperature of 30°C (303 K) was employed. Methane at ion source pressures of 2-4 torr was used as the major (bath) gas. Reactant (SB) concentrations ranged from 0.1 mtorr for compounds with high bromide affinities up to 600 mtorr for those with low.

Bromide ions were generated in the ion source on dissociative electron capture of near thermal secondary electrons by dibromomethane, CH_2Br_2, present in 1.0-5.0 mtorr concentrations in the ion source. No higher order cluster ions, $(SB)_{n>1}\cdot Br^-$, or $CH_2Br_2\cdot Br^-$ adducts [47] were observed under the experimental conditions described.

An intensity versus time profile of the ions involved in an association equilibrium (3.1) is shown in Figure 3.1. Thermodynamic equilibrium is assumed to be achieved between the substituted nitrobenzene adduct, m-CNNB·Br$^-$, and Br$^-$ about ~0.5 ms after the short 20 μs electron pulse. An ion extraneous to the equilibrium studied is the radical anion m-CNNB$^-$. The decrease in the intensity of the three ions after ~0.7 ms is due to diffusion of the ions to the ion source wall.

The equilibrium constants, K_{BrA}, for reaction (3.1) involving different singly substituted benzenes and singly substituted nitrobenzenes are shown in Figures 3.2 and 3.3. K_{BrA} was determined at three different ion source pressures between 2 and 4 torr for a constant SB/methane partial pressure ratio. This procedure was repeated with a different SB/methane partial pressure ratio where the ratio was changed by at least a factor of five. From Figures 3.2 and 3.3, K_{BrA} is observed to be independent of the partial pressure of SB for different SB/methane ratios. However, a slight decrease in K_{BrA} with increasing ion source pressure is observed for constant SB/methane ratios (represented by similar symbols in Figures 3.2 and 3.3). This is also observed

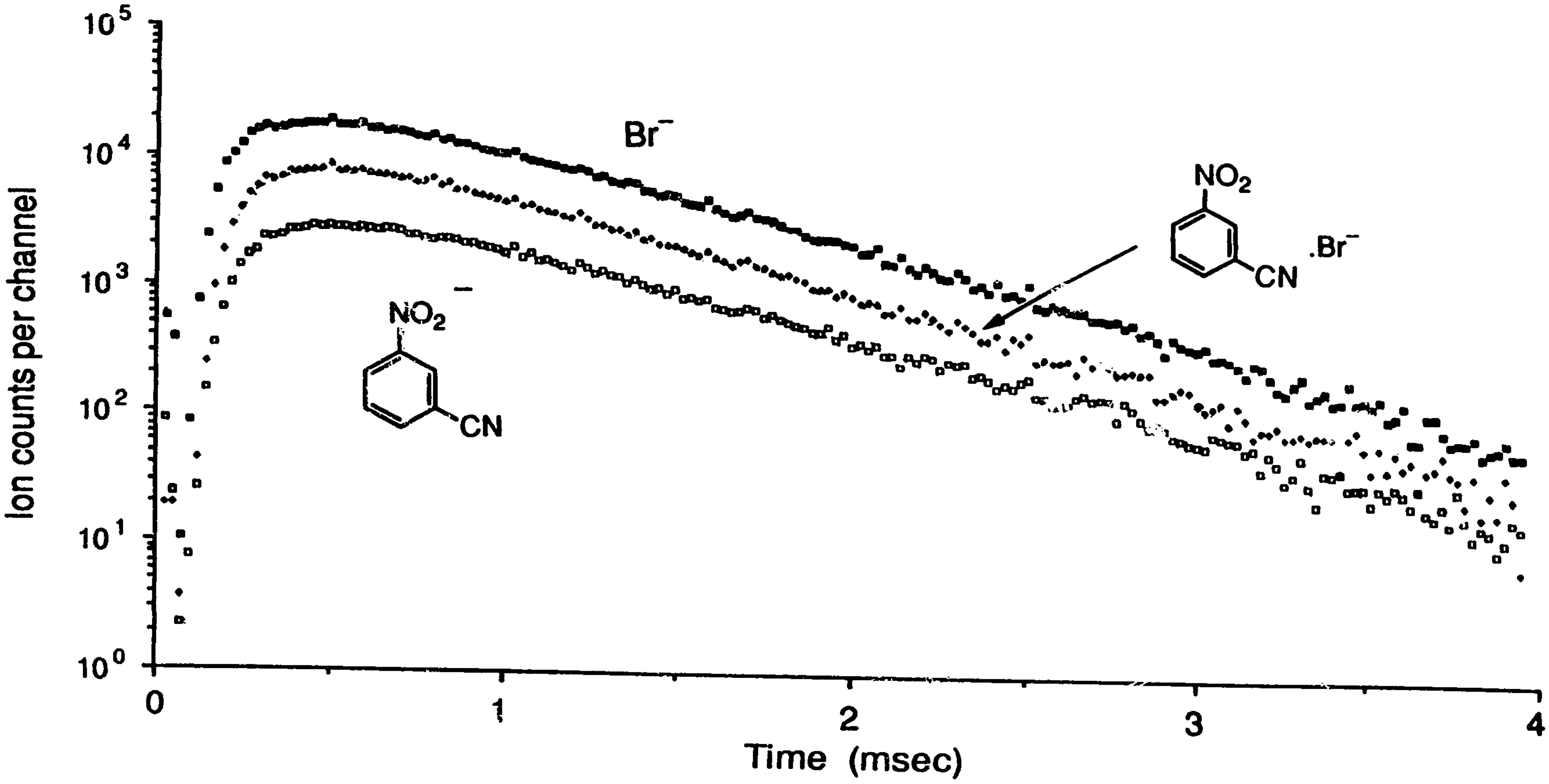

Figure 3.1 Ion intensity versus time after the 20 μs ionizing electron pulse. Obtained with a gas mixture of 2.8 torr CH_4, 0.65 mtorr m-CNNB and 2.1 mtorr CH_2Br_2 at 423K. Br^- ions result from dissociative electron capture by CH_2Br_2. The Br^- attachment equilibrium (3.1): m-CNNB + Br^- = m-CNNB·Br^-, becomes established some 0.5 ms after the electron pulse. The decrease of ion intensity after ~0.7 ms is due to diffusion of the ions to the wall.

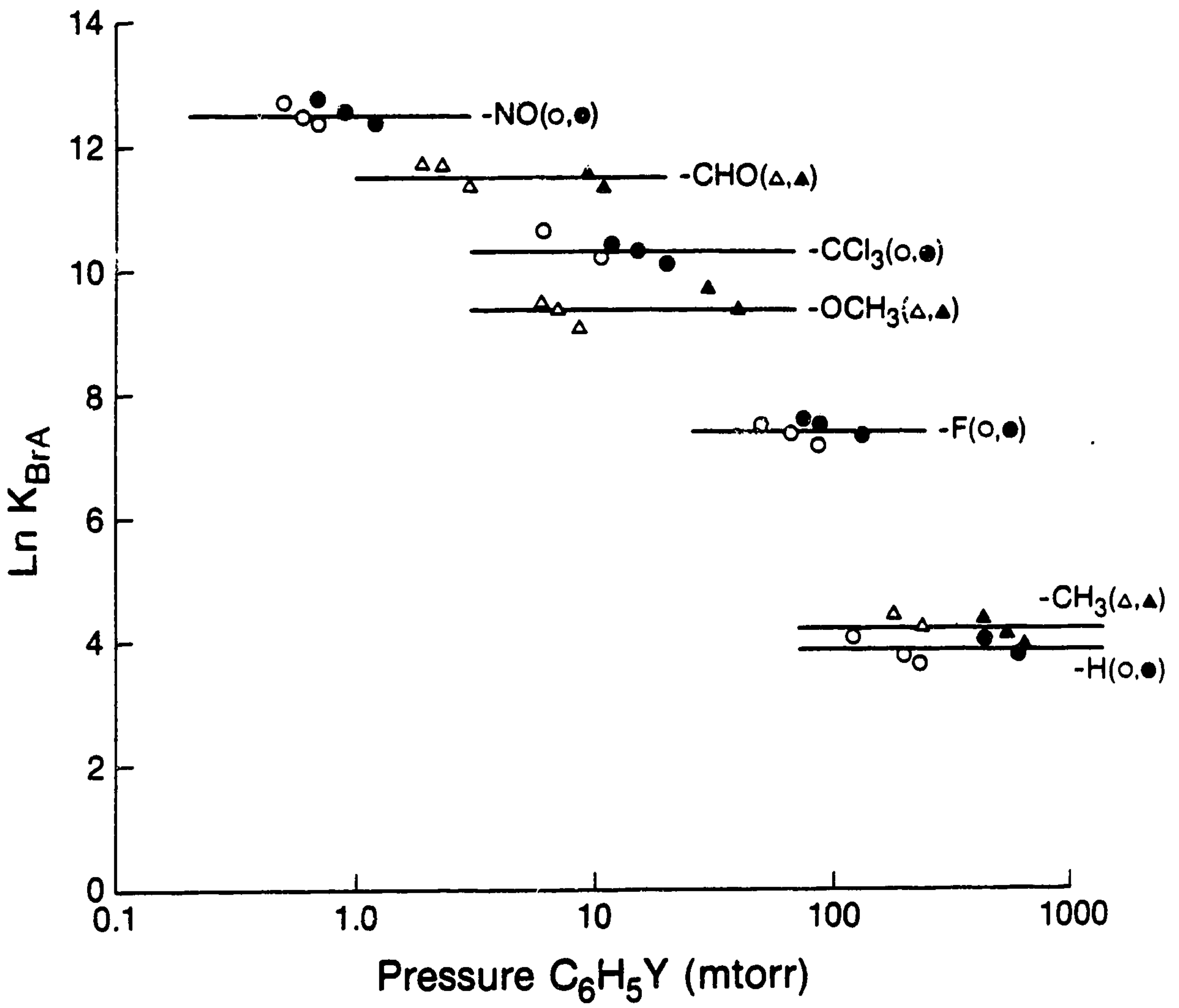

Figure 3.2 K_{BrA} for reaction (3.1) involving different singly substituted benzenes, C_6H_5Y, versus C_6H_5Y partial pressure in the ion source. Ion source temperature, 303K. CH_4 pressure changes from 2-4 torr in runs with the same symbol. In such runs, the CH_4 to C_6H_5Y pressure ratio is constant. K_{BrA} is independent of C_6H_5Y pressure for different C_6H_5Y/methane ratios. However a slight decrease in K_{BrA} is observed with increase of CH_4 pressure for constant C_6H_5Y/methane experiments.

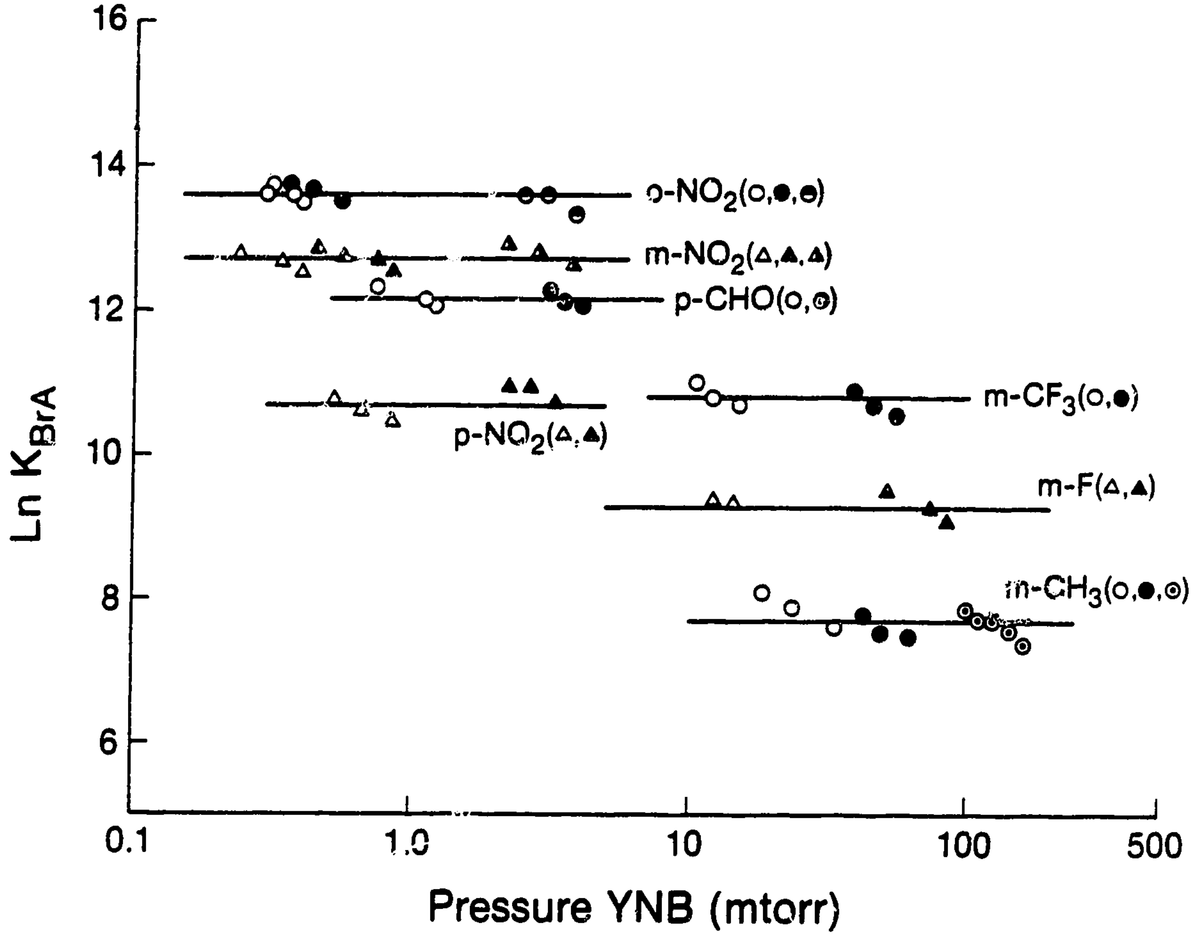

Figure 3.3 K_{BrA} for reaction (3.1) involving different singly substituted nitrobenzenes, YNB, versus YNB partial pressure in the ion source. Ion source temperature, 423K. CH_4 pressure changes from 2-4 torr in runs with the same symbol. In such runs, the CH_4 to YNB pressure ratio is constant. K_{BrA} is independent of YNB pressure for different YNB/methane ratios. However a slight decrease in K_{BrA} is observed with increase of CH_4 pressure for constant YNB/methane experiments.

in Figure 3.4 from plots of K_{BrA} for singly substituted benzenes versus ion source pressure.

The most common source of error believed to occur in PHPMS measurements of association equilibria such as (3.1) is the decomposition of adducts outside the ion source due to collisionally induced dissociation (CID) [48-50]. The occurrence of CID has been proposed in previous measurements of association equilibria (3.1) involving the unsubstituted benzene ($X^- = Cl^-$, Br^- and I^-) [23] and substituted benzenes ($X^- = Cl^-$) [13]. CID is most likely to take place in the region just outside the ion exit slit (Figure 1.3) where the gas pressure is much higher than in the rest of the vacuum chamber. Here if the possibility of collision exists between an accelerated $SB{\cdot}Br^-$ adduct and a neutral then dissociation to SB and Br^- may occur. This would result in a K_{BrA} lower than the true value being determined. Under CID conditions the number of dissociative collisions which occur outside the ion source would be expected to increase with an increase in ion source pressure. Hence, the occurrence of CID should lead to a negative ion source pressure dependence of K_{BrA}. This is observed in Figures 3.2-3.4.

An ion acceleration voltage of +1200 V (ion source voltage = -1200 V, magnetic sector entrance slit = 0 V) and voltage differential of ~+500 V between the ion exit slit and first ion acceleration electrode were employed in equilibrium (3.1) measurements in the present work. The voltage differential between the ion exit slit and first ion acceleration electrode is the most important with respect to CID effects. Tests were performed on equilibrium (3.1) measurements ($X^- = Br^-$) involving nitrobenzene (NB) to check if changing the voltage on the ion source or ion acceleration electrodes had any effect on K_{BrA}. K_{BrA} was first measured varying the ion source voltage from -1200 V to -1800 V. This corresponded to a change in potential between the ion exit slit and first

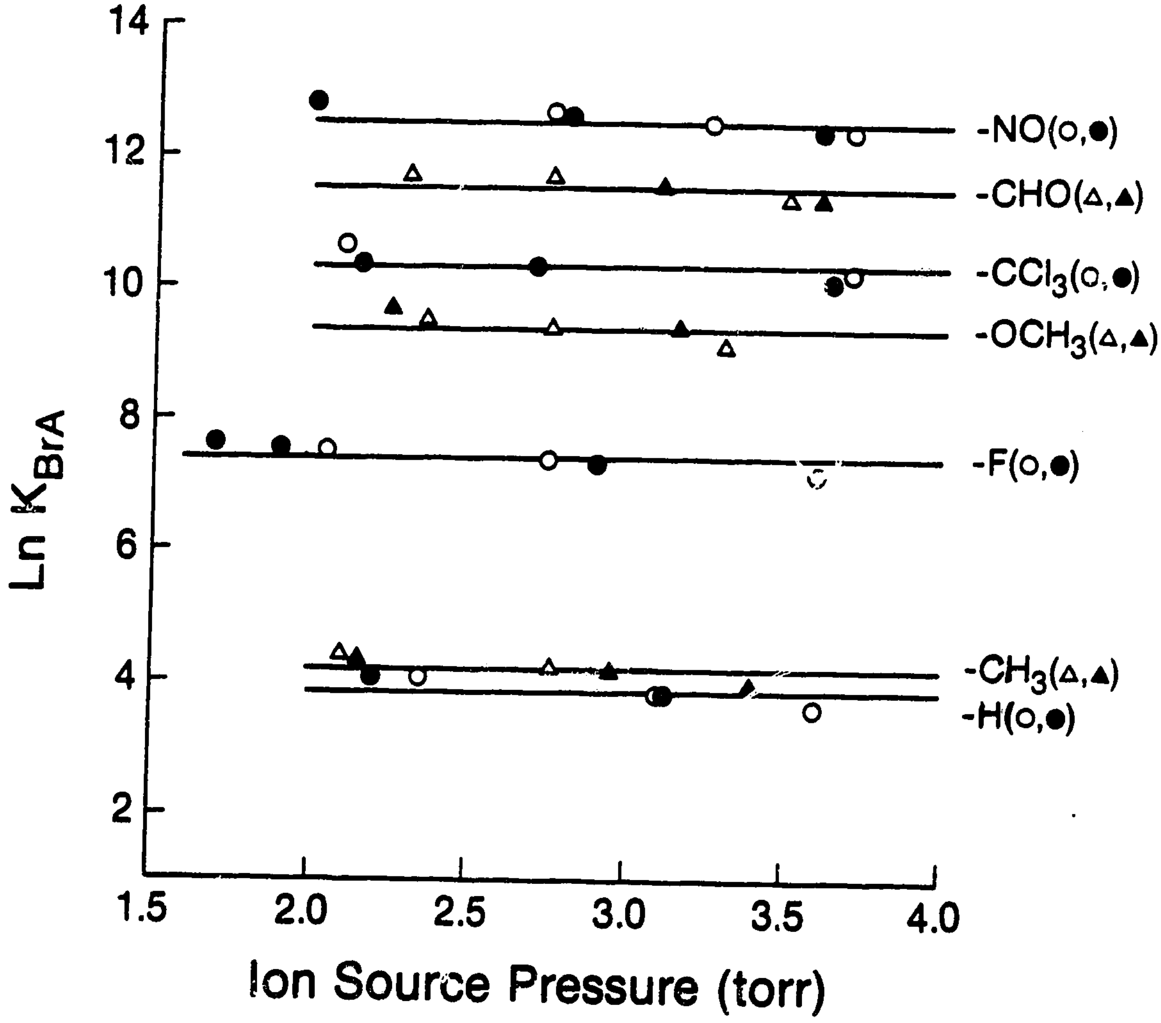

Figure 3.4 K_{BrA} for reaction (3.1) involving singly substituted benzenes versus total ion source pressure. Ion source temperature, 303K. Symbols correspond to those in Figure 3.2. A slight decrease in K_{BrA} with increased ion source pressure is observed.

ion acceleration electrode of +500 to +750 V. From the plot of K_{BrA} versus ion source voltage shown in Figure 3.5, K_{BrA} is observed to be essentially invariant with respect to the voltage change. The next test involved a much smaller voltage differential between the ion exit slit and first ion acceleration electrode, i.e., 50 V. This focusing arrangement was also observed to have little effect on K_{BrA}; see Figure 3.5. The virtual invariance of K_{BrA} under different ion accelerating conditions suggests CID, if present, has only a small effect on equilibrium constant determinations.

Because of the possibility of CID the concentrations of SB in the ion source were specifically chosen so as to maximize the intensity of the bromide ion to that of the adduct. This condition was easily achieved for most equilibrium (3.1) measurements.

Relative bond free energies ($-\Delta\Delta G^{o}_{BrA}$) were also determined in the present work by measurements of bromide transfer (BrTr) equilibria (3.2). These measurements were performed at both 303 K and 423 K. $-\Delta G^{o}_{BrTr,303K}$ is presumed equal to $-\Delta G^{o}_{BrTr,423K}$ based on the assumption there is no entropy change between products and reactants in reaction (3.2). Bromide transfer equilibria were measured for two SB/SB' partial pressure ratios at ion source pressures between 2 and 4 torr. The K_{BrTr} values from measurements of transfer equilibria (3.2) involving singly substituted benzenes plotted against ion source pressure are shown in Figure 3.6. K_{BrTr} is observed to be pressure independent. This suggests the error in $-\Delta\Delta G^{o}_{BrA}$ determinations is smaller than that for absolute determinations of $-\Delta G^{o}_{BrA}$ from measurements of equilibria (3.1). This is not surprising as $I(Br^-)$ is not present in the equilibrium constant expression for reaction (3.2), i.e., Br^- is a product of the collisionally induced dissociation of $SB{\cdot}Br^-$ and $SB'{\cdot}Br^-$, and any CID effects on the bromide adducts would be expected to mostly cancel out. Hence $-\Delta G^{o}_{BrTr}$ (or $-\Delta\Delta G^{o}_{BrA}$) values

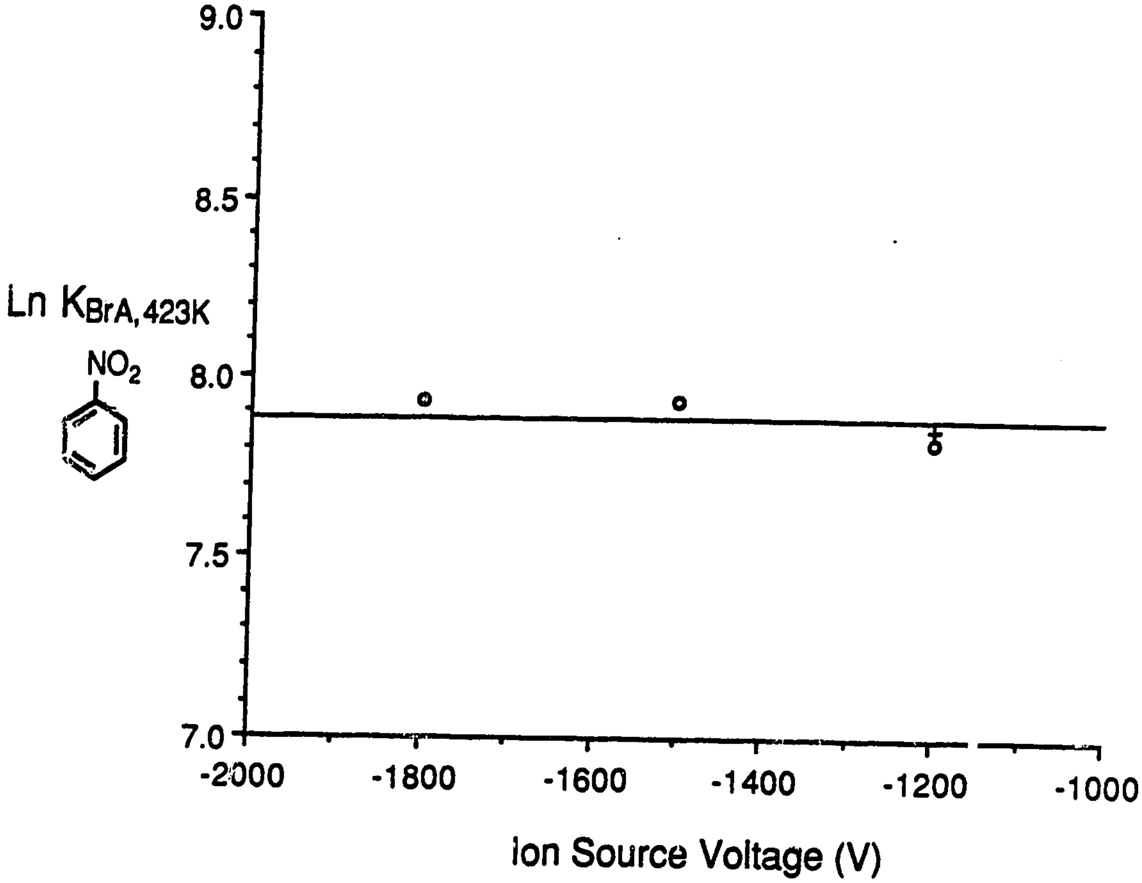

Figure 3.5 o:- Equilibrium constants for reaction (3.1): NB + Br^- = $NB{\cdot}Br^-$, versus ion source voltage. Potential difference between ion source exit slit and first ion acceleration electrode ranges from 500 V (ion source voltage, -1200 V) to 750 V (ion source voltage, -1800 V). K_{BrA} obtained with a gas mixture of 4 torr CH_4, 150 mtorr NB and 5.0 mtorr CH_2Br_2 at 423K.

+:- Measurement of K_{BrA}(NB) with potential difference of 50 V between ion source exit slit and first ion acceleration electrode. Ion source voltage -1200 V. Ion source conditions as above.

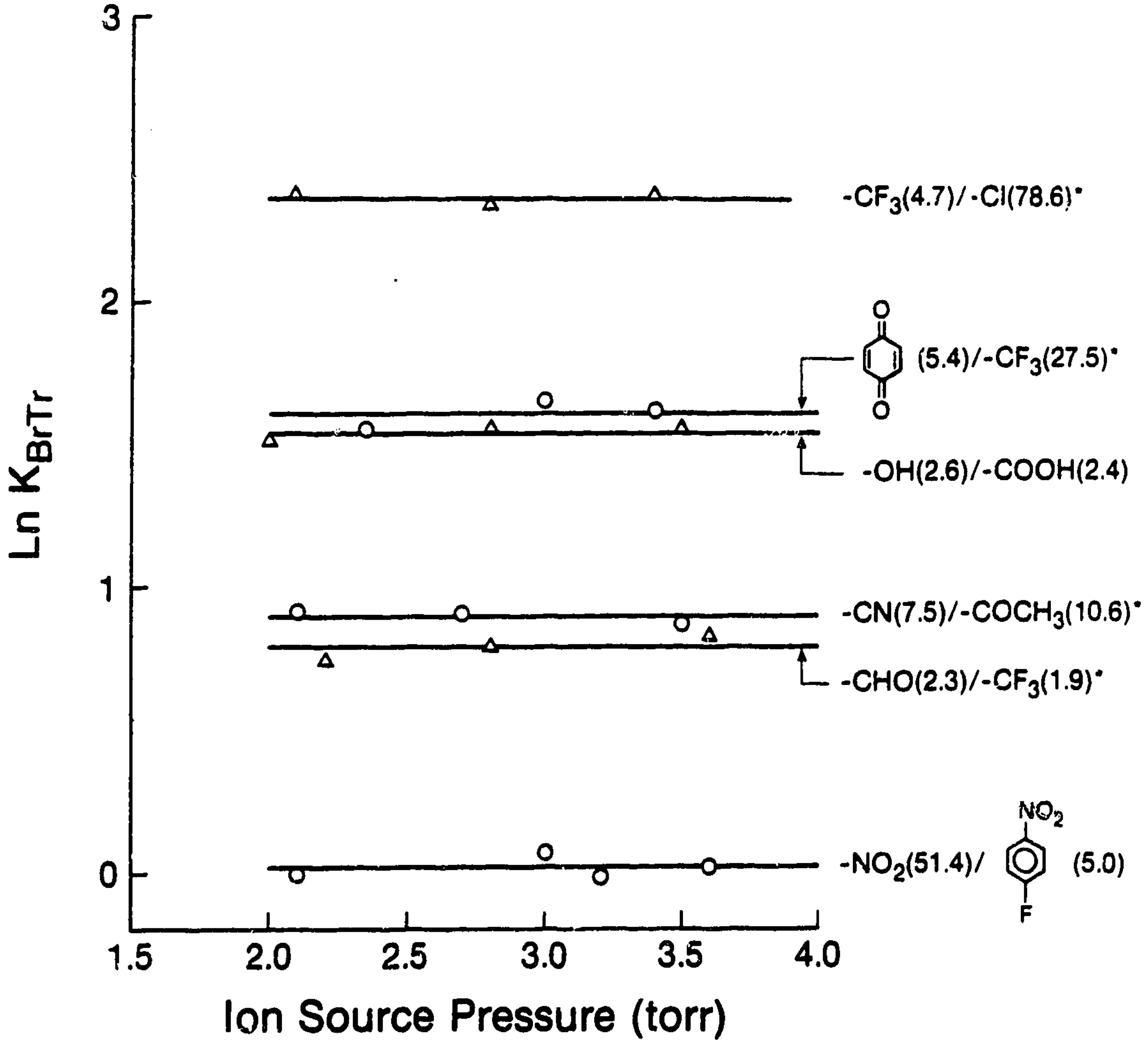

Figure 3.6 K_{BrTr} for bromide transfer equilibria (3.2): $SB{\cdot}Br^- + SB' = SB + SB'{\cdot}Br^-$, involving singly substituted benzenes (C_6H_5Y) versus total ion source pressure. Reactant (SB, SB') pressures given in figure (in mtorr). CH_4 pressure, 3 torr and CH_2Br_2 pressure, 4.1 mtorr. Transfer equilibria measured at 303K (*) and 423K. K_{BrTr} is independent of ion source pressure.

provide a good check on the relative bond free energies predicted by the directly determined $-\Delta G^{o}_{BrA}$ values. The greater accuracy of relative bond free energy determinations compared to absolute determinations has been commented on in previous work involving the PHPMS [16, 51].

More thermochemical information on bromide attachment to a representative singly substituted benzene, nitrobenzene (NB), and to a singly substituted nitrobenzene, m-CF_3 nitrobenzene (m-CF_3NB), was obtained by means of van't Hoff plots. The entropy changes, ΔS^{o}_{BrA}, of these reactions (3.1) are required to estimate bond free energies at 423 K ($-\Delta G^{o}_{BrA,423K}$) of $SB{\cdot}Br^-$ adducts whose association equilibria (3.1) were measured at 303 K. The entropy changes for a series of related association reactions like (3.1) are often found to be relatively independent of the nature of the molecule [44, 45, 51].

In the van't Hoff experiments the temperature dependence of the equilibrium constant, K_{BrA}, was measured and the bond enthalpy, $-\Delta H^{o}_{BrA}$, and entropy, $-\Delta S^{o}_{BrA}$, corresponding to reaction (3.1) determined by plotting $\ln K_{BrA}$ against 1/T; see equations (3.4) and (3.5).

$$\Delta G^{o}_{BrA} = -RT\ln K_{BrA} = \Delta H^{o}_{BrA} - T\Delta S^{o}_{BrA} \qquad (3.4)$$

$$\ln K_{BrA} = \frac{-\Delta H^{o}_{BrA}}{RT} + \frac{\Delta S^{o}_{BrA}}{R} \qquad (3.5)$$

It is important to note that the enthalpy change is a weak function of temperature due to the difference in heat capacities (ΔC_p) of products and reactants. Using calculated vibrational frequencies, Castleman et al. [20] evaluated $-\Delta H^{o}_{ClA,298K}(H_2O)$ and $-\Delta H^{o}_{ClA,0K}(H_2O)$ (= D_{0K}, the bond energy) at 14.9 and 14.2 kcal/mol respectively. Thus, discussing measured enthalpy changes in terms of bond energies appears to be a reasonable approximation [20].

The temperature dependence of K_{BrA} was measured by letting the ion source temperature decrease slowly (100°C drop over ~8 hours). Two separate experiments with SB/methane ratios differing by a factor of 5 were performed. Measurements were performed at ~15°C intervals with an overall range of ~100°C being covered. All equilibrium measurements were performed at the same ion source pressure, 2 torr. The concentration of SB in the ion source and the temperature range investigated were pre-selected to give the maximum intensity possible for the bromide ion with respect to the adduct .

The van't Hoff plots for NB and m-CF_3NB are shown in Figure 3.7. The data points from the different SB/methane experiments are included in each plot. Straight line dependencies are observed with no "bending over" at lower temperatures which is characteristic of the occurrence of CID [49]. The $-\Delta H^{o}_{BrA}$ and $-\Delta S^{o}_{BrA}$ values from the plots are given in the figure caption. Errors in $-\Delta H^{o}_{BrA}$ and $-\Delta S^{o}_{BrA}$ were assessed from separate determinations of $-\Delta H^{o}_{BrA}$ and $-\Delta S^{o}_{BrA}$ for each SB/methane ratio. Excellent agreement was observed for $-\Delta G^{o}_{BrA,423K}$ of NB and m-CF_3NB evaluated from $-\Delta H^{o}_{BrA}$ and $-\Delta S^{o}_{BrA}$ values (using $-\Delta G^{o}_{BrA} = -\Delta H^{o}_{BrA} + T\Delta S^{o}_{BrA}$) with the bond free energies determined independently at 423 K; see Figure 3.7 and Tables 3.1 and 3.2, Results and Discussion.

3.3 Results and Discussion

3.3a Results

The $-\Delta G^{o}_{BrA,423K}$ values for singly substituted benzenes and singly and doubly substituted nitrobenzenes, obtained from measurements of equilibria (3.1), are shown on scales of increasing $-\Delta G^{o}_{BrA,423K}$ in Figures 3.8

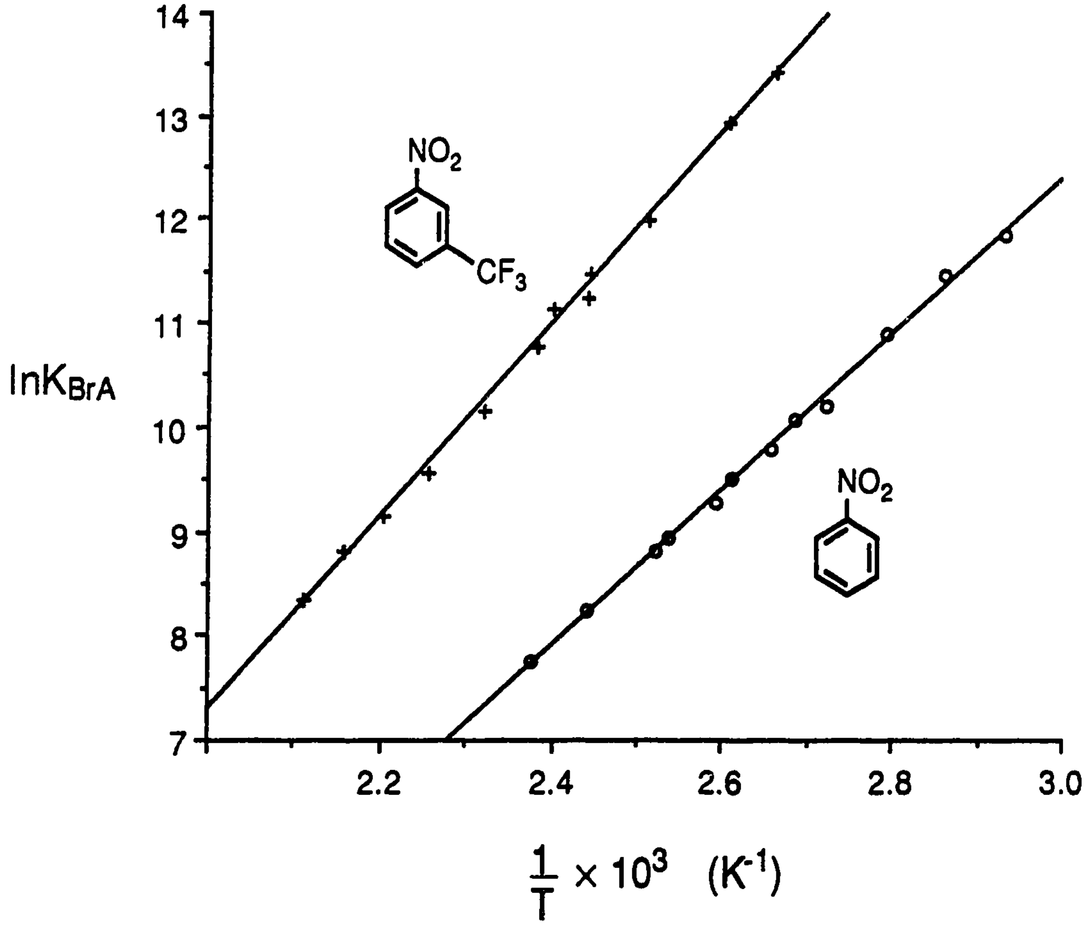

Figure 3.7 van't Hoff plots of equilibrium constants for bromide attachment (3.1) to NB and m-CF_3NB. From slope of plot: $-\Delta H^{\circ}_{BrA}$(NB) = 15.0 kcal/mol ,$-\Delta H^{\circ}_{BrA}$(m-CF_3NB) = 18.4 kcal/mol. Error ±2 kcal/mol. From intercept: $-\Delta S^{\circ}_{BrA}$(NB) = 20.2 cal/deg mol, $-\Delta S^{\circ}_{BrA}$(m-CF_3NB) = 22.3 cal/deg mol. Error ±3 cal/deg mol. From $-\Delta H^{\circ}_{BrA} = -\Delta G^{\circ}_{BrA} - T\Delta S^{\circ}_{BrA}$, $-\Delta G^{\circ}_{BrA,423K}$(NB) = 6.5 kcal/mol and $-\Delta G^{\circ}_{BrA,423K}$(m-$CF_3$NB) = 9.0 kcal/mol. These values are in good agreement with those determined directly at 423K, see Tables 3.1 and 3.2.

and 3.9 (standard state, 1 Atm). The $-\Delta S^o_{BrA}$ values given in Figure 3.7 ($-\Delta S^o_{BrA}$(NB) = 20.2 cal $deg^{-1}mol^{-1}$ and $-\Delta S^o_{BrA}$(m-CF_3NB) = 22.3 cal $deg^{-1}mol^{-1}$) are used to convert $-\Delta G^o_{BrA,303K}$ values to $-\Delta G^o_{BrA,423K}$. Benzene has a high rotational symmetry number, $\sigma = 12$, and is the only compound for which formation of the Br^- complex, presumed to be of structure I and $\sigma = 2$, leads to a large rotational entropy symmetry change: ΔS^o_{BrA} = Rln6 = 3.5 cal $deg^{-1}mol^{-1}$. Therefore for benzene the $-\Delta G^o_{BrA}$ from 303 K to 423 K was calculated by using $-\Delta S^o_{BrA}$ = 17 cal $deg^{-1}mol^{-1}$. Absolute $-\Delta G^o_{BrA}$ values are probably accurate to ±1 kcal/mol [16]. This error bar adequately covers the observed decrease in K_{BrA} over the ion source pressure range which corresponds to an error of ±0.2 kcal/mol in $-\Delta G^o_{BrA}$. The lengths of the arrows shown in Figures 3.8 and 3.9 correspond to $-\Delta G^o_{BrTr}$ ($-\Delta\Delta G^o_{BrA}$) determinations. An accuracy of ±0.2 kcal/mol was previously quoted for halide transfer free energy determinations [16] and this error bar is in line with the spread of $-\Delta G^o_{BrTr}$ values determined from different SB/SB' ratio experiments. In all cases, the arrows in Figures 3.8 and 3.9 are within ±0.3 kcal/mol of the relative bond free energies ($-\Delta\Delta G^o_{BrA}$) predicted by the independently determined $-\Delta G^o_{BrA,423K}$ values.

The $-\Delta G^o_{BrA,423K}$ data are summarized in Tables 3.1 and 3.2. Approximate $-\Delta H^o_{BrA}$ values can be obtained from $-\Delta H^o_{BrA} = -\Delta G^o_{BrA} - T\Delta S^o_{BrA}$ and the $-\Delta G^o_{BrA,423K}$ values given in Tables 3.1 by assuming $-\Delta S^o_{BrA}$ = 20 cal deg^{-1} mol^{-1} for all compounds except benzene where $-\Delta S^o_{BrA}$ = 17 cal $deg^{-1}mol^{-1}$. For the compounds in Table 3.2 $-\Delta S^o_{BrA}$ = 22 cal $deg^{-1}mol^{-1}$ may be more appropriate.

The $-\Delta G^o_{BrA,423K}$ value for C_6H_6 is ~1 kcal/mol lower than the value reported by Hiraoka et al. [23] The reason for this discrepancy is not known. Checks on $-\Delta G^o_{BrA,423K}(C_6H_6)$ with a different PHPMS yielded values within 0.3 kcal/mol of that given in Table 3.1.

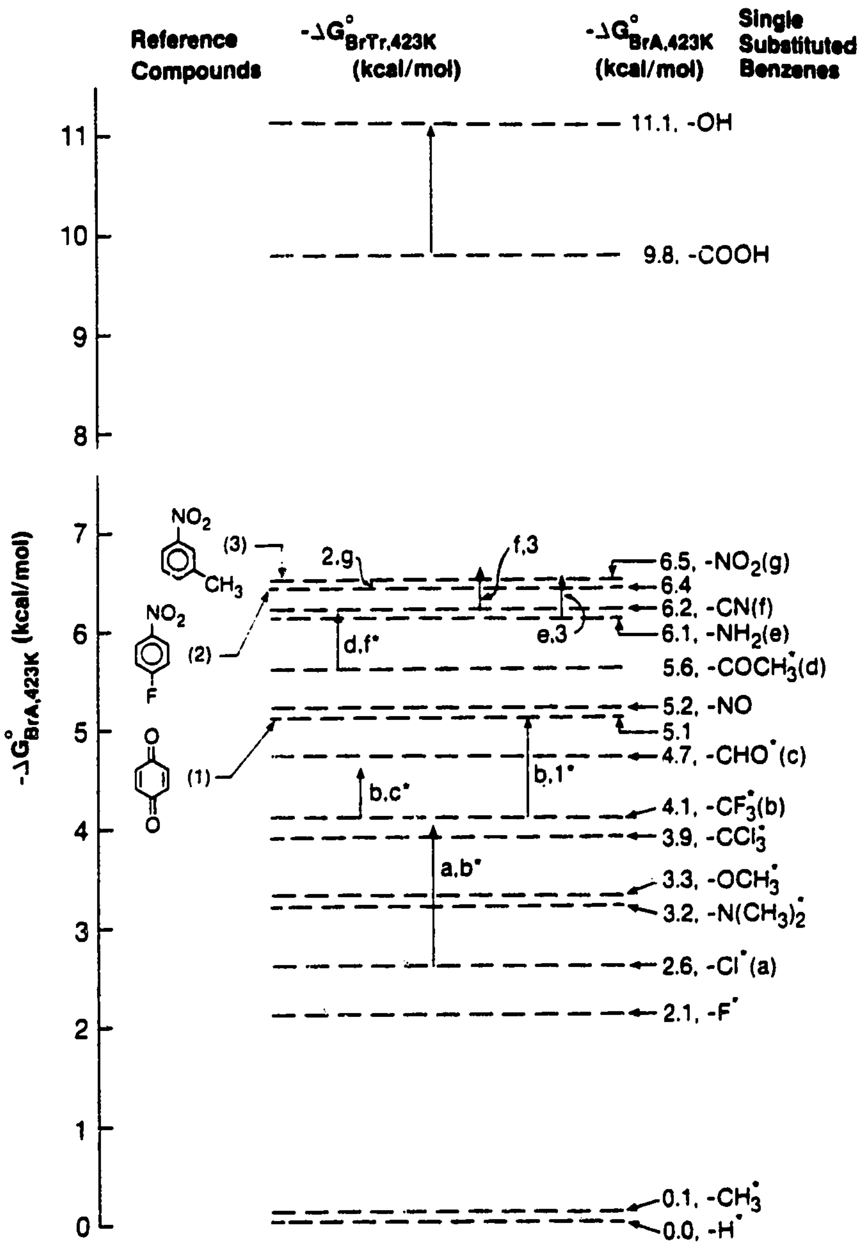

Figure 3.8 Scale of $-\Delta G^{o}_{BrA,423K}$ for reaction (3.1): SB + Br$^-$ = SB·Br$^-$ where SB are singly substituted benzenes. Association equilibria (3.1) measured at 303K (*) and 423K. For conversion of $-\Delta G^{o}_{BrA,303K}$ to $-\Delta G^{o}_{BrA,423K}$, see text. Lengths of arrows shown correspond to determinations of $-\Delta G^{o}_{BrTr}$ (= $-\Delta\Delta G^{o}_{BrA}$) from measurements of bromide transfer equilibria (3.2): SB·Br$^-$+ SB' = SB + SB'·Br$^-$, at 303K (*) and 423K. SB and SB' identified by letters beside arrows. $-\Delta G^{o}_{BrA,423K}$ of reference compounds involved in equilibrium (3.2) measurements from Table 3.2 and Table 5.1.

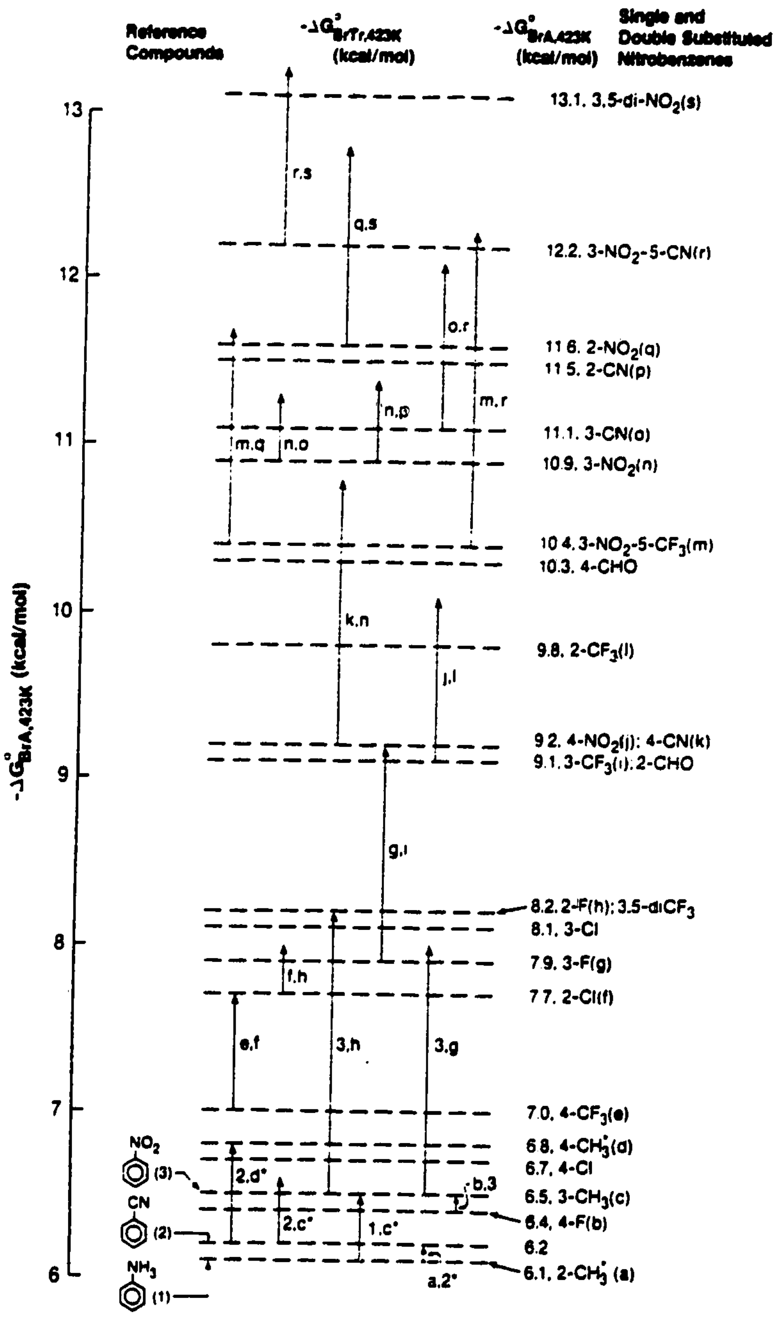

Figure 3.9 Scale of $-\Delta G^{o}_{BrA,423K}$ for reaction (3.1): SB + Br^- = SB·Br^- where SB are substituted nitrobenzenes. Association equilibria (3.1) measured at 303K (*) and 423K. Lengths of arrows shown correspond to determinations of $-\Delta G^{o}_{BrTr}$ (= $-\Delta\Delta G^{o}_{BrA}$) from measurements of bromide transfer equilibria (3.2): SB·Br^-+ SB' = SB + SB'·Br^-, at 303K (*) and 423K. SB and SB' identified by letters beside arrows. $-\Delta G^{o}_{BrA,423K}$ of reference compounds involved in equilibrium (3.2) measurements from Table 3.1.

Table 3.1 [a] Free energy change $-\Delta G^{o}_{BrA,423K}$ for reaction (3.1): $Br^- + YC_6H_5 = YC_6H_5 \cdot Br^-$.

Y	$-\Delta G^{o}_{BrA,423K}$ (kcal/mol)
H	0.0[b]
CH_3	0.1[c]
F	2.1[c]
Cl	2.6[c]
$N(CH_3)_2$	3.2[c]
OCH_3	3.3[c]
CCl_3	3.9[c]
CF_3	4.1[c]
CHO	4.7[c]
NO	5.2[c]
$COCH_3$	5.6[c]
NH_2	6.1
CN	6.2
NO_2	6.5
COOH	9.8
OH	11.1

a. Data from Figure 3.8. C_6H_5Y are substituted benzenes. Standard state 1 Atm.

b. Bond free energy determined at 303K. $-\Delta G^{o}_{BrA,423K}(C_6H_6)$ estimated using $-\Delta S^{o}_{BrA} = 17.0$ cal degree^{-1} mol^{-1}, see text.

c. Bond free energy determined at 303K. $-\Delta G^{o}_{BrA,423K}$ estimated using $-\Delta S^{o}_{BrA}(NB) = 20.2$ cal degree^{-1} mol^{-1}, see Figure 3.7.

Table 3.2[a] Free energy change $-\Delta G^{o}_{BrA,423K}$ for reaction (3.1): $Br^{-} + SB = SB \cdot Br^{-}$ involving singly and doubly substituted nitrobenzenes.

SB	$-\Delta G^{o}_{BrA,423K}$ (kcal/mol)	SB	$-\Delta G^{o}_{BrA,423K}$ (kcal/mol)
2-CH_3NB	6.1[b]	2-CHONB	9.1
3-CH_3NB	6.5	3-CHONB	10.3
4-CH_3NB	6.8[b]	2-CNNB	11.5
NB	6.5	3-CNNB	11.1
2-FNB	8.2	4-CNNB	9.2
3-FNB	7.9	2-NO_2NB	11.6
4-FNB	6.4	3-NO_2NB	10.9
2-ClNB	7.7	4-NO_2NB	9.2
3-ClNB	8.1	3,5-diCF_3NB	8.2
4-ClNB	6.7	3-NO_2-5-CF_3NB	10.4
2-CF_3NB	9.8	3-NO_2-5-CNNB	12.2
3-CF_3NB	9.1	3,5-diNO_2NB	13.1
4-CF_3NB	7.0		

a. Data from Figure 3.9. Standard state 1 Atm.

b. Bond free energy determined at 303K. $-\Delta G^{o}_{BrA,423K}$ estimated using $-\Delta S^{o}_{BrA}$(3-CF_3NB) = 22.3 cal degree^{-1} mol^{-1}, see Figure 3.7.

3.3b Singly Substituted Benzenes

The experimentally determined bond free energies, $-\Delta G^{o}_{BrA,423K}$, for the complexes of Br^- with C_6H_5Y (Table 3.1) are seen to increase as the substituent Y becomes more strongly electron withdrawing. In analogy with the theoretical result [31] for $NO_2C_6H_5{\cdot}F^-$ which predicted the most stable structure to be the C-H$\cdots$$F^-$ hydrogen bonded complex VI (see Introduction) where F^- is interacting with the C-H hydrogen in position para to the NO_2, it is assumed that all the $YC_6H_5{\cdot}Br^-$ complexes are C-H hydrogen bonded, i.e., have structure I. Since Br^- has a much lower tendency to form σ bonds than F^-, the theoretical result [31] certainly excludes the σ bonded structures IV as a possibility for $YC_6H_5{\cdot}Br^-$.

The $-\delta\Delta G^{o}_{BrA,423K}$ for C_6H_5Y are shown in Figure 3.10 plotted versus the dipole moment of the substituted benzene. The $-\delta\Delta G^{o}_{BrA,423K}$ values correspond to the free energy change for reaction (3.6) and are evaluated from the

$$C_6H_6{\cdot}Br^- + YC_6H_5 = C_6H_6 + YC_6H_5{\cdot}Br^- \qquad (3.6)$$

$-\Delta G^{o}_{BrA,423K}$ data in Table 3.1. An excellent correlation (correlation coefficient r = 0.997) is observed with the dipole moment when the hydrogen bonding substituents (labelled o in Figure 3.10) are excluded. The relationship is consistent with C-H$\cdots$$X^-$ hydrogen bonding and indicates that the field effect of the substituent will be the dominant substituent effect.

In the following discussion use will made of the substituent effect concepts developed by Taft and Topsom [43].

$$\delta\Delta G^{\circ} = \rho_R\sigma_R + \rho_F\sigma_F + \rho_\alpha\sigma_\alpha \qquad (3.7)$$

In equation (3.7) the total energy change, $\delta\Delta G^{\circ}$, due to a given substituent is separated into contributions due to resonance ($R = \rho_R\sigma_R$), field effect ($F = \rho_F\sigma_F$)

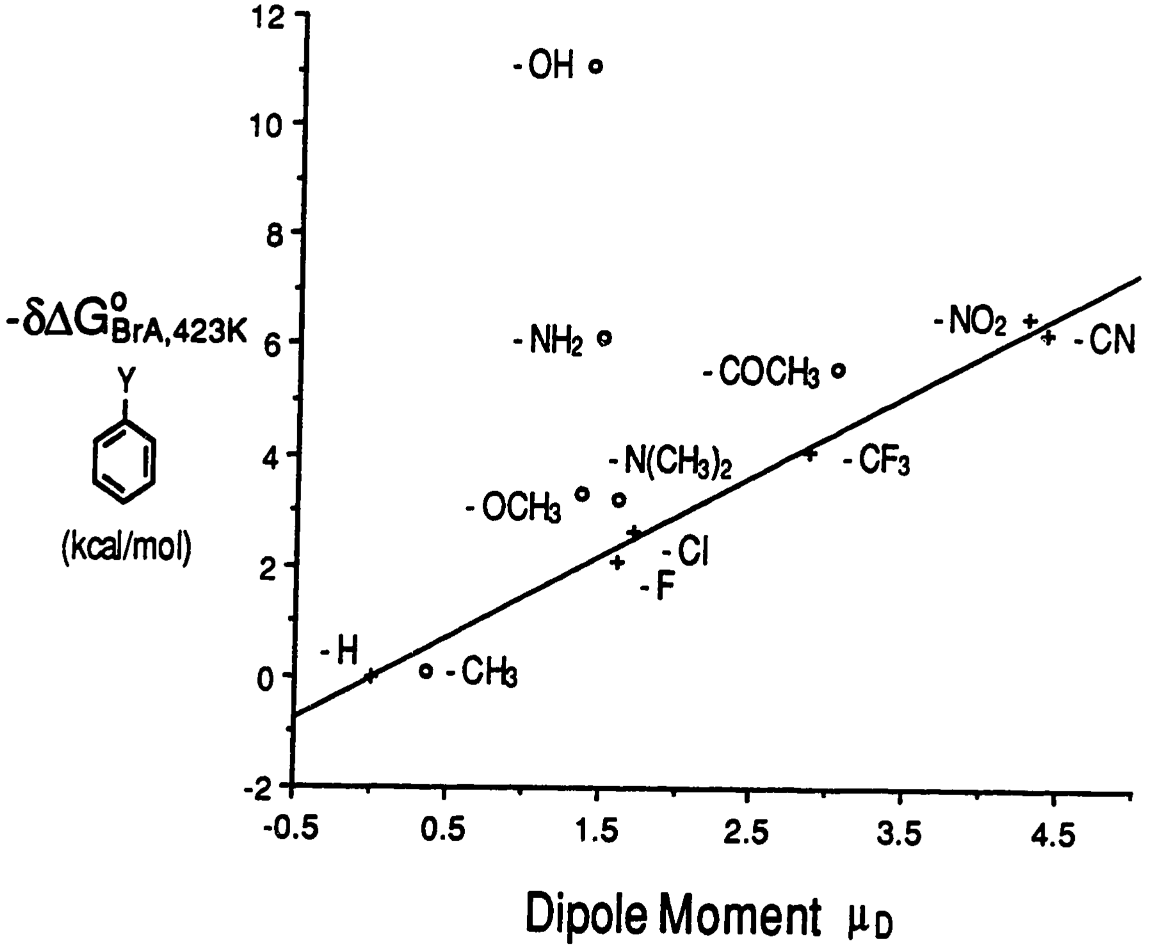

Figure 3.10 Plot of $-\delta\Delta G^{o}_{BrA,423K}$ for Br^- bonding to singly substituted benzenes, C_6H_5Y, versus dipole moment of C_6H_5Y. Excellent correlation, $r = 0.997$, for singly substituted benzenes containing only aromatic protons (+).

and polarizability $P = \rho_\alpha \sigma_\alpha$. The σ parameters are constants for the given substituent and are tabulated [43, 52] while the ρ values are dependent on the given reaction series and are determined by best fit regression analysis to the experimental $\delta\Delta G^\circ$ values.

The experimentally determined $-\delta\Delta G^\circ_{BrA,423K}$ versus the calculated $-\delta\Delta G^\circ_{BrA,423K}$ with the best fit parameters is shown in Figure 3.11. A very good correlation ($r = 0.987$) is observed. The ρ values obtained from the fit are given in Table 3.3. It was found that inclusion of the polarizability term improved the fit very little and had only a very small effect on the ρ_R and ρ_F values (Table 3.3). Therefore, for simplicity, the discussion will be based on the field and resonance effects only.

In order to provide the actual magnitude of the energy contribution of the resonance and field effect to the bond free energies, the evaluated $R = \rho_R \sigma_R$ and $F = \rho_F \sigma_F$ are given in Table 3.4. Examination of these data shows that even for substituents like NO_2, which are strong π acceptors, the R energy term is close to five times smaller than the F term. This result which shows that electrostatic field effects dominate the bond interactions is in line with dependence on the dipole moments observed in Figure 3.10.

More limited data for $-\Delta G^\circ_{XA}$, $X^- = Cl^-$, are available from previous determinations performed in this laboratory [13, 44, 45]. These were used to obtain the plot shown in Figure 3.12. The bonding energies of Cl^- to the substituted benzenes are only slightly larger than those for Br^- and this is reflected in the similarity of the resulting ρ values obtained from the two sets of data; see Figures 3.11 and 3.12 and Tables 3.3 and 3.4.

Also given in Tables 3.3 and 3.4 for comparison are the ρ values and the R and F values for the gas phase acid dissociation, equation (3.8), of benzoic acids and phenols obtained from the corresponding $-\delta\Delta G^\circ_{Acid}$ values [43].

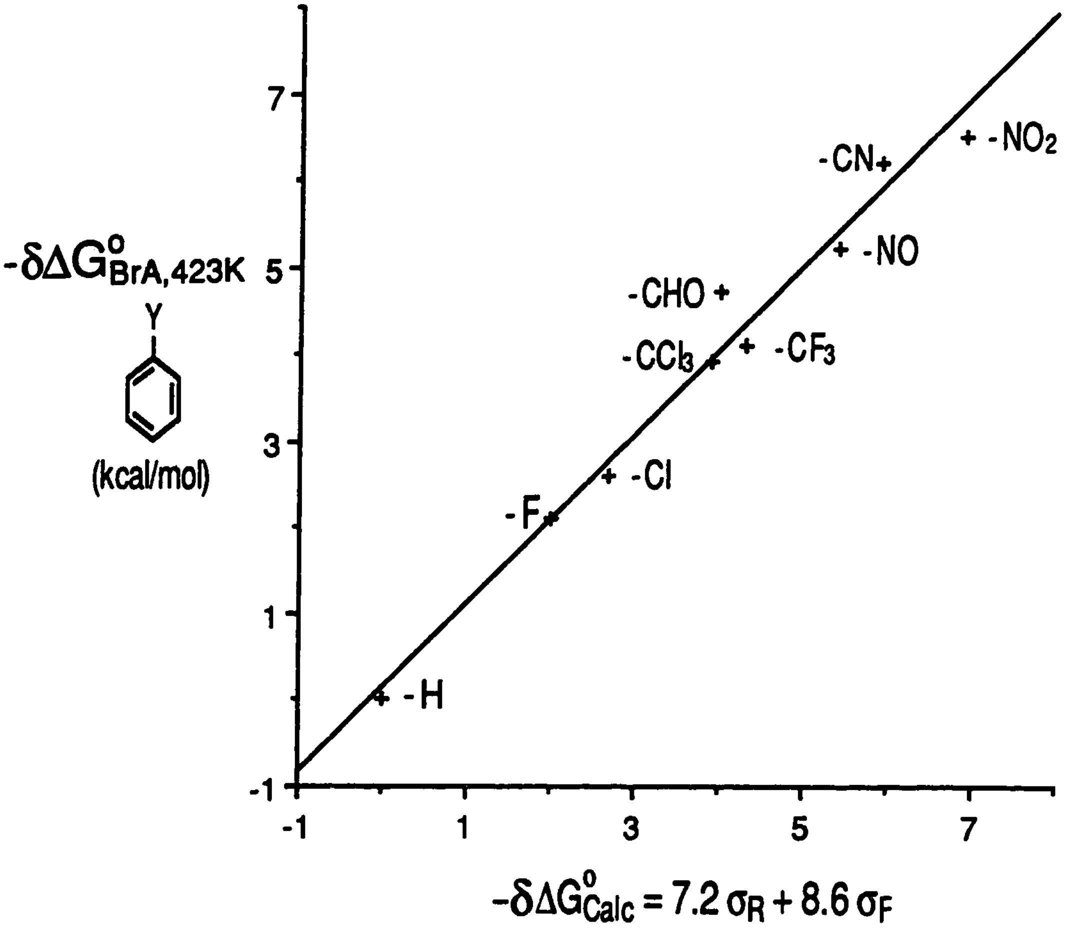

Figure 3.11 $-\delta\Delta G^{o}_{BrA,423K}$ for Br^- and singly substituted benzenes versus $-\delta\Delta G^{o}_{Calc}$ calculated with Taft σ parameters, see equation (3.7). $-\delta\Delta G^{o}_{BrA,423K} = 0$ for Y = H. Correlation coefficient r = 0.987.

Table 3.3 Values for Resonance ρ_R, Field ρ_F and Polarizability ρ_α Parameters; Taft Equation (3.7)[a]

Reaction	ρ_R	ρ_F	ρ_α	r[b]	**Origin of data**
$YC_6H_5{\cdot}Br^-$ [a]	7.2±0.8	8.6±0.3	-	0.987	Table 3.1
	7.0±0.8	8.3±0.5	-0.5±0.6	0.990	
$YC_6H_5{\cdot}Cl^-$ [a]	6.6±0.6	9.1±0.2	-	0.998	[13, 44, 45]
	6.4±0.5	8.9±0.4	-0.5±0.7	0.999	
4-$YPhCO_2H$[c]	14.6±0.7	15.0±0.6	0.1±1.0	0.997	Taft [43]
4-YPhOH[c] π acceptors	49.0±1.5	18.6±0.5	0.6±0.8	0.999	Taft [43]

a. ρ values obtained from linear regression analysis of eq. (3.7), where $\delta\Delta G^{o}_{XA,423K}$ corresponds to experimentally determined ΔG° for reaction $YC_6H_5 + C_6H_6{\cdot}X^- = YC_6H_5{\cdot}X^- + C_6H_6$ (X^- = Br^- and Cl^-). Since $\delta\Delta S^{o}_{XA} \approx 0$, $-\delta\Delta G^{o}_{ClA}$, even though determined at 300K is also valid at 423K, i.e., $-\delta\Delta G^{o}_{ClA,300K} \approx -\delta\Delta G^{o}_{ClA,423K}$.

b. Correlation coefficient.

c. Gas phase acidities.

Table 3.4 Resonance R and Field F Contributions of Substituents[a]

Substituent	$YC_6H_5{\cdot}Br^-$ [b]		$YC_6H_5{\cdot}Cl^-$ [c]		4-YPhOH[d]		$4\text{-}YPhCO_2H$[d]	
	R	F	R	F	R	F	R	F
$-NO_2$[f]	1.3	5.6	1.2	5.9	8.8	12.1	2.6	9.8
-CN[f]	0.7	5.2	0.7	5.5	4.9	11.2	1.5	9.0
-CHO[f]	1.3	2.7	-	-	9.3	5.8	2.8	4.7
$-CF_3$[f]	0.5	3.8	-	-	3.4	8.2	1.0	6.6
-H	0.0	0.0	0.0	0.0	0.0	0.0	0.0	0.0
-Cl[g]	-1.2	3.9	-1.1	4.1	e	e	-2.5	6.8
-F[g]	-1.8	3.8	-1.7	4.0	e	e	-3.7	6.6

a. Contribution: $R = \rho_R\sigma_R$ and $F = \rho_F\sigma_F$ in kcal/mol to $-\delta\Delta G^{\circ}$, see eq. (3.7), for given substituent.

b. $-\delta\Delta G^{\circ}_{BrA,423K}$ for reaction (3.1) involving singly substituted benzenes.

c. $-\delta\Delta G^{\circ}_{ClA,423K}$ for reaction (3.1) involving singly substituted benzenes.

d. $-\delta\Delta G^{\circ}_{Acid}$ for gas phase acidities of phenols and benzoic acids.

e. π donor substituents require a separate fit; see Chapter 2.

f. π acceptor substituent.

g. π donor substituent.

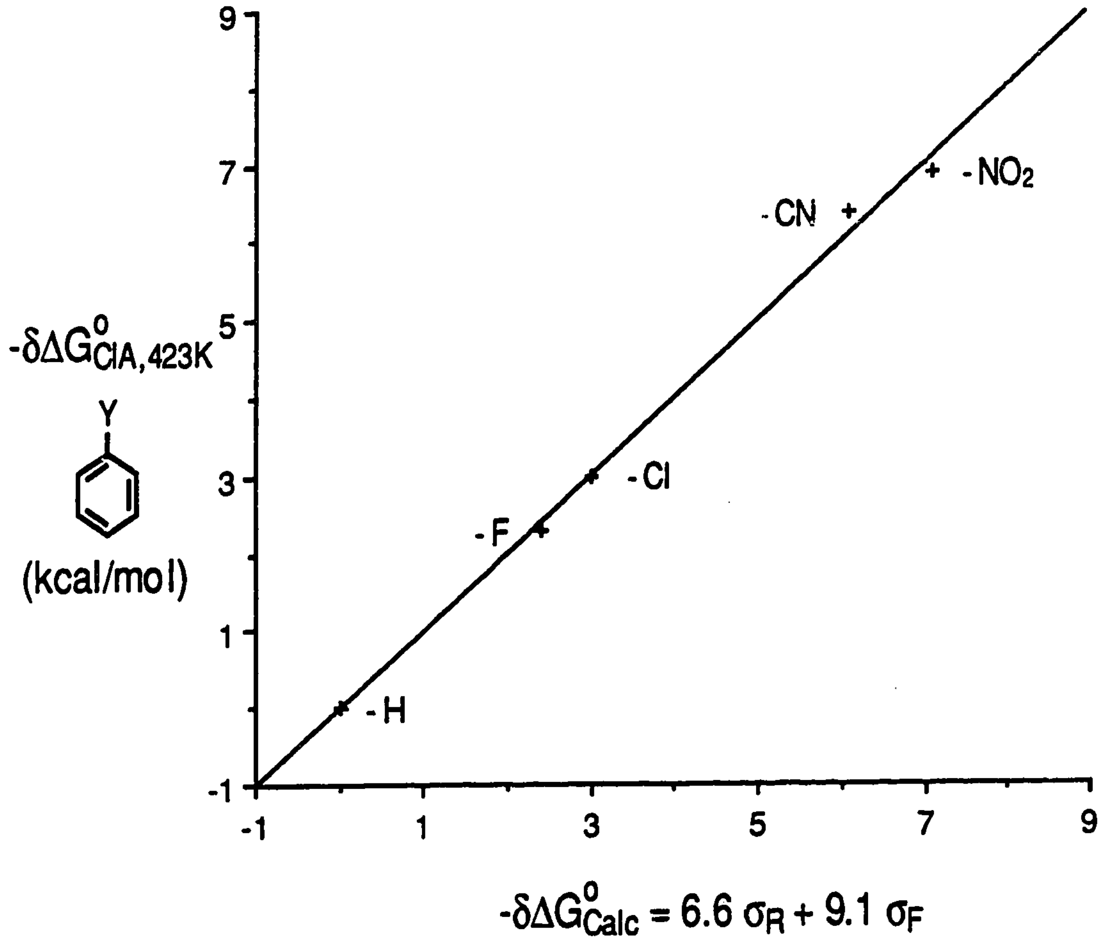

Figure 3.12 Plot of $-\delta\Delta G^o_{ClA,423K}$ for Cl^- bonding to singly substituted benzenes versus $-\delta\Delta G^o_{Calc}$ calculated with Taft σ parameters, see equation (3.7). $-\delta\Delta G^o_{ClA,423K}$ determined from chloride attachment equilibria (3.1) measurements at 300K [13, 44, 45]. $-\delta\Delta S^o_{ClA} \approx 0$. Correlation coefficient r = 0.998.

$$MH = M^- + H^+ \tag{3.8}$$

The acid dissociation reactions have played an important role in the development of the treatment of substituent effects [43]. The ρ_R and ρ_F values (Table 3.3) are: ~7, ~9 for Cl^- and Br^-; ~14, ~15 for para substituted benzoic acids and ~49, 19 for the para substituted phenols. Thus, the ratio ρ_R/ρ_F for the Cl^- and Br^- complexes is very similar to that for the acidities of benzoic acids while the resonance effect is relatively much larger for the phenols. Correspondingly a good linear correlation (r = 0.991) is observed between the substituent effect on the Br^- bond energies and the acidities of benzoic acids (Figure 3.13) while a much poorer correlation (r = 0.956) is obtained from a plot of the same bond energies versus the phenol acidities; see Figure 3.14. Only σ acceptor, π acceptor substituents (CF_3, CHO, NO, CN, NO_2) were used in the plot of phenol acidities since π donor substituents lead to a separate correlation; see Chapter 2.

The similarity in the relative F and R effects of the Cl^- and Br^- bonding energies with those for the acidities of the benzoic acids are expected on the basis of the major contributing resonance structures for the anions occurring in these systems; shown below for the CN substituent (structures X and XI).

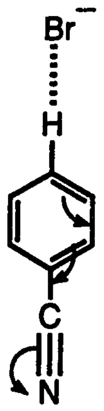

X

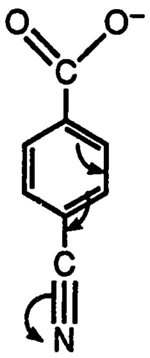

XI

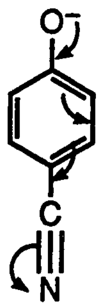

XII

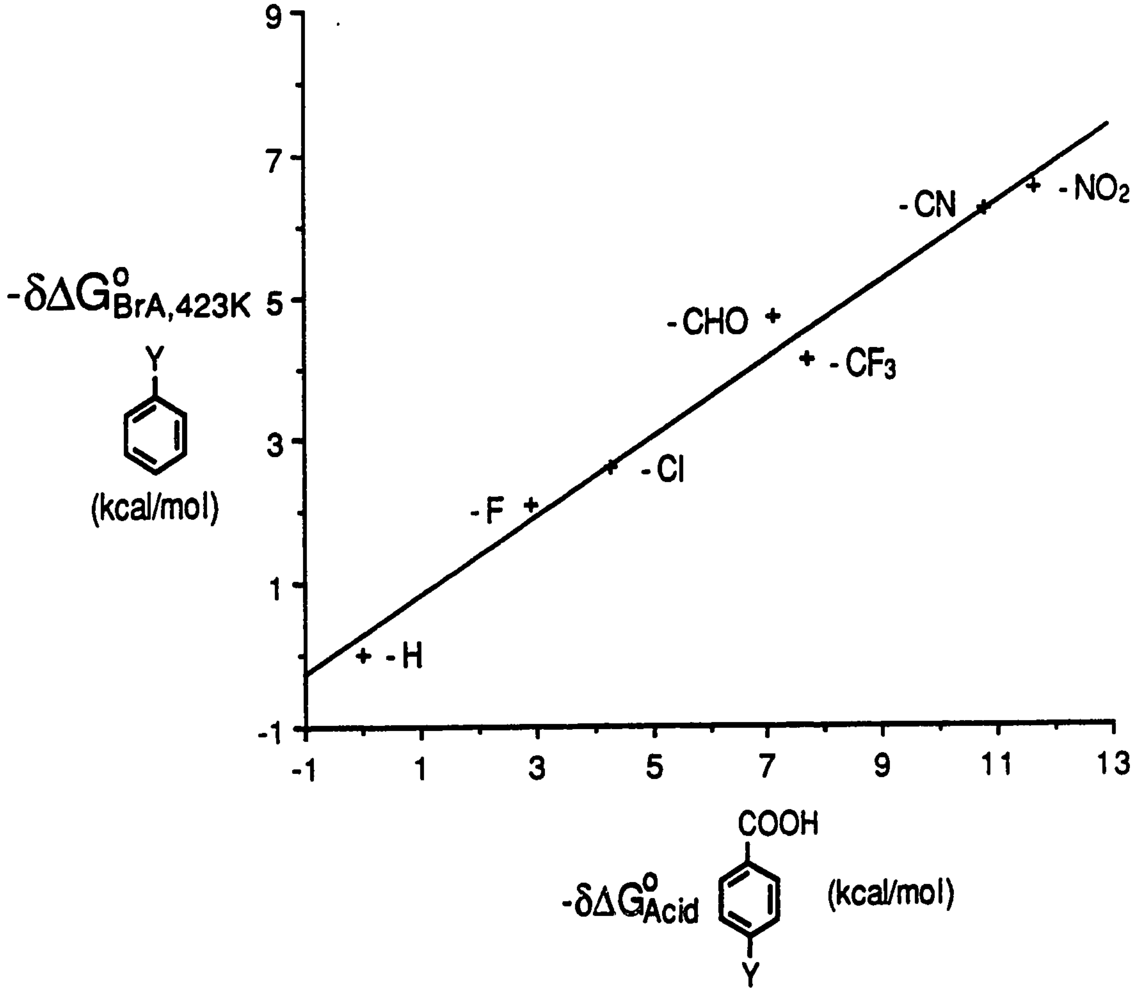

Figure 3.13 Plot of $-\delta\Delta G^{o}_{BrA,423K}$ for Br^- bonding to singly substituted benzenes versus relative gas phase acidities of para-substituted benzoic acids. Correlation coefficient $r = 0.991$.

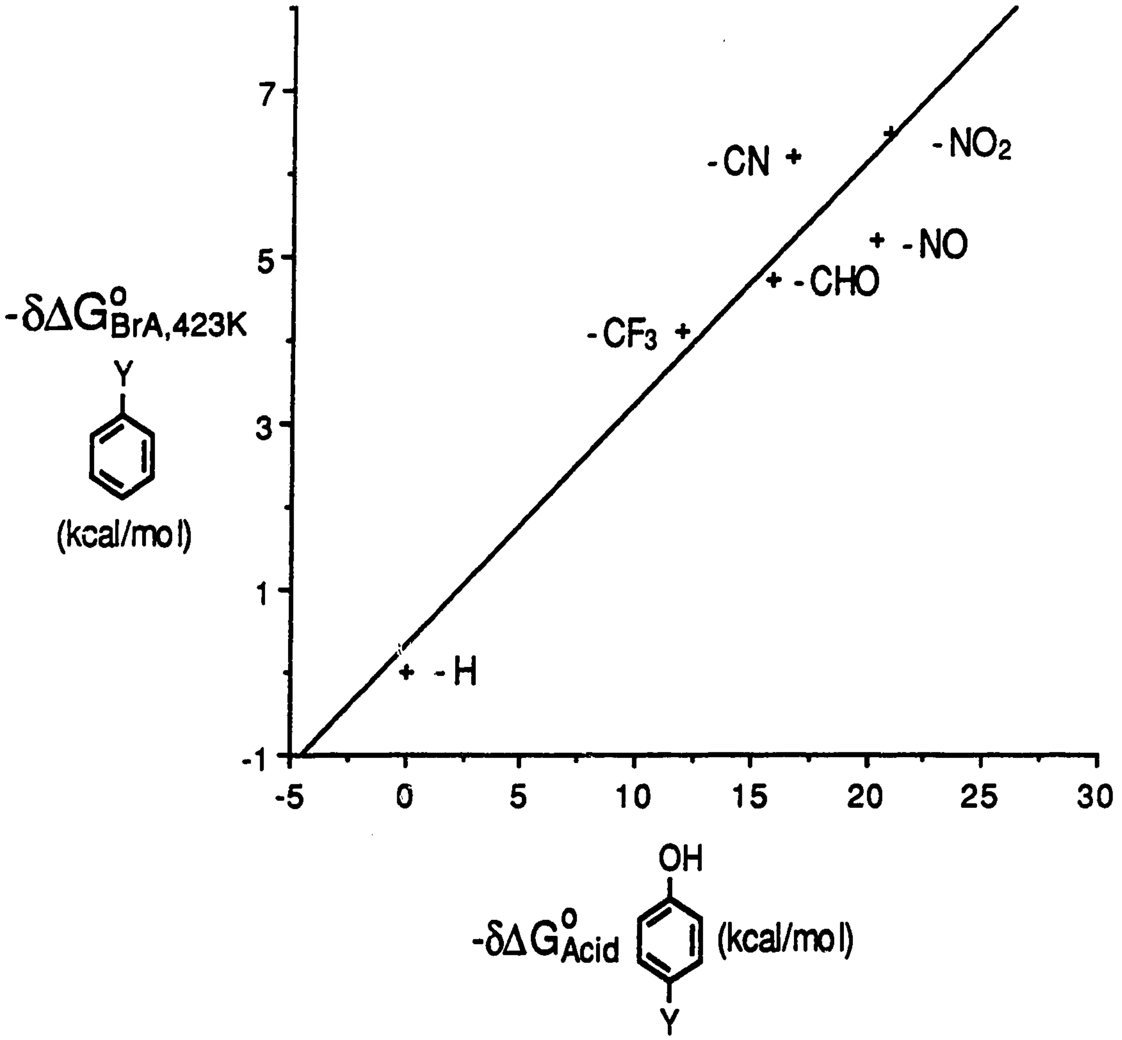

Figure 3.14 Plot of $-\delta\Delta G^{o}_{BrA,423K}$ for Br^{-} bonding to singly substituted benzenes versus relative gas phase acidities of para-substituted phenols. Only π acceptor substituents. Correlation coefficient $r = 0.956$.

These resonance structures are very much less important than the direct into the ring conjugation occurring for the phenoxide anion (structure XII).

The contribution of resonance to the bonding in the Cl^- and Br^- complexes with YC_6H_5 and particularly where strongly π accepting substituents like CN, NO_2 and CHO are involved can be viewed as consisting of two parts. One is the favorable charge distribution induced in the neutral C_6H_5Y. The second part would be the enhancement of the same type of resonance structure on approach of the negative ion.

The application of the Taft relationship equation (3.7) to the Br^- and Cl^- bonding to the singly substituted benzenes implies that the position of the $C-H \cdots X^-$ hydrogen bond relative to that of the substituent remains constant and it is assumed that for the strongly electron withdrawing σ and π acceptor substituents (CF_3, CHO, CN and NO_2) the $C-H \cdots X^-$ bond forms in position para to the substituent. For π donor substituents like F and Cl the bond will be para to the substituent only if the field effect is completely dominant. However, since π donation by the substituent increases the negative charge in the para position, hydrogen bonding meta to the substituent can not be excluded. In fact, as mentioned in the Introduction, the STO-3G calculations [13] predict for fluorobenzene and Cl^- that the meta C-H bond is slightly stronger ($-\Delta E^o_{ClA} = 10.8$ kcal/mol) than that for para position ($-\Delta E^o_{ClA} = 10.3$ kcal/mol). The difference is very small and essentially compatible with near dominance of the field effect. Therefore, the fact that the most stable C-H bond may actually be in position meta to the π donors substituents does not invalidate the use of the Taft relationship. This is also indicated by the relatively good fit observed in Figures 3.11 and 3.12.

The fact that a good correlation is obtained with Taft's substituent effect relationship strongly suggests that the type of bonding (structure I) for $YC_6H_5 \cdot X^-$

($X^- = Cl^-$ and Br^-) is preserved throughout the whole series of singly substituted benzenes. Both a change to the σ bonded complexes IV and a change to the axial electrostatic complexes III can be excluded for this series on this basis.

3.3c Multiply Substituted Benzenes

The experimental bond free energies ($-\Delta G^{o}_{XA,423K}$) for $X^- = Br^-$ and multiply substituted benzenes are summarized in Table 3.2. All the doubly substituted benzenes have one NO_2 substituent, i.e., are singly substituted nitrobenzenes (YNB).

The bonding trends with relative position of the substituents depend on the nature of the second substituent. Thus, for the strongly σ and π accepting substituents increases are observed to occur in the order: para, meta, ortho, as illustrated by the $-\Delta G^{o}_{BrA,423K}$ values (in kcal/mol) listed below:

p-CF_3NB	m-CF_3NB	o-CF_3NB
7.0	9.1	9.8
p-CNNB	m-CNNB	o-CNNB
9.2	11.1	11.5
p-NO_2NB	m-NO_2NB	o-NO_2NB
9.2	10.9	11.6

The order para < meta < ortho suggests the field effect for these substituents is dominant, as was shown in Section 3.3b. The alignment of the substituent produced dipoles with the negative ion becomes progressively more favorable in the above order. This is illustrated in structure XIII for the o-$NO_2NB{\cdot}Br^-$ complex. It is also likely that for the m-NO_2NB (structure XIV) which maximizes the field effect, is slightly more stable than XV which maximizes the

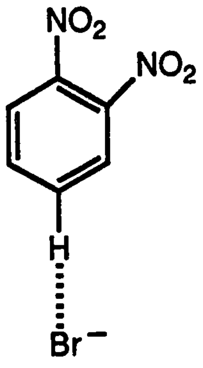

XIII

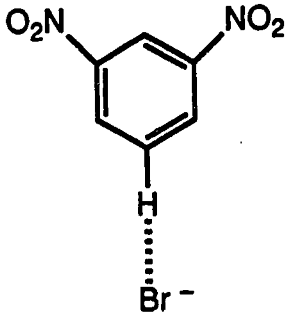

XIV

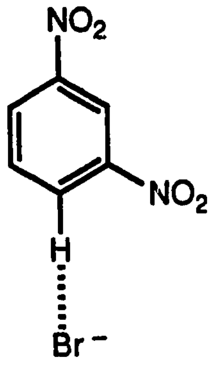

XV

resonance stabilization.

It is interesting to note that the CHO substituted nitrobenzene shows the higher bond energy for the meta rather than for the para isomer.

m-CHONB	p-CHONB
10.3	9.1

For the complex of m-CHONB with Br$^-$, the structure XVI may be expected.

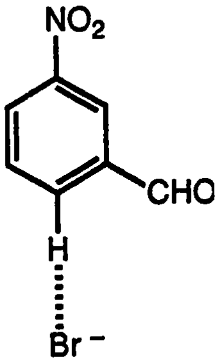

The bond energy order meta > para and structure XVI are consistent with the known large resonance and small field contribution of the CHO substituent [43, 52]. Therefore for CHO a structure like XVI which maximizes its resonance contribution while the dipole orientation is less favorable appears most likely.

The order of Br^- bonding energies for FNB is: para < meta ≤ ortho, Table 3.2. This indicates a structure as in XVII.

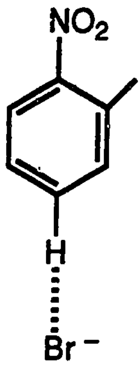

XVII

The result ortho < meta observed for ClNB, is difficult to understand.

The Br^- bonding to methyl substituted nitrobenzenes increases in the order: ortho < meta < para; see Table 3.2. Clearly the situation here is very different. Probably, the Br^- bonds not to an aromatic hydrogen but to one of the methyl hydrogens. The early STO-3G calculations [13] for bonding of Cl^- to toluene predicted that bonding to the methyl hydrogen is only slightly less favorable than that to the aromatic H. The presence of the nitro group (+R) in the present case can be expected to make bonding to the methyl hydrogen more favorable and particularly so for the p-MeNB, and this conforms to the observed order in Table 3.2.

$-\Delta G^o_{XA,423K}$ values were determined in earlier work of this laboratory [46] for substituted nitrobenzenes and $X^- = NO_2^-$. A comparison of the bond free energies in the complexes $YNB{\cdot}Br^-$ and $YNB{\cdot}NO_2^-$ is provided by the plot of Figure 3.15. A close correlation is observed. Furthermore, the $-\Delta G^o_{XA,423K}$ values for Br^- and NO_2^- are seen to be very close. The close correlation suggests that the type of bonding is the same for both negative ions. The negative charge in NO_2^- is delocalized over the two oxygen atoms and, from an

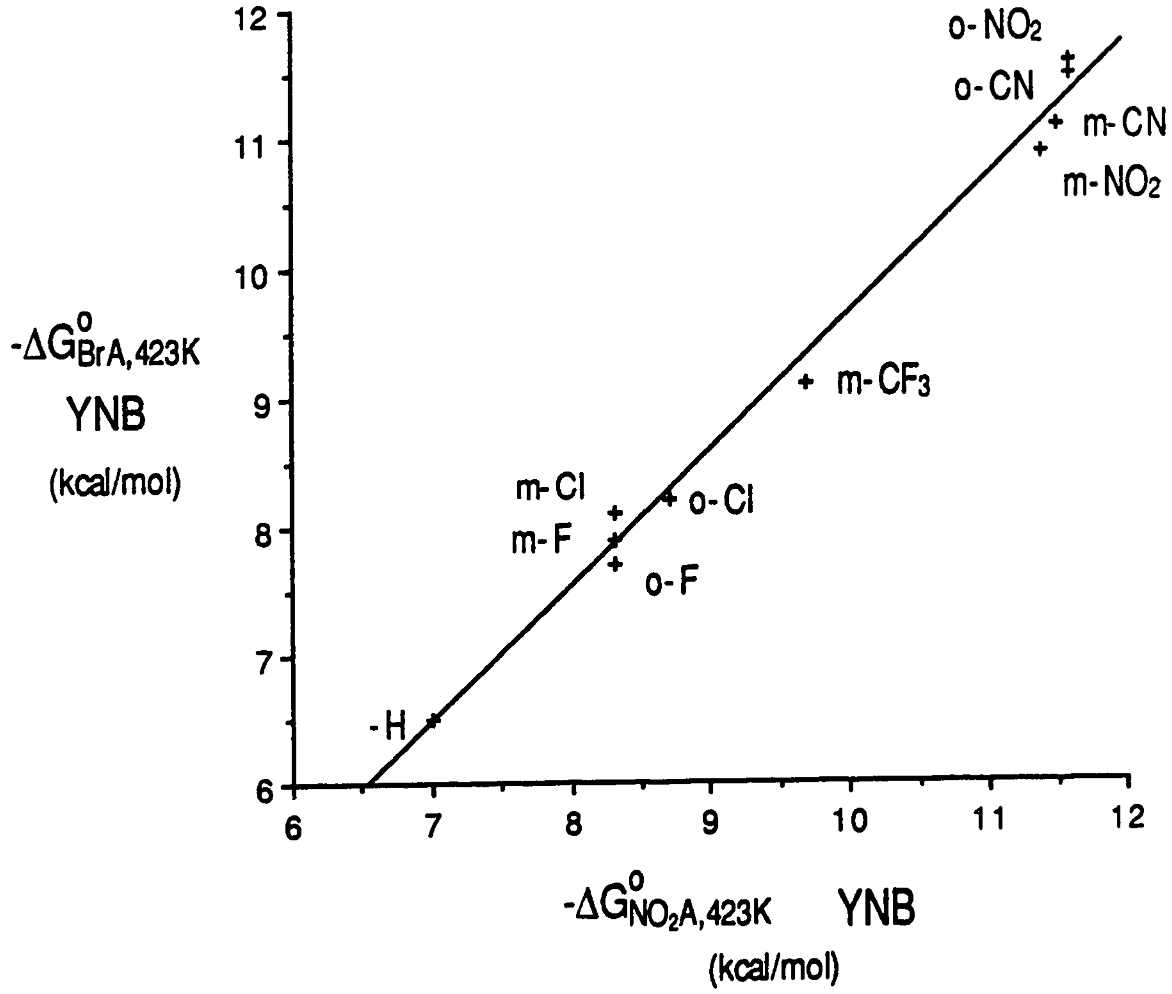

Figure 3.15 $-\Delta G^{o}_{BrA,423K}$ versus $-\Delta G^{o}_{NO_2A,423K}$ for Br$^-$ and NO$_2^-$ bonding to ortho and meta-substituted nitrobenzenes. Excellent correlation (r = 0.998) and slope near unity (= 0.998) suggests similar bonding in the complexes YNB·Br$^-$ and YNB·NO$_2^-$.

electrostatic standpoint, NO_2^- may be viewed as an ion with radius similar to that of Br^-. The similarity of bonding is, thus, not surprising.

In the discussion above, it was assumed that aromatic C-H hydrogen bonding (structure I) occurs for the singly substituted nitrobenzenes, except for the nitrotoluenes. This assumption is also supported by the magnitudes of the observed changes of the bond free energies on double substitution with the same substituent. The $-\Delta G^o_{BrA,423K}$ values and observed changes (in kcal/mol) are shown in Scheme I.

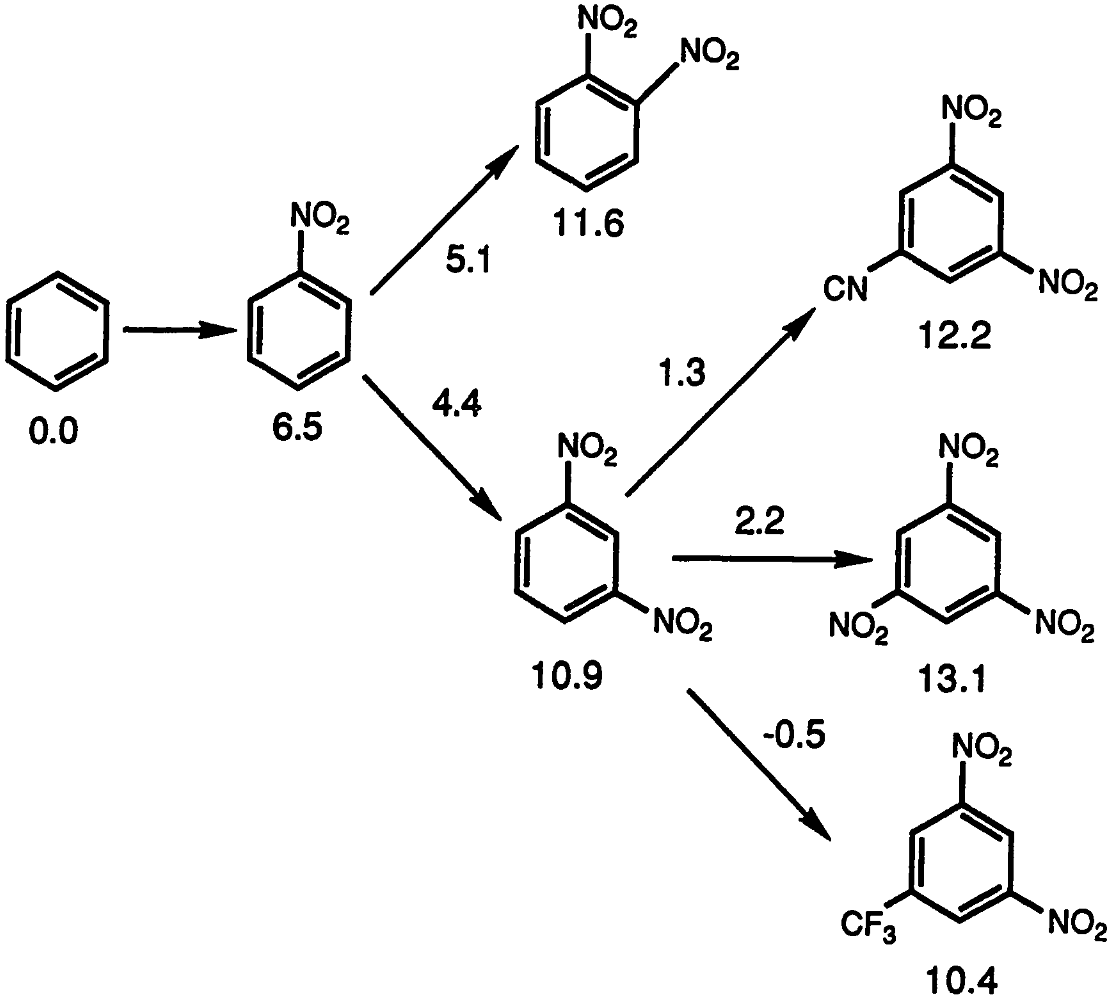
NO2
NO2
NO2
NO2
NO2
0.0
6.5
5.1
11.6
4.4
1.3
CN
NO2
12.2
NO2
NO2
10.9
2.2
NO2
NO2
NO2
13.1
-0.5
NO2
CF3
NO2
10.4

Scheme I

It is seen that the effect of the NO_2 substituent on second substitution is attenuated but not by much, i.e., from 6.5 to 5.1 kcal/mol. This is expected if C-H···X^- bonding carries on and the dominant stabilization is the field effect, since it is generally observed that stabilization due to the field effect attenuates much more slowly than that due to resonance [52-54].

Also given in Scheme I is the bond energy change on introduction of a third substituent. The stabilization due to the third substituent is seen to be strongly attenuated. Assuming that C-H···Br^- bonding still leads to the most stable structure in the triply 1,3,5-substituted benzenes, the large decrease of stabilization can be explained as due to the removal by the third substituent of the last C-H position for which the substituent dipoles are still favorably oriented. In the 1,3,5-substituted benzenes, the C-H···Br^- bond must occur ortho to two of the substituents and only the resonance stabilization operates for these positions. Furthermore, resonance stabilization attenuates significantly with multiple substitution [52-54].

The discussion just given shows that the observed energy changes are consistent with C-H···Br^- bonding also in the triply substituted benzenes shown in Scheme I. However, since the tendency towards σ bonded complexes IV and the axial electrostatic complexes III increases with multiple substitution with CN, CF_3 and NO_2, probably the energies of these Br^- complexes come quite close to that of the C-H···Br^- complex for the triply substituted benzenes and for these complexes all three forms of bonding become competitive.

REFERENCES

1. T. D. Mark and A. W. Castleman, Jr., Adv. Atom. Molec. Phys., 20, 65 (1985).
2. J. M. Riveros, S. M. Jose and K. Takashima, Adv. Phys. Org. Chem., 21, 197 (1985).
3. J. March, "Advanced Organic Chemistry". 2nd Ed. McGraw-Hill. New York (1977).
4. J. Miller, "Aromatic Nucleophilic Substitution". Elsevier. Amsterdam (1968).
5. T. O. Tiernan, C. Chang and C. C. Cheng, Environ. Health Perspect., 36, 47 (1980).
6. H. P. Tannenbaum, J. D. Roberts and R. C. Dougherty, Anal. Chem., 47, 49 (1975).
7. G. W. Caldwell, J. A. Masucci and M. G. Ikonomou, Org. Mass Spectrom., 24, 8 (1989).
8. C. Lange, C. Guette, J. Berthelot and J. J. Basselier, Org. Mass Spectrom., 22, 123 (1987).
9. P. Kebarle, Ann. Rev. Phys. Chem., 28, 445, (1977).
10. R. Yamdagni and P. Kebarle, J. Am. Chem. Soc., 93, 7139 (1971).
11. R. Yamdagni, J. D. Payzant and P. Kebarle, Can. J. Chem., 51, 2507 (1973)
12. M. Arshadi, R. Yamdagni and P. Kebarle, J. Phys. Chem., 74, 1475 (1970).
13. M. A. French, S. Ikuta and P. Kebarle, Can. J. Chem., 60, 1907 (1982).
14. T. F. Magnera, G. Caldwell, J. Sunner, S. Ikuta and P. Kebarle, J. Am. Chem. Soc., 106, 6140 (1984).

15. G. Caldwell and P. Kebarle, Can. J. Chem., 63, 1399 (1985).

16. G. Caldwell and P. Kebarle, J. Am. Chem. Soc., 106, 967 (1984).

17. J. W. Larson and T. B. McMahon, J. Am. Chem. Soc., 105, 2944 (1983).

18. J. W. Larson and T. B. McMahon, J. Am. Chem. Soc., 106, 517 (1984).

19. J. W. Larson and T. B. McMahon, J. Am. Chem. Soc., 107, 766 (1985).

20. R. G. Keese and A. W. Castleman, Jr., J. Phys. Chem. Ref. Data, 15, 1011 (1986).

21. A. Pross and L. Radom, Prog. Phys. Org. Chem., 13, 1 (1981).

22. M. Meot-Ner and S.A. Kafafi, J. Am. Chem. Soc., 110, 6297 (1988).

23. K. Hiraoka, S. Mizuse, and S. Yamabe, Chem. Phys. Lett., 147, 174 (1988).

24. G. A. Artamkina, M. P. Egorov and I. P. Beletskaya, Chem. Rev., 82, 427 (1982).

25. F. Terrier, Chem. Rev., 82, 77 (1982).

26. J. M. Riveros, Adv. Mass Spectrom., 6, 277 (1974).

27. S. M. J. Briscese and J. M. Riveros, J. Am. Chem. Soc., 97, 230 (1975).

28. J. M. Riveros and K. Takashima, Can. J. Chem., 54, 1839 (1976).

29. J. H. Bowie and B. J. Stapleton, Aust. J. Chem., 30, 795 (1977).

30. S. Ingemann and N. M. M. Nibbering, J. Org. Chem., 48, 183 (1983).

31. G. Paul, K. Hirao, S. Obata and P. Kebarle, in preparation.

32. A. J. Birch, A. L. Hinde and L. Radom, J. Am. Chem. Soc., 102, 6430 (1980).

33. S. K. Dotterer and R. I. Harris, J. Org. Chem., 53, 777 (1988).

34. J. Sunner, K. Nishizawa and P. Kebarle, J. Phys. Chem., 85,1814 (1981).

35. M. R. Battaglia, A. D. Buckingham and J. H. Williams, Chem. Phys. Lett., 78, 421 (1981).

36. W. D. Reents, Jr., and B. S. Freiser, J. Am. Chem. Soc., 102, 271 (1980).

37. Y. K. Lau and P. Kebarle, J. Am. Chem. Soc., 98, 7452 (1976).

38. F. Cacace, M. E. Crestoni, S. Fornaini and R. Gabrielli, Int. J. Mass Spectrom. Ion Proc., 84, 17 (1988).

39. M. Attina, F. Cacace, and M. Yanez, J. Am. Chem. Soc., 109, 5092 (1987).

40. K. Hiraoka, S. Misuze and S. Yamabe, J. Phys. Chem., 91, 5294 (1987).

41. K. Hiraoka, S. Misuze and S. Yamabe, J. Chem. Phys., 86, 4102 (1987).

42. G. W. Dillow and P. Kebarle, J. Am. Chem. Soc., 110, 4877 (1988).

43. R. W. Taft and R. D. Topsom, Prog. Phys. Org. Chem., 16, 1 (1987).

44. S. Chowdhury and P. Kebarle, J. Chem. Phys., 85, 4989 (1986).

45. S. Chowdhury, Ph. D. Thesis, University of Alberta (1986).

46. E. P. Grimsrud, S. Chowdhury and P. Kebarle, Int. J. Mass Spectrom. Ion Proc., 68, 57 (1986).

47. K. Hiraoka, S. Mizuse, and S. Yamabe, J. Chem. Phys., 87, 3647 (1987).

48. J. Sunner and P. Kebarle, J. Phys. Chem., 85, 327 (1981).

49. K. Hiraoka and P. Kebarle, J. Am. Chem. Soc., 97, 4179 (1975).

50. K. Hiraoka, J. Chem. Phys., 87, 4048 (1987).

51. J. B. Cumming, M. A. French and P. Kebarle, J. Am. Chem. Soc., 99, 6999 (1977).

52. R. W. Taft, J. L. M. Abboud, F. Anvia, M. Berthelot, M. Fujio, J.-F. Gal, A. D. Headley, W. G. Henderson, I. Koppel, J. H. Qian, M. Mishima, M. Taagepera and S. Uegi, J. Am. Chem. Soc., 110, 1797 (1988).

53. S. Chowdhury, H. Kishi, G. W. Dillow and P. Kebarle, Can J. Chem., 67, 603 (1989).

54. S. Chowdhury, T. Heinis and P. Kebarle, J. Am. Chem. Soc., 108, 4662 (1986).

CHAPTER 4

STABILITIES OF σ BONDED AND ELECTROSTATIC COMPLEXES, $C_6F_5Y{\cdot}X^-$, OF PERFLUOROBENZENES, C_6F_5Y, WITH HALIDE ANIONS X^- (F^-, Cl^-, Br^- and I^-)

4.1 Introduction

In Chapter 3 substituent effect analysis of the experimentally determined bond free energies of Y-substituted benzene complexes $YC_6H_5{\cdot}X^-$ ($X^- = Cl^-$ and Br^-) was performed to provide information on the mode of bonding in these complexes. The results of the analysis combined with STO-3G calculations [1] indicate hydrogen bonded structures I and II are the most stable when Y contains no protic hydrogens.

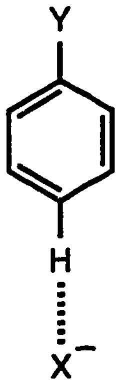

Y = σ acceptor, π acceptor

I

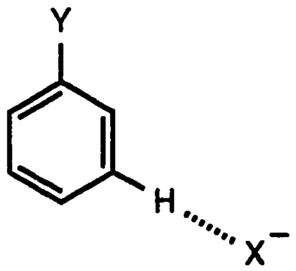

Y = σ acceptor, π donor

II

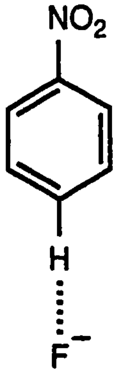

III

An ab initio MO study by Hirao et al. [2] predicts similar hydrogen bonding in the complex $NO_2C_6H_5{\cdot}F^-$, structure III, where Y is a strong σ acceptor, π acceptor.

An alternate form of bonding is present in the perfluorobenzene complexes $C_6F_5Y{\cdot}X^-$ ($X^- = F^-$, Cl^-, Br^- and I^-) due to the absence of ring protons. Theoretical and experimental work on the complexes $C_6F_6{\cdot}X^-$ ($X^- = F^-$, Cl^-, Br^-

and I^-) has been performed by Hiraoka et al. [3, 4]. These investigations indicate different modes of interaction of F^- and X^- (X^- = Cl^-, Br^- and I^-) with C_6F_6. Strong covalent bonding is predicted in $C_6F_6{\cdot}F^-$ [3], i.e., $C_6F_7^-$, while an electrostatic interaction is preferred in $C_6F_6{\cdot}X^-$ (X^- = Cl^-, Br^- and I^-) [4]; see structures IV and V.

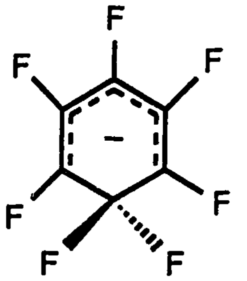
IV

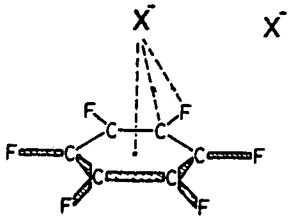
X^- = Cl^-, Br^-, I^-

V

Anionic complexes such as structure IV which form as stable or transient species upon covalent addition of nucleophiles to substituted aromatic or heteroaromatic compounds have been known since 1900 [5]. Jackson and Gazzolo [5] proposed structure VI for the red colored species resulting from the reaction of 1-methoxy-2,4,6-trinitrobenzene with potassium ethoxide.

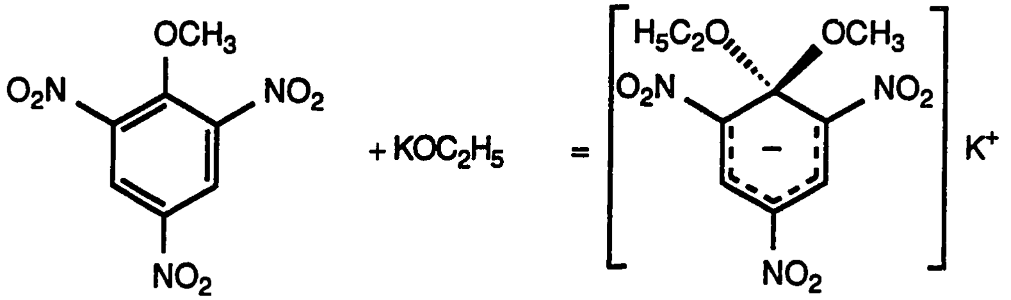
VI

Since the first chemical evidence for structure VI was provided by Meisenheimer in 1902 [6], σ bonded anionic complexes are now commonly referred to as Meisenheimer complexes. Research in this area was strongly stimulated in the 1950s by Bunnett's proposal that many aromatic nucleophilic substitution (S_NAr) reactions most likely proceed via such intermediates [7]; see Scheme I.

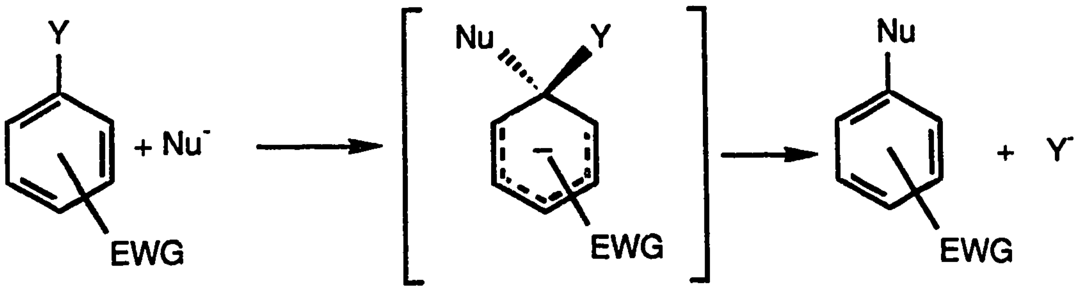

EWG = Electron withdrawing group(s)

Scheme I

Following this proposal many studies were devoted to the structural characterization of Meisenheimer complexes; for example, see references [8-10]. NMR spectroscopy and crystal structure determinations were the principal techniques used in these investigations. Studies of the relative stabilities of Meisenheimer complexes were initiated by Caldin et al. [11] who investigated the reaction of the ethoxide ion with some trinitrobenzene derivatives in ethanol. Rate and equilibrium measurements in solution involving Meisenheimer complexes have been reviewed recently [12, 13].

Nucleophilic aromatic substitution (S_NAr) at the fluorine-bearing carbon atoms of the perfluorobenzenes C_6F_6 [14, 15] and $C_6F_5OCH_3$ [16-18] has been observed in the gas phase. Perfluorobenzenes are also known to be susceptible to nucleophilic attack on ring carbons in the liquid phase [19, 20]. The gas phase reactions involved nucleophilic attack of the perfluorobenzenes by the strong bases OR^- (R = H, alkyl) [14, 16-18], SR^- (R = H, alkyl) [16, 17], NH_2^- [16] and CH_3^- [15]. S_NAr was proposed as one of the reaction channels based on analysis of the products of reaction. In all cases the S_NAr reactions were expected to proceed via a Meisenheimer complex intermediate analogous to structure IV, stabilized by the electron withdrawing F atoms on the aromatic ring. The S_NAr reaction pathway proposed by Nibbering [16, 17] on OR^- (R = H, alkyl) attack of $C_6F_5OCH_3$ is shown in Scheme II.

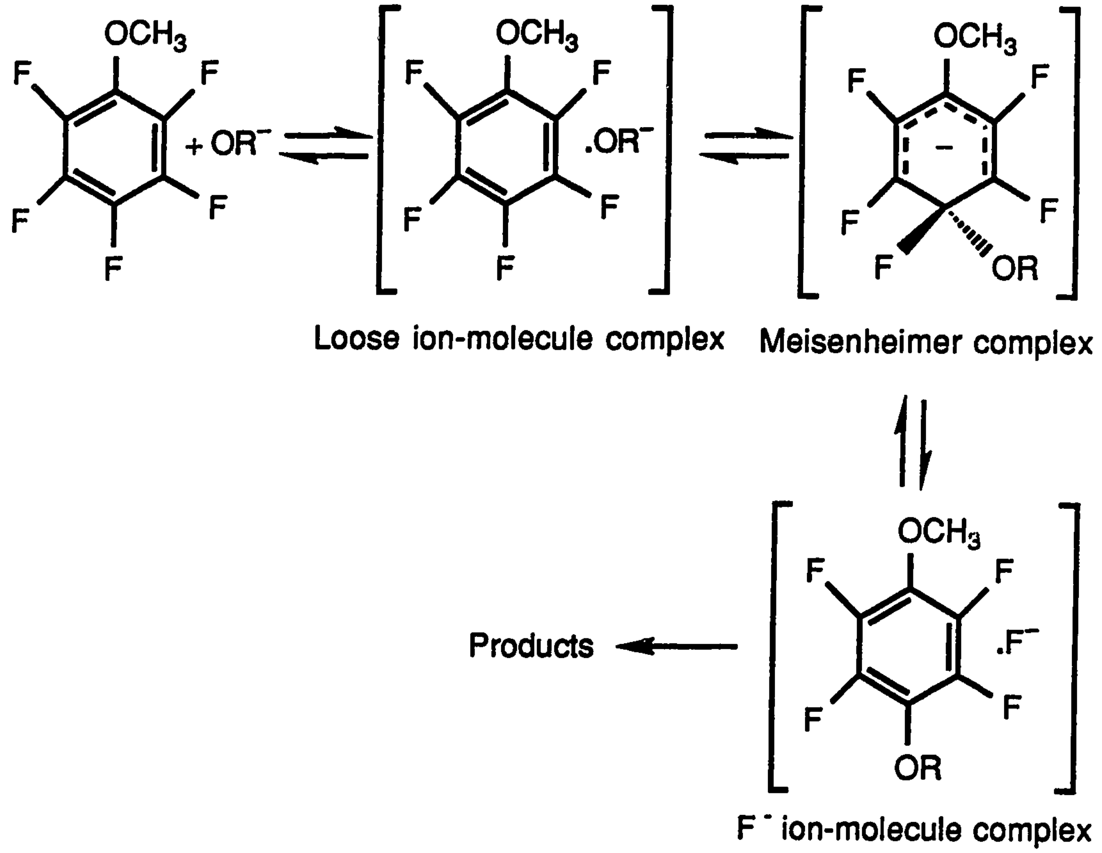
OCH3
F
+OR⁻
.OR⁻
OR
Loose ion-molecule complex
Meisenheimer complex
Products
.F⁻
F⁻ ion-molecule complex

Scheme II

Of interest in Scheme II is the formation of a loose ion-molecule complex [16, 17] as a precursor to the Meisenheimer complex intermediate. This complex may have a geometry similar to structure V predicted for the $C_6F_6{\cdot}X^-$ complexes (X^- = Cl^-, Br^- and I^-) [4].

In the present work the bond free energies of the complexes $C_6F_5Y{\cdot}X^-$ (X^- = F^-, Cl^-, Br^- and I^-) were determined by measurements of the association (4.1) and transfer equilibria (4.2)

$$C_6F_5Y + X^- = C_6F_5Y{\cdot}X^- \qquad (4.1)$$

$$C_6F_5Y{\cdot}X^- + C_6F_5Y' = C_6F_5Y + C_6F_5Y'{\cdot}X^- \qquad (4.2)$$

with the PHPMS. Substituent effect analysis of the $C_6F_5Y{\cdot}X^-$ bond free energies was employed to provide information on whether the anticipated σ ($X^- = F^-$) and electrostatic ($X^- = Cl^-$, Br^- and I^-) bonding is present in these families. Stabilities of σ and electrostatic bonded complexes are of interest as these complexes are possible intermediates in nucleophilic aromatic substitution reactions.

4.2 Experimental

4.2a Experimental Conditions Used in Equilibrium Measurements

The association (4.1) and transfer equilibria (4.2) where $X^- = F^-$, Cl^-, Br^- and I^- were measured at 423 K using the pulsed electron high pressure mass spectrometer described in Chapter 1. The method of equilibrium measurement was as described in Chapter 2.

Efficient Cl^-, Br^- and I^- production was achieved by dissociative electron capture of tetrachloromethane, CCl_4 (ion source pressure = 1.0-5.0 mtorr), dibromomethane, CH_2Br_2 (1.0-5.0 mtorr), and methyl iodide, CH_3I (1.0-3.0 mtorr), respectively. Methane at ion source pressures of 2-4 torr was used as the major (bath) gas. Reactant (C_6F_5Y, C_6F_5Y') concentrations in the ion source ranged from 0.1-160 mtorr.

An intensity versus time profile of ions involved in reaction (4.1) is shown in Figure 4.1. Thermodynamic equilibrium is established between the perfluorobenzene adduct, $C_6F_5CF_3{\cdot}Br^-$, and the halide ion, Br^-, some 0.3 ms after the short 20 µs pulse. The radical anion $C_6F_5CF_3^-$ is also present in the

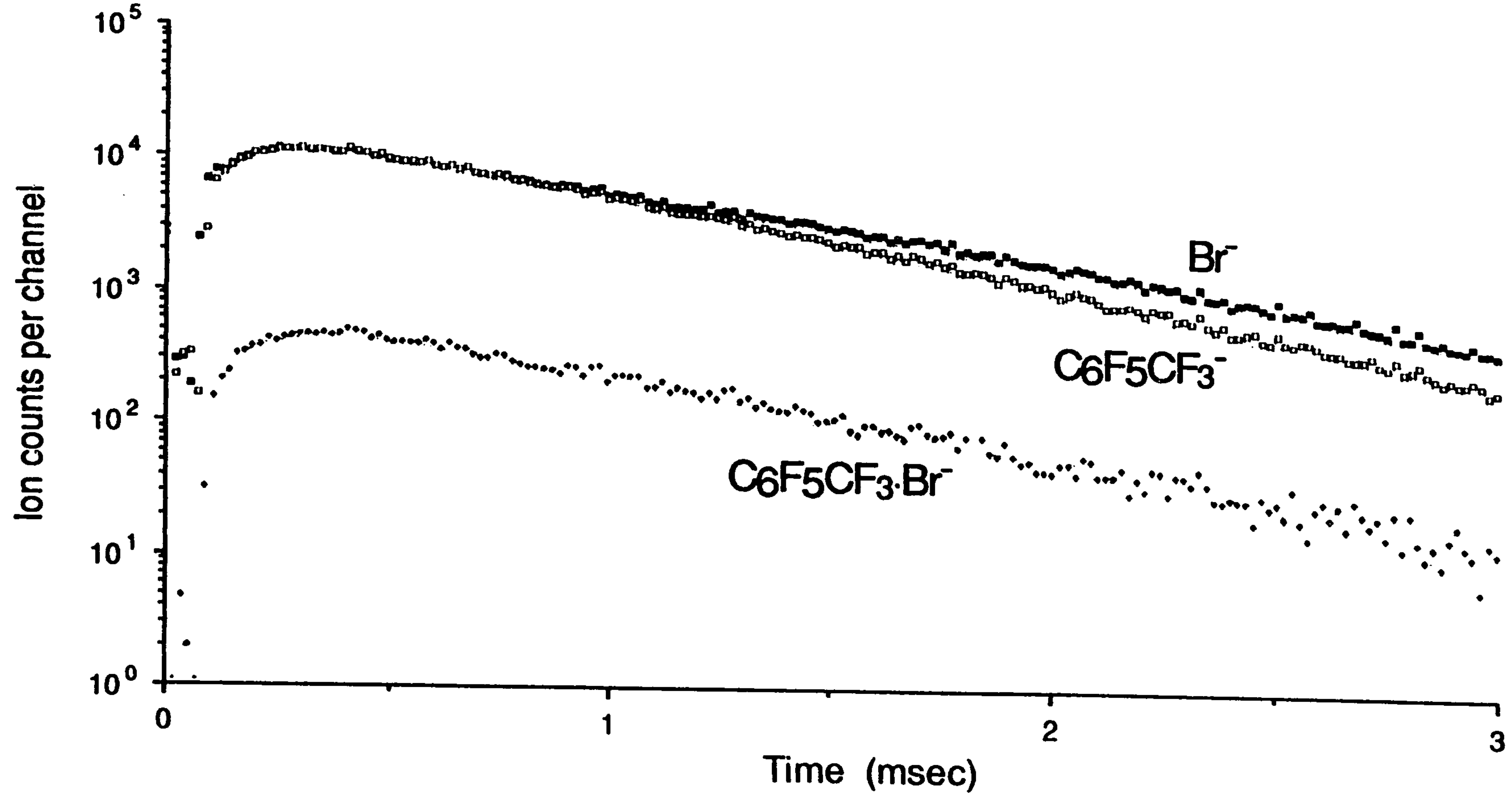

Figure 4.1 Ion intensity versus time after the 20 μs ionizing electron pulse. Obtained with a gas mixture of 2.2 torr CH_4, 8.2 mtorr $C_6F_5CF_3$ and 2.1 mtorr CH_2Br_2 at 423 K. Br^- ions result from dissociative electron capture by CH_2Br_2. The Br^- attachment equilibrium (4.1): $C_6F_5CF_3 + Br^- = C_6F_5CF_3 \cdot Br^-$, becomes established some 0.5 ms after the electron pulse. The radical anion $C_6F_5CF_3^-$ is also present in the ion source. The decrease of ion intensity after ~0.7 ms is due to diffusion of the ions to the wall.

ion source. The decrease in the intensity of the ions after ~0.5 ms is due to diffusion of the ions to the ion source wall.

The equilibrium constants, K_{XA}, for reaction (4.1) where $X^- = Cl^-$ and Br^- are shown in Figures 4.2 and 4.3. K_{XA} was determined at three different ion source pressures between 2 and 4 torr for a constant C_6F_5Y/methane partial pressure experiment. This procedure was repeated with a different C_6F_5Y/methane partial pressure ratio where the ratio was changed by at least a factor of five. From Figures 4.2 and 4.3 K_{XA} is observed to be independent of partial pressure of C_6F_5Y for different C_6F_5Y/methane ratios. However, a slight decrease of K_{XA} with increasing ion source pressure is observed in constant C_6F_5Y/methane experiments (represented by similar symbols in the Figures 4.2 and 4.3). Collisionally induced dissociation of adduct ions outside the ion source is a possible cause of this effect; see Chapter 3. The error in K_{XA} over the ion source pressure range (±20%) is comparable to that for the bromide association equilibrium constants determined in Chapter 3.

Similar checks on the equilibrium constants for halide transfer reactions (4.2) were performed, varying the ratio of the two reacting perfluorobenzenes. K_{XTr} was seen to be independent of the C_6F_5Y/C_6F_5Y' ratio.

The enthalpy and entropy values for reaction (4.1) involving bromide attachment to C_6F_6, C_6F_5CN and 1,4-diCNC_6F_4 were determined by means of van't Hoff plots. These plots were obtained by the experimental procedure described in Chapter 3.

Measurements of transfer equilibria (4.2) where $X^- = F^-$ are an extension of earlier work performed in this laboratory [21]. In the present work fluoride adduct formation was observed upon ionization of a mixture of C_6F_5CN and $C_6F_5NO_2$ (ion source pressures 1-10 mtorr) in 2-4 torr methane bath gas.

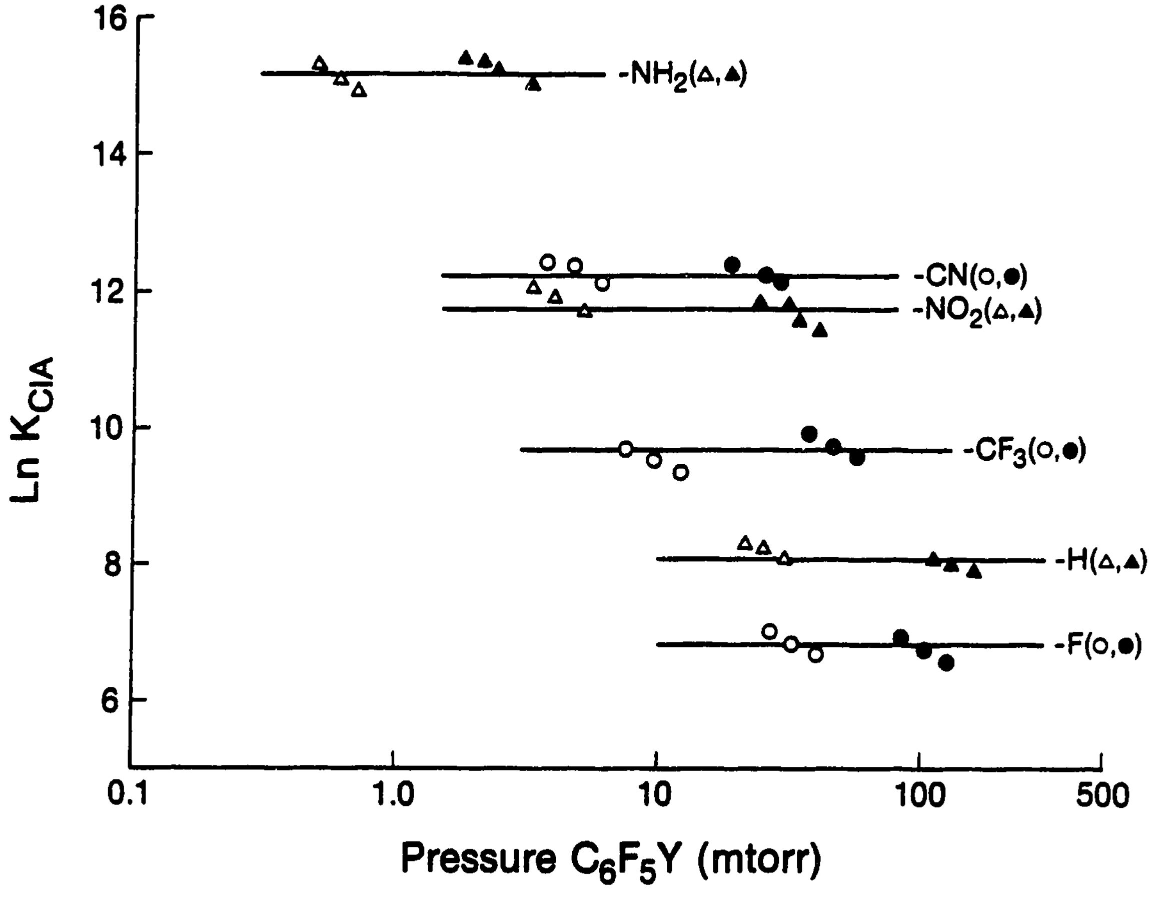

Figure 4.2 K_{CIA} for reaction (4.1) involving different perfluorobenzenes, C_6F_5Y, versus C_6F_5Y partial pressure in the ion source. Ion source temperature, 423 K. CH_4 pressure changes from 2-4 torr in runs with the same symbol. In such runs, the CH_4 to C_6H_5Y pressure ratio is constant. K_{CIA} is independent of C_6F_5Y pressure for different C_6F_5Y/methane ratios. However a slight decrease in K_{CIA} is observed with increase of CH_4 pressure for constant C_6F_5Y/methane experiments.

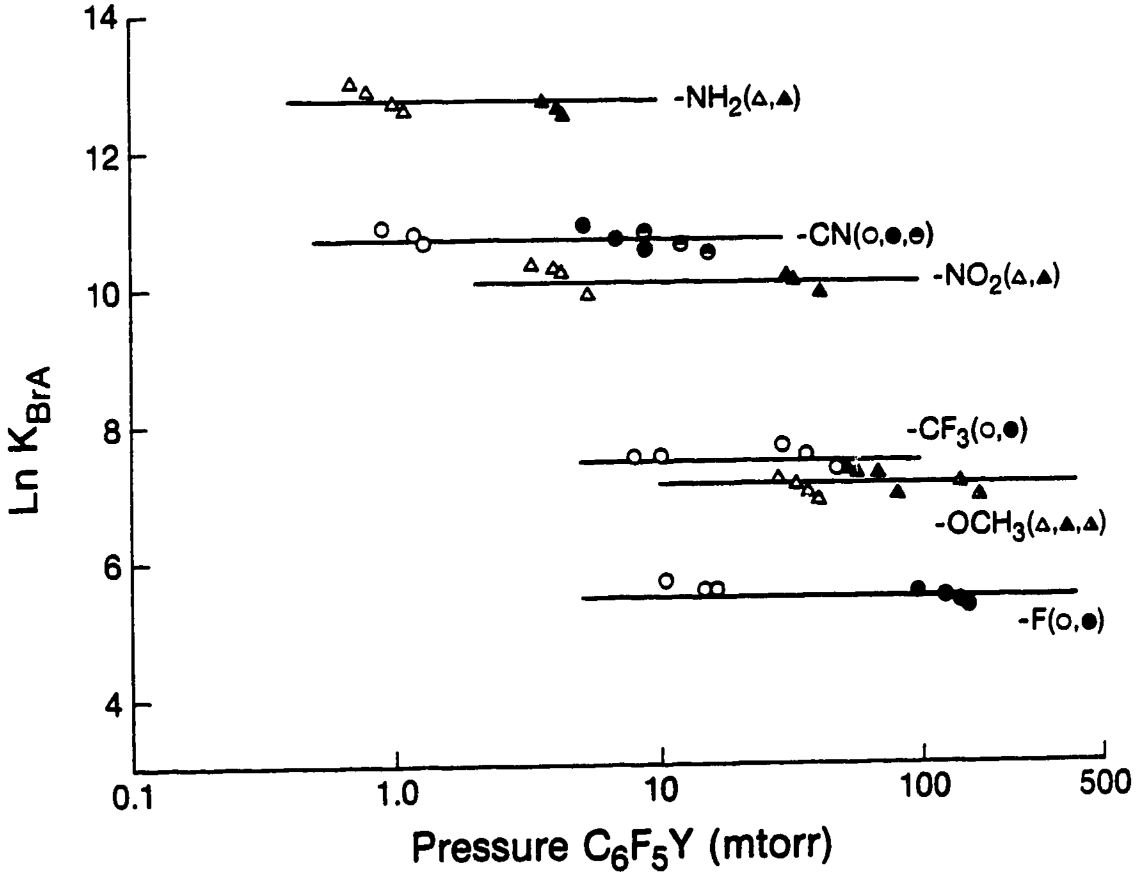

Figure 4.3 K_{BrA} for reaction (4.1) involving different perfluorobenzenes, C_6F_5Y, versus C_6F_5Y partial pressure in the ion source. Ion source temperature, 423 K. CH_4 pressure changes from 2-4 torr in runs with the same symbol. In such runs, the CH_4 to C_6F_5Y pressure ratio is constant.

$$C_6F_5NO_2 + C_6F_5CN{\cdot}F^- = C_6F_5NO_2{\cdot}F^- + C_6F_5CN \qquad (4.3)$$

The intensity versus time profile of the ions involved in fluoride transfer equilibria (4.3) is shown in Figure 4.4. Transfer equilibrium is established between the $C_6F_5CN{\cdot}F^-$ and $C_6F_5NO_2{\cdot}F^-$ adducts some 0.5 ms after the electron pulse. As no F^- signal was detected fluoride association equilibria (4.1) could not be measured. Also present in the ion source were the perfluorophenoxides $CNC_6F_4O^-$ and $NO_2C_6F_4O^-$; see Figure 4.4. The perfluorobenzene radical anions $C_6F_5CN^-$ and $C_6F_5NO_2^-$ were not detected. For a discussion on $C_6F_5Y{\cdot}F^-$ and $OC_6F_4Y^-$ production in the ion source, see Section 4.2b.

The equilibrium constant for reaction (4.3) was in close agreement with that determined by Dillow et al. [21]. Addition of perfluorobenzenes with similar fluoride affinities to the gas mixture resulted in fluoride transfer equilibria involving these compounds.

In previous PHPMS measurements of fluoride association (4.1) and transfer (4.2) equilibria involving perfluorobenzenes, F^- was generated in the ion source by dissociative electron capture of NF_3 [21, 22].

$$NF_3 + e^- = F^- + NF_2 \qquad (4.4)$$

There are problems, however, in using NF_3 [21, 22]. NF_3 has a small capture coefficient for thermal electrons and high ion source concentrations (~250 mtorr [21]) have to be used in order to achieve good F^- production relative to $C_6F_5Y^-$, since perfluorobenzenes have larger capture coefficients [21]. High pressures of NF_3 in the ion source present a problem as NF_3 contains a small amount of HF as an impurity. HF has a strong fluoride affinity

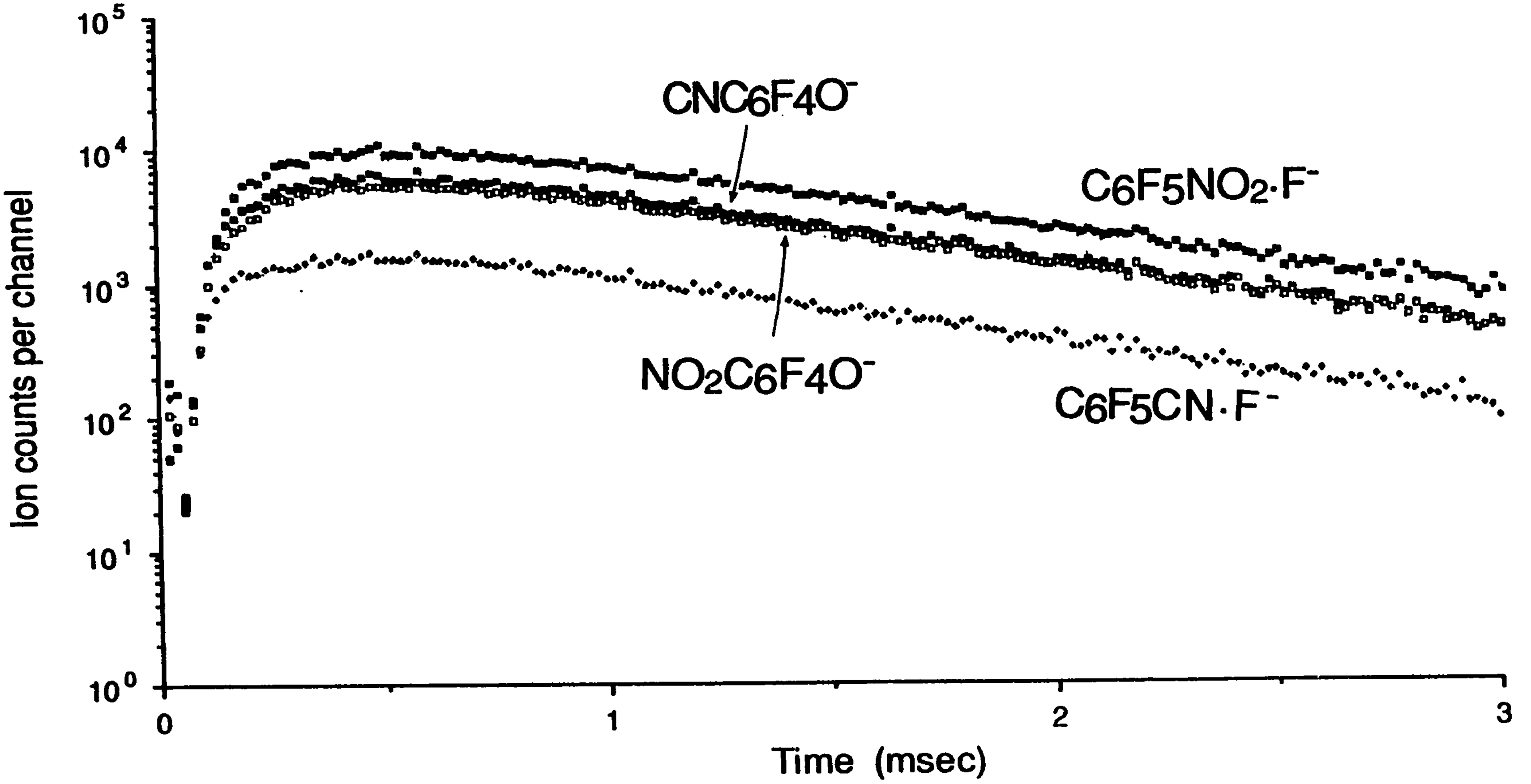

Figure 4.4 Ion intensity versus time after the 20 μs ionizing electron pulse. Obtained with a gas mixture of 3.2 torr CH_4, 6.3 mtorr $C_6F_5NO_2$ and 8.9 mtorr C_6F_5CN at 423 K. The F^- transfer equilibrium (4.3): $C_6F_5NO_2 + C_6F_5CN{\cdot}F^- = C_6F_5NO_2{\cdot}F^- + C_6F_5CN$, becomes established some 0.7 ms after the electron pulse. Also present in the ion source are the perfluorophenoxides $NO_2C_6F_4O^-$ and $CNC_6F_4O^-$. The decrease of ion intensity after ~0.8 ms is due to diffusion of the ions to the wall.

($-\Delta H^{o}_{FA}$ = 38.6 kcal/mol [23]) and has to be removed to prevent fluoride transfer reaction (4.5)

$$C_6F_5Y{\cdot}F^- + HF = C_6F_5Y + FH{\cdot}F^- \qquad (4.5)$$

from occurring. Since part of the gas handling plant is made out of glass, the presence of HF will also lead to the production of BF_3, SiF_4 and other fluorinated silanes which interfere with equilibria measurements due to their high fluoride affinities [21].

Procedures by Hiraoka et al. to remove HF from NF_3 were only partially successful [22]. Despite passing NF_3 through glass tubing packed with NaF powder at 120°C ($HF + NaF = NaHF_2$) measurement of the fluoride association equilibrium of C_6F_6 was still difficult due to the formation of $FH{\cdot}F^-$ in large quantities in the ion source [22].

Thus, the method employed to generate fluoride adducts in the present work is a useful way to obtain F^- transfer equilibria (4.2) data without the problems involved in using NF_3.

4.2b $C_6F_5Y{\cdot}F^-$ and $YC_6F_4O^-$ Production in the Ion Source

As mentioned in Section 4.2a, the fluoride adducts $C_6F_5NO_2{\cdot}F^-$ and $C_6F_5CN{\cdot}F^-$ and the perfluorophenoxides $NO_2C_6F_4O^-$ and $CNC_6F_4O^-$ were observed in the ion source upon ionization of a mixture of $C_6F_5NO_2$ and C_6F_5CN in the bath gas methane. The fluoride adduct $C_6F_6{\cdot}F^-$ and perfluorophenoxides $C_6F_5O^-$ and $NO_2C_6F_4O^-$ have been observed in previous PHPMS work performed in this laboratory [24-26]. A brief investigation of the conditions which lead to $C_6F_5Y{\cdot}F^-$ and $YC_6F_4O^-$ formation in the ion source was conducted in the present work in an attempt to gain insight into the reaction pathways.

In the initial set of experiments in this investigation the negative ion mass spectra of various C_6F_5Y/CH_4 gas mixtures (Y = -CN, $-NO_2$, $-CF_3$, -Cl and -CHO) were collected. C_6F_5Y concentration in the ion source ranged from 0.1-10.0 mtorr while methane pressures were ~3 torr. The ion source temperature was 423 K. The total ion source pressure and temperature were kept constant for all the experiments described in this section. The negative ion mass spectrum for the C_6F_5CN/CH_4 gas mixture is shown in Figure 4.5a. The molecular ion peak, $C_6F_5CN^-$, represents over 95 % of the total ion signal. The molecular ion peaks, $C_6F_5Y^-$, were equally dominant in the C_6F_5Y/CH_4 mass spectra where Y = $-CF_3$, -Cl and -CHO. No perfluorophenoxides, $YC_6F_4O^-$, or fluoride adducts, $C_6F_5Y{\cdot}F^-$, were present in any of these mass spectra (Y = -CN, $-CF_3$, -Cl and -CHO).

In contrast, the major ion observed in the negative ion mass spectrum of $C_6F_5NO_2/CH_4$ is the perfluorophenoxide, $NO_2C_6F_4O^-$; see Figure 4.5b. The $NO_2C_6F_4O^-$ peak represents over 90% of the total ion signal. A very weak $C_6F_5NO_2{\cdot}F^-$ peak is also present.

The $NO_2C_6F_4O^-$ ion was observed in previous PHPMS work by Dillow et al. [24]. The formation of $NO_2C_6F_4O^-$ was attributed to the presence of oxygen in the ion source. In another PHPMS study [25], the perfluorophenoxide $C_6F_5O^-$ and fluoride adduct $C_6F_6{\cdot}F^-$ were amongst the negative ions present in the negative ion mass spectrum of a C_6F_6/CH_4 gas mixture. A trace concentration of oxygen in the ion source (~0.1 mtorr) originating from a minor leak in the gas handling plant was believed responsible for $C_6F_5O^-$ production [25]. An attempt was made by Nicol [26] to explain the pathway to $C_6F_5O^-$ formation upon ionization of the C_6F_6/CH_4 gas mixture. However, the negative ion mass spectrum contained more than sixteen peaks which made interpretation of the reaction pathway very difficult [26].

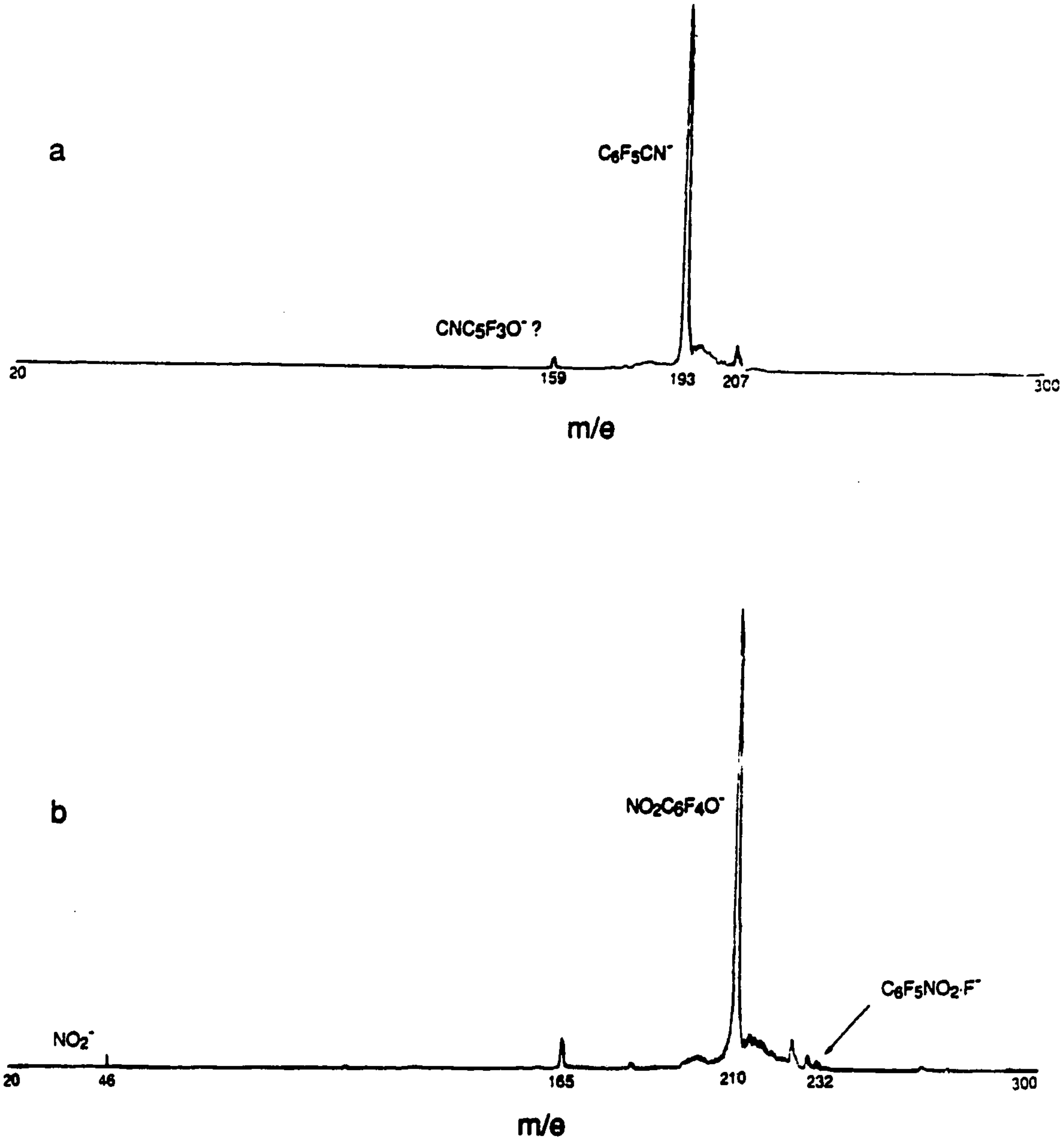

Figure 4.5 Negative ion mass spectra obtained with a gas mixture of a) 3.0 torr CH_4 and 1.8 mtorr C_6F_5CN b) 3.0 torr CH_4 and 0.9 mtorr $C_6F_5NO_2$. Ion source temperature, 423 K. The molecular ion peak $C_6F_5CN^-$ is dominant in mass spectrum (a) while the perfluorophenoxide $NO_2C_6F_4O^-$ is the major ion in mass spectrum (b).

Phenoxide ions of the form $(M\text{-}Cl+O)^-$, where M^- represents the molecular ion, were observed in the negative chemical ionization mass spectra of aromatic chlorinated pesticides, i.e, M [27]. The experimental conditions were; 0.1-1.0 mtorr of M, 0.33 torr of bath gas (isobutane) and ion source temperature, 200°C. Since M^- ions were also observed in the mass spectra it was assumed phenoxide formation occurred through reaction of M^- with oxygen (reaction (4.6)).

$$M^- + O_2 \longrightarrow (M\text{-}Cl+O)^- + OCl \qquad (4.6)$$

The source of oxygen in these experiments was not disclosed. Similar $(M\text{-}Cl+O)^-$ phenoxide ions were observed in the negative chemical ionization mass spectra of polycyclic chlorinated insecticides [28]. The experimental conditions were; 10^{-5}-2.0 torr of M, 0.75 torr of bath gas (methane) and ion source temperature, 100-200°C.

A study on the production of the phenoxides $(M\text{-}Cl+O)^-$ in the ion source was performed by Horning et al. [29] using the atmospheric pressure ion source. Chlorinated aromatics were used as analytes and were present in the ion source in concentrations of ~0.1 mtorr. The oxygen concentration in the ion source was kept low (~0.5 mtorr) by the use of ultra high purity nitrogen (0.5 ppm O_2) as the bath gas. The ion source temperature range was between 100-200°C. In one set of experiments the negative ion mass spectra of the isomers ortho-, meta- and para-chloronitrobenzene (o-, m-, p-ClNB) were collected. The negative ion mass spectra of p-ClNB [29] follows:

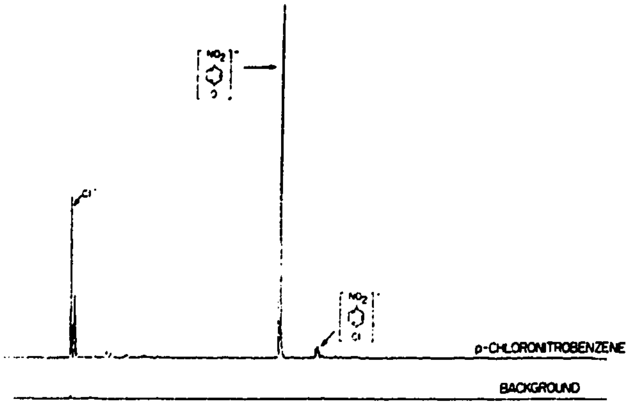

A similar mass spectrum was obtained for o-ClNB. The mass spectrum of m-ClNB, however, contained only the molecular ion peak, m-ClNB^{-}.

The appearance of the respective mass spectra were explained by Horning [29] in terms of reaction (4.6). The proposed reaction pathway to phenoxide formation on reaction of p-ClNB with O_2 is shown below.

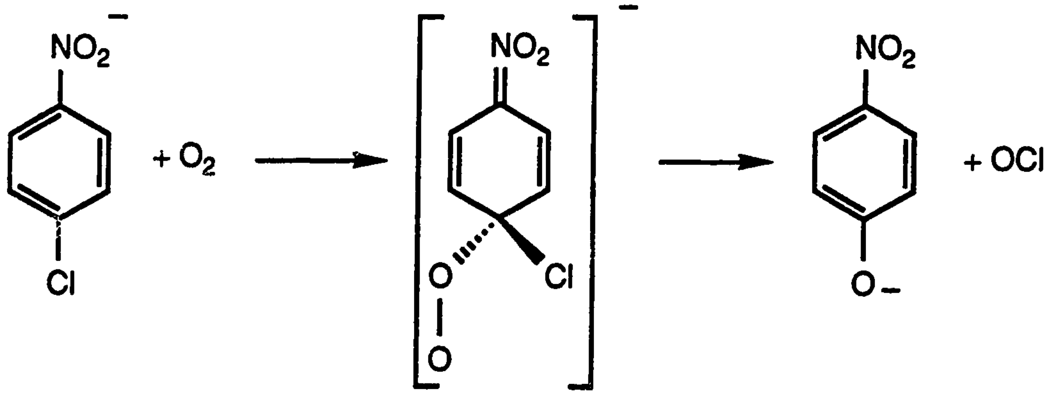

Scheme III

The inability of the meta isomer to form the intermediate resonance structure shown above was used to explain the presence of only the molecular ion in the negative ion mass spectrum of m-ClNB [29]. As Cl^{-} was only observed in the mass spectra of o- and p-ClNB, its formation was linked with phenoxide (M-Cl+O)$^{-}$ formation. Further reaction of the neutral radical ClO in the ion source was suggested as a possible route to Cl^{-} [29].

In order to confirm Scheme III, an experiment involving p-ClNB was conducted where $^{18}O_2$ was added to the ion source [29]. The resulting phenoxide ions contained both oxygen isotopes which was taken as proof of the occurrence of reaction (4.6).

Hence, it is possible the analogous reaction (4.7) is the pathway to the observed $NO_2C_6F_4O^-$ formation in the ion source (Y = $-NO_2$).

$$C_6F_5Y^- + O_2 \longrightarrow YC_6F_4O^- + OF \qquad (4.7)$$

The presence of oxygen in the ion source in the present work may be due to a minor leak in the gas handling plant. The anticipated intermediate in reaction (4.7) is the Meisenheimer complex, structure VII (analogous to the intermediate in Scheme III), which would be stabilized by the presence of strong electron withdrawing groups on the benzene ring.

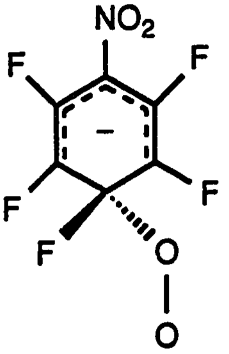

VII

It is interesting that only a small intensity F^- adduct peak is observed in the mass spectrum of $C_6F_5NO_2/CH_4$; see Figure 4.5b. This suggests, if reaction (4.7) is proceeding, the neutral radical formed, OF, is fairly stable.

As mentioned earlier in this section, no perfluorophenoxide ions were present in the C_6F_5Y/CH_4 mass spectra where Y = -CN, CF_3, -Cl and -CHO.

Oxygen (5-17 mtorr) was added to each of these gas mixtures in order to see if reaction (4.7) proceeds under these experimental conditions.

The negative ion mass spectra collected for C_6F_5Cl/CH_4 and $C_6F_5Cl/O_2/CH_4$ gas mixtures are shown in Figure 4.6. Upon addition of O_2 to the ion source, an intense peak is observed at m/e =183 which likely corresponds to the perfluorophenoxide $C_6F_5O^-$; see Figure 4.6b. Also present with smaller intensity is a peak at m/e = 199 which likely corresponds to $^{35}ClC_6F_4O^-$. The isotope peak $^{37}ClC_6F_4O^-$ at m/e = 201 is not distinguishable due to the large intensity of the molecular ion peak ($C_6F_5{}^{35}Cl^-$) at m/e = 203. $C_6F_5O^-$ formation from reaction (4.6) would be expected to be favored over $ClC_6F_4O^-$ production from the analogous reaction (4.7) as the C-Cl bond is weaker than C-F [4]. Also of interest in the $C_6F_5Cl/CH_4/O_2$ mass spectrum (Figure 4.6b) is the presence of a large intensity Cl^- peak. The intensity of the Cl^- peak in the C_6F_5Cl/CH_4 mass spectrum was weak (Figure 4.6a) which suggests Cl^- results from reaction (4.6).

The negative ion mass spectra for C_6F_5CN/CH_4, with and without oxygen, are shown in Figure 4.7. No $CNC_6F_4O^-$ formation is observed on addition of oxygen. The only possible oxygen related peaks are those at m/e = 178, 159 and 128 which could correspond to $CNC_5F_4O^-$, $CNC_5F_3O^-$ and $CNC_4F_2O^-$, respectively. Perfluorophenoxide ions, $YC_6F_4O^-$, were also absent from the C_6F_5CHO (0.3 mtorr)/O_2 (11.0 mtorr)/CH_4 and $C_6F_5CF_3$ (1.5 mtorr)/O_2 (16.5 mtorr)/CH_4 mass spectra.

The absence of perfluorophenoxide ions in the $C_6F_5Y/O_2/CH_4$ (Y = -CN, CF_3 and -CHO) mass spectra is surprising if reaction (4.7) is indeed responsible for $NO_2C_6F_4O^-$ formation. The anticipated Meisenheimer complex intermediate for reaction (4.7) where Y = -CN is shown by structure VIII.

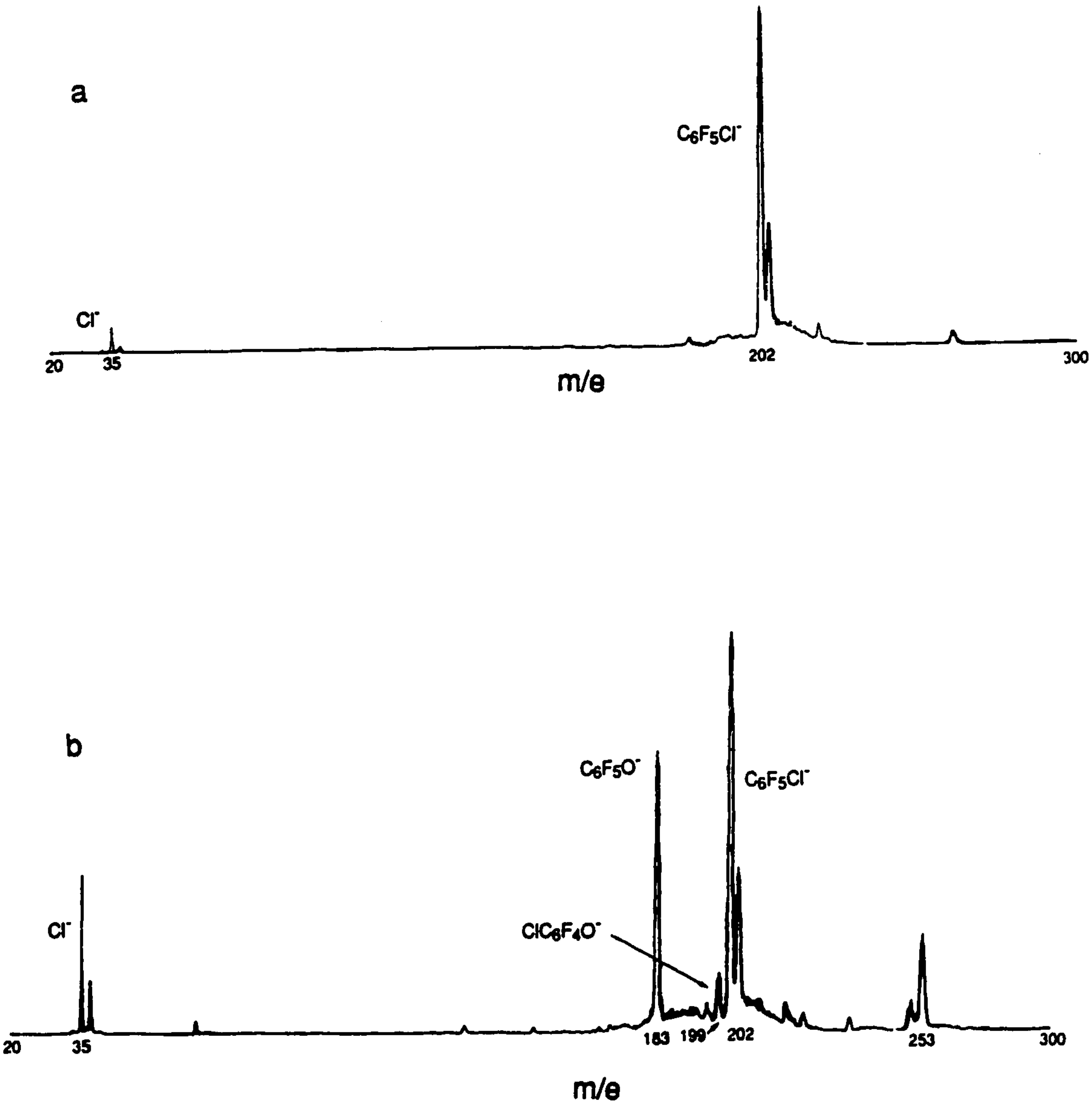

Figure 4.6 Negative ion mass spectra obtained with a gas mixture of a) 3.0 torr CH_4 and 9.0 mtorr C_6F_5Cl b) 3.0 torr CH_4, 9.0 mtorr C_6F_5Cl and 11.5 mtorr O_2. Ion source temperature, 423 K. The perfluorophenoxide ions $ClC_6F_4O^-$ and $C_6F_5O^-$ are observed upon addition of O_2 to the ion source.

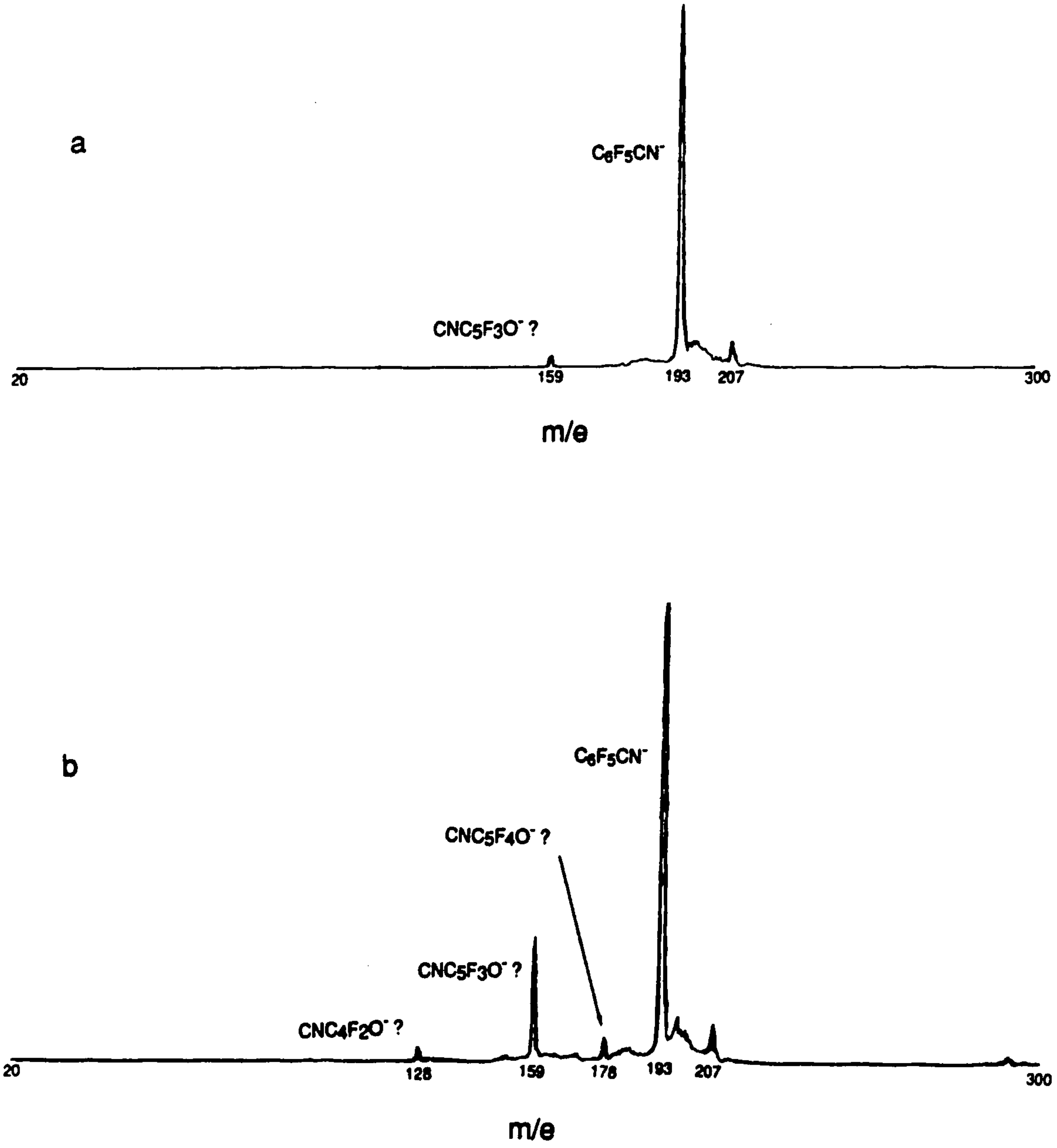

Figure 4.7 Negative ion mass spectra obtained with a gas mixture of a) 3.0 torr CH_4 and 1.8 mtorr C_6F_5CN b) 3.0 torr CH_4, 1.8 mtorr C_6F_5CN and 5.2 mtorr O_2. Ion source temperature, 423 K. The perfluorophenoxide ion $CNC_6F_4O^-$ is not observed upon addition of O_2 to the ion source.

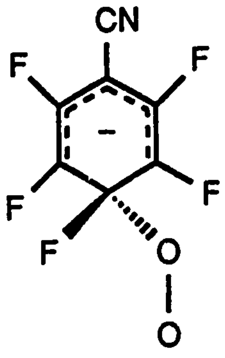

VII

This complex would be expected to be of a similar stability to the analogous perfluoronitrobenzene intermediate (structure VII) as -CN and -NO_2 are both strong π and σ charge acceptors. Hence, it is unexpected by the reaction (4.7) pathway that ionization of $C_6F_5NO_2/CH_4$ should lead to intense perfluorophenoxide formation ($NO_2C_6F_4O^-$) where only trace concentrations of O_2 (~0.1 mtorr) are anticipated in the ion source while the perfluorophenoxide ion ($CNC_6F_4O^-$) is not observed in the C_6F_5CN/O_2 (5.2 mtorr)/CH_4 mass spectrum.

One possible explanation is that $NO_2C_6F_4O^-$ is formed from a nucleophilic aromatic substitution reaction (S_NAr) involving attack of $C_6F_5NO_2$ by the radical anion $C_6F_5NO_2^-$ (reaction (4.8)).

$$C_6F_5NO_2^- + C_6F_5NO_2 = NO_2C_6F_4O^- + C_6F_5NOF \qquad (4.8)$$

The proposed reaction pathway is shown in Figure 4.8. The unpaired electron in the $C_6F_5NO_2^-$ radical anion is in a π^* orbital which extends over the nitro group and the aromatic ring [24]. The negative charge is expected to be largely located on the electronegative oxygens in the nitro group. This assumption is based on the large difference in the electron affinity of $C_6F_5NO_2$ ($-\Delta G^o_{eA,423K}$ = 35.0 kcal/mol [24]) with respect to C_6F_6 ($-\Delta G^o_{eA,423K}$ = 14.9 kcal/mol [30]). If a S_NAr reaction is taking place, nucleophilic attack of the carbon atom in the para

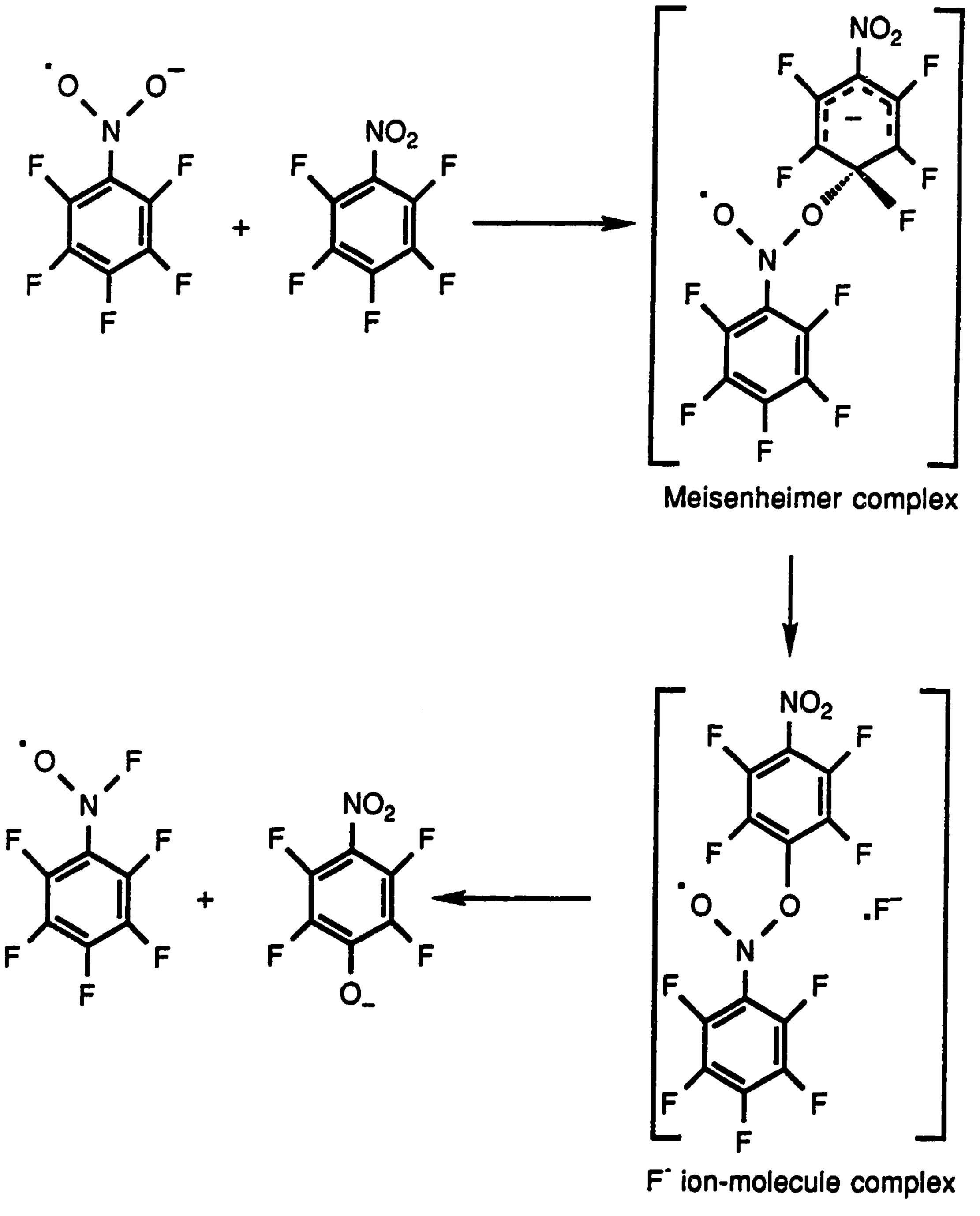
NO2
N
O
F
+
Meisenheimer complex
.F⁻
F⁻ ion-molecule complex

Figure 4.8 Proposed S_NAr reaction pathway for the attack of $C_6F_5NO_2$ by the radical anion $C_6F_5NO_2^{-}$.

position to the -NO_2 substituent is expected on qualitative grounds. The carbon atom in the para position of perfluoronitrobenzene is anticipated to have the lowest π electron density due to the +R effect of the substituent [31, 32] and may be expected to be the site of nucleophilic attack by strong bases. Furthermore, the resulting σ bonded intermediate is strongly stabilized by the same +R effect of the substituent.

A reaction pathway analogous to that shown in Figure 4.8 was proposed by Nibbering et al. [16, 17] to describe nucleophilic aromatic substitution involving attack of $C_6F_5OCH_3$ by the strong bases OR^- and NR^- (R = H, alkyl); see Introduction. In that work the departure of F^- from the Meisenheimer complex was predicted to lead to the formation of a F^- ion-molecule complex as simple dissociation to F^- as an ionic product was not observed. Within the F^- ion-molecule complex, reattack by F^- of the newly formed molecule was proposed to occur which resulted in the product ions observed [16, 17]. Since $OC_6F_4NO_2^-$ is the major peak in the negative ion mass spectrum of $C_6F_5NO_2/CH_4$ (Figure 4.5a), it appears this reaction pathway is followed if nucleophilic attack of $C_6F_5NO_2$ by $C_6F_5NO_2^-$ is indeed occurring. The stability of the neutral radical, C_6F_5NOF, formed in the reaction pathway shown in Figure 4.8, is unknown.

Finally the reaction leading to fluoride adduct formation in the ion source, i.e., ionization of $C_6F_5NO_2/C_6F_5CN/CH_4$, was investigated. In the initial experiment the negative ion mass spectrum of the C_6F_5CN (8.9 mtorr)/CH_4 gas mixture was collected; see Figure 4.9a. As expected, the molecular ion, $C_6F_5CN^-$, is the major peak observed with the small peak at m/z = 159 possibly corresponding to $CNC_5F_3O^-$. No fluoride adduct formation was observed. The negative ion mass spectrum collected upon addition of a small amount of $C_6F_5NO_2$ (0.08 mtorr) to the C_6F_5CN/CH_4 gas mixture is shown in Figure 4.9b.

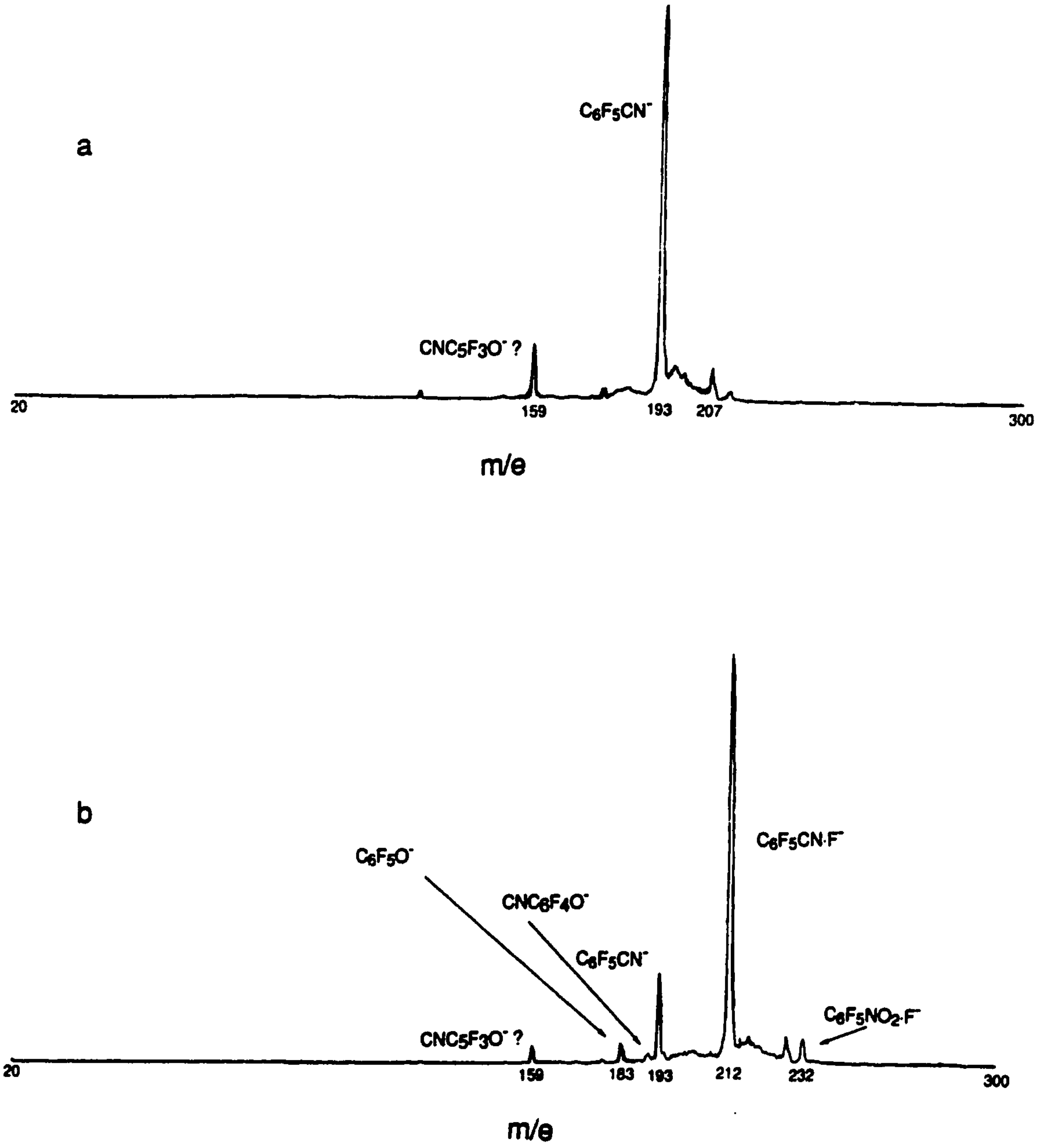

Figure 4.9 Negative ion mass spectra obtained with a gas mixture of a) 3.0 torr CH_4 and 8.9 mtorr C_6F_5CN b) 3.0 torr CH_4, 8.9 mtorr C_6F_5CN and 0.08 mtorr $C_6F_5NO_2$. Ion source temperature, 423 K. The fluoride adduct $C_6F_5CN{\cdot}F^-$ is the major ion present on addition of $C_6F_5NO_2$ to the ion source.

The major peak observed is the fluoride adduct $C_6F_5CN{\cdot}F^-$ with a weak $C_6F_5NO_2{\cdot}F^-$ peak also present. No $NO_2C_6F_4O^-$ is observed and only a small $CNC_6F_4O^-$ peak is present. The presence of an intense $C_6F_5CN{\cdot}F^-$ peak is unexpected as strong fluoride adduct formation is not observed in either the $C_6F_5NO_2/CH_4$ or C_6F_5CN/CH_4 mass spectra (Figures 4.5 and 4.9a). One possible explanation for the changes observed in the C_6F_5CN/CH_4 and $C_6F_5NO_2/C_6F_5CN/CH_4$ mass spectra (Figures 4.9a and 4.9b) is the occurrence of nucleophilic aromatic substitution involving attack of C_6F_5CN and $C_6F_5NO_2$ by the perfluorophenoxide $NO_2C_6F_4O^-$ (resulting from reaction (4.7) and/or reaction (4.8)). The possible S_NAr reaction pathways are shown in Figure 4.10 (Y = $-NO_2$ and -CN). Reaction pathway A in Figure 4.10 would appear favored from the negative ion mass spectrum shown in Figure 4.9b. The observed fluoride adducts $C_6F_5CN{\cdot}F^-$ and $C_6F_5NO_2{\cdot}F^-$ would be anticipated to be formed on collision of the perfluorobenzene neutrals with F^- ion-molecule complexes, i.e., F^- transfer. Both perfluorobenzenes are known to have strong fluoride affinities [21]. The fluoride adducts would then engage in the fluoride transfer equilibrium (4.3). The larger $C_6F_5CN{\cdot}F^-$ peak with respect to $C_6F_5NO_2{\cdot}F^-$ in Figure 4.9b is the result of the much higher concentration of C_6F_5CN in the ion source. Reaction pathway A also explains the virtual absence of the perfluorophenoxide ions $NO_2C_6F_4O^-$ and $CNC_6F_4O^-$ in the mass spectrum shown in Figure 4.9b.

An interesting question which arises is, if reaction pathway A (Figure 4.10) is indeed responsible for F^- adduct formation, why is intense F^- adduct formation not observed upon ionization of the $C_6F_5NO_2/CH_4$ gas mixture (Y = $-NO_2$ in Figure 4.10)? The reaction pathway shown in Figure 4.8, which may be responsible for the presence of $OC_6F_4NO_2^-$ in the $C_6F_5NO_2/CH_4$ mass spectrum, is also a potential source of F^- as the stability of the proposed neutral

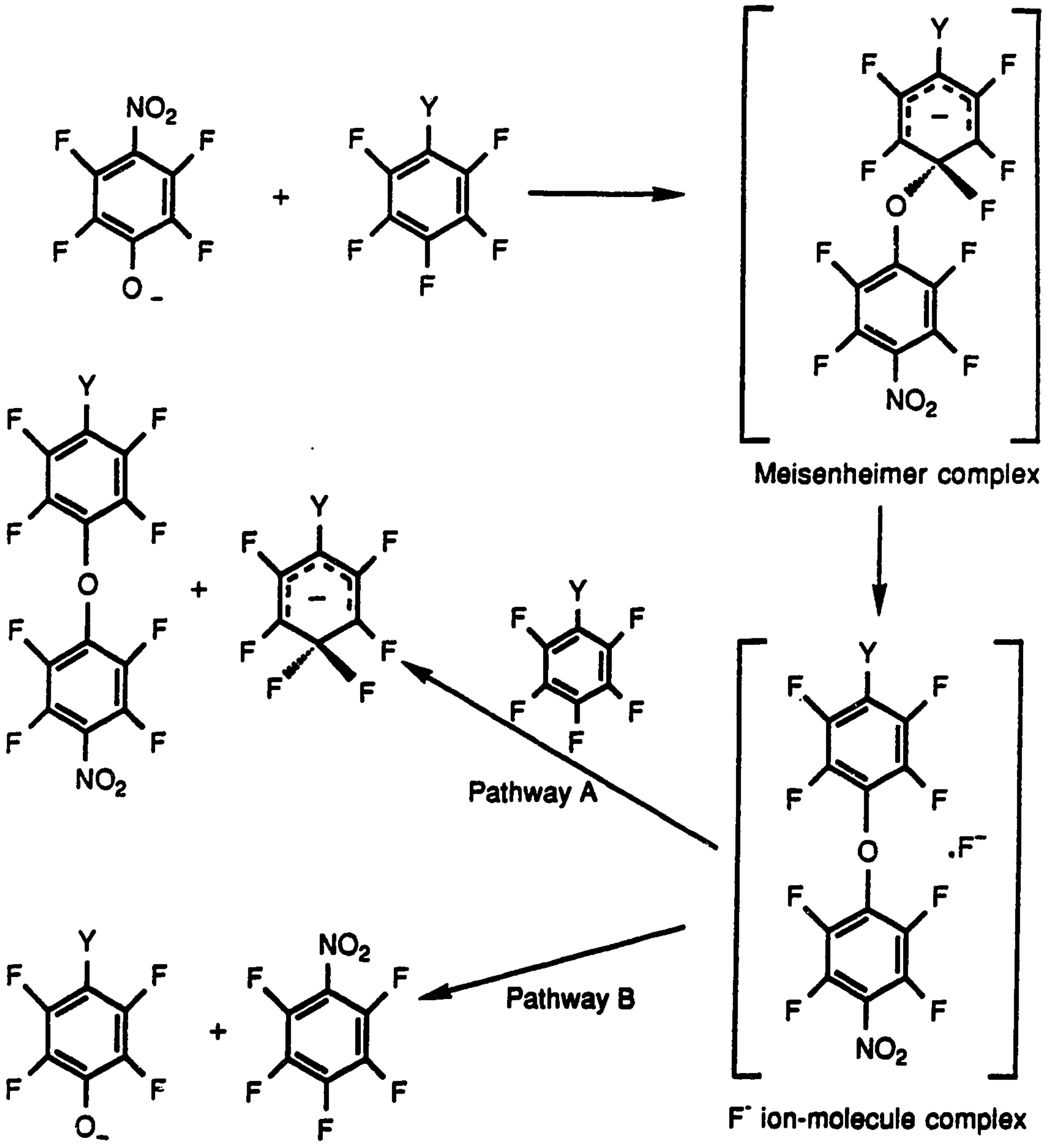
Meisenheimer complex
Pathway A
Pathway B
F⁻ ion-molecule complex
.F⁻

Figure 4.10 Proposed S_NAr reaction pathways for the attack of C_6F_5Y (Y = CN, NO_2) by the perfluorophenoxide $NO_2C_6F_4O^-$.

radical C_6F_5NOF is unknown. A speculative explanation is that F^- adduct formation does, in fact, occur upon ionization of the $C_6F_5NO_2/CH_4$ gas mixture but a F^- transfer reaction channel (reaction (4.2)) is required in order to see the $C_6F_5NO_2{\cdot}F^-$ adduct; see Scheme IV.

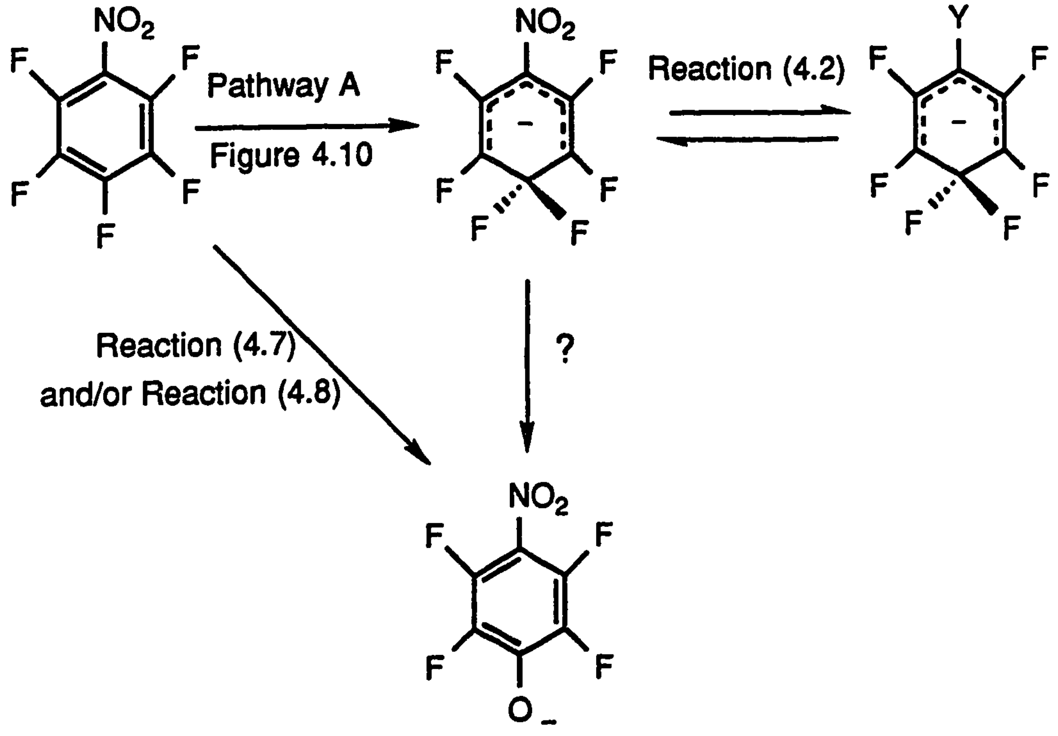

Without the fluoride transfer reaction channel, $C_6F_5NO_2{\cdot}F^-$ may react fully to form the perfluorophenoxide $NO_2C_6F_4O^-$; see Figure 4.5b. The pathway of this reaction, if indeed occurring, is unknown at present.

Upon addition of more $C_6F_5NO_2$ (0.8 mtorr) to the $C_6F_5NO_2/C_6F_5CN/CH_4$ gas mixture, four major ions are observed in the negative ion mass spectrum: the fluoride adducts $C_6F_5NO_2{\cdot}F^-$ and $C_6F_5CN{\cdot}F^-$ and perfluorophenoxides $NO_2C_6F_4O^-$ and $CNC_6F_4O^-$; see Figure 4.11. The formation of these ions may be explained in terms of the reaction pathways shown in Figure 4.10.

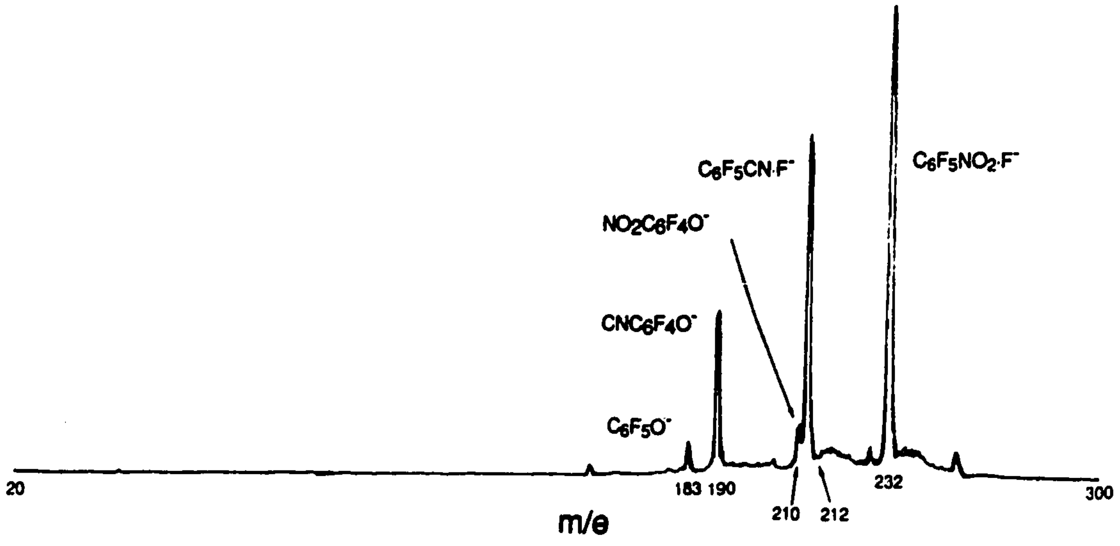

Figure 4.11 Negative ion mass spectrum obtained with a gas mixture of 3.0 torr CH_4 and 8.9 mtorr C_6F_5CN and 0.9 mtorr $C_6F_5NO_2$ at 423 K. The fluoride adducts $C_6F_5CN{\cdot}F^-$ and $C_6F_5NO_2{\cdot}F^-$ and the perfluorophenoxides $CNC_6F_4O^-$ and $NO_2C_6F_4O^-$ are all observed in the mass spectrum.

The previous discussion is a speculative interpretation of the work to date concerning $YC_6F_4O^-$ and $C_6F_5Y{\cdot}F^-$ production in the ion source. The observations are interesting and further work is planned. Addition of $^{18}O_2$ to the $C_6F_5NO_2/CH_4$ gas mixture should help to establish whether O_2 (reaction (4.7)) or $C_6F_5NO_2^-$ (reaction (4.8)) is responsible for $NO_2C_6F_4O^-$ formation. Collection of the negative ion mass spectra of various $C_6F_5Y/C_6F_5Y'/CH_4$ gas mixtures would also be expected to help rationalize reaction pathways to $YC_6F_4O^-$ and $C_6F_5Y{\cdot}F^-$ formation in the ion source.

4.3 Results and Discussion

4.3a Results

The $-\Delta G^o_{ClA,423K}$ and $-\Delta G^o_{BrA,423K}$ values for C_6F_5Y obtained from measurement of association equilibria (4.1) are shown on scales of increasing $-\Delta G^o_{XA,423K}$ in Figures 4.12 and 4.13. Also present are some bond free energy determinations for doubly and triply substituted perfluorobenzene complexes. The $-\Delta G^o_{ClA,423K}$ and $-\Delta G^o_{BrA,423K}$ values are probably accurate to ±1 kcal/mol. The lengths of the arrows shown in the figures correspond to the independently determined $-\Delta G^o_{ClTr,423K}$ ($-\Delta\Delta G^o_{ClA,423K}$) and $-\Delta G^o_{BrTr,423K}$ ($-\Delta\Delta G^o_{BrA,423K}$) values from transfer equilibrium (4.2) measurements. Some of the bromide transfer equilibrium measurements involved the reference compounds tetracyanoethylene (TCNE), tetrafluoro-para-benzoquinone (F_4-p-BQ) and tetrachloro-para-benzoquinone (Cl_4-p-BQ); see Figure 4.12. The absolute $-\Delta G^o_{BrA,423K}$ for these compounds are available from equilibrium measurements reported in Chapter 5. An agreement of ±0.5 kcal/mol is observed in Figures 4.12 and 4.13 between the relative bond free energies ($-\Delta G^o_{XTr,423K}$) and those predicted by absolute free energy determinations (X = Cl and Br). In most

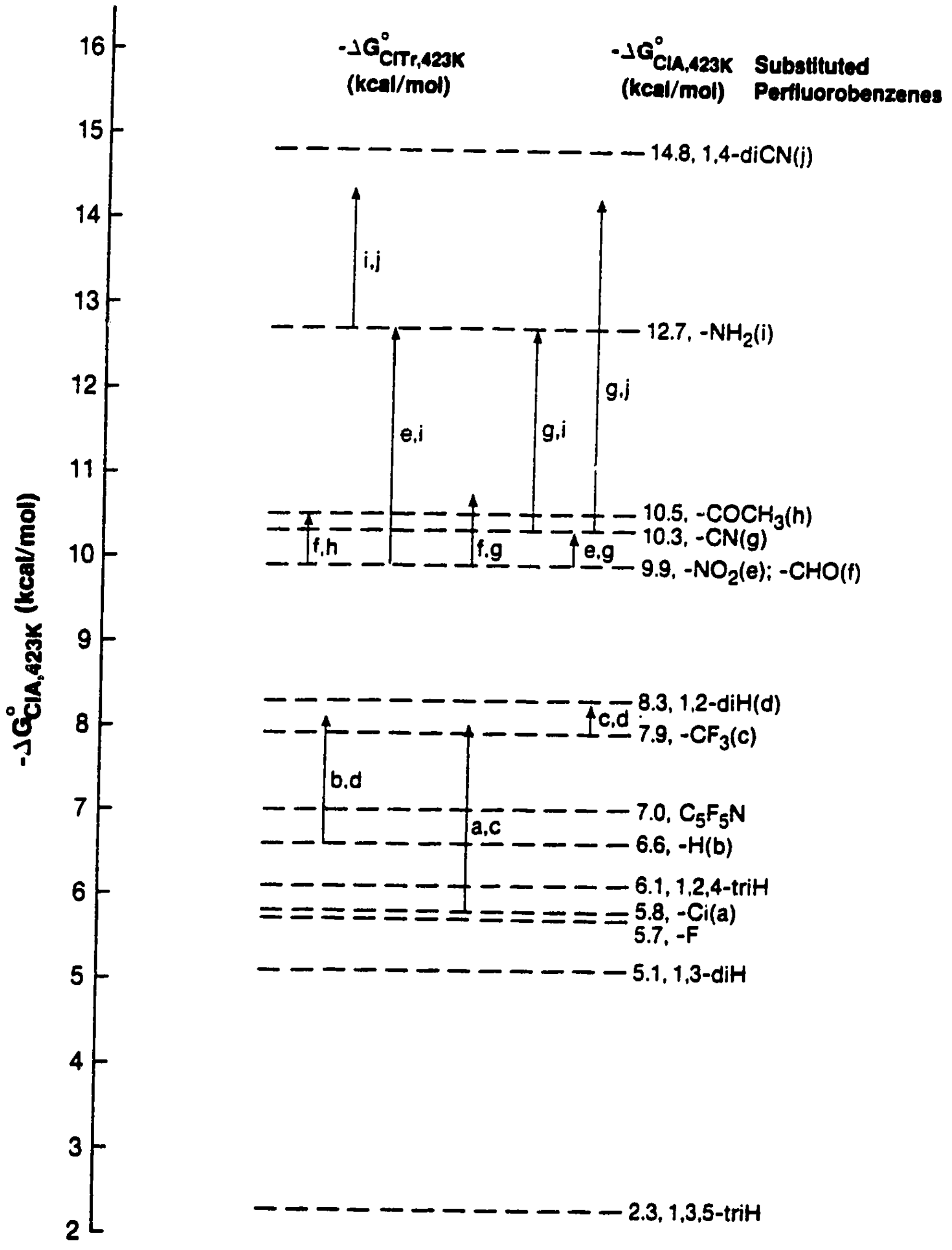

Figure 4.12 Scale of $-\Delta G^{o}_{ClA,423K}$ for reaction (4.1): $C_6F_5Y + Cl^- = C_6F_5Y{\cdot}Cl^-$. Also shown are $-\Delta G^{o}_{ClA,423K}$ values for some doubly and triply substituted perfluorobenzenes. Lengths of arrows shown correspond to determinations of $-\Delta G^{o}_{ClTr,423K}$ mostly for reaction (4.2): $C_6F_5Y{\cdot}Cl^- + C_6F_5Y' = C_6F_5Y'{\cdot}Cl^- + C_6F_5Y'$. C_6F_5Y and C_6F_5Y' identified by letters beside arrows.

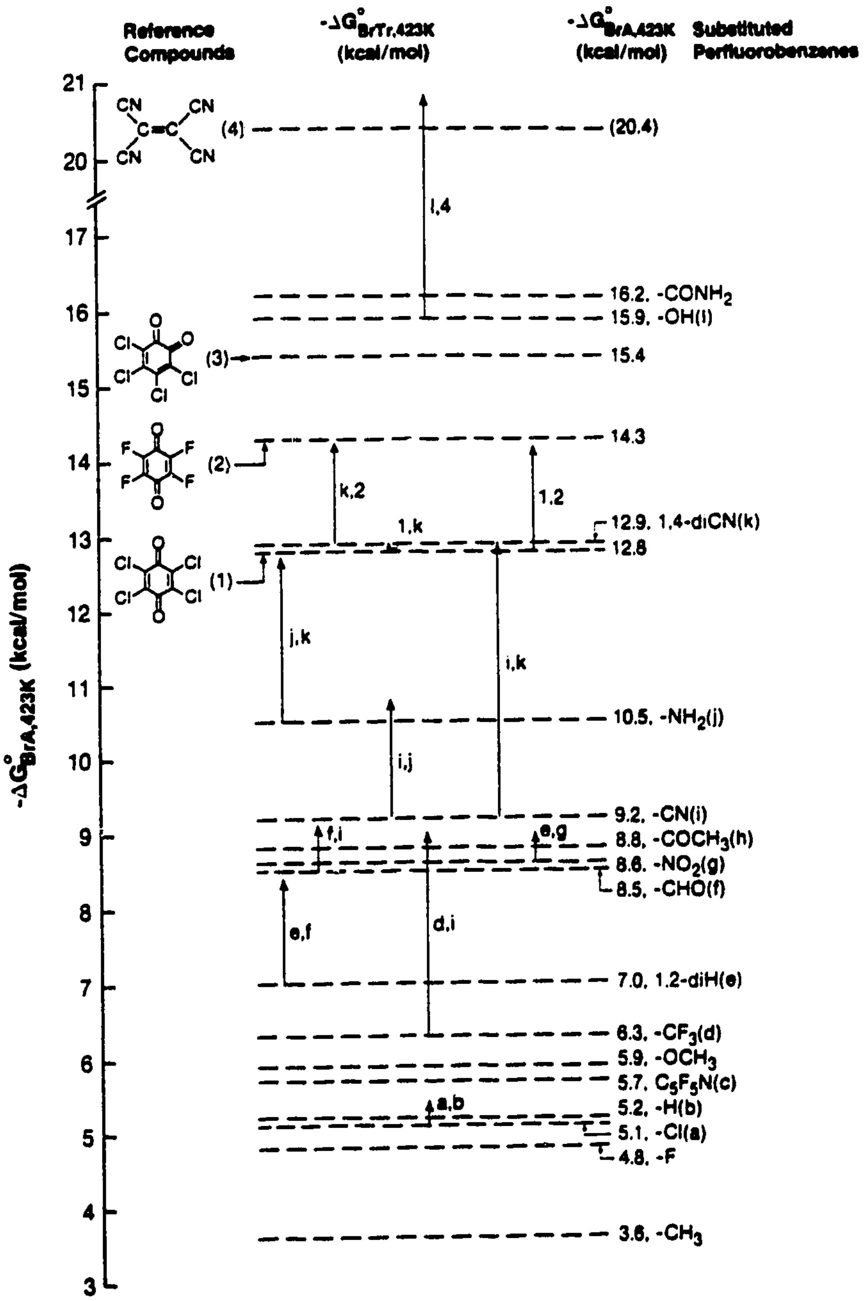
Reference Compounds
$-\Delta G^{\circ}_{BrTr,423K}$ (kcal/mol)
$-\Delta G^{\circ}_{BrA,423K}$ (kcal/mol)
Substituted Perfluorobenzenes
$-\Delta G^{\circ}_{BrA,423K}$ (kcal/mol)
21
20
17
16
15
14
13
12
11
10
9
8
7
6
5
4
3
(4)
(3)
(2)
(1)
(20.4)
16.2, -CONH$_2$
15.9, -OH(l)
15.4
14.3
12.9, 1,4-diCN(k)
12.8
10.5, -NH$_2$(j)
9.2, -CN(i)
8.8, -COCH$_3$(h)
8.6, -NO$_2$(g)
8.5, -CHO(f)
7.0, 1,2-diH(e)
6.3, -CF$_3$(d)
5.9, -OCH$_3$
5.7, C$_5$F$_5$N(c)
5.2, -H(b)
5.1, -Cl(a)
4.8, -F
3.6, -CH$_3$
l,4
k,2
l,2
l,k
j,k
i,k
i,j
f,i
e,g
e,f
d,i
a,b

Figure 4.13 Scale of $-\Delta G^{\circ}_{BrA,423K}$ for reaction (4.1): $C_6F_5Y + Br^- = C_6F_5Y{\cdot}Br^-$. Also shown are $-\Delta G^{\circ}_{BrA,423K}$ values for some doubly substituted perfluorobenzenes. Lengths of arrows shown correspond to determinations of $-\Delta G^{\circ}_{BrTr,423K}$ mostly for reaction (4.2): $C_6F_5Y{\cdot}Br^- + C_6F_5Y' = C_6F_5Y + C_6F_5Y'{\cdot}Br^-$. C_6F_5Y and C_6F_5Y' identified by letters beside arrows. $-\Delta G^{\circ}_{BrA,423K}$ of reference compounds involved in bromide transfer equilibria measurements from Table 5.1.

cases, the $-\Delta G^{o}_{XTr,423K}$ are consistent with the difference of $-\Delta G^{o}_{XA,423K}$ values to within ±0.2 kcal/mol.

The directly determined $-\Delta G^{o}_{ClA,423K}$, $-\Delta G^{o}_{BrA,423K}$ and $-\Delta G^{o}_{IA,423K}$ values are summarized in Table 4.1. An agreement of 1 kcal/mol is observed in Table 4.1 for the $-\Delta G^{o}_{ClA,423K}$ and $-\Delta G^{o}_{BrA,423K}$ values of C_6F_6 determined in the present work with those obtained via van't Hoff plots by Hiraoka et al. [4].

The ladder of the interconnecting F^- exchange equilibria (4.2) is shown in Figure 4.14. The bond free energy of $C_6F_5CN \cdot F^-$ ($-\Delta G^{o}_{FA,423K} = 28.3$ kcal/mol) determined by Dillow et al. [21] was used to anchor the scale. $-\Delta G^{o}_{FA,423K}(C_6F_5CN)$ was not measured directly (equilibrium (4.1)) by Dillow et al. but through measurements of F^- transfer equilibria (4.2) [21]. In that study [21] $-\Delta G^{o}_{FA,423K}(C_6F_6)$ was used to anchor the scale and this value was calculated from the directly determined values of $-\Delta H^{o}_{FA}(C_6F_6)$ and $-\Delta S^{o}_{FA}(C_6F_6)$ [3]. The consistency of data in Figure 4.11 can be checked by the multiple thermodynamic cycles present in the ladder. For example, F^- transfer from C_6F_5CN to $C_6F_5NO_2$ has a $-\Delta G^{o}_{FTr,423K}$ of 1.8 kcal/mol and from $C_6F_5NO_2$ to $C_6F_4(CN)_2$ has a $-\Delta G^{o}_{FTr,423K}$ of 2.3 kcal/mol while the direct F^- transfer from C_6F_5CN to $C_6F_4(CN)_2$ has a $-\Delta G^{o}_{FTr,423K}$ of 3.9 kcal/mol. An agreement of 0.2 kcal/mol is also observed for the other cycles in the ladder. The $-\Delta G^{o}_{FA,423K}$ determinations from the present work are given in Table 4.1 along with those from Dillow et al. [21] and Hiraoka et al. [3].

The van't Hoff plots for bromide attachment to C_6F_6, C_6F_5CN and $C_6F_4(CN)_2$ are shown in Figure 4.15. Straight line dependencies are observed in all cases. The $-\Delta H^{o}_{BrA}$ (bond strength) and $-\Delta S^{o}_{BrA}$ values calculated from these plots are given in Table 4.2. These $-\Delta S^{o}_{BrA}$ values, combined with the $-\Delta G^{o}_{BrA,423K}$ values in Table 4.1, can be used to estimate the bond strengths ($-\Delta H^{o}_{BrA}$) of other $C_6F_5Y \cdot Br^-$ complexes, i.e., $-\Delta H^{o}_{BrA} = -\Delta G^{o}_{BrA} - T\Delta S^{o}_{BrA}$. Bond

Table 4.1 $-\Delta G^o_{XA,423K}$ values (±1 kcal/mol) for reaction (4.1): $C_6F_5Y + X^- = C_6F_5Y{\cdot}X^-$ where $X^- = F^-, Cl^-, Br^-, I^-$ [a]

Y	$-\Delta G^o_{XA,423K}$ (kcal/mol)			
	F^-	Cl^-	Br^-	I^-
$CONH_2$			16.2	
OH			15.9	
1,4-diCNC_6F_4 [b]	32.3	14.8	12.9	10.7
NH_2	28.7	12.7	10.5	7.8
$COCH_3$	26.8 26.5[d]	10.5	8.8	
CN	28.3 28.3[d]	10.3	9.2	7.1
NO_2	30.1 30.1[d]	9.9	8.6	6.4
CHO	26.6	9.9	8.5	
1,2-diHC_6F_4 [b]		8.3	7.0	
CF_3	22.6[d]	7.9	6.3	
OCH_3			5.9	
C_5F_5N [c]			5.6	
H	18.2[d]	6.6	5.2	
Cl		5.8	5.1	
F	17.5[e]	5.7 6.0[f]	4.8 5.7[f]	3.7[f]
CH_3			3.6	

a. $-\Delta G^o_{XA,423K}$ (X = Cl, Br, I) from direct measurements of association equilibria (4.1), see Figures 4.12 and 4.13. $-\Delta G^o_{FA,423K}$ obtained indirectly from measurements of transfer equilibria (4.2), see Figure 4.14. b. $-\Delta G^o_{XA,423K}$ for doubly substituted perfluorobenzenes. c. pentafluoropyridine. d. From Dillow et al. [21]. e. From Hiraoka et al. [3]. f. From Hiraoka et al. [4].

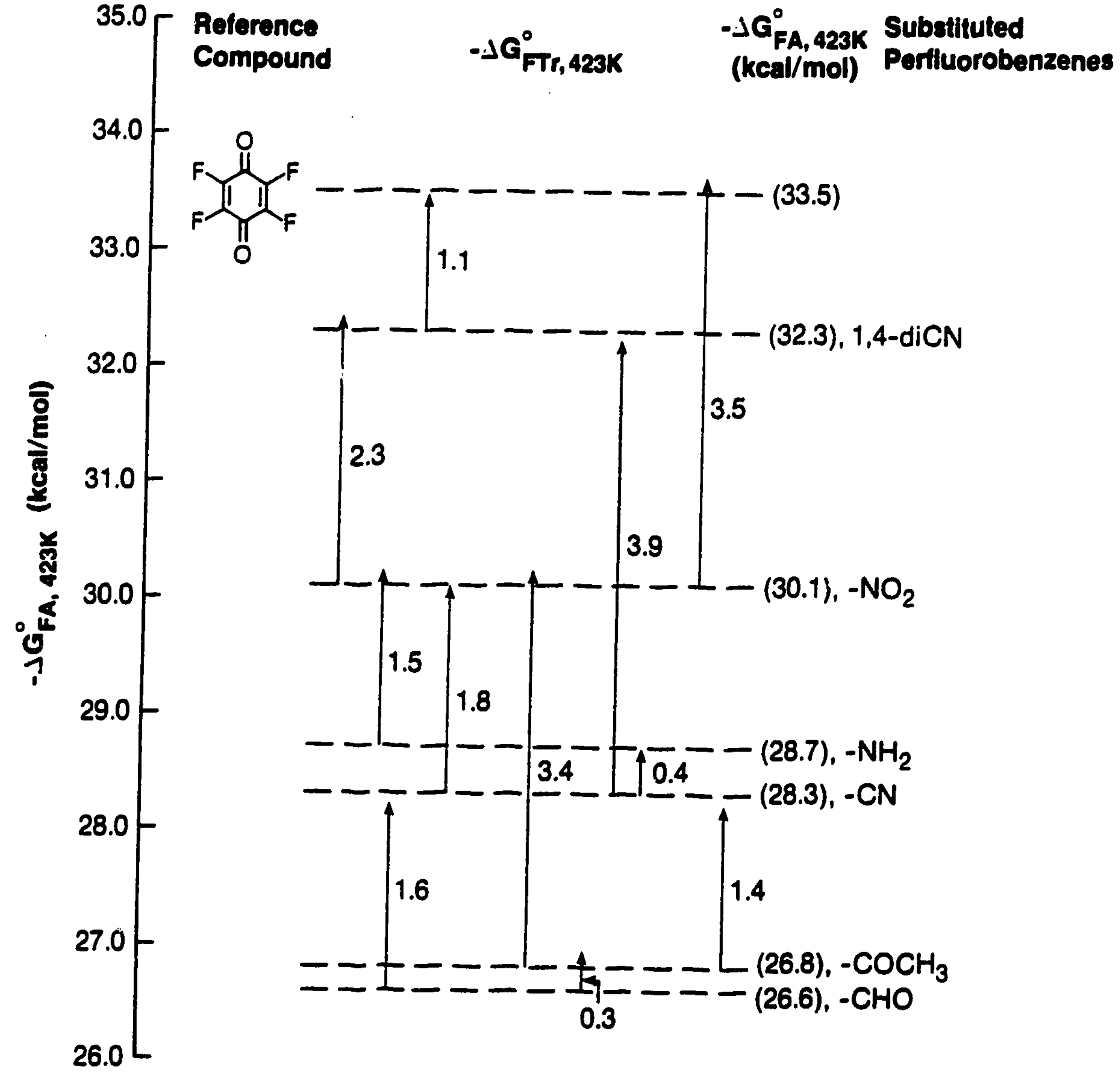
35.0
34.0
33.0
32.0
31.0
30.0
29.0
28.0
27.0
26.0
$-\Delta G^{o}_{FA,423K}$ (kcal/mol)
Reference Compound
$-\Delta G^{o}_{FTr,423K}$
$-\Delta G^{o}_{FA,423K}$ (kcal/mol)
Substituted Perfluorobenzenes
1.1
2.3
3.5
3.9
1.5
1.8
3.4
0.4
1.6
1.4
0.3
(33.5)
(32.3), 1,4-diCN
(30.1), -NO$_2$
(28.7), -NH$_2$
(28.3), -CN
(26.8), -COCH$_3$
(26.6), -CHO

Figure 4.14 Ladder of interconnecting $-\Delta G^{o}_{FTr,423K}$ values for reaction (4.2): $C_6F_5Y{\cdot}F^- + C_6F_5Y' = C_6F_5Y + C_6F_5Y'{\cdot}F^-$. The doubly substituted perfluorobenzene 1,4-diCNC$_6$F$_4$ and tetrafluoro-para-benzoquinone were also involved in flouride transfer equilibria measurements. Lengths of arrows correspond to determinations of $-\Delta G^{o}_{FTr,423K}$. $-\Delta G^{o}_{FA,423K}$ of $C_6F_5CN{\cdot}F^-$ from Dillow et al. [21] is used to anchor the bond free energy scale. The indirectly obtained $-\Delta G^{o}_{FA,423K}$ values are shown in parenthesis.

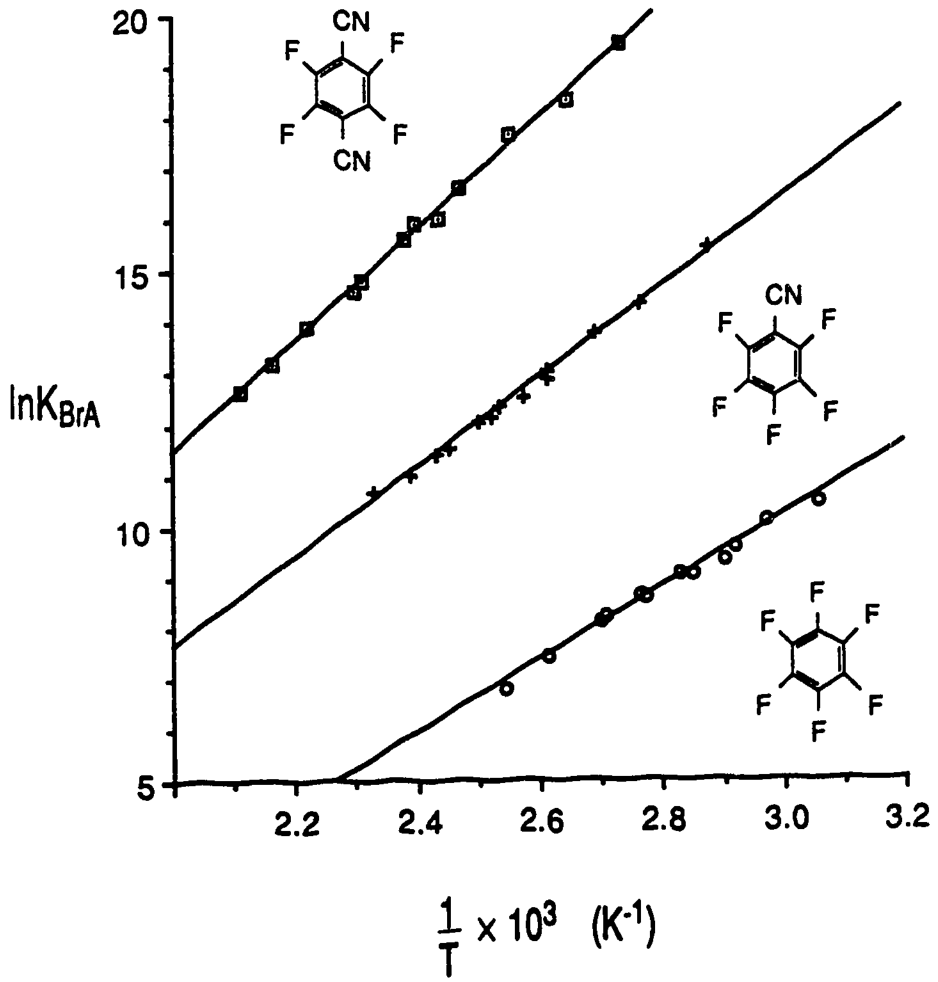

Figure 4.15 van't Hoff plots of equilibrium constants for bromide attachment to C_6F_6, C_6F_5CN and 1,4-diCNC_6F_4. $-\Delta H^{o}_{BrA}$ and $-\Delta S^{o}_{BrA}$ values obtained from plots are given in Table 4.2.

Table 4.2 Thermochemical data for bromide attachment to C_6F_6, C_6F_5CN and 1,4-diCNC_6F_4 via van't Hoff plots (Figure 4.15). The errors are estimated at ±2 kcal/mol for $-\Delta H^{\circ}_{BrA}$ and ±3 cal/deg.mol for $-\Delta S^{\circ}_{BrA}$ [a]

	$-\Delta H^{\circ}_{BrA}$ (kcal/mol)	$-\Delta S^{\circ}_{BrA}$ (cal/deg.mol)	$-\Delta G^{\circ}_{BrA,423K}$ [b] (kcal/mol)
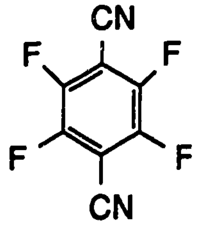	21.6	20.6	12.9
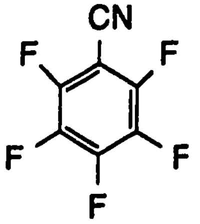	17.5	19.9	9.1
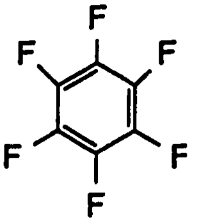	14.0 13.9[c]	21.8 19.4[c]	4.8 5.7[c]

a. Approximate $-\Delta H^{\circ}_{BrA}$ values for other substituted perfluorobenzenes can be obtained from the $-\Delta S^{\circ}_{BrA}$ values in this table and the $-\Delta G^{\circ}_{BrA,423K}$ values in Table 4.1 using $-\Delta H^{\circ}_{BrA} = -\Delta G^{\circ}_{BrA} - T\Delta S^{\circ}_{BrA}$.

b. $-\Delta G^{\circ}_{BrA,423K}$ calculated from $-\Delta H^{\circ}_{BrA}$ and $-\Delta S^{\circ}_{BrA}$ values in the table.

c. From Hiraoka et al.[4].

strength estimates of the complexes $C_6F_5Y{\cdot}X^-$ (X^- = F^-, Cl^- and I^-) can also be made from the data in Table 4.1 and previous $-\Delta S^o_{XA}$ (C_6F_5Y) determinations [3, 4, 33]. The $-\Delta H^o_{BrA}$ and $-\Delta S^o_{BrA}$ values for C_6F_6 determined by Hiraoka et al. [3] are given in Table 4.2 and are observed to be within the estimated error limit of the present determinations ($-\Delta H^o_{BrA} = \pm 2$ kcal/mol, $-\Delta S^o_{BrA} = \pm 3$ cal/degree mol; see Chapter 3). Good agreement is observed (±0.1 kcal/mol) between the $-\Delta G^o_{BrA,423K}$ values calculated from $-\Delta H^o_{BrA}$ and $-\Delta S^o_{BrA}$ (Table 4.2) and those determined independently by experiment at 423 K (Table 4.1).

4.3b σ Bonding in the Complexes $C_6F_5Y{\cdot}F^-$

From the bond free energy values given in Table 4.1 the stability order of the complexes $C_6F_5Y{\cdot}X^-$ is $C_6F_5Y{\cdot}F^- \gg C_6F_5Y{\cdot}Cl^- > C_6F_5Y{\cdot}Br^- > C_6F_5Y{\cdot}I^-$. This trend was also observed in theoretical ($-\Delta E^o_{XA}$) and experimental ($-\Delta H^o_{XA}$) determinations of $C_6F_6{\cdot}X^-$ (X^- = F^-, Cl^-, Br^- and I^-) bond strengths by Hiraoka et al. [3, 4]. Stronger bond energies are anticipated in the $C_6F_5Y{\cdot}F^-$ adducts due to the higher gas phase basicity of F^- which results from its smaller ionic radius. The large jump in basicity of F^- compared to the other halides is reflected in the gas phase acidities ($HX \rightarrow H^+ + X^-$) of the conjugate acids: ΔH^o_{Acid} (HF) = 371 kcal/mol (least acidic), ΔH^o_{Acid} (HCl) = 333.7 kcal/mol, ΔH^o_{Acid} (HBr) = 323.0 kcal/mol and ΔH^o_{Acid} (HI) = 314.3 kcal/mol (most acidic) [34]. However, on the basis of ab initio MO calculations (3-21G plus diffuse functions) where optimized geometries of $C_6F_6{\cdot}X^-$ complexes (X^- = F^-, Cl^-, Br^- and I^-) were determined, Hiraoka et al. [3, 4] also explained the differences in $C_6F_6{\cdot}X^-$ bond strengths in terms of differing adduct geometries.

The optimized geometry of $C_6F_6{\cdot}F^-$ determined by Hiraoka et al. [3] is shown in Figure 4.16. F^- is predicted to add covalently to one of the unsaturated carbons in C_6F_6 to form a tetrahedral Meisenheimer complex; see also structure IV in Introduction. The electron withdrawing -F substituents in C_6F_6 prompt the benzene ring to accept the F^- electron density and the negative charge is distributed almost equally amongst the seven fluorine atoms; see Mulliken electron populations given in Figure 4.16. The $C_6F_6{\cdot}F^-$ geometry (Figure 4.16) is distorted significantly relative to that of C_6F_6 (C-C = 1.37 Å and C-F = 1.35 Å [3]) due to the destruction of aromaticity in the ring on σ bond formation.

Experimental evidence for a σ bonded $C_6F_6{\cdot}F^-$ (or $C_6F_7^-$) complex comes from the dramatic drop in binding energy (~20 kcal/mol) observed on association of $C_6F_6{\cdot}F^-$ with a second C_6F_6 molecule [3, 4].

$$C_6F_6 + F^- = C_6F_6{\cdot}F^- \qquad -\Delta H^\circ = 27.5 \text{ kcal/mol} \qquad (4.9)$$

$$C_6F_6 + C_6F_6{\cdot}F^- = (C_6F_6)_2{\cdot}F^- \qquad -\Delta H^\circ = 7.5 \text{ kcal/mol} \qquad (4.10)$$

The dispersion of negative charge in a $C_6F_6{\cdot}F^-$ Meisenheimer complex is most likely responsible for further clustering being less favorable. A much smaller drop in energy (1-2 kcal/mol) relative to the bond strengths in the complexes $C_6F_6{\cdot}X^-$ (X^- = Cl^-, Br^- and I^-) is observed on association of C_6F_6 with $C_6F_6{\cdot}X^-$ [4]. The small energy change is explained by electrostatic interactions in $C_6F_6{\cdot}X^-$ where very little charge transfer from X^- (X^- = Cl^-, Br^- and I^-) to C_6F_6 takes place; see Section 4.3c.

The intrinsic reaction coordinates (IRC), or minimum reaction path, of the reaction C_6F_6 + F^- has been computed by Hirao et al. using the minimal STO-3G basis set [2]. The IRC of C_6F_6 + F^- is of interest as it provides information on the formation of Meisenheimer type complexes. The IRC of C_6F_6 + F^- and corresponding potential energy diagram are shown in Figures 4.17 and 4.18. At large intermolecular distances F^- approaches C_6F_6 along the C_6 symmetry

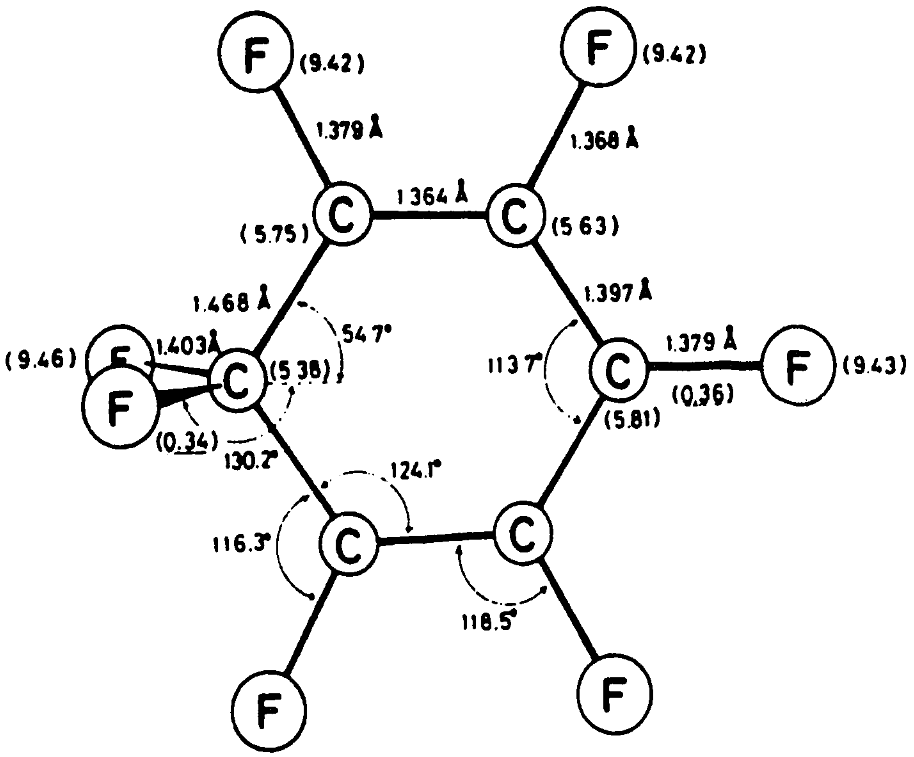
F
(9.42)
1.379 Å
F
(9.42)
1.368 Å
1.364 Å
(5.75)
C
C
(5.63)
1.468 Å
1.397 Å
54.7°
(9.46)
F
1.403Å
C
(5.38)
F
113.7°
C
1.379 Å
F
(9.43)
(0.36)
(5.81)
(0.34)
130.2°
124.1°
116.3°
C
C
118.5°
F
F

Figure 4.16 Optimized geometry of $C_6F_6{\cdot}F^-$ ($C_6F_7^-$) from theoretical calculations due to Hiraoka et al. [3]. Values in parentheses are electron densities and the underlined numbers in parentheses are bond populations.

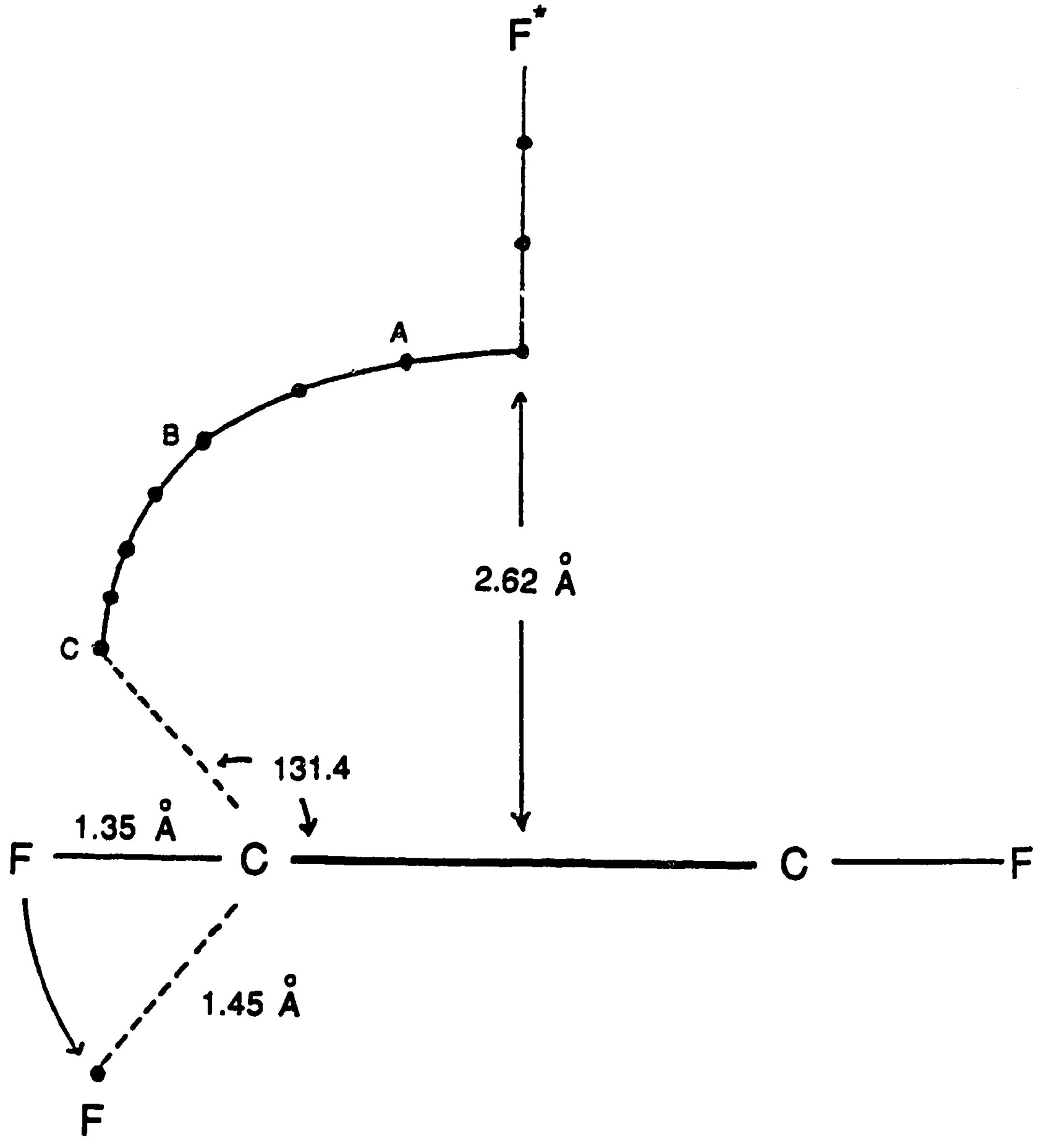
F*
A
B
C
2.62 Å
131.4
1.35 Å
F
C
C
F
1.45 Å
F

Figure 4.17 Intrinsic Reaction Coördinates (IRC) of $F^- + C_6F_6$ from theoretical calculations due to Hirao et al. [2]. F^* represents incoming F^- ion which charge transfers to the C_6F_6 ring.

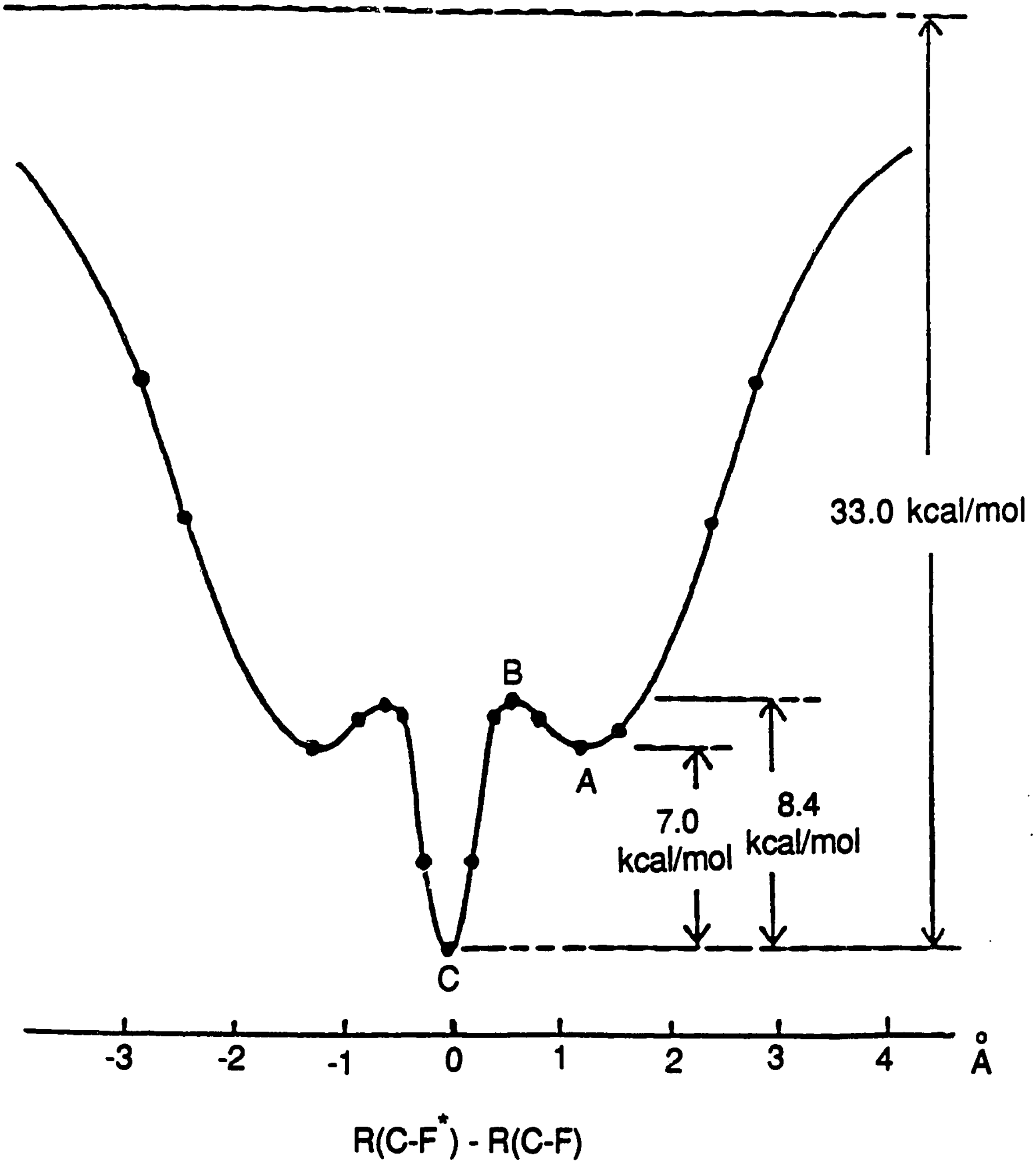

Figure 4.18 Potential energy diagram for the reaction $F^- + C_6F_6$ corresponding to the IRC shown in Figure 4.17. From theoretical calculations due to Hirao et al. [2].

axis of C_6F_6 due to a long range interaction between F^- and the quadrupole moment of C_6F_6 perpendicular to the plane of C_6F_6. The experimentally measured quadrupole moment (Q_{zz}) in C_6F_6 is $Q_{zz}(C_6F_6) = +9.5 \times 10^{-26}$ esu [35], i.e., reversed when compared to that of C_6H_6 (see Chapter 3) and attractive to negative ions. This reversal must be due to the large C^+-F^- bond dipoles in C_6F_6 which result from the high electronegativity of F. At position A of the IRC (Figure 4.17), where F^- is ~2.6 Å from the molecular plane of C_6F_6, a minimum exists in the potential energy surface (Figure 4.18) which corresponds to the most stable geometry for the electrostatically bonded $C_6F_6 \cdot F^-$ complex, see structure IX.

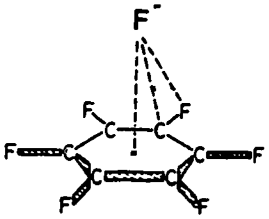

IX

This axial structure is analogous to the geometry predicted most stable for the complexes $C_6F_6 \cdot X^-$ ($X^- = Cl^-$, Br^- and I^-) [4]; see structure V in Introduction.

Moving along the IRC (Figure 4.17) F^- undergoes a secondary reaction with C_6F_6 where the ring acquires a negative charge relative to the initial C_6F_6 and F becomes σ bonded to one of the ring carbons, i.e., position C of the IRC. In the potential energy diagram of the $C_6F_6 + F^-$ reaction (Figure 4.18) the Meisenheimer $C_6F_6 \cdot F^-$ complex corresponds to the central minimum (labelled C) and represents the overall most stable geometry of $C_6F_6 \cdot F^-$. Also present in the potential energy diagram is a maximum (or saddle point) at position B between the electrostatic and Meisenheimer $C_6F_6{\cdot}F^-$ complex minima. This maximum presents a small activation energy barrier of 1.4 kcal/mol to the formation of the Meisenheimer complex. Electronic repulsion between F^- and the π electron cloud of C_6F_6 as F^- approaches the C_6F_6 molecular plane is a possible contributor to the saddle point.

The optimized geometries of $C_6F_6{\cdot}F^-$, where the attacking fluoride is in positions A, B and C of the IRC, are shown in Figure 4.19. Also given in the figure is the stabilization energy ($-\Delta E^o_{FA}$) for each complex geometry. These were determined by single point calculations using the 3-21G plus diffuse functions basis set [2]. A bond strength of ~26 kcal/mol was determined for the electrostatic $C_6F_6{\cdot}F^-$ complex where F^- is in position A of the IRC. This is much stronger than the electrostatic bond strength of ~5 kcal/mol anticipated by Dillow et al. [21] and only ~7 kcal/mol smaller than the predicted bond strength in the Meisenheimer $C_6F_6{\cdot}F^-$ complex. Interestingly, Hiraoka et al. [4] found the optimized electrostatic $C_6F_6{\cdot}F^-$ geometry (structure IX) to be unstable by STO-3G vibrational analysis, i.e., the electrostatic $C_6F_6{\cdot}F^-$ complex corresponded to a saddle point on the potential energy surface. The reason for difference in potential energy surfaces of the $C_6F_6 + F^-$ reaction as calculated by Hiraoka et al. [4] and Hirao et al. [2] is unknown at present.

The bond strength in the σ bonded $C_6F_6{\cdot}F^-$ complex, $-\Delta E^o_{FA} = 33$ kcal/mol (Figure 4.19), is ~5 kcal/mol higher than that determined theoretically (3-21G basis set) and experimentally (via van't Hoff plots) by Hiraoka et al. [3]. Error limits were not reported for any of these values [2, 3]. Significant error may be present in the experimentally determined $-\Delta H^o_{FA}(C_6F_6)$ value [3] as difficulties were encountered in measuring association equilibrium (4.9) due to the use of NF_3 as a source of F^- in the ion source; see Section 4.2a. The bond strength in the Meisenheimer $C_6F_6{\cdot}F^-$ complex, $-\Delta E^o_{FA} = 33$ kcal/mol [2], represents a

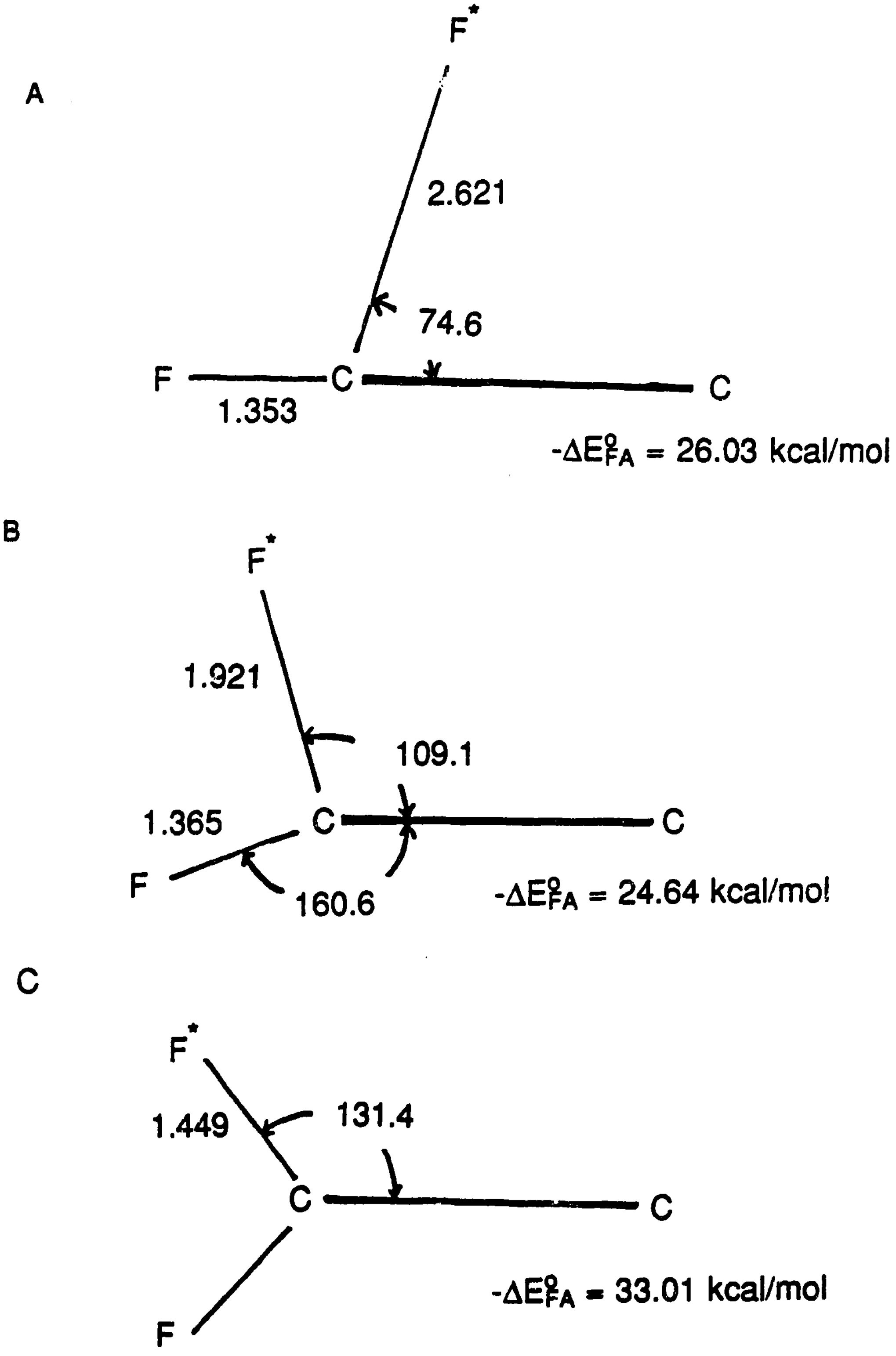
A
F*
2.621
74.6
F
C
C
1.353
-ΔE°FA = 26.03 kcal/mol
B
F*
1.921
109.1
1.365
C
C
F
160.6
-ΔE°FA = 24.64 kcal/mol
C
F*
1.449
131.4
C
C
F
-ΔE°FA = 33.01 kcal/mol

Figure 4.19 Optimized geometries of $C_6F_6{\cdot}F^-$ where the attacking fluorine F^* is in position A, B and C of the IRC (Figure 4.17).

balance between the energy stabilization on C-F bond formation (~116 kcal/mol [3]) and destabilization due to the destruction of the aromaticity in the C_6F_6 ring, i.e., deformation of the C_6F_6 structure on formation of the tetrahedral anionic complex.

Information on whether σ bonding is present in the complexes $C_6F_5Y{\cdot}F^-$ is gained by the use of substituent effect concepts developed by Taft et al. [36]. The substituent effect, $-\delta\Delta G^o_{FA,423K}$, for each perfluorobenzene relative to pentafluorobenzene (Y = H), is evaluated from the $-\Delta G^o_{FA,423K}$ data in Table 4.1.

$$-\delta\Delta G^o_{FA,423K} = \rho_R\sigma_R + \rho_F\sigma_F \qquad (4.11)$$

In equation (4.11) the $-\delta\Delta G^o_{FA,423K}$ due to a given substituent is separated into contributions from resonance $R = \rho_R\sigma_R$ and field $F = \rho_F\sigma_F$ effects. The σ parameters are constant for a given substituent and are tabulated [36] while the ρ values are dependent on the given reaction series and are determined by best fit regression analysis of equation (4.11) with the experimental $-\delta\Delta G^o_{FA,423K}$ values.

A plot of the experimentally determined $-\delta\Delta G^o_{FA,423K}$ versus the calculated $-\delta\Delta G^o_{FA,423K}$ with best fit parameters is shown in Figure 4.20. A fairly good correlation (correlation coefficient r = 0.966) is observed. Only σ acceptor, π acceptor substituents (Y = CF_3, CHO, $COCH_3$, CN and NO_2) are used in the plot as σ bonding is anticipated in the $C_6F_5Y{\cdot}F^-$ complexes, i.e., F^- is expected to be strongly π donating and σ acceptor, π donor substituents will lead to a separate correlation; see Chapter 2. Substituents were also separated into σ acceptor, π acceptor and σ acceptor, π donor groups on analysis of the substituent effects on the electron attachment free energies of the perfluorobenzenes [24].

The ρ_R and ρ_F values from best fit regression analysis of equation (4.11) are shown in Table 4.3. Inclusion of the polarizability term (P) improved the fit

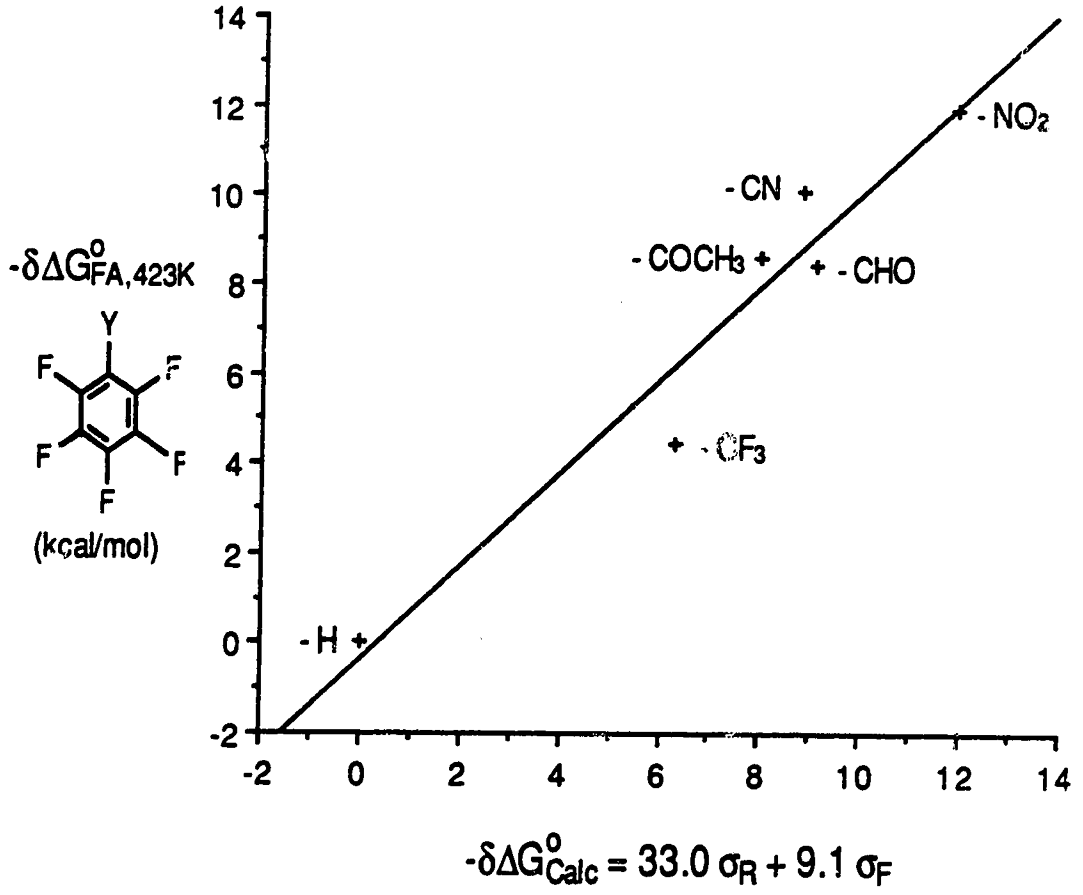

Figure 4.20 $-\delta\Delta G^{o}_{FA,423K}$ for F^- bonding to the perfluorobenzenes, C_6F_5Y, versus $-\delta\Delta G^{o}_{Calc}$ calculated with Taft σ parameters, see equation (4.11). $-\delta\Delta G^{o}_{FA,423K} = 0$ for Y = H. σ acceptor, π acceptor substituents. Correlation coefficient $r = 0.966$.

Table 4.3 Values for Resonance ρ_R and Field ρ_F Parameters, Taft Equations (4.11) and (4.12) [a]

Reaction	ρ_R	ρ_F	r^b	**Origin of data**
$C_6F_5Y{\cdot}F^-$ [a] π acceptors	33.0±8.7	9.1±2.7	0.966	Table 4.1
$C_6F_5Y{\cdot}Cl^-$ [a]	10.3±1.7	3.0±0.6	0.958	Table 4.1
$C_6F_5Y{\cdot}Br^-$ [a]	8.8±2.0	3.5±0.7	0.934	Table 4.1
$C_6F_5Y^-$ [c] π acceptors	66.3±9.4	20.3±2.6	0.996	Kebarle [24]
4-YPhOH[d] π acceptors	49.0±1.5	18.6±0.5	0.999	Taft [36]
$4\text{-}YPhCO_2H$[d]	14.6±0.7	15.0±0.6	0.997	Taft [36]

a. ρ values obtained from linear regression analysis of equations (4.11) and (4.12) where $\delta\Delta G^\circ_{XA,423K}$ corresponds to experimentally determined ΔG° for reaction: $C_6F_5Y + C_6F_5H{\cdot}X^- = C_6F_5Y{\cdot}X^- + C_6F_5H$ ($X^- = F^-, Cl^-, Br^-$).

b. Correlation coefficient.

c. Gas phase electron affinities.

d. Gas phase acidities.

very little and had only a small effect on the ρ_R and ρ_F values. The actual magnitude of the energy contribution of the resonance ($R = \rho_R\sigma_R$) and field effect ($F = \rho_F\sigma_F$) to $-\delta\Delta G^{o}_{FA,423K}$ are shown in Table 4.4. Examination of these data shows that the resonance R effect makes a significant contribution to the bond free energy change which suggests F^- transfers negative charge directly into the C_6F_5Y ring on complex formation, i.e., σ bond formation occurs.

Also given in Table 4.3 for comparison are the ρ values for the gas phase dissociation of benzoic acids and phenols obtained from the corresponding $-\delta\Delta G^{o}_{Acid}$ values [36]. The ρ_R and ρ_F values (Table 4.3) are: ~33, ~9 for F^- bond free energies; ~49, ~19 for para substituted phenol acidities and ~14, ~15 for para substituted benzoic acid acidities. The ρ_R/ρ_F ratio for the $C_6F_5Y{\cdot}F^-$ bond free energies is close to that for the phenol acidities while the resonance effect is relatively smaller for the benzoic acids. The similarity in the relative F and R effects of F^- bond free energies with those for the acidities of phenols is expected on the basis of the direct into the ring π donation by the negative functional group occurring for both the Meisenheimer $C_6F_5Y{\cdot}F^-$ (or $C_6F_6Y^-$) complex and the phenoxide anion; see structures X and XI.

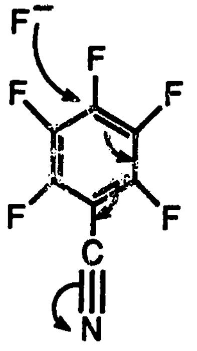

X

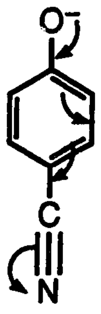

XI

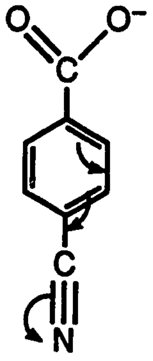

XII

These resonance structures are more important than the π shift from the ring into the substituent induced by the negative charge on the oxygen in the

Table 4.4 Resonance R and Field F Contributions of Substituents [a]

Substituent	$C_6F_5Y{\cdot}F^-$ [b]		$C_6F_5Y{\cdot}Cl^-$ [b]		$C_6F_5Y{\cdot}Br^-$ [b]		$C_6F_5Y^-$ [c]	
	R	F	R	F	R	F	R	F
$-NO_2$[e]	5.9	5.9	1.8	2.0	1.6	2.3	11.9	13.2
-CN[e]	3.3	5.5	1.1	1.8	0.9	2.1	6.6	12.2
-CHO[e]	6.3	2.8	2.0	0.9	1.7	1.1	12.6	6.3
$-CF_3$[e]	2.3	4.0	0.7	1.3	0.6	1.5	4.6	9.0
-H	0.0	0.0	0.0	0.0	0.0	0.0	0.0	0.0
-Cl[f]	d	d	-1.8	1.4	-1.5	1.6	d	d
-F[f]	d	d	-2.6	1.3	-2.2	1.5	d	d

a. Contribution: $R = \rho_R\sigma_R$ and $F = \rho_F\sigma_F$ in kcal/mol to $-\delta\Delta G^\circ$ for given substituent, see equations (4.11) and (4.12).

b. $-\delta\Delta G^\circ_{XA,423K}$ for reaction (4.1) involving perfluorobenzenes, X = F, Cl, Br.

c. $-\delta\Delta G^\circ_{eA,423K}$ for gas phase electron affinities of perfluorobenzenes.

d. π donor substituents require a separate fit, see text.

e. π acceptor substituent.

f. π donor substituent.

benzoate anion, shown in structure XII. Correspondingly, a fairly good linear correlation is observed in the plot of relative bond free energies of $C_6F_5Y{\cdot}F^-$ (relative to Y = H) versus the relative acidities of phenols (r = 0.961) while a much poorer correlation (r = 0.878) is obtained in the plot of the same relative bond free energies of $C_6F_5Y{\cdot}F^-$ versus relative benzoic acid acidities (σ acceptor, π acceptor substituents only for both plots).

A plot of the fluoride attachment free energies of C_6F_5Y from Table 4.1 versus the electron attachment free energies ($-\Delta G^o_{eA,423K}$) from Dillow et al. [24] is shown in Figure 4.21. A fairly good linear correlation is observed (r = 0.943) which is not unexpected. The energy of the π^* LUMO of C_6F_5Y, which accepts the electron that leads to radical anion formation, is decreased by the presence of electron withdrawing substituents, Y [24]. The π^* LUMO of C_6F_5Y, mixed with the lowest σ^*, is also proposed to make a contribution to the stability of the $C_6F_5Y{\cdot}F^-$ Meisenheimer complexes [3]. The best fit ρ_R and ρ_F values from substituent effect analysis [24] involving the electron attachment free energies of C_6F_5Y (Y = σ acceptor, π acceptor) are shown in Table 4.3 and the R and F contributions to $-\delta\Delta G^o_{eA,423K}$ are shown in Table 4.4. The ρ_R/ρ_F ratio for the $C_6F_5Y^-$ radical anions ($\rho_R/\rho_F \sim 66/20$) is close to that for the bond free energies of $C_6F_5Y{\cdot}F^-$ ($\rho_R/\rho_F \sim 33/9$) which is probably due to a similarity of charge stabilization in the respective anions. The magnitude of the ρ_R and ρ_F values (and also R and F) for fluoride association are observed to be roughly half of those for electron attachment (Tables 4.3 and 4.4) which is presumably due to the extra electron withdrawing fluorine atom in the Meisenheimer complex.

The application of the Taft relationship (equation (4.11)) to F^- bonding to the perfluorobenzenes C_6F_5Y (Y = σ acceptor, π acceptor and H) implies the position of the newly formed C-F bond relative to the substituent remains constant. On qualitative grounds it is expected that nucleophilic attack of the

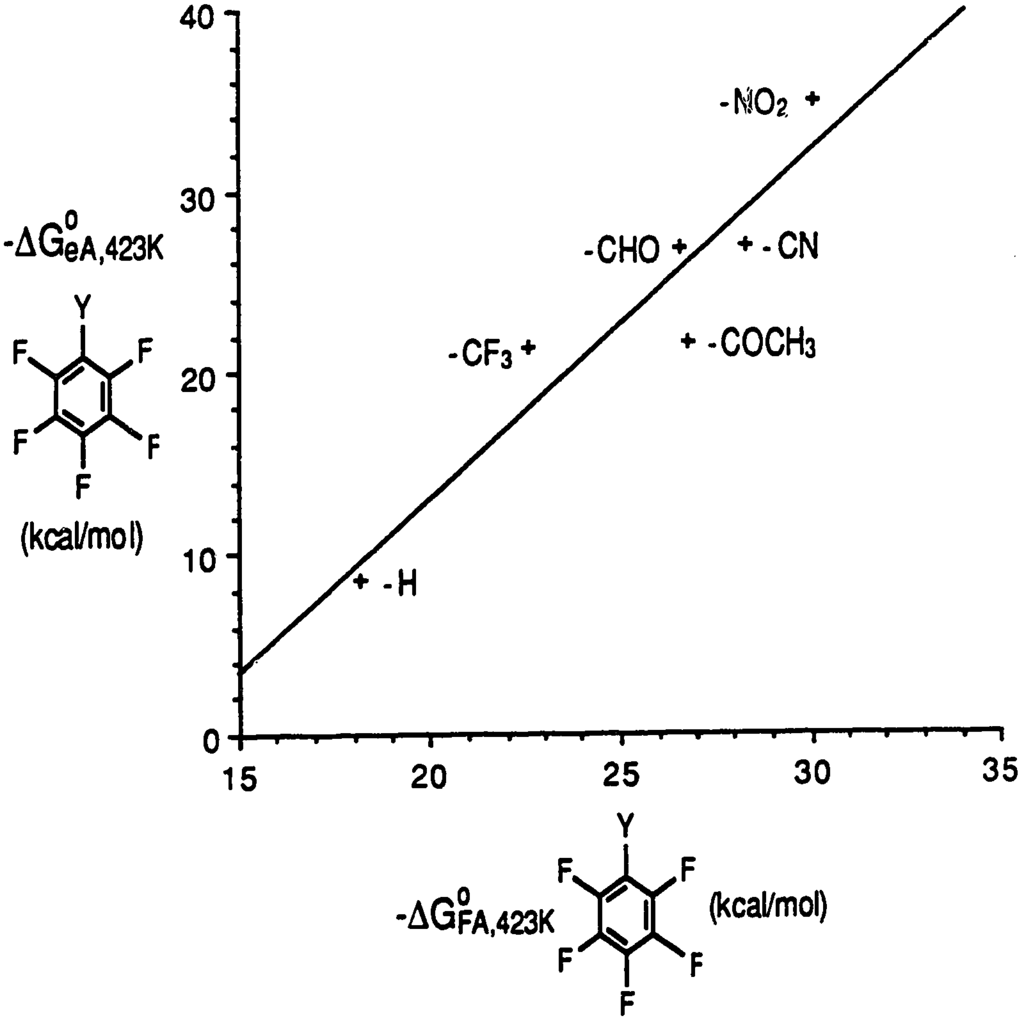

Figure 4.21 Plot of fluoride attachment free energies versus electron attachment free energies for the perfluorobenzenes, C_6F_5Y. σ acceptor, π acceptor substituents. $-\Delta G^{o}_{eA,423K}$ from Dillow et al. [24], $-\Delta G^{o}_{FA,423K}$ from Table 4.1. Fair correlation ($r = 0.942$) suggests similar negative charge stabilization in the $C_6F_5Y{\cdot}F^-$ adducts and $C_6F_5Y^-$ radical anions.

carbon atom in the para position to the σ acceptor, π acceptor substituent will occur (structure X) as this carbon atom is anticipated to have the lowest π electron density due to the +R effect of the substituent [31, 32]. Furthermore, the resulting σ bonded complex is strongly stabilized by the same +R effect of the substituent. F^- attack at the carbon atom para to the H substituent is also anticipated for the fluoride adduct of C_6F_5H; see structure XIII.

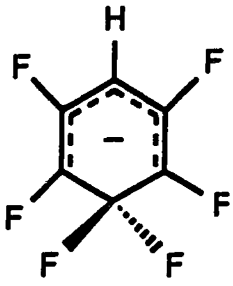

XIII

In structure XIII the destabilizing π donation by F in the para position to nawly formed σ bond is avoided while σ stabilization by F is obtained in the other positions, particularly the ipso and meta positions [20, 21, 37]. On this basis the higher bond strength determined for $C_6F_5H{\cdot}F^-$ relative to $C_6F_6{\cdot}F^-$ by Dillow et al. [21] is not unexpected; see Table 4.1. Analysis of the products from solution phase aromatic nucleophilic substitutions involving perfluorobenzenes also indicate the nucleophile F^- inserts preferentially into the para position relative to the substituent when Y is either a π acceptor or H [19, 20]. Thus, the use of the Taft relationship (equation (4.11)) to describe the bonding contributions in $C_6F_5Y{\cdot}F^-$ appears valid. This is also indicated by the fairly good fit observed in Figure 4.20.

Interestingly, from the $-\Delta G^{o}_{FA,423K}$ data in Table 4.1, it is observed that the the gas phase bond free energy of $C_6F_5NH_2{\cdot}F^-$ determined in the present work is ~10 kcal/mol stronger than that for $C_6F_5H{\cdot}F^-$ [21]. The NH_2 group is a strongly destabilizing π donor and kinetic studies on nucleophilic aromatic substitution in solution observed attack of $C_6F_5NH_2$ by the strong base CH_3O^- was ~200 times slower than attack of C_6F_5H due to the powerful deactivating -R effect of the substituent [20]. Hence, it appears in the gas phase that hydrogen bonding of F^- to the NH_2 substituent is favored over Meisenheimer complex formation with the presence of five electron withdrawing F substituents on the the benzene ring increasing the protic character of the substituent protons.

4.3c Electrostatic Bonding in the Complexes $C_6F_5Y{\cdot}X^-$ (X^- = Cl^-, Br^- and I^-)

From the bond free energies given in Table 4.1 it is observed that the bond strengths of the complexes $C_6F_5Y{\cdot}X^-$ (X^- = Cl^-, Br^- and I^-) are substantially weaker than those for the σ bonded $C_6F_5Y{\cdot}F^-$ complexes, i.e., ~10-20 kcal/mol smaller. Ab initio MO calculations [4] (3-21G plus diffuse functions) involving the complexes $C_6F_6{\cdot}X^-$ predict a largely electrostatic interaction with X^- positioned on the C_6 axis perpendicular to the C_6F_6 molecular plane; see structure V in Introduction. The distances of X^- from the center of the C_6F_6 ring are so large (r = 3.222 Å (X^- = Cl^-), r = 3.419 Å (X^- = Br^-) and r = 3.839 Å (X^- = I^-) [4]) that charge transfer from X^- is very small. The axial position of X^- maximizes the interaction with the positive quadrupole moment of C_6F_6 (Q_{zz}) perpendicular to the C_6F_6 plane [35, 38]. An analogous axial geometry (structure IX) was predicted for the electrostatic $C_6F_6{\cdot}F^-$ complex observed initially in the IRC of the F^- + C_6F_6 reaction; see Figure 4.17.

The different modes of interaction of F^- and X^- (X^- = Cl^-, Br^- and I^-) with C_6F_6 are of considerable interest. As discussed in Section 4.3b, $C_6F_6{\cdot}F^-$ is a Meisenheimer complex, i.e $C_6F_7^-$, where F^- bonds covalently to an unsaturated carbon atom in C_6F_6. Cl^-, Br^- and I^- cannot bond in the same manner as the stabilization energy on C-X bond formation (C-Cl ~80 kcal/mol, C-Br ~70 kcal/mol, C-I ~50 kcal/mol [4]) cannot compensate the destabilization due to the destruction of aromaticity. Thus Cl^-, Br^- and I^- prefer an electrostatic interaction with C_6F_6 where the aromaticity of C_6F_6 is soundly preserved. Experimental evidence for an electrostatic interaction in the complexes $C_6F_6{\cdot}X^-$ has also been collected by Hiraoka et al. [4]; see also Section 4.3b.

Information on the bonding in the perfluorobenzene complexes $C_6F_5Y{\cdot}Cl^-$ and $C_6F_5Y{\cdot}Br^-$ can be gained from substituent effect analysis as described in Section 4.3b, using the bond free energy values given in Table 4.1.

$$-\delta\Delta G^{o}_{XA,423K} = \rho_R\sigma_R + \rho_F\sigma_F \qquad (4.12)$$

Plots of the experimentally determined $-\delta\Delta G^{o}_{XA,423K}$ (X = Cl and Br) versus $-\delta\Delta G^{o}_{XA,423K}$ calculated from equation (4.12) with best fit parameters are shown in Figures 4.22 and 4.23. Fair straight line relationships are observed in both plots: $r = 0.958$ for $C_6F_5Y{\cdot}Cl^-$ bond free energies (Figure 4.22), $r = 0.934$ for $C_6F_5Y{\cdot}Br^-$ bond free energies (Figure 4.23). The small magnitude of the $-\delta\Delta G^{o}_{XA,423K}$ values is possibly responsible for the lower level of correlation than observed in previous analyses; see Chapters 2 and 3. σ acceptor, π donor substituents (Y = F and Cl) were included in the plots as little charge transfer is anticipated in the $C_6F_5Y{\cdot}X^-$ complexes.

The ρ_R and ρ_F values from best fit regression analysis of equation (4.12) are shown in Table 4.3. Inclusion of the polarizability term (P) improved the fit very little and had only a small effect on the ρ_R and ρ_F values. The resonance ($R = \rho_R\sigma_R$) and field effect ($F = \rho_F\sigma_F$) contributions to $-\delta\Delta G^{o}_{XA,423K}$ are shown in Table 4.4. Examination of these data shows that the magnitudes of both R and F substituent effects in these complexes are small. Small R and F effects are

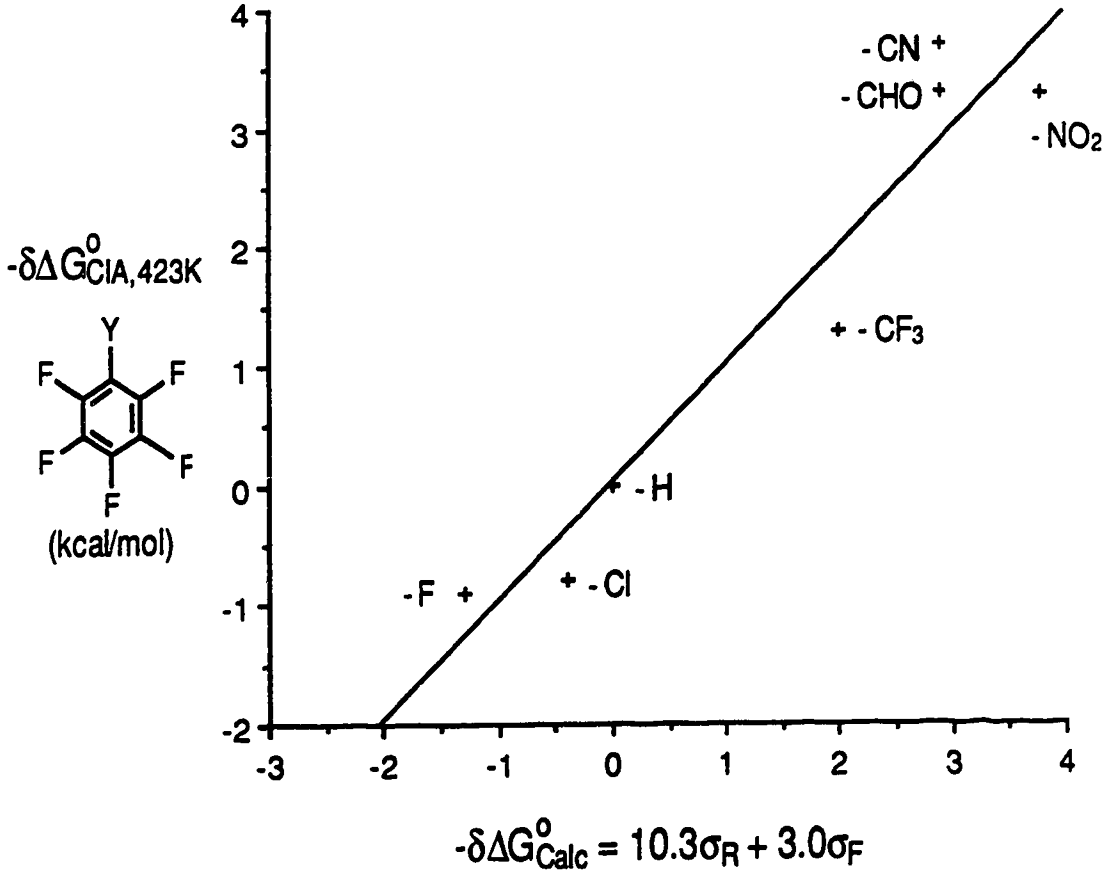

Figure 4.22 $-\delta\Delta G^{o}_{ClA,423K}$ for Cl^- bonding to the perfluorobenzenes, C_6F_5Y, versus $-\delta\Delta G^{o}_{Calc}$ calculated with Taft σ parameters, see equation (4.12). $-\delta\Delta G^{o}_{ClA,423K} = 0$ for Y = H. σ acceptor, π acceptor and σ acceptor, π donor substituents. Correlation coefficient r = 0.958.

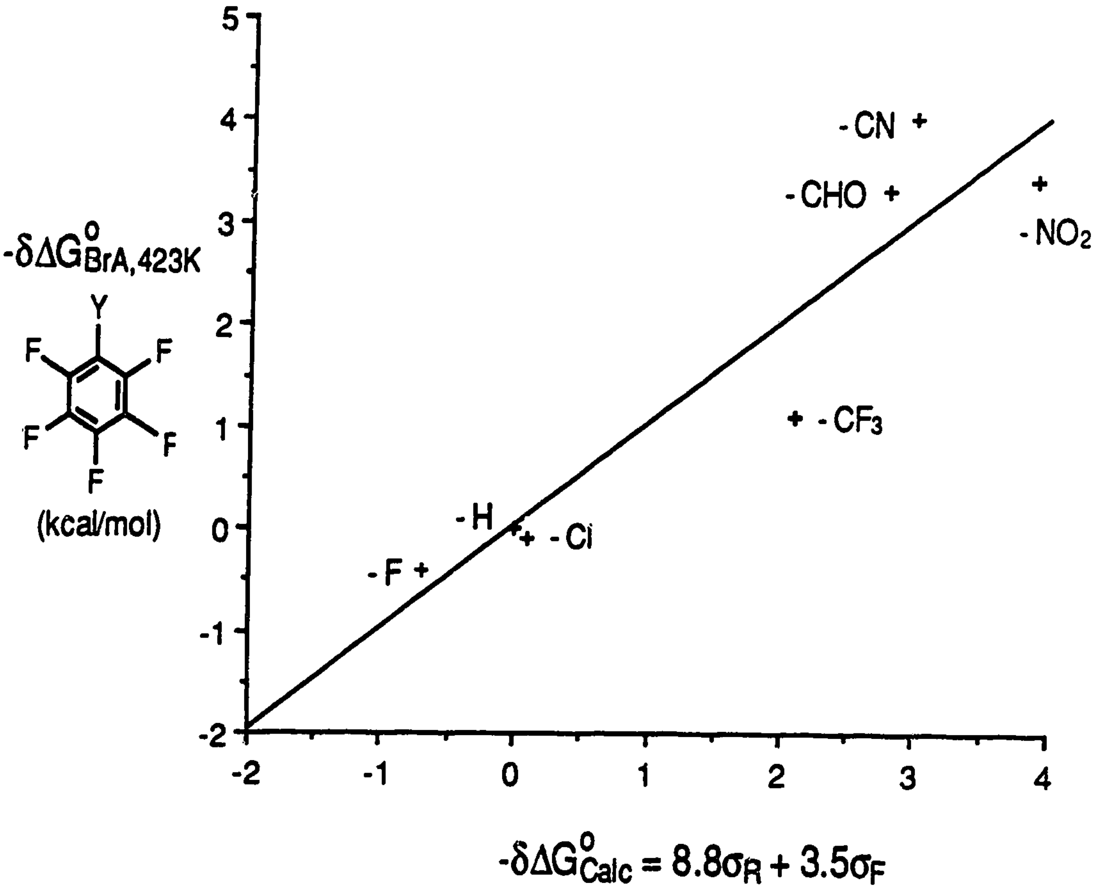

Figure 4.23 $-\delta\Delta G^{o}_{BrA,423K}$ for Br^- bonding to the perfluorobenzenes, C_6F_5Y, versus $-\delta\Delta G^{o}_{Calc}$ calculated with Taft σ parameters, see equation (4.12). $-\delta\Delta G^{o}_{BrA,423K} = 0$ for Y = H. σ acceptor, π acceptor and σ acceptor, π donor substituents. Correlation coefficient $r = 0.934$.

consistent with axial $C_6F_5Y{\cdot}X^-$ geometries (X^- = Cl^- and Br^-), analogous to those predicted for $C_6F_6{\cdot}X^-$ [4], see structure V in introduction.

A small R substituent effect is expected for the axial $C_6F_5Y{\cdot}X^-$ complexes as charge transfer into the C_6F_5Y ring is anticipated to be small. This is in contrast to the direct into the ring charge transfer by F^- on attack of the perfluorobenzene molecules. The difference in π charge stabilization by the substituent in $C_6F_5Y{\cdot}F^-$ and $C_6F_5Y{\cdot}X^-$ (X^- = Cl^- and Br^-) is clearly illustrated by the ρ_R values in Table 4.3: ρ_R ~33 for $C_6F_5Y{\cdot}F^-$, ρ_R ~10, ~9 for $C_6F_5Y{\cdot}Cl^-$, $C_6F_5Y{\cdot}Br^-$.

A small substituent F effect is also anticipated for the axial $C_6F_5Y{\cdot}X^-$ complexes. The electrostatic bonding in the axial $C_6F_5Y{\cdot}X^-$ complexes is probably due to an interaction of negative charge on X^- with the expected positive quadrupole moment of C_6F_5Y perpendicular to the molecular plane. The positive quadrupole moment of C_6F_5Y is most likely due to the C^+-F^- and C^+-Y^- bond dipoles where the major contribution to Q_{zz} is from the five C-F bond dipoles. Hence, the change in Q_{zz} with different Y substituents is anticipated to be small and result in only a small F effect for the axial $C_6F_5Y{\cdot}X^-$ complexes, as observed in Table 4.4. The remoteness of the negative charge in axial $C_6F_5Y{\cdot}X^-$ complexes also contributes to the very small ρ_F values observed in Table 4.3: ρ_F ~3, ~4 for $C_6F_5Y{\cdot}Cl^-$, $C_6F_5Y{\cdot}Br^-$.

The strongest substituent effect observed for the complexes $C_6F_5Y{\cdot}X^-$ (X^- = Cl^- and Br^-) occurs when the substituent contains protic hydrogens, i.e., $CONH_2$, OH and NH_2; see Table 4.1. The presence of five electron withdrawing fluorine atoms on the benzene ring increases the protic character of the substituent protons and results in a hydrogen bonded interaction being favored in these complexes. The relatively strong $-\delta\Delta G^{o}_{B/A,423K}$ values for $C_6F_5CONH_2$ (11.0 kcal/mol), C_6F_5OH (10.7 kcal/mol) and $C_6F_5NH_2$ (5.3 kcal/mol) relative to pentafluorobenzene (Table 4.1) would not be anticipated if electrostatic or σ bonding were present in these complexes, i.e., OH and NH_2 are strong π destabilizers. Comparing the bond free energies in $C_6F_5OH{\cdot}Br^-$ and $C_6F_5NH_2{\cdot}Br^-$ (Table 4.1) with those in $C_6H_5OH{\cdot}Br^-$ and $C_6H_5NH_2{\cdot}Br^-$ (Table 3.1), an increase in hydrogen bond strength of 4.4 and 4.8 kcal/mol respectively is observed upon fluorine substitution of the benzene ring.

REFERENCES

1. M. A. French, S. Ikuta and P. Kebarle, Can. J. Chem., 60, 1907 (1982).
2. G. Paul, K. Hirao, S. Obata and P. Kebarle, in preparation.
3. K. Hiraoka, S. Misuze and S. Yamabe, J. Chem. Phys., 86, 4102 (1987).
4. K. Hiraoka, S. Misuze and S. Yamabe, J. Phys. Chem., 91, 5294 (1987).
5. C. J. Jackson and F. H. Gazzolo, J. Am. Chem. Soc., 23, 376 (1900).
6. J. Meisenheimer, Justus Liebigs Ann. Chem., 323, 205 (1902).
7. J. F. Bunnett and R. E. Zahler, Chem Rev., 49, 273 (1951).
8. H. Ueda, N. Sakabe, J. Tanaka and A. Furusaki, Nature, 215, 956 (1967).
9. M. J. Strauss, Chem Rev., 70, 667 (1970).
10. G. A. Artamkina, M. P. Egorov and I. P. Beletskaya, Chem. Rev., 82, 427 (1982).
11. E. F. Caldin and G. Long, Proc. R. Soc. London, Ser. A, 226, 263 (1955).
12. F. Terrier, Chem. Rev., 82, 77 (1982).
13. G. Illuminati and F. Stegel, Adv. Hetero. Chem., 34, 305 (1983).
14. S. M. J. Briscese and J. M. Riveros, J. Am. Chem. Soc., 97, 230 (1975).
15. R. Squires and S. T. Graul, J. Am. Chem. Soc., 111, 892 (1989).
16. S. Ingemann, N. M. M. Nibbering, S. A. Sullivan and C. H. Depuy, J. Am. Chem. Soc., 104, 6520 (1982).
17. S. Ingemann and N. M. M. Nibbering, Nouv. J. Chem., 8, 299 (1984).
18. J. C. Kleingeld and N. M. M. Nibbering, Tetrahedron Lett., 21, 1687 (1980).
19. J. Miller, "Aromatic Nucleophilic Substitution". Elsevier. Amsterdam (1968).
20. K. C. Ho and J. Miller, Aust. J. Chem., 19, 423 (1966).
21. G. W. Dillow and P. Kebarle, J. Am. Chem. Soc., 110, 4877 (1988).

22. K. Hiraoka, S. Misuze and S. Yamabe, J. Chem. Phys., 86, 4102 (1987).

23. J. W. Larson and T. B. McMahon, J. Am. Chem. Soc., 105, 2944 (1983).

24. G. W. Dillow and P. Kebarle, J. Am. Chem. Soc., 111, 5592 (1989).

25. S. Chowdhury, E. P. Grimsrud, T. Heinis and P. Kebarle, J. Am. Chem. Soc., 108, 3630 (1986).

26. G. R. Nichol, Ph.D. Thesis, University of Alberta (1988).

27. R. C. Dougherty, J. D. Roberts and F. J. Biros, Anal. Chem., 47, 53 (1975).

28. R. C. Dougherty, J. Dalton and F. J. Biros, Org. Mass Spec., 6, 1171 (1972).

29. I. Dzidic, D. I. Carroll, R. N. Stillwell and E. C. Horning, Anal. Chem., 47, 1308 (1975).

30. S. Chowdhury, G. Nicol and P. Kebarle, Chem. Phys. Letters, 127, 130 (1986).

31. J. Burdon, Tetrahedron, 21, 3373 (1965).

32. J. Burdon and I. W. Parsons, J. Am. Chem. Soc., 99, 7445 (1977).

33. S. Chowdhury and P. Kebarle, J. Chem. Phys., 85, 4989 (1986).

34. S. G. Lias, J. E. Bartmess, J. F. Liebman, J. L. Holmes, R. D. Levin, and W. G. Mallard, J. Phys. Chem. Ref. Data, 17, Suppl. No. 1 (1988).

35. M. R. Battaglia, A. D. Buckingham and J. H. Williams, Chem. Phys. Lett., 78, 421 (1981).

36. R. W. Taft and R. D. Topsom, Prog. Phys. Org. Chem., 16, 1 (1987).

37. A. J. Birch, A. L. Hinde and L. Radom, J. Am. Chem. Soc., 102, 6430 (1980).

38. T. D. Gierke, H. L. Tigelaar and W. H. Flygare, J. Am. Chem. Soc., 94, 330 (1972).

CHAPTER 5

STABILITIES OF COMPLEXES OF SUBSTITUTED QUINONES (SQ) AND ETHYLENES (SE) WITH HALIDE ANIONS X^- (F^-, Cl^- AND Br^-)

5.1 Introduction

In Chapter 4 substituent effect analysis of experimentally determined bond free energies suggested different modes of interaction are present in the perfluorobenzene complexes $C_6F_5Y{\cdot}X^-$ where X^- are the halide ions F^-, Cl^-, Br^- and I^-. The strong nucleophile F^- is predicted to bond covalently to C_6F_5Y while an electrostatic interaction is preferred in the complexes $C_6F_5Y{\cdot}X^-$ ($X^- = Cl^-$, Br^- and I^-). Ab initio MO calculations [1] support these proposed geometries.

In the present work the modes of bonding in the complexes $SQ{\cdot}X^-$ and $SE{\cdot}X^-$ ($X^- = F^-$, Cl^- and Br^-) are investigated, where SQ and SE are quinones and ethylenes substituted with strong electron withdrawing groups, e.g., tetrafluoro-para-benzoquinone (F_4-p-BQ), tetrachloro-para-benzoquinone (Cl_4-p-BQ), tetrachloro-ortho-benzoquinone (Cl_4-o-BQ), tetracyanoethylene (TCNE).

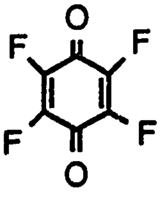
F_4-p-BQ

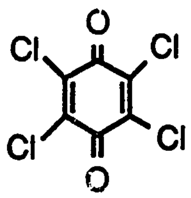
Cl_4-p-BQ

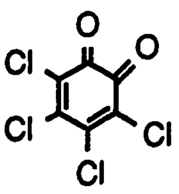
Cl_4-o-BQ

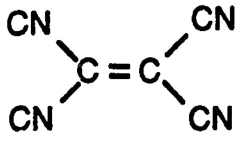
TCNE

These π conjugated systems were chosen as they are strong electron acceptors, i.e., have large electron affinities [2, 3], and may stabilize σ bond formation on attack by the weaker halide nucleophiles ($X^- = Cl^-$ and Br^-). σ bonding has been proposed in the complexes $TCNE{\cdot}X^-$ ($X^- = Cl^-$, Br^- and I^-) based on gas phase work performed with an ICR (ion cyclotron resonance) mass spectrometer [4]. The complexes F_4-p-BQ·X^-, Cl_4-p-BQ·X^- and TCNE·X^- (X^- = Cl^-, Br^- and I^-) have also been observed in the solution phase [5-8].

The bond strengths in the complexes SQ·X^- and SE·X^- (X^- = F^-, Cl^- and Br^-) were determined in the present work by gas phase measurements of halide association and transfer equilibria with the pulsed electron high pressure mass spectrometer (PHPMS). Hirao et al. [9] have also performed ab initio MO calculations on the systems TCNE·X^- (X^- = F^-, Cl^- and Br^-) and F_4-p-BQ·X^- (X^- = Cl^- and Br^-) where complex geometries and stabilization energies were determined. The chemical bonding in SQ·X^- and SE·X^- is discussed on the grounds of these theoretical and experimental determinations.

5.2 Experimental

$$SQ + X^- = SQ{\cdot}X^- \tag{5.1}$$

$$SE + X^- = SE{\cdot}X^- \tag{5.2}$$

Association equilibria (5.1) and (5.2) involving substituted quinones and ethylenes with X^- (X^- = Cl^- and Br^-) were measured with the PHPMS described in Chapter 1. The method of equilibrium measurement was as described in Chapter 2.

The majority of the solid compounds used were dissolved in dimethylformamide (DMF) prior to injection into the 5 l bulb of the gas handling plant (GHP). Tetracyanoethylene (TCNE) and fumaronitrile (trans-1,2-dicyanoethylene) were found to dissolve only in acetonitrile and toluene, respectively. As TCNE is reported to have a low vapor pressure [10, 11], a gas handling plant temperature of 200°C was maintained for equilibrium measurements involving this compound (GHP typically at temperature of ~150°C).

Br^- and Cl^- production in the ion source was achieved by dissociative electron capture of CH_2Br_2 and CCl_4, respectively. These compounds were present in concentrations of 1-5 mtorr in the ion source. Methane at ion source pressures of 2-4 torr was used as the bath gas. Reactant (SQ, SE) concentrations in the ion source ranged from 0.1-20 mtorr.

The majority of the bond free energy determinations were conducted at 150°C. Association equilibrium (5.1) measurements involving the weakly bound para-benzoquinone·Br^- (p-BQ·Br^-) adduct were performed at 30°C. Measurements of association equilibria (5.2) involving TCNE were not possible at 150°C due to the large bond strength of TCNE·X^- (X^- = Cl^- and Br^-). In these experiments, the X^- intensity was too small for reliable equilibrium measurement.

$$C_6F_5OH{\cdot}Br^- + TCNE = C_6F_5OH + TCNE{\cdot}Br^- \qquad (5.3)$$

The bond free energy of TCNE·Br^- at 150°C was obtained indirectly by measurement of bromide transfer equilibrium (5.3); see Figure 4.13. The directly determined value of $-\Delta G^o_{BrA,423K}(C_6F_5OH)$ is also given in Figure 4.13. The bond free energy of TCNE·Cl^- could not be determined either directly or indirectly at 150°C due to the large bond strength of the complex. $-\Delta G^o_{ClA,423K}(TCNE)$ was evaluated using $-\Delta H^o_{ClA}$ and $-\Delta S^o_{ClA}$ values obtained from a van't Hoff plot (see later) where equilibrium constants for reaction (5.2) involving TCNE were determined at higher ion source temperatures (~250-350°C).

An intensity versus time profile of ions involved in reaction (5.1) is shown in Figure 5.1. Thermodynamic equilibrium is established between the adduct F_4-p-BQ·Br^- and Br^- ~1.0 ms after the 20 µs electron pulse. An ion extraneous to the equilibrium studied was the radical anion F_4-p-BQ$^-$. The decrease in

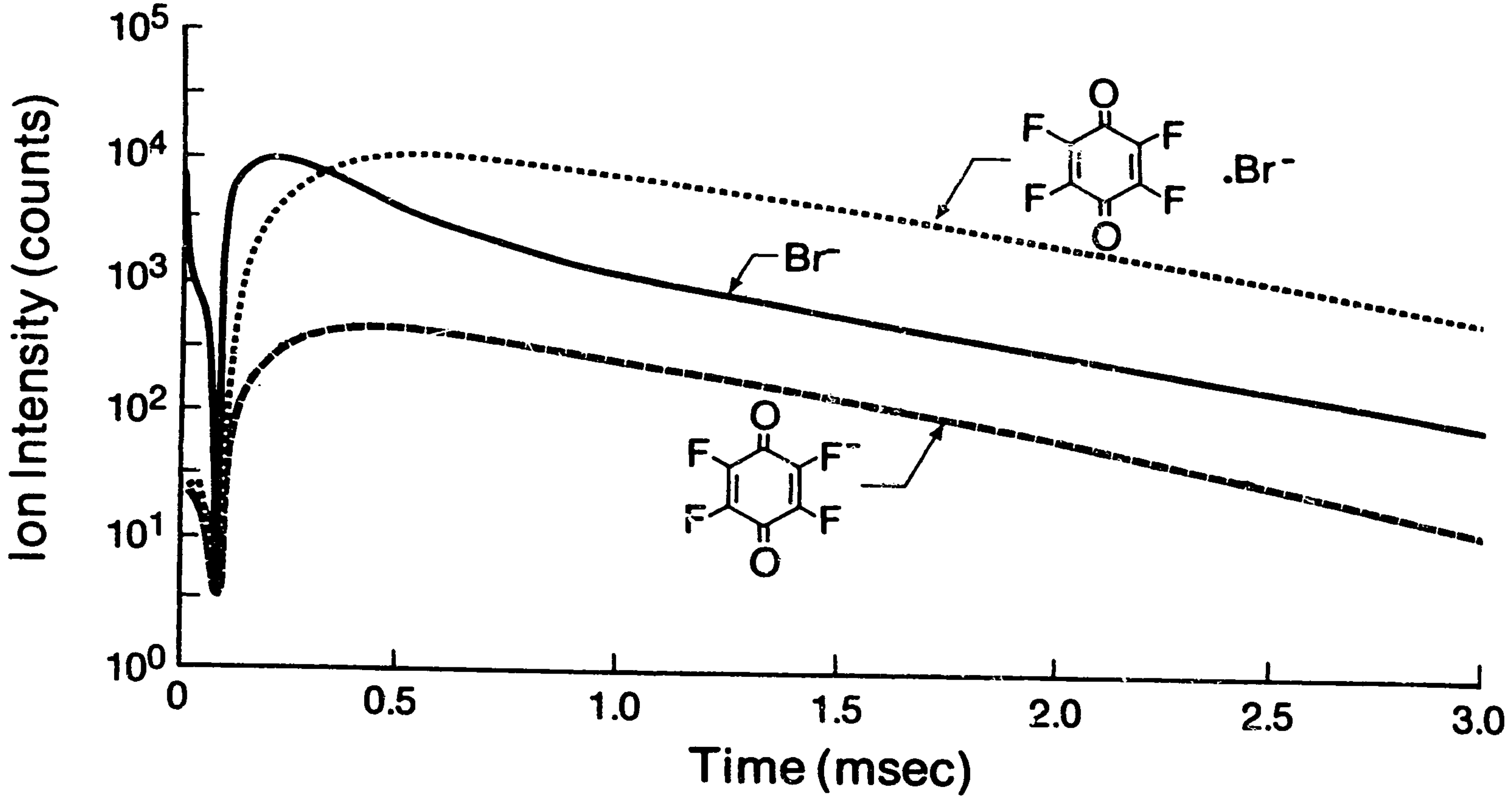

Figure 5.1 Raw data plot: ion intensity versus time after a 20 μs ionizing electron pulse. Obtained with a gas mixture of 2.65 torr CH_4, 0.25 mtorr F_4-p-BQ and 3.9 mtorr CH_2Br_2 at 423 K. The Br^- attachment equilibrium: F_4-p-BQ + Br^- = $F_4BQ{\cdot}Br^-$, becomes established ~1 ms after the electron pulse. The radical anion F_4BQ^- is also present in the plot.

intensity of the three ions after ~0.5 ms is due to diffusion of the ions to the ion source wall.

Checks were performed on the equilibrium constants for reactions (5.1) and (5.2) involving different partial pressures of SQ and SE. K_{BrA} and K_{ClA} were found to be essentially invariant of the partial pressure of SQ and SE for the strongly bound substituted quinone and ethylene complexes.

$$F_4\text{-p-BQ} + X^- = F_4\text{-p-BQ}\cdot X^- \qquad (5.4)$$

$$\text{TCNE} + X^- = \text{TCNE}\cdot X^- \qquad (5.5)$$

Enthalpy (ΔH^o_{XA}) and entropy (ΔS^o_{XA}) values for reactions (5.4) and (5.5) where X^- = Cl^- and Br^- were obtained by means of van't Hoff plots; see also Chapter 3. These plots are shown in Figure 5.2. K_{XA} values for reactions (5.4) and (5.5) were determined as the ion source temperature was slowly decreased for constant F_4-p-BQ/methane and TCNE/methane gas mixtures. This procedure was repeated for different F_4-p-BQ/methane and TCNE/methane gas mixtures where the ratios were changed by a factor of five. Measurements were performed at intervals of ~15°C with an overall range of ~100°C being covered. Equilibrium constants for reaction (5.5) were measured between 250°C and 350°C because of the large bond strengths of the complexes TCNE·Br^- and TCNE·Cl^-. The data for reaction (5.4) where X^- = Cl^- is from Chowdhury et al. [12].

5.3 Results and Discussion

5.3a Results

The directly and indirectly determined $-\Delta G^o_{BrA,423K}$ and $-\Delta G^o_{ClA,423K}$ values for the substituted quinones and ethylenes are given in Table 5.1. Also

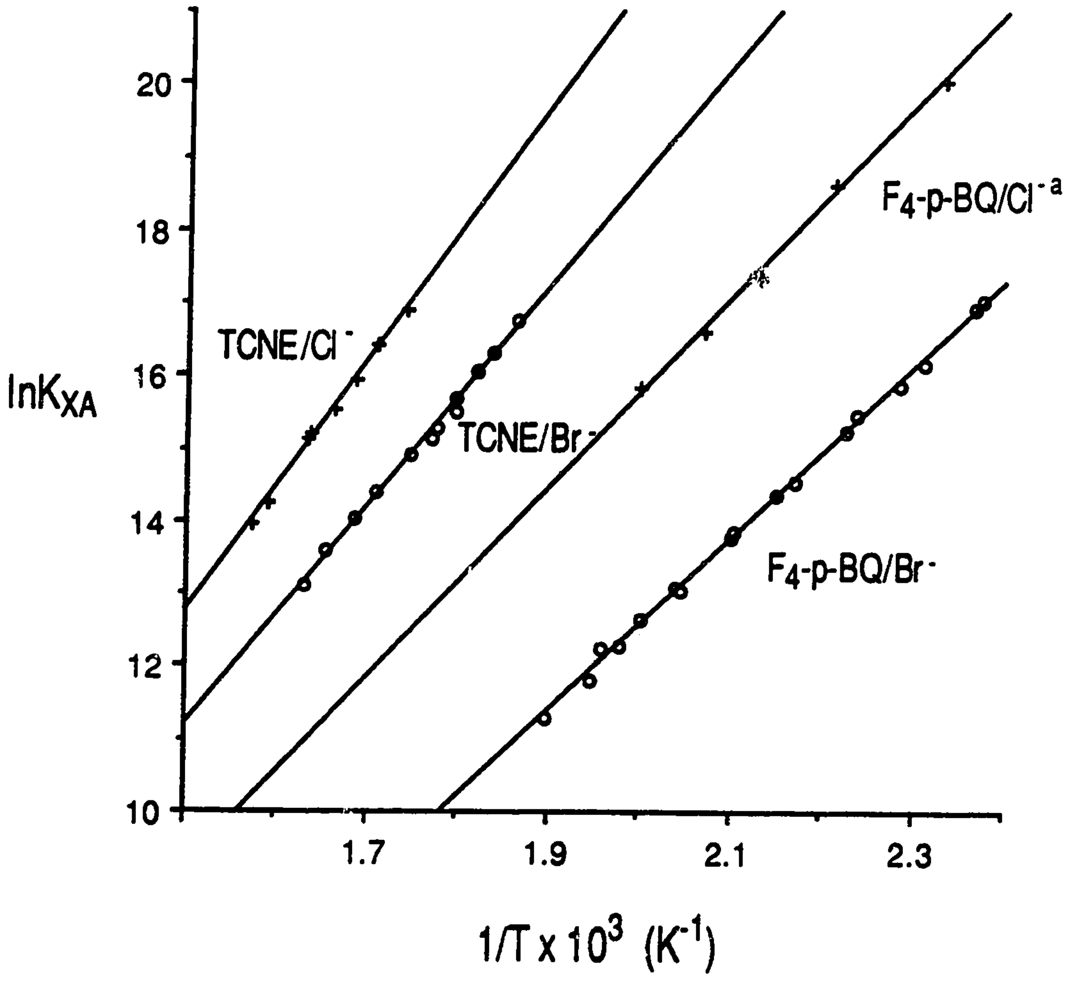

Figure 5.2 van't Hoff plots of K_{XA} for the reactions: TCNE + X^- = TCNE·X^- and F_4-p-BQ + X^- = F_4-p-BQ·X^- where X^- = Cl^-, Br^-. a) From Chowdhury et al. [12].

Table 5.1 $-\Delta G^{o}_{XA,423K}$ for reaction (5.1): $SQ + X^- = SQ{\cdot}X^-$ and reaction (5.2): $SE + X^- = SE{\cdot}X^-$, where SQ, SE are substituted quinones and ethylenes and $X^- = F^-, Cl^-, Br^-, I^-$

SQ/SE	$-\Delta G^{o}_{XA,423K}$ (kcal/mol)			
	F^-	Cl^-	Br^-	I^-
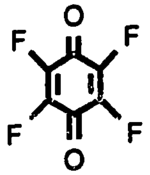	33.5^{b}	16.6^{a}	14.3^{a}	11.1^{c}
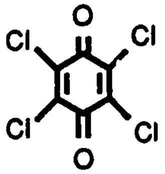			12.8^{a}	
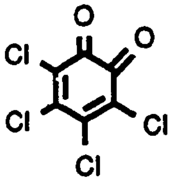			15.4^{a}	
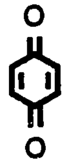		7.0^{d}	5.0^{e}	
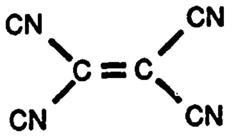		23.3^{f}	20.8^{g}	
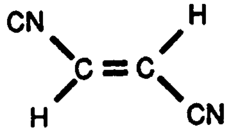		12.8^{a}	10.7^{a}	

---

a. From direct measurement of equilibrium (5.1) or (5.2) at 423 K. b. From $-\Delta G^{o}_{FTr,423K}$ measurements, see Figure 4.14. c. From direct measurement of equilibrium $F_4\text{-p-BQ} + I^- = F_4\text{-p-BQ}{\cdot}I^-$ at 423 K. d. From Chowdhury et al. [12]. Equilibrium (5.1) measured at 303 K. $-\Delta G^{o}_{ClA,423K}$(p-BQ) estimated using $-\Delta S^{o}_{ClA}$(p-BQ) = 20.0 cal/deg.mol. e. Equilibrium (5.1) measured at 303 K. $-\Delta G^{o}_{BrA,423K}$(p-BQ) estimated using $-\Delta S^{o}_{BrA}$(p-BQ) = 20.0 cal/deg.mol. f. From $-\Delta H^{o}_{ClA}$(TCNE) and $-\Delta S^{o}_{ClA}$(TCNE) values, Table 5.2. g. Indirectly determined at 423 K by measurement of bromide transfer equilibrium (5.3), see Figure 4.13.

included in Table 5.1 are the bond free energies at 423 K for F_4-p-BQ·F^- (Figure 4.14) and F_4-p-BQ·I^- which were determined by methods described in Chapter 4.

The bond enthalpy ($-\Delta H^{o}_{XA}$) and entropy ($-\Delta S^{o}_{XA}$) values corresponding to reactions (5.4) and (5.5) where X^- = Cl^- and Br^- are given in Table 5.2. Also present in Table 5.2 are the $-\Delta G^{o}_{XA,423K}$ values evaluated from $-\Delta H^{o}_{XA}$ and $-\Delta S^{o}_{XA}$. These values are in good agreement with those values given in Table 5.1.

5.3b Bonding in the Complexes SQ·X^- where SQ = Substituted Quinones and X^- = F^-, Cl^- and Br^-

The geometries and bond strengths of the complexes F_4-p-BQ·X^- (X^- = Cl^- and Br^-) and TCNE·X^- (X^- = F^-, Cl^- and Br^-) were determined by Hirao et al. [9] using ab initio MO calculations. Each geometry was fully optimized with the minimal STO-3G basis set. Then a single-point calculation was carried out with the 3-21G plus diffuse functions basis set to obtain the energy at the optimized geometry. Diffuse functions are well known to be important for describing the electronic structure of anions, particularly with first row elements [13].

The optimized geometries of F_4-p-BQ and the complexes F_4-p-BQ·X^- (X^- = Cl^- and Br^-) are shown in Figures 5.3-5.8. Bond distances (in angstroms) and bond angles (in degrees) are given and the values in parenthases are the Mulliken electron populations (electron densities). The calculated stabilization energy, $-\Delta E^{o}_{XA}$ ($\approx -\Delta H^{o}_{XA}$), on complex formation, i.e, the bond strength, is also given. These values are summarized in Table 5.3. Also present in Table 5.3 are the experimentally determined complex bond strengths, $-\Delta H^{o}_{XA}$.

There are two active sites for X^- attack of F_4-p-BQ to yield a σ bonded (Meisenheimer) complex. One is at the carbon atom connected to oxygen

Table 5.2 Thermochemical data for reaction (5.4): F_4-p-BQ + X^- = F_4-p-BQ·X^- and reaction (5.5): TCNE + X^- = TCNE·X^- (X^- = Cl^-, Br^-), obtained via van't Hoff plots (Figure 5.2)[a]

	X^-	$-\Delta H^{o}_{XA}$ (kcal/mol)	$-\Delta S^{o}_{XA}$ (cal/deg.mol)	$-\Delta G^{o}_{XA,423K}$[c] (kcal/mol)
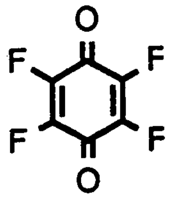	Br^-	23.6	22.3	14.2
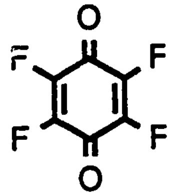	Cl^-	27.0[b]	22.7[b]	17.4[b]
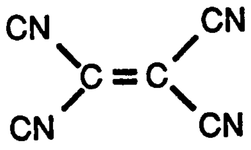	Br^-	30.1	22.9	20.4
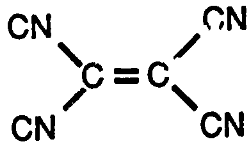	Cl^-	34.4	26.3	23.3

---

a. The errors are estimated at ±2 kcal/mol for $-\Delta H^{o}_{BrA}$ and ±3 cal/deg.mol for $-\Delta S^{o}_{BrA}$.

b. From Chowdhury et al. [12].

c. $-\Delta G^{o}_{XA,423K}$ calculated from $-\Delta H^{o}_{XA}$ and $-\Delta S^{o}_{XA}$ values in the table.

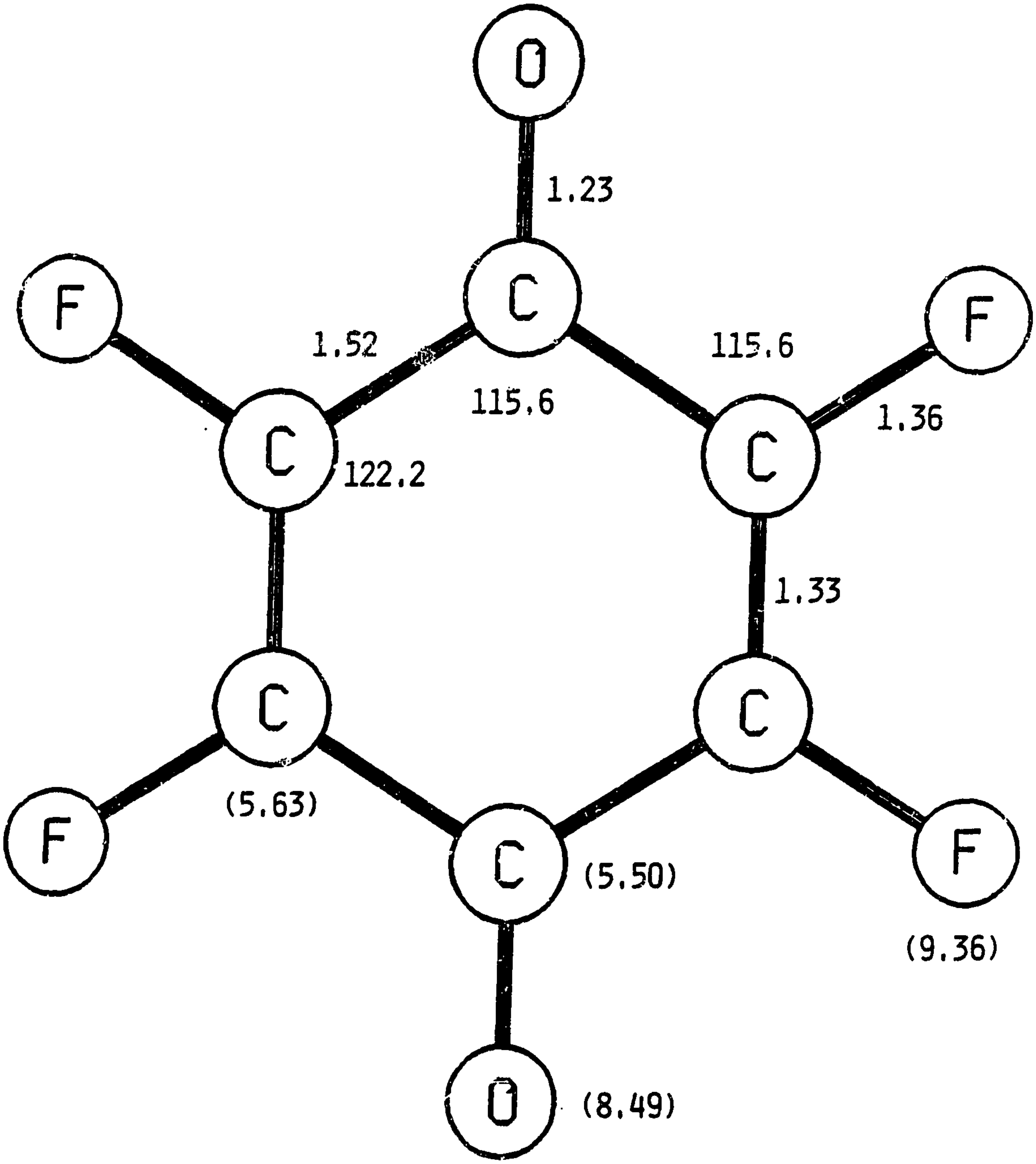
O
1.23
C
F
F
1.52
115.6
115.6
C
C
1.36
122.2
1.33
C
C
F
(5.63)
F
C
(5.50)
(9.36)
O
(8.49)

Figure 5.3 Optimized geometry of F_4-p-BQ due to Hirao et al. [9]. The values in parentheses are electron densities. The bond lengths are in angstroms and the bond angles are in degrees.

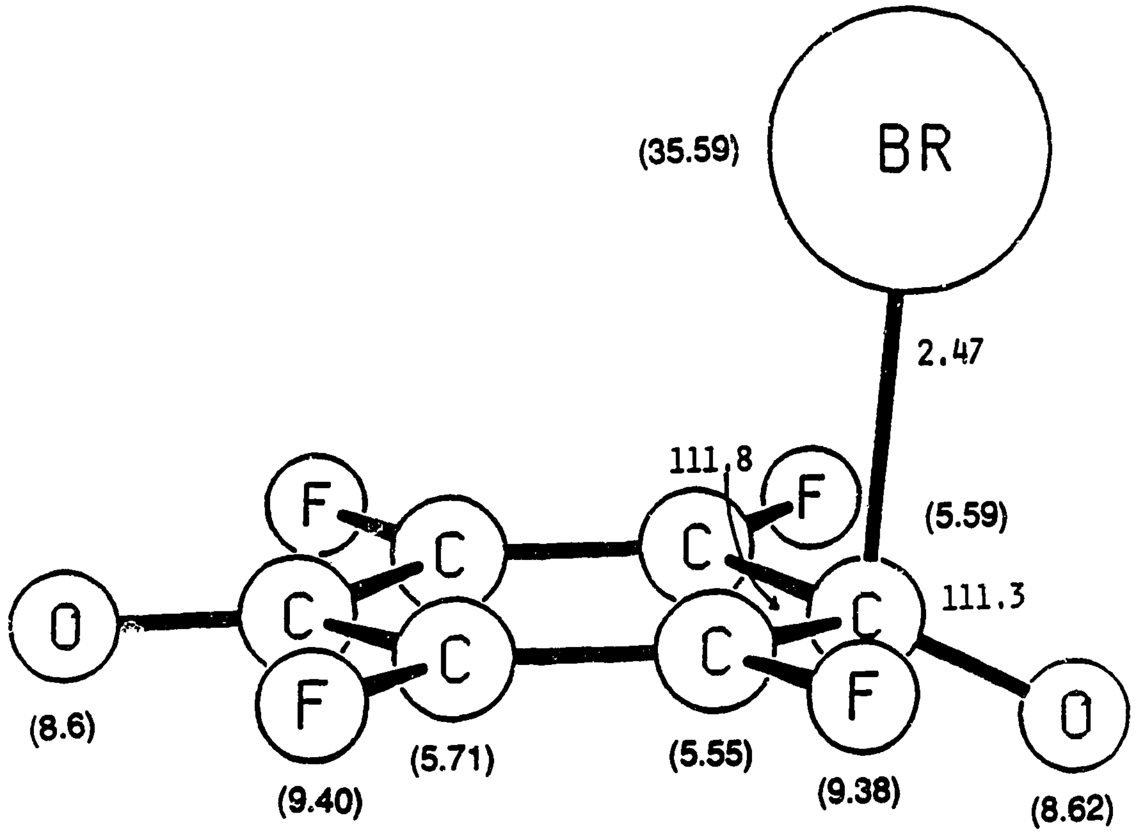
(35.59)
BR
2.47
111.8
F
F
(5.59)
C
C
O
C
C
111.3
C
C
F
F
O
(8.6)
(5.71)
(5.55)
(9.40)
(9.38)
(8.62)

$$-\Delta E^{o}_{BrA} = 16.0 \text{ kcal/mol}$$

Figure 5.4 Optimized geometry of the F_4-p-BQ·Br^- partial charge transfer complex due to Hirao et al. [9]. The values in parentheses are electron densities. The bond lengths are in angstroms and the bond angles are in degrees.

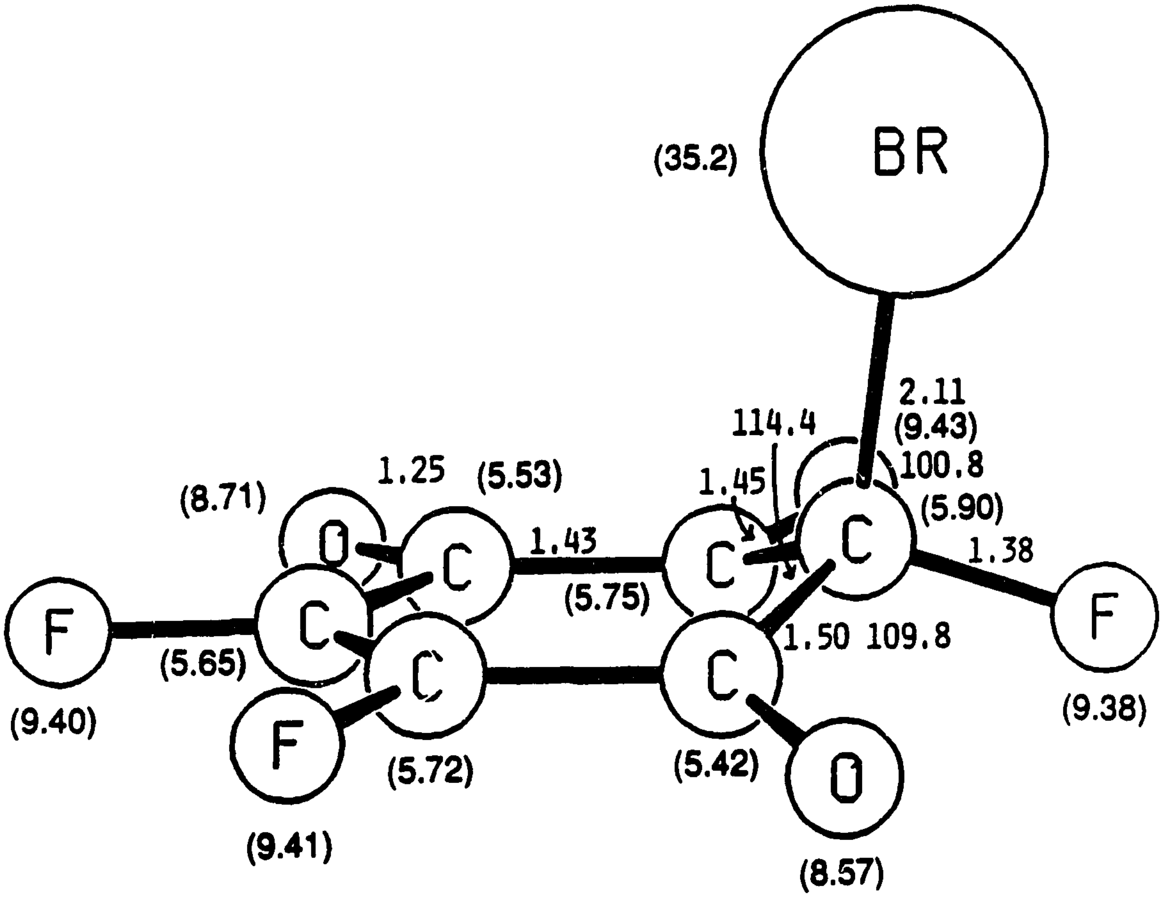

(35.2)
BR
2.11
(9.43)
114.4
100.8
(5.90)
(8.71)
1.25
(5.53)
1.45
O
C
1.43
C
C
1.38
F
C
(5.75)
1.50
109.8
F
C
(5.65)
C
C
(9.38)
(9.40)
F
(5.72)
(5.42)
O
(9.41)
(8.57)

$$-\Delta E^{0}_{BrA} = 6.6 \text{ kcal/mol}$$

Figure 5.5 Optimized geometry of the F_4-p-BQ·Br^- Meisenheimer complex due to Hirao et al. [9]. The values in parentheses are electron densities. The bond lengths are in angstroms and the bond angles are in degrees.

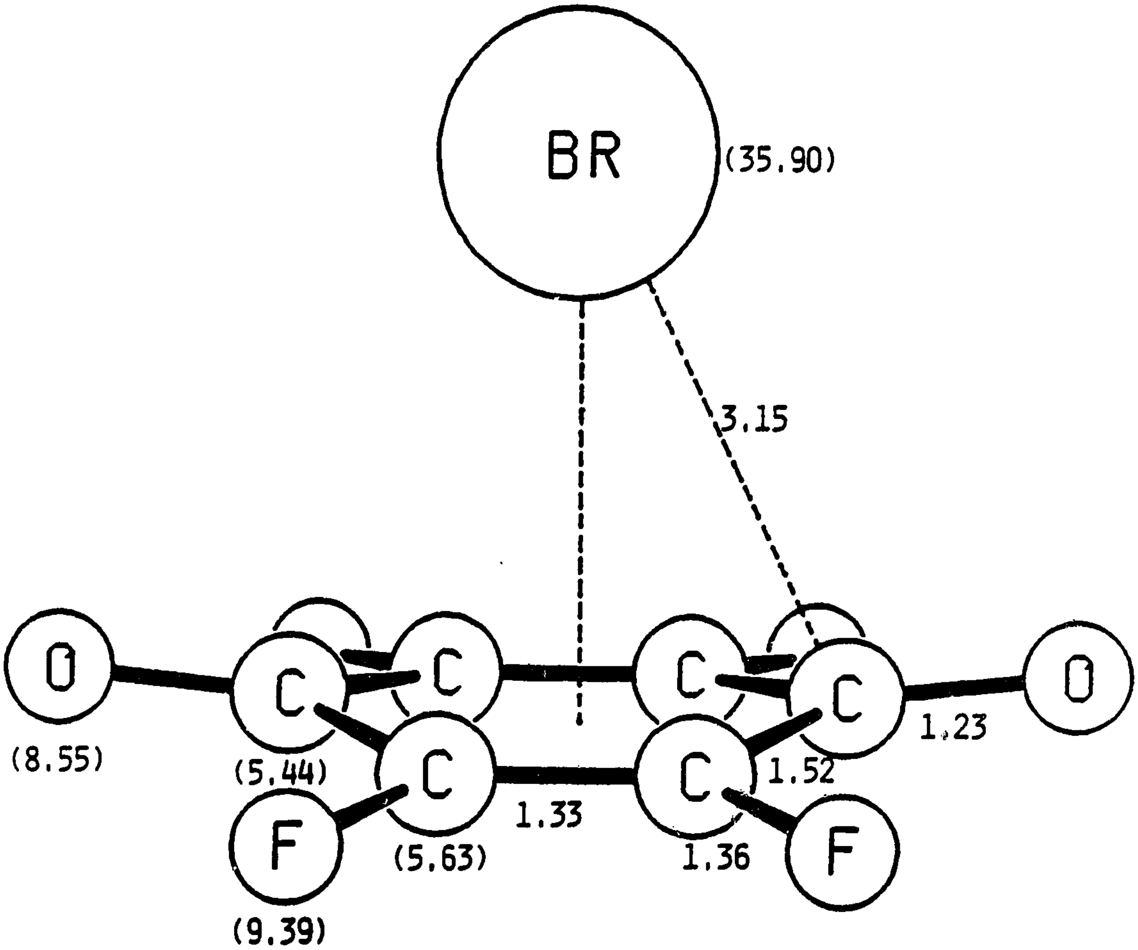
BR
(35.90)
3.15
O
(8.55)
C
C
(5.44)
C
F
(9.39)
(5.63)
1.33
C
C
C
1.52
1.36
F
1.23
O

$-\Delta E^{o}_{BrA} = 15.3$ kcal/mol

Figure 5.6 Optimized geometry of the F_4-p-BQ·Br^- electrostatic complex due to Hirao et al. [9]. The values in parentheses are electron densities. The bond lengths are in angstroms and the bond angles are in degrees.

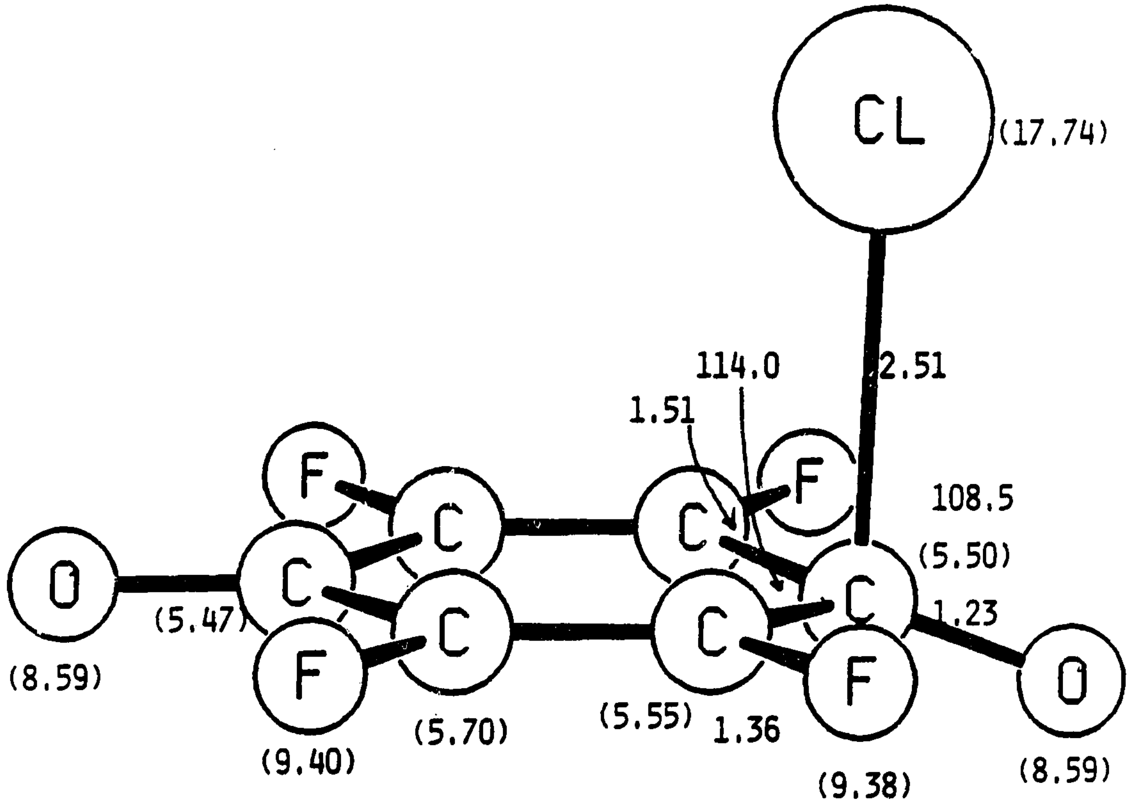
CL
(17.74)
2.51
114.0
1.51
F
108.5
(5.50)
1.23
O
(8.59)
C
C
C
C
C
C
F
F
F
O
(8.59)
(5.47)
(9.40)
(5.70)
(5.55)
1.36
(9.38)
(8.59)

$$-\Delta E^{o}_{ClA} = 26.3 \text{ kcal/mol}$$

Figure 5.7 Optimized geometry of the F_4-p-BQ·Cl^- partial charge transfer complex due to Hirao et al. [9]. The values in parentheses are electron densities. The bond lengths are in angstroms and the bond angles are in degrees.

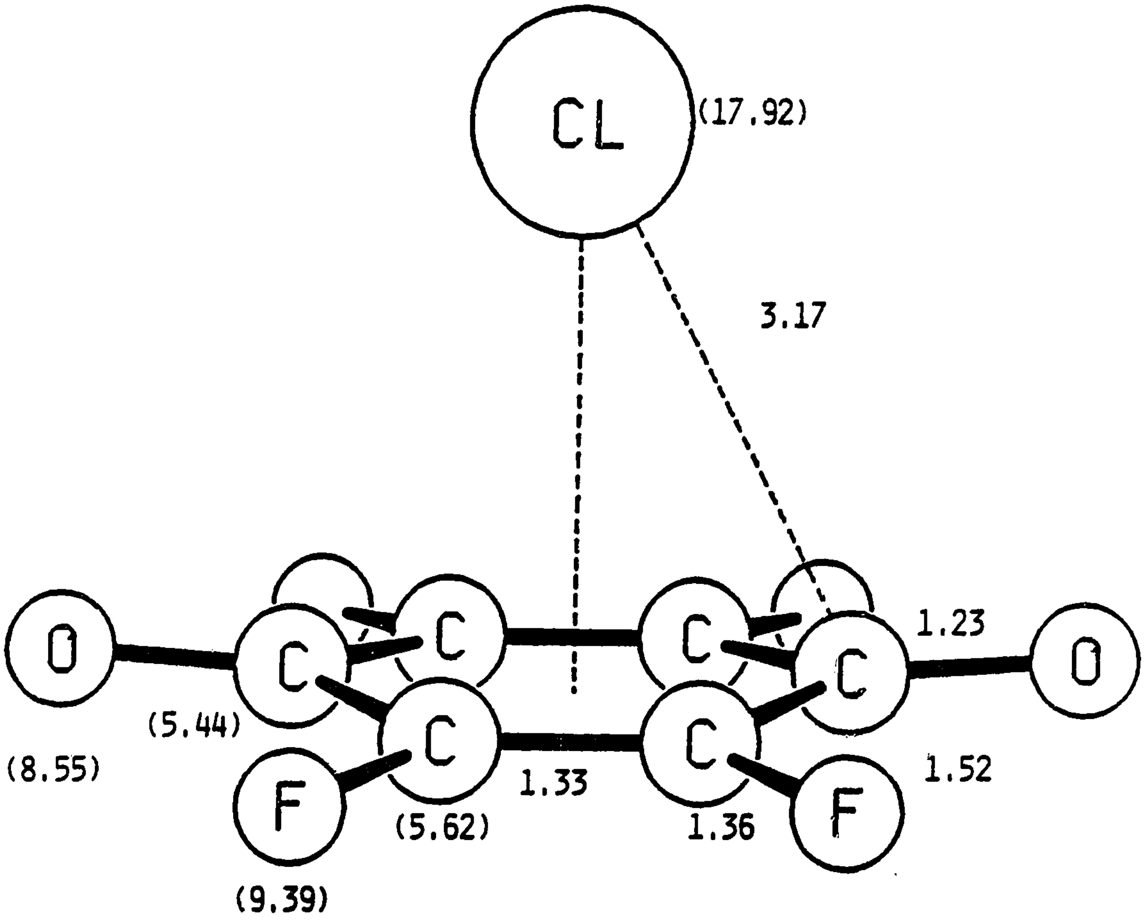
CL
(17.92)
3.17
O
C
C
C
C
C
C
O
F
F
1.23
(5.44)
(8.55)
1.33
1.52
(5.62)
1.36
(9.39)

$$-\Delta E^{o}_{ClA} = 24.8 \text{ kcal/mol}$$

Figure 5.8 Optimized geometry of the F_4-p-BQ·Cl^- electrostatic complex due to Hirao et al. [9]. The values in parentheses are electron densities. The bond lengths are in angstroms and the bond angles are in degrees.

Table 5.3 Bond strength determinations corresponding to reaction (5.4): F_4-p-BQ + X^- = F_4-p-BQ·X^- (X^- = Cl^-, Br^-) and reaction (5.5): TCNE + X^- = TCNE·X^- (X^- = F^-, Cl^-, Br^-)

	$-\Delta E^{o}_{XA}$[a] Meisenheimer Complex (kcal/mol)	$-\Delta E^{o}_{XA}$[a] Partial Charge Transfer Complex (cal/deg.mol)	$-\Delta E^{o}_{XA}$[a] Electrostatic Complex (kcal/mol)	$-\Delta H^{o}_{XA}$[b]
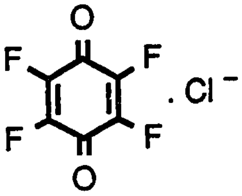		26.3 (Fig.5.7[c])	24.8 (Fig.5.8[c])	27.0
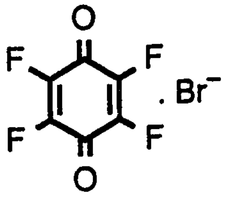	6.6 (Fig.5.5[c])	16.0 (Fig.5.4[c])	15.3 (Fig.5.6[c])	23.6
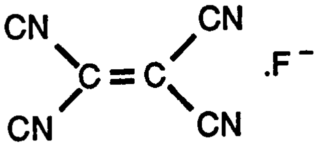	43.5 (Fig.5.10[c])			
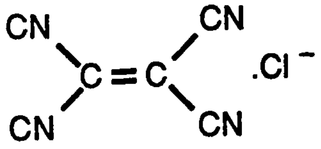	5.3 (Fig.5.11[c])		19.4 (Fig.5.12[c])	34.4
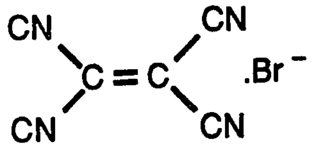	0.6 (Fig.5.13[c])		13.8 (Fig.5.14[c])	30.1

---

a. Bond strength determinations from ab initio MO calculations due to Hirao et al. [9]. b. Experimentally determined bond strengths, see Table 5.2. c. Figure number in parenthesis shows location in text of predicted complex geometry due to Hirao et al. [9].

(reaction (5.6)) and the other is at the carbon atom linked to fluorine (reaction (5.7)).

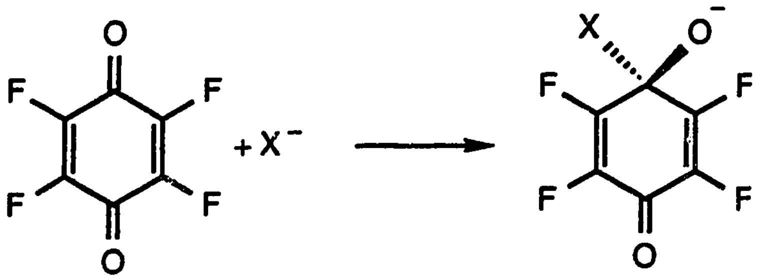
(5.6)

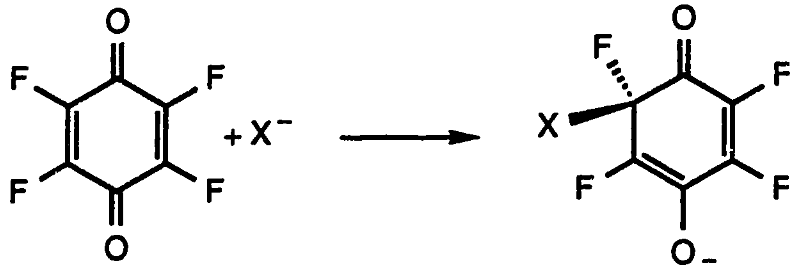
(5.7)

The electropositive character of the carbon atoms in the F_4-p-BQ ring (Figure 5.3) is due to the σ electron withdrawing (+F) fluorine and oxygen atoms [14]. The field/inductive effect of these substituents will in turn stabilize the negative charge on X^- upon Meisenheimer complex formation. π charge stabilization in the σ bonded F_4-p-BQ·X^- complexes is shown in reactions (5.6) and (5.7).

Br^- is predicted to attack both C=O and C-F sites and form charge transfer complexes (Figures 5.4 and 5.5). Attack of the C=O site ($-\Delta E^{o}_{BrA} = 16.0$ kcal/mol) is found to be more favorable than attack of the C-F site ($-\Delta E^{o}_{BrA} = 6.6$ kcal/mol). However, from the geometries and electron densities shown in Figures 5.4 and 5.5, the predicted degree of charge transfer in these complexes is different. On attack of C=O only partial charge transfer of the Br^- electron density occurs (Figure 5.4). Little deformation of the F_4-p-BQ ring is observed as a result of this interaction. Attack of C-F leads to σ bond formation (C-Br) with a tetrahedral Meisenheimer complex formed; see Figure 5.5. Comparison of the bond lengths and electron densities shown in Figure 5.3 (neutral F_4-p-BQ) and Figure 5.5 nicely illustrates the formation of a σ bonded complex which corresponds to the resonance structure shown in reaction (5.7). The weak bond energy determined for the Meisenheimer F_4-p-BQ·Br^- complex ($-\Delta E^o_{BrA}$ = 6.6 kcal/mol) is a consequence of the loss of π conjugation throughout F_4-p-BQ upon σ bond formation, i.e., energy destabilization due to ring deformation (Figure 5.5). The energy stabilization achieved through C-Br bond formation (C-Br bond energy ~70 kcal/mol [1]) counterbalances this effect. For the partial charge transfer F_4-p-BQ·Br^- complex (Figure 5.4) the magnitudes of both these effects are reduced and the presence of an ion-quadrupole electrostatic interaction leads to a stronger overall bond energy. Interestingly, σ bonded complex formation was found to be energetically unfavorable for C_6F_6·Br^- by the ab initio MO calculations of Hiraoka et al. (3-21G basis set) [1]. This suggests the contribution to stabilization of the Br^- electron density from π delocalization involving the carbonyl group (reaction (5.7)) is important for stable Meisenheimer F_4-p-BQ·Br^- complex formation. From previous gas phase electron affinity determinations [2, 15, 16], F_4-p-BQ is known to be a much better electron acceptor than C_6F_6, i.e, EA(F_4-p-BQ) is ~30 kcal/mol greater than EA(C_6F_6).

An electrostatic complex of comparable stability to the partial charge transfer complex (Table 5.3) was also predicted for F_4-p-BQ·Br^-. In the electrostatic complex Br^- is positioned on the central axis of F_4-p-BQ ~2.8 Å above the molecular plane (Figure 5.6). In this position Br^- is anticipated to experience a strong interaction with the expected positive quadrupole moment of F_4-p-BQ perpendicular to the molecular plane (Q_{zz}). The anticipated positive quadrupole moment of F_4-p-BQ is due to the C^+-F^- and C^+-O^- bond dipoles; see Figure 5.3. The geometry of the electrostatic F_4-p-BQ·Br^- complex is analogous to those predicted for the complexes $C_6F_6{\cdot}X^-$ (X^- = Cl^-, Br^- and I^-) [1]. The larger predicted charge distribution in C=O ($C^{+0.50}$--$O^{-0.50}$ [9]) opposed to C-F ($C^{+0.37}$--$O^{-0.37}$ [1, 9]) is possibly responsible for the closer intermolecular distance and stronger bond energy determined for F_4-p-BQ·Br^- compared to $C_6F_6{\cdot}Br^-$ ($-\Delta E^{o}_{BrA}(F_4\text{-p-BQ})$ = 15.3 kcal/mol [9], $-\Delta E^{o}_{BrA}(C_6F_6)$ = 13.9 kcal/mol [1]).

The experimentally determined $-\Delta H^{o}_{XA}$ for F_4-p-BQ·Br^- is observed in Table 5.3 to be ~8 kcal/mol greater than that predicted for the most favorable F_4-p-BQ·Br^- geometry, the partial charge transfer complex [9]. Basis set deficiency and the absence of an electron correlation correction may be responsible for the error in the theoretical bond strength determination.

The stable geometries of F_4-p-BQ·Cl^- [9] are shown in Figures 5.7 and 5.8. The partial charge transfer complex is again observed to be energetically slightly favored over the electrostatic complex (Table 5.3). Meisenheimer complex formation on attack of the fluorine carrying carbon atom was predicted to be energetically unfavorable. The calculated bond strength ($-\Delta E^{o}_{ClA}$) for the partial charge transfer complex is in excellent agreement with the experimentally determined $-\Delta H^{o}_{ClA}(F_4\text{-p-BQ})$ given in Table 5.3. The bond strength in F_4-p-BQ·Cl^- is determined to be greater than that in F_4-p-BQ·Br^- both by experiment and theoretical calculations. This increase in bond strength is because Cl^- is a stronger base than Br^- due to its smaller ionic radius.

From the bond free energy values given in Table 5.1, the stability order of the complexes F_4-p-BQ·X^- is F_4-p-BQ·F^- >> F_4-p-BQ·Cl^- > F_4-p-BQ·Br^- > F_4-p-BQ·I^-. This is the same order as observed for the complexes $C_6F_5Y{\cdot}X^-$ (Table 4.1). The large increase in stability of F_4-p-BQ·F^- (~20 kcal/mol) possibly results from σ bond formation. A strong Meisenheimer complex is anticipated for F_4-p-BQ·F^- as a stable σ bonded complex is predicted for F_4-p-BQ·Br^- (Figure 5.5) where the C-Br stabilization energy is ~46 kcal/mol lower than that on C-F formation, i.e., the bond energies of C-F and C-Br are ~116 kcal/mol and ~70 kcal/mol, respectively [1]. Attack by F^- of a C-F site in F_4-p-BQ (reaction (5.7)) may be preferred as a reaction of this type results in the only stable Meisenheimer complex predicted for F_4-p-BQ·Br^- (only partial charge transfer is predicted on Br^- attack of C=O). However, in solution phase studies the strong base OH^- has been proposed to add reversibly to the carbonyl group of a number of substituted quinones [17, 18]. For example, Tong et al. [17] proposed Scheme I for attack of OH^- on Cl_4-p-BQ on the basis of UV spectral data.

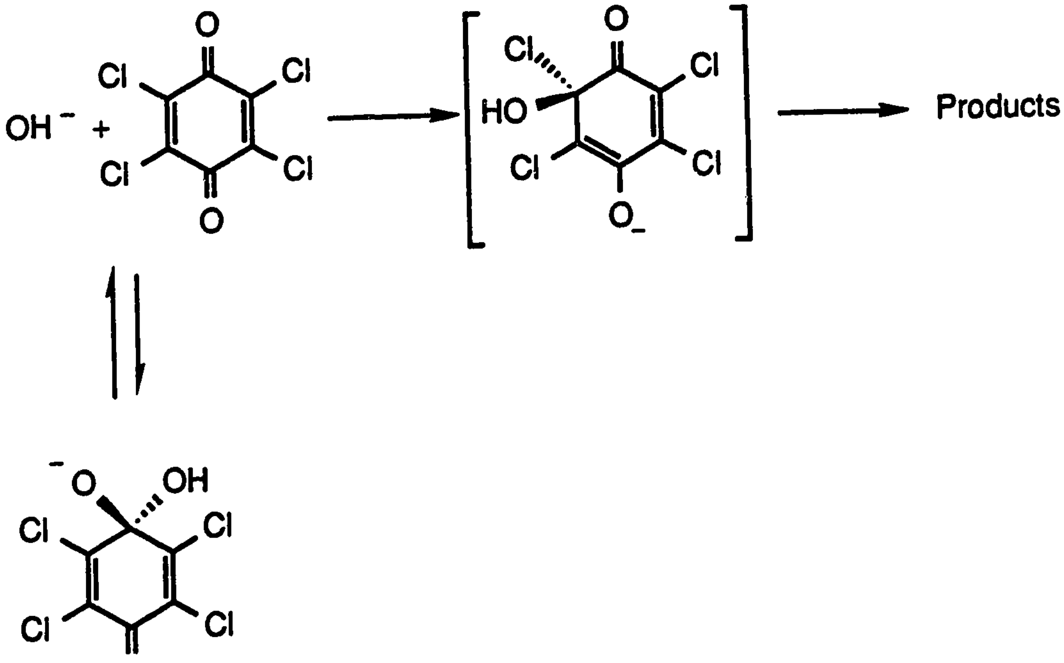

Scheme !

Reversible addition of OH^- to a carbonyl group in Cl_4-p-BQ was believed to occur before nucleophilic aromatic substitution on attack of a C-Cl site [17].

Covalent bonding has also been predicted in the complex $C_6F_6{\cdot}F^-$ (Chapter 4). From the $-\Delta H^o_{FA}$ and $-\Delta S^o_{FA}$ values determined by Hiraoka [19], a bond free energy (at 423 K) of 17.5 kcal/mol is calculated for this complex. This is ~16 kcal/mol smaller than the experimentally determined $-\Delta G^o_{FA,423K}(F_4\text{-p-BQ})$ value given in Table 5.1. The difference in bond free energies illustrates the large contribution to F_4-p-BQ·F^- Meisenheimer complex stability provided by π charge delocalization involving the carbonyl group (reaction 5.6 or reaction 5.7).

From Table 5.1 the bond free energy of Cl_4-p-BQ·Br^- is observed to be 1.5 kcal/mol less than that for F_4-p-BQ·Br^-. This is opposite to the trend in electron attachment energies where $-\Delta G^{o}_{eA,423K}$(Cl_4-p-BQ) is larger by 1.7 kcal/mol [2]. The lower bond strength in Cl_4-p-BQ·Br^- possibly results from smaller C^+-Cl^- bond dipoles in Cl_4-p-BQ compared to C^+-F^- bond dipoles in F_4-p-BQ, i.e., F is more electronegative than Cl. Electron densities in the C-Cl and C-F bonds in C_6Cl_6 and C_6F_6 have been calculated by Almlof and Faegri [20] using ab initio MO methods (double-ζ basis set). A net charge of +0.34 was predicted on each ring carbon of C_6F_6 compared to -0.05 on each carbon atom in C_6Cl_6. Hence, as the most stable geometries of F_4-p-BQ·Br^- are predicted to involve electrostatic interactions of the negative charge on Br^- with the electropositive ring carbon atoms (Figures 5.4 and 5.6), a lower bond strength in a similarly bonded Cl_4-p-BQ·Br^- complex is not surprising. If covalent bonding was preferred in the complexes F_4-p-BQ·Br^- and Cl_4-p-BQ·Br^- a different stability order would be expected. Chlorine substituents would be anticipated to stabilize charge transfer from Br^- into the ring better than fluorine substituents as the destabilizing -R effect of the halogens (π donation into the ring) is greater for fluorine [14]. The strong field/inductive effect (+F) of the halogens, which would stabilize the negative charge of Br^-, is of similar magnitude for fluorine and chlorine substituents [14]. The stronger -R effect of fluorine is responsible for the lower electron affinity of F_4-p-BQ with respect to Cl_4-p-BQ [2].

Also of interest in Table 5.1 is the stronger bond free energy determined for Cl_4-o-BQ·Br^- compared to Cl_4-p-BQ·Br^- (2.6 kcal/mol greater). The increase in energy can be explained in terms of either partial charge transfer or an electrostatic interaction. The positioning of two carbonyl groups next to each other on the ring may well lead to increased charge transfer from Br$^-$ into the C=O sites and an overall increase in complex stability. Also possible is the charge distribution in the ortho isomer, i.e., two strongly electropositive neighboring carbon atoms, results in a stronger electrostatic interaction with Br$^-$.

The absence of electron withdrawing halogen substituents leads to a large drop in the bond free energy determined for p-BQ·X$^-$ (X$^-$ = Br$^-$ and Cl$^-$); see Table 5.1. Nucleophilic attack at the carbonyl group of p-BQ by the strong base CH$_3^-$ has been observed in solution [21] but a predominantly electrostatic interaction is anticipated in p-BQ·X$^-$. Covalent bonding in p-BQ·X$^-$ (X$^-$ = Br$^-$ and Cl$^-$) is very unlikely as only a weak bond strength was predicted for the Meisenheimer F$_4$-p-BQ·Br$^-$ complex and formation of the corresponding F$_4$-p-BQ·Cl$^-$ complex was found to be energetically unfavorable [9]. Possible geometries for p-BQ·X$^-$ have X$^-$ positioned above the molecular plane of p-BQ (analogous to the geometries of F$_4$-p-BQ·Cl$^-$ shown in Figures 5.7 and 5.8) or hydrogen bonded to a ring proton or protons as shown below:

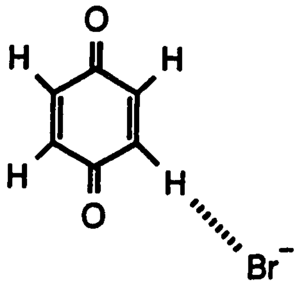

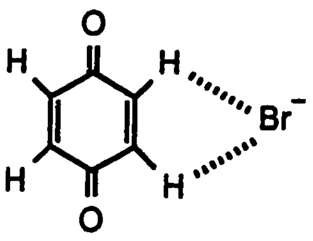

5.3b Bonding in the Complexes SE·X$^-$ where SE = Substituted Ethylenes and X$^-$ = F$^-$, Cl$^-$ and Br$^-$

The optimized geometries of TCNE and the complexes TCNE·X$^-$ (X$^-$ = F$^-$, Cl$^-$ and Br$^-$) [9] are shown in Figures 5.9-5.14. The predicted bond strengths of the complexes are given in Table 5.3 along with the experimentally determined $-\Delta H^{o}_{XA}$ values.

The strongest halide nucleophile, F$^-$, is predicted [9] to bond covalently to TCNE and form a stable Meisenheimer complex (Figure 5.10). Nucleophilic F$^-$ attack is proposed to occur at the C=C site. The electron withdrawing -CN substituents [14] are responsible for the electropositive character of the carbon atoms in the double bond ($C^{+0.14}=C^{+0.14}$, see Figure 5.9). The field/inductive effect (+F) of -CN also stabilizes F$^-$ electron density on Meisenheimer TCNE·F$^-$ complex formation. In addition, -CN substituents are π electron acceptors (+R) and the σ bonded TCNE·F$^-$ complex is further stabilized by π delocalization, as shown Scheme II.

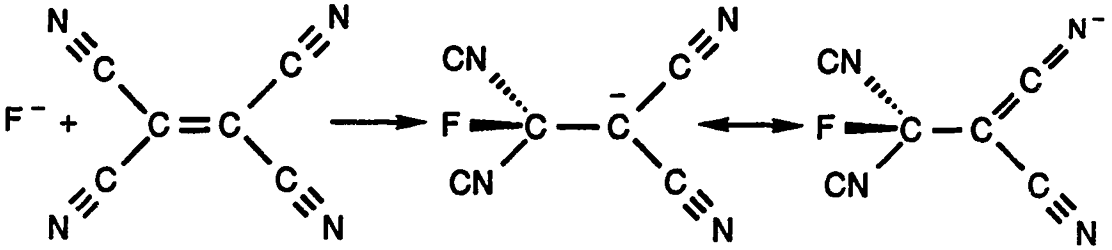

Scheme II

The geometries of TCNE and TCNE·F$^-$ shown in Figures 5.9 and 5.10 support the above resonance structures. The central C-C bond length of TCNE increases on addition of F$^-$ due to rupture of the C=C bond. The +F and +R effects of -CN coupled with formation of a strong C-F bond counteract the

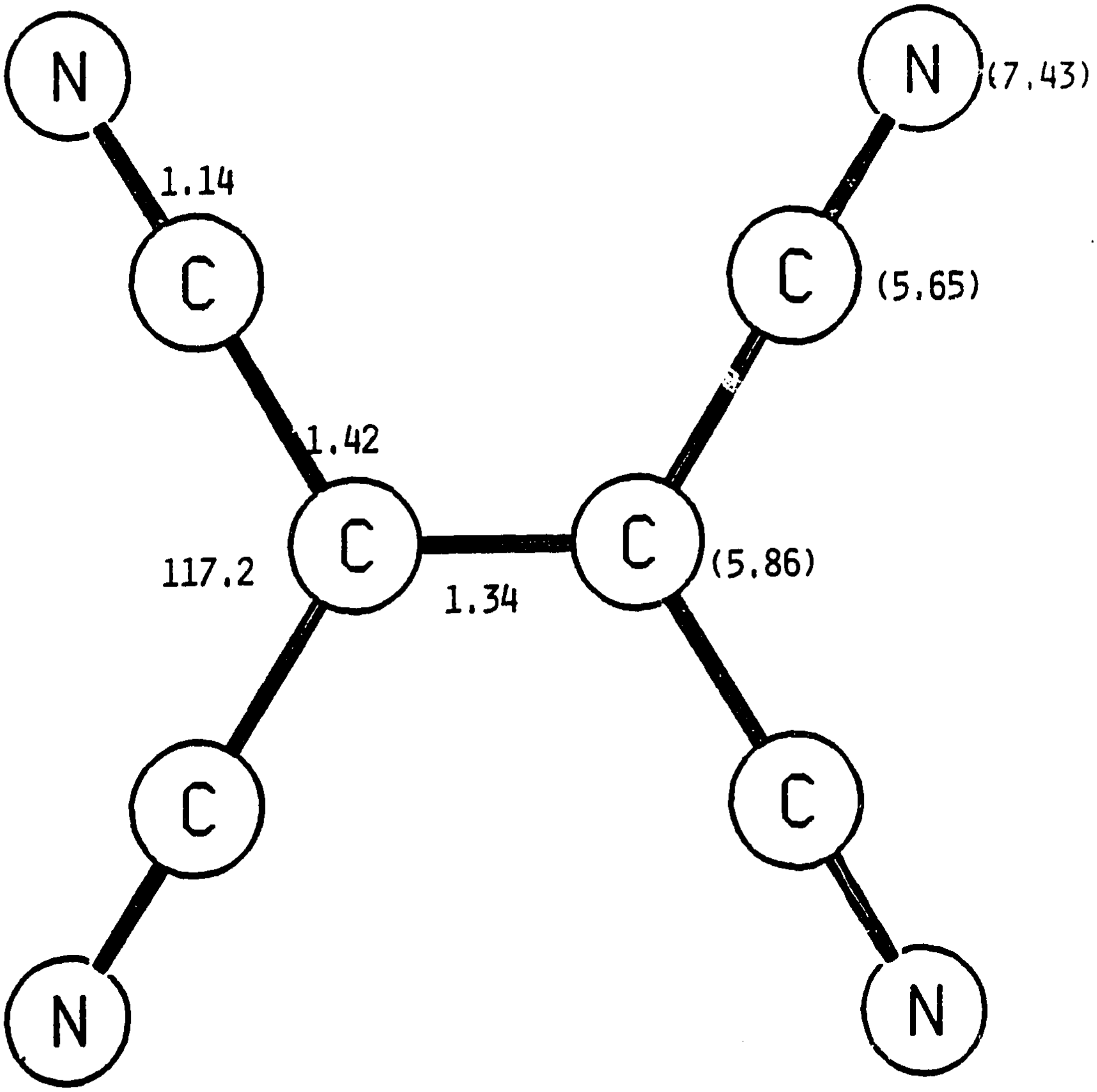
N
N
(7.43)
1.14
C
C
(5.65)
1.42
117.2
C
C
(5.86)
1.34
C
C
N
N

Figure 5.9 Optimized geometry of TCNE due to Hirao et al. [9]. The values in parentheses are electron densities. The bond lengths are in angstroms and the bond angles are in degrees.

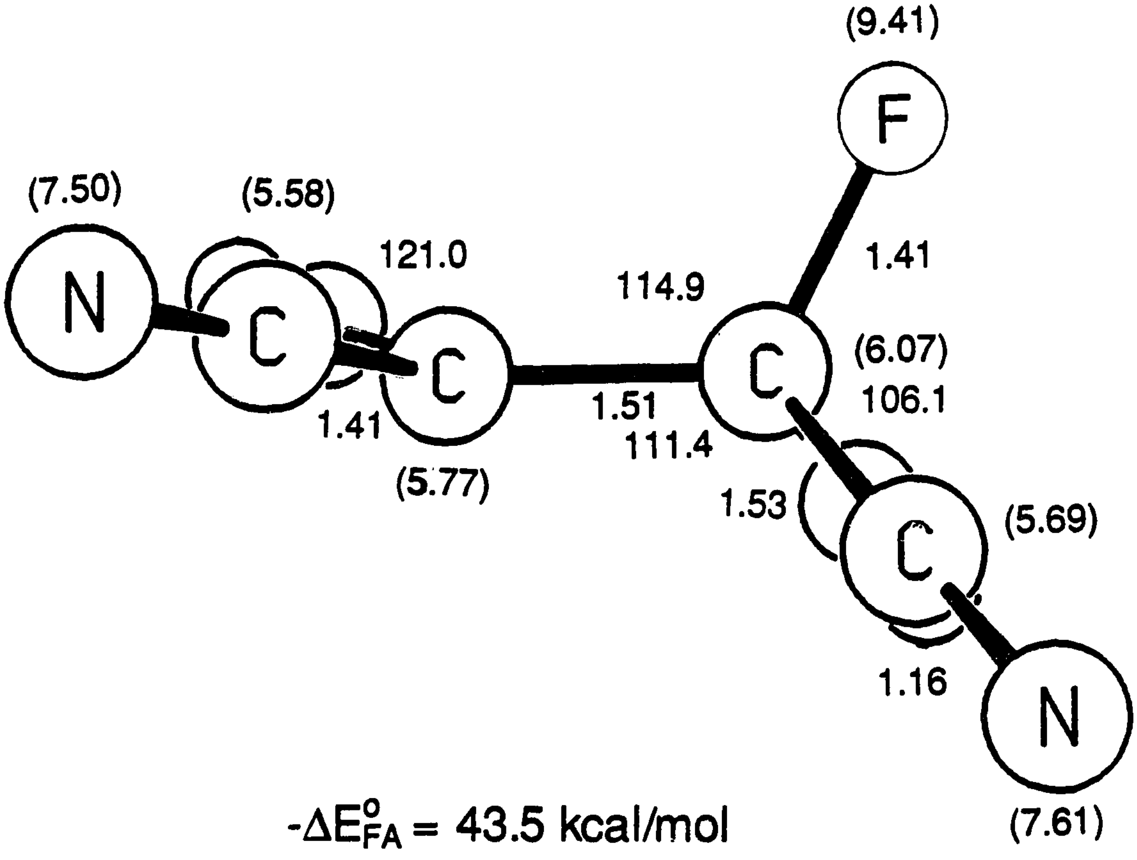
(9.41)
F
(7.50)
(5.58)
N
C
121.0
114.9
1.41
C
C
(6.07)
106.1
1.41
1.51
111.4
(5.77)
1.53
C
(5.69)
1.16
N
(7.61)
$-\Delta E^{o}_{FA} = 43.5$ kcal/mol

Figure 5.10 Optimized geometry of the TCNE·F$^-$ Meisenheimer complex due to Hirao et al. [9]. The values in parentheses are electron densities. The bond lengths are in angstroms and the bond angles are in degrees.

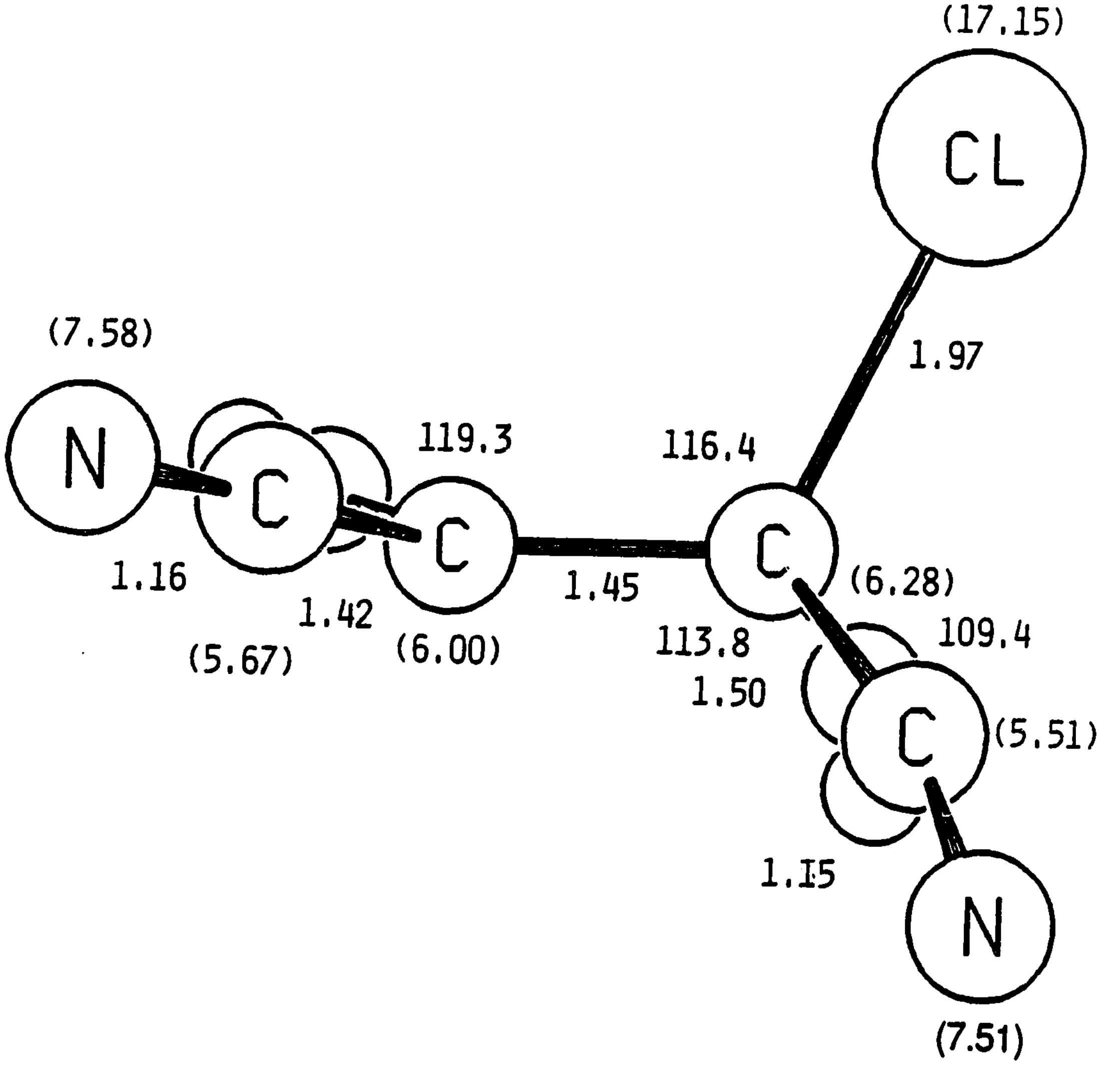
(17.15)
CL
1.97
(7.58)
N
C
C
119.3
116.4
C
1.16
1.42
1.45
(6.28)
(5.67)
(6.00)
113.8
109.4
1.50
C
(5.51)
1.15
N
(7.51)

$-\Delta E^{o}_{ClA} = 5.3$ kcal/mol

Figure 5.11 Optimized geometry of the TCNE·Cl$^-$ Meisenheimer complex due to Hirao et al. [9]. The values in parentheses are electron densities. The bond lengths are in angstroms and the bond angles are in degrees.

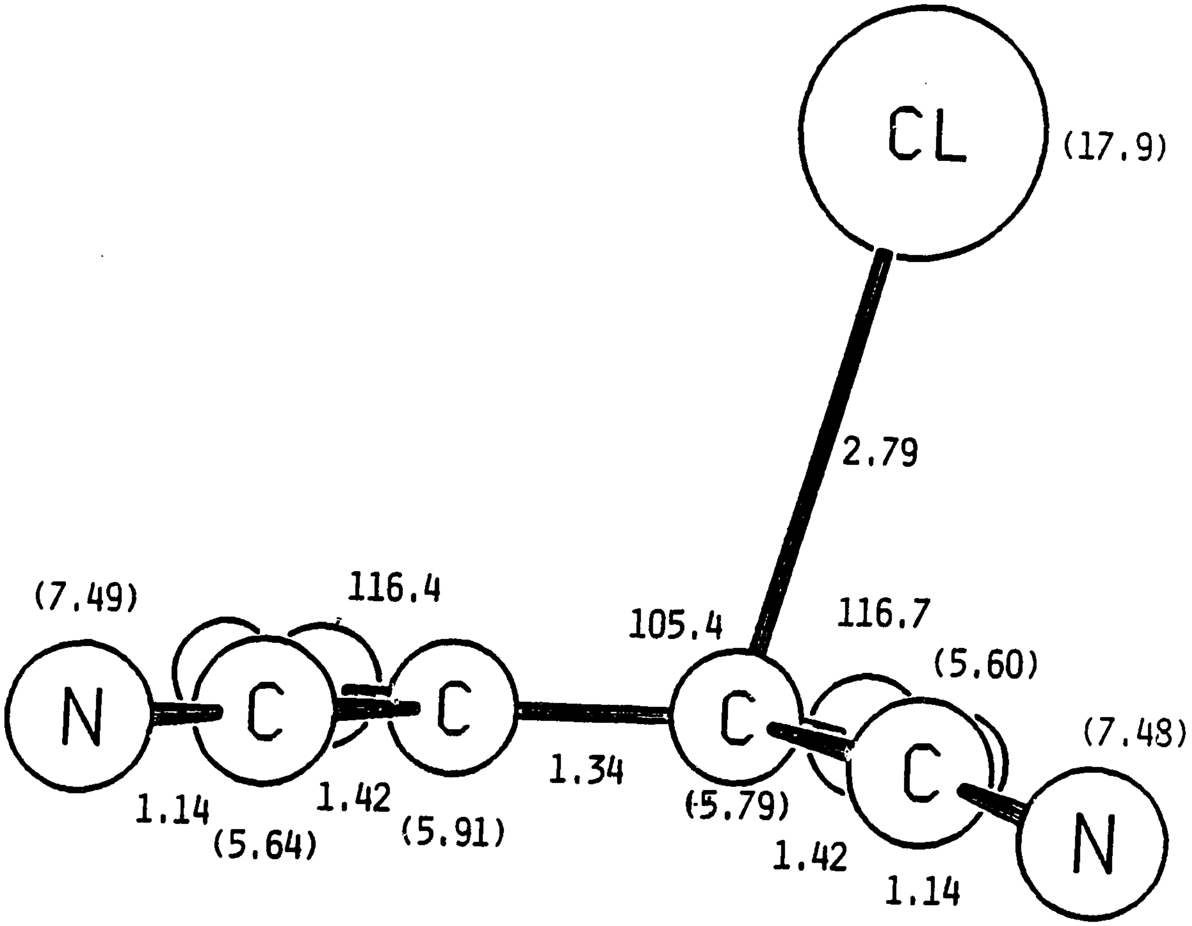
CL
(17.9)
2.79
(7.49)
116.4
105.4
116.7
(5.60)
N
C
C
C
C
(7.48)
N
1.14
1.42
1.34
(5.64)
(5.91)
(5.79)
1.42
1.14

$$-\Delta E^{o}_{ClA} = 19.4 \text{ kcal/mol}$$

Figure 5.12 Optimized geometry of the TCNE·Cl$^-$ electrostatic complex due to Hirao et al. [9]. The values in parentheses are electron densities. The bond lengths are in angstroms and the bond angles are in degrees.

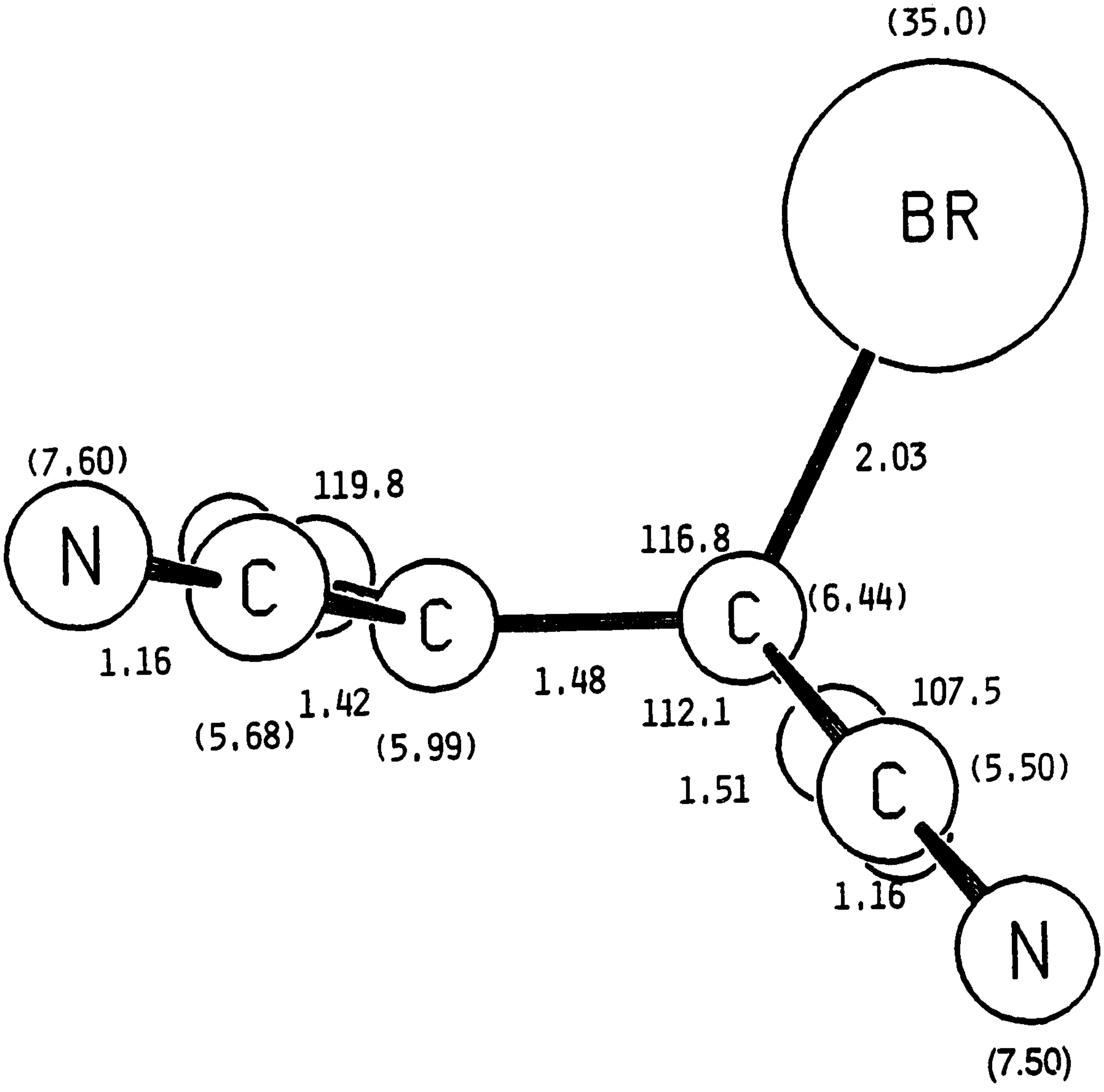
(35.0)
BR
2.03
(7.60)
N
C
C
119.8
116.8
C
(6.44)
1.16
1.42
(5.68)
(5.99)
1.48
112.1
107.5
C
(5.50)
1.51
1.16
N
(7.50)

$-\Delta E^{o}_{BrA} = 0.6$ kcal/mol

Figure 5.13 Optimized geometry of the TCNE·Br⁻ Meisenheimer complex due to Hirao et al. [9]. The values in parentheses are electron densities. The bond lengths are in angstroms and the bond angles are in degrees.

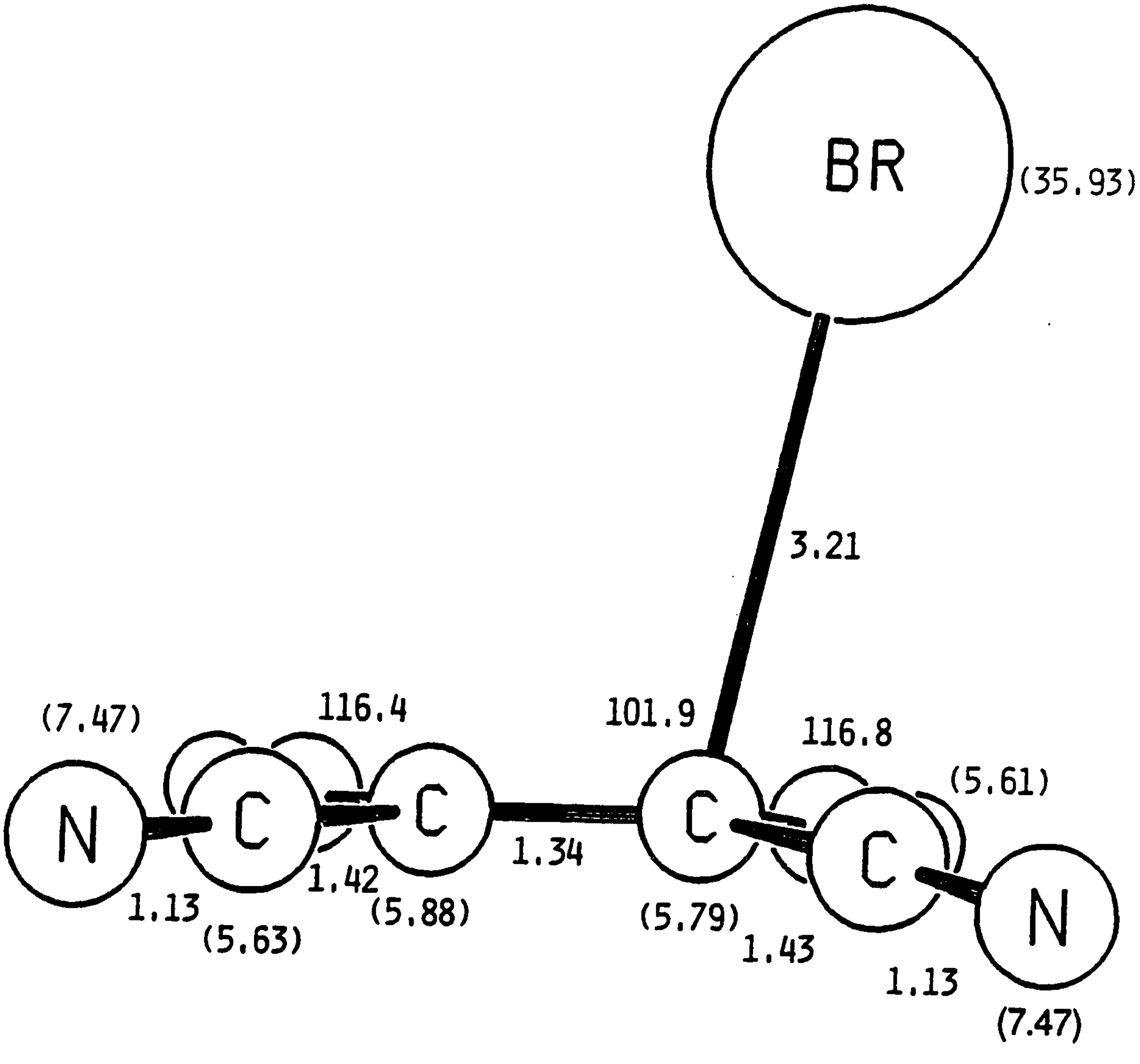
BR
(35.93)
3.21
(7.47)
116.4
101.9
116.8
(5.61)
N
C
C
C
C
N
1.34
1.42
1.13
(5.63)
(5.88)
(5.79)
1.43
1.13
(7.47)

$$-\Delta E^{o}_{BrA} = 13.8 \text{ kcal/mol}$$

Figure 5.14 Optimized geometry of the TCNE·Br$^-$ electrostatic complex due to Hirao et al. [9]. The values in parentheses are electron densities. The bond lengths are in angstroms and the bond angles are in degrees.

energy destabilization due to tetrahedral complex formation and a strong Meisenheimer complex results ($-\Delta E^{o}_{FA}$(TCNE) = 43.5 kcal/mol).

σ bonded complexes have been proposed as intermediates in gas phase addition-elimination reactions involving nucleophilic attack of substituted ethylenes by strong bases [22-24]. For example, the proposed reaction pathway for OR^- (R = alkyl) attack of 1,1-difluoroethylene [22] is as follows:

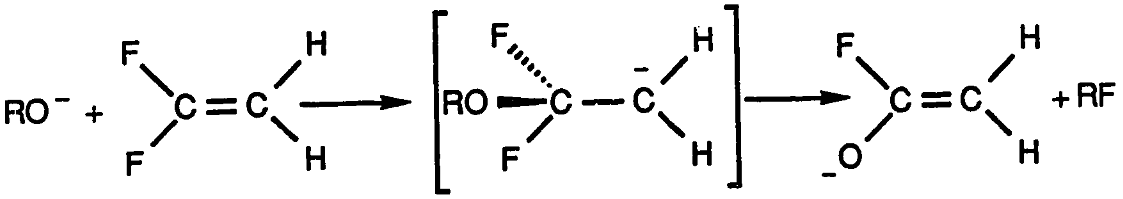

The optimized geometries of the complexes TCNE·Cl^- and TCNE·Br^- are shown in Figures 5.11-5.14. Stable electrostatic and Meisenheimer complexes were proposed for each. Electrostatic bonding was predicted to be ~15 kcal/mol more favorable than σ bonding in these complexes; see Table 5.3. The lower stabilities of σ bonded TCNE·Cl^- (Figure 5.11) and TCNE·Br^- (Figure 5.13) complexes relative to TCNE·F^- are due to the lesser energy stabilization on C-X bond formation. The bond strengths of C-F, C-Cl and C-Br are ~116 kcal/mol, ~80 kcal/mol and 70 kcal/mol, respectively [1]. The differences in stabilities of the Meisenheimer complexes TCNE·X^- (X^- = F^-, Cl^- and Br^-) are directly related to the differences in C-X bond strengths (Table 5.3).

In the energetically favored electrostatic complexes, X^- (X^- = Cl^- and Br^-) is positioned above the molecular plane of TCNE, presumably in order to gain the strongest electrostatic interaction with the electropositive carbon atoms in TCNE; see Figures 5.12 and 5.14. The position of X^- reflects the larger cationic character of the carbon atoms positioned next to the electronegative N atom rather than the carbon atoms in the C=C bond (for electron densities in TCNE see Figure 5.9). The π conjugation in TCNE is soundly preserved in the electrostatic TCNE·X$^-$ complexes and no deformation of the TCNE structure occurs (Figures 5.12 and 5.14).

Calculations concerning the complex TCNE·Cl$^-$ have been performed by Sillion et al. [25] using the minimal STO-3G basis set. The mode of interaction in the complex was predicted to be mainly electrostatic and a bond strength of 20.0 kcal/mol was evaluated. These results are in good agreement with those of Hirao et al. [9] shown in Table 5.3.

Interestingly, Bowie et al. [4] have proposed covalent bonding in the adducts TCNE·X$^-$ (X$^-$ = Cl$^-$, Br$^-$ and I$^-$) based on gas phase work with an ICR mass spectrometer. In cyclotron ejection experiments involving X$^-$ (X$^-$ = Cl$^-$, Br$^-$ and I$^-$) and TCNE, the initially formed TCNE·X$^-$ adducts were observed to decompose to the ion $C_5N_3^-$.

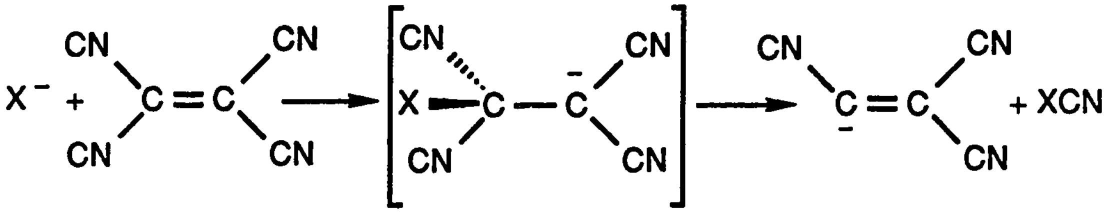

The formation of $C_5N_3^-$ was proposed to occur through the addition-elimination reaction shown above involving a σ bonded TCNE·X$^-$ intermediate. This reaction pathway is not consistent with the electrostatic TCNE·X$^-$ complex formation predicted by Hirao et al. (X$^-$ = Cl$^-$ and Br$^-$) [9] and Sillion et al. (X$^-$ = Cl$^-$) [25].

It is interesting to see in Table 5.3 fairly large disagreements of the theoretically determined bond strengths for TCNE·X$^-$ (X$^-$ = Cl$^-$ and Br$^-$) with those obtained experimentally (~15 kcal/mol difference). As previously mentioned, basis set deficiency and lack of an electron correlation correction in the theoretical calculations may be responsible for the differences.

From Table 5.1 a 10 kcal/mol drop in bond free energies are observed for the chloride and bromide complexes of fumaronitrile (trans-1,2-dicyanoethylene) with respect to TCNE·X^-. The presence of only two electron withdrawing CN substituents means covalent bonding is very unlikely in fumaronitrile·X^-, i.e., only weak bond energies were predicted in the σ bonded TCNE·X^- complexes (X^- = Cl^- and Br^-) with four CN substituents present (Table 5.3). The strength of an electrostatic interaction analogous to the one predicted in TCNE·X^- (Figures 5.12 and 5.14) will obviously also be weakened by the absence of two CN groups. Hydrogen bonding of X^- in the molecular plane of fumaronitrile may instead be preferred; see structure below.

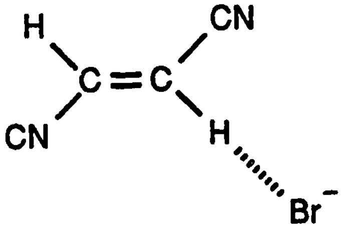

REFERENCES

1. K. Hiraoka, S. Misuze and S. Yamabe, J. Phys. Chem., 91, 5294 (1987).
2. T. Heinis, S. Chowdhury, S. L. Scott and P. Kebarle, J. Am. Chem. Soc., 110, 400 (1988).
3. S. Chowdhury and P. Kebarle, J. Am. Chem. Soc., 108, 5453 (1986).
4. J. Bowie, Aust. J. Chem., 30, 2161 (1977).
5. G. Briegleb, W. Liptay and R. Fick, Z. Physik. Chem., 33, 181 (1962).
6. G. Heublein, S. Spange and P. Hallpap, J. Prakt. Chem., 321, 503 (1979).
7. J. A. A. de Boer, D. N. Reinhoudt, J. W. H. M. Uiterwijk and S. Harkema, J. Chem. Soc., Chem. Commun., 194 (1982).
8. S. Spange and G. Heublein, Z. Chem., 28, 218 (1988).
9. G. Paul, K. Hirao, S. Obata and P. Kebarle, in preparation.
10. R. N. McDonald and P. L. Schell, Organometallics, 7, 1806 (1988).
11. R. N. McDonald and P. L. Schell, Organometallics, 7, 1820 (1988).
12. S. Chowdhury and P. Kebarle, J. Chem. Phys., 85, 4989 (1986).
13. J. Gao, D. S. Garner and W. L. Jorgensen, J. Am. Chem. Soc., 108, 4784 (1986).
14. R. W. Taft and R. D. Topsom, Prog. Phys. Org. Chem., 16, 1 (1987).
15. S. Chowdhury, E. P. Grimsrud, T. Heinis and P. Kebarle, J. Am. Chem. Soc., 108, 3630 (1986).
16. S. Chowdhury, G. Nicol and P. Kebarle, Chem. Phys. Letts., 127, 130 (1986).
17. C. A. Bishop and L. K. J. Tong, Tetrahedron Letters, 41, 3043 (1964).
18. J. L. Roberts, Jr., H. Sugimoto, W. C. Barrette, Jr., and D. T. Sawyer, J. Am. Chem. Soc., 107, 4556 (1985).
19. K. Hiraoka, S. Misuze and S. Yamabe, J. Chem. Phys., 86, 4102 (1987).

20. J. Almlof and K. Faegri, Jr., J. Am. Chem. Soc., 105, 2965 (1983).

21. M. Solomon, W. C. L. Jamison, M. McCormick, D. Liotta, D. A. Cherry, J. E. Mills, R. D. Shah, J. D. Rodgers, and C. A. Maryanoff, J. Am. Chem. Soc., 110, 3702 (1988).

22. J. M. Riveros and K. Takashima, Can. J. Chem., 54, 1839 (1976).

23. S. A. Sullivan and J. L. Beauchamp, J. Am. Chem. Soc., 99, 5017 (1977).

24. R. N. McDonald, A. K. Chowdhury and D. W. Setser, J. Am. Chem. Soc., 102, 6491 (1980).

25. C. Ghio, J. Tomasi, J. Weill and B. Sillion, J. Mol. Struct. (Theochem), 135, 299 (1986).

CHAPTER 6

THE THERMODYNAMICS OF THE ASSOCIATION REACTIONS $HO^- + H_2O = HO^- \cdot HOH$ AND $CH_3O^- + CH_3OH = CH_3O^- \cdot HOCH_3$ IN THE GAS PHASE

6.1 Introduction

The early determinations [1, 2] of the thermodynamic quantities ΔG_1^o, ΔH_1^o and ΔS_1^o of reaction (6.1) based on measurements of the gas phase equilibrium (6.1) with a high pressure mass spectrometer were followed by a number of theoretical calculations in which

$$HO^- + HOH = HO^- \cdot HOH \qquad (6.1a)$$

$$DO^- + DOD = DO^- \cdot DOD \qquad (6.1b)$$

$$CH_3O^- + CH_3OH = CH_3O^- \cdot HOCH_3 \qquad (6.2)$$

the electronic energy E_e^o of the reactants and thus also ΔE_e^o was evaluated with ab initio MO methods [3-8]. The theoretical work also provided information on the geometry of the dimer $HO^- \cdot HOH$. In some of this work the frequencies of the normal vibrations were also evaluated [8] and these data, when combined with statistical mechanics equations, lead to the thermodynamic quantities ΔE_1^o, ΔH_1^o and ΔS_1^o.

The theoretical calculations, which through use of more extended basis sets and inclusion of electron correlation were becoming more refined [5, 6, 8],

---

1. A version of this chapter has been published: G. J. C. Paul and P. Kebarle, J. Phys. Chem., 94, 5184 (1990).

predicted $-\Delta H_1^o$ = 27 kcal/mol, a value that is more exothermic than the experimentally measured $-\Delta H_1^o$ = 22.5 and 24 kcal/mol [1, 2]. For detailed numerical data see Table 6.1 in Results and Discussion.

The analogous reaction (6.2) which involves the methoxide anion and methanol is also of fundamental interest. Furthermore, the thermochemistry of reactions (6.1) and (6.2) enters into a number of important thermodynamic cycles. Thus, Caldwell et al. [9], using ion cyclotron resonance (ICR), were able to measure a large number of transfer equilibria (6.3).

$$B^-\cdot HA + HR = B^-\cdot HR + HA \qquad (6.3)$$

$$\Delta H_3 = D(B^- \text{-} HA) - D(B^- \text{-} HR) \qquad (6.3a)$$

$$B^-\cdot HA + YH = Y^-\cdot HA + BH \qquad (6.4)$$

$$\Delta H_4 = D(Y^- \text{-} H^+) - D(B^- \text{-} H^+) + D(B^- \text{-} HA) - D(Y^- \text{-} HA) \qquad (6.4a)$$

Data of the type shown in eq. (6.3a) provide relative hydrogen bond energies for two hydrogen donors, HA and HR, to the same ion, B^-. Using available thermochemical information on gas phase acidities [10], e.g., $D(Y^-\text{-}H^+)$ and $D(B^-\text{-}H^+)$, one can use transfer reactions also to obtain relative bond energies for the same H donor, HA, bonding to two different anions, B^- and Y^- as shown in eq. (6.4). Caldwell et al. [9] used the absolute value for $D(CH_3O^-\text{-}HOCH_3) = -\Delta H_2^o$ = 21.8 kcal/mol to convert their relative hydrogen bond energies into absolute ones. Association equilibria like (6.1) and (6.2) are third body dependent and are too slow to be measurable at the low pressures (10^{-5} torr) used in ICR. Therefore, the value used for $-\Delta H_2^o$ was obtained by Caldwell in preliminary measurements with a pulsed electron high pressure mass spectrometer (PHPMS) in this laboratory [11]. Nibbering et al. [12] also used measurements of transfer equilibria (6.3) and (6.4) to provide the bond strengths of various anions attached to carbonyl containing compounds, where D(CH_3O^--$HOCH_3$) = 23.6 kcal/mol was used to anchor the scale. The choice of this anchor value was based on the subsequent good agreement observed between the experimentally determined bond strengths and those predicted theoretically [12]. Meot-Ner and Sieck [13] have published results of equilibrium measurements for reactions (6.1) and (6.2) obtained with PHPMS that led to ΔH_1^o = -26.8 kcal/mol and ΔH_2^o = -29.3 kcal/mol, the latter value being ~7 kcal/mol higher than the previous experimental determination by Caldwell [11]. On the other hand, Brauman et al. [14], on the basis of electron photodetachment measurements from $CH_3O^- \cdot HOCH_3$, estimated a $\Delta H_2^o = -19 \pm 3$ kcal/mol, which is lower but close to Caldwell's value [11].

Accurate determinations of the exothermicities of reactions (6.1) and (6.2) are important for obtaining anchor values for CH_3O^- and HO^- affinity scales involving aromatic compounds and small molecules. In preliminary PHPMS studies [15, 16], reactions (6.5) and (6.6)

$$CH_3O^- \cdot HOCH_3 + p\text{-}CF_3C_6H_4CN = CH_3OH + p\text{-}CF_3C_6H_4CN \cdot {}^-OCH_3 \qquad (6.5)$$

$$CH_3O^- \cdot HOCH_3 + CF_3CN = CH_3OH + CF_3CN \cdot {}^-OCH_3 \qquad (6.6)$$

were determined by equilibrium measurements to have $-\Delta H^o$ values of 8.2 kcal/mol and 7.2 kcal/mol, respectively. By combining these values with that for reaction (6.2) the absolute methoxide binding energies for p-$CF_3C_6H_4CN$ and CF_3CN can be obtained. These values cannot be determined directly using PHPMS due to the high reaction exothermicities. Establishing transfer ladders based on these and analogous absolute hydroxide binding energies would be of interest due to potential covalent bond formation in methoxide and hydroxide adducts. For a discussion on σ bond formation upon nucleophilic addition to aromatic compounds, see Chapters 4 and 5.

Knowledge of the thermodynamics of reactions (6.1) and (6.2) is also necessary in order to rationalize the behavior of "nude" hydroxide and methoxide anions and singly solvated anions $HO^{-}\cdot HOH$ and $CH_3O^{-}\cdot HOCH_3$ in kinetics and energetics studies of proton transfer involving these species [17, 18]. Studies of this nature are extremely important as stepping stones in the elucidation of the influence of intrinsic molecular parameters and ion-solvent interactions upon reactivity [19-21].

In the present work, results from new measurements of equilibria (6.1) and (6.2) with PHPMS are presented. Because of the conflicting previous results, some possible sources of error such as temperature measurement and side reactions were re-examined.

6.2 Experimental

6.2a Apparatus and Temperature Measurements

The general features of the PHPMS apparatus and the general methodology are described in Chapters 1-3. Equilibrium (6.1) and (6.2) measurements were made at different static temperatures and different partial pressures of the clustering gas, D_2O and CH_3OH, respectively. A first set of measurements of the temperature dependence of equilibria (6.1) and (6.2) led to van't Hoff plots whose slopes gave ΔH_1^o and ΔH_2^o values in substantial agreement with those obtained by Meot-Ner [13]; see plots 1 in Figures 6.8 and 6.9 of Results and Discussion. However, the intercepts of the lines in the present work were displaced downwards when compared to those obtained by Meot-Ner [13], which means that the present $-\Delta S_1^o$ and $-\Delta S_2^o$ values were higher.

Since the measurement of the temperature of the gas in which the equilibria occur is difficult, some changes were made to the ion source that are illustrated in Figure 6.1. The position of the original thermocouple Tc 1 is shown in Figure 6.1b. This thermocouple was of a design used in earlier work [22]. The iron/constantan type J wire had a junction fused into a small silver ball. The silver ball junction was pressed by means of a hollow screw into a well drilled into the ion source. The well terminated near the inner ion source wall. In the improved design, Figure 6.1, two thermocouples, Tc 2 and Tc 3, were used. Tc 2 was of the same design as Tc 1 and in the same position; however, the well in the ion source was drilled through and then plugged with a small silver ball so that when Tc 2 was screwed in, its silver plug pressed very firmly against the silver plugged inner wall of the ion source; see 8 in Figure 6.1b. Tc 3 was of fine iron/constantan wires whose junction was spotwelded to the repeller in the ion source; see 12 in Figure 6.1a. The repeller itself was held in position by a thin walled ceramic tube of low thermal conductivity.

Since the temperature of the gas in the region close to the ion exit slit is decisive for the equilibrium measurements, the temperature of the bottom of the ion source, where the slit is located, was brought closer to the temperature of the main ion source block by embedding two cartridge heaters in the flange 13, Figure 6.1, which holds the ion exit slit plate. The temperature of this flange, measured with thermocouple 14, was held to within ±2 deg of the temperature of the ion source, as measured by Tc 2 and Tc 3.

The temperatures registered by Tc 2 and Tc 3, when the above arrangements were used and with gas in the ion source, are shown in Figure 6.2. The two temperatures are very close at low temperatures but in the high temperature range Tc 3 registers somewhat lower temperature, a maximum difference of 7 °C occurring at the highest temperature. A difference of 7 °C

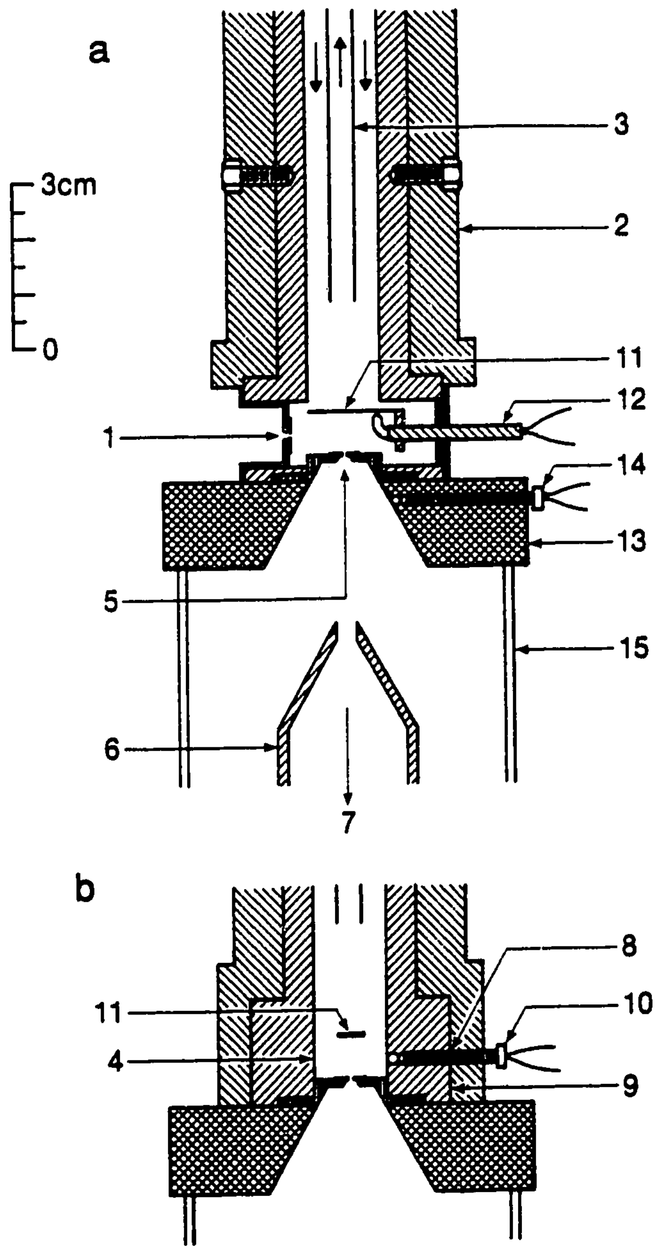

Figure 6.1 Ion source, shown in two perpendicular cross sections: (1) electron entrance slit; (2) heating mantle; (3) reactant gas supply and circulation; (4) actual ionization and ion-molecule reaction region; (5) ion exit slit; (6) first ion acceleration electrode; (7) to ion acceleration tower and magnetic sector mass analysis; (8) thermocouple Tc 2, consisting of iron constantan wires with junction fused to small silver ball pressed against wall of ion source by means of hollow screw; (9) ion source; (10) hollow screw; (11) ion repeller electrode, normally at same voltage as ion source; (12) thermocouple Tc 3 and ceramic tube; (13) bottom flange of ion source block with embedded cartridge heaters; (14) thermocouple.

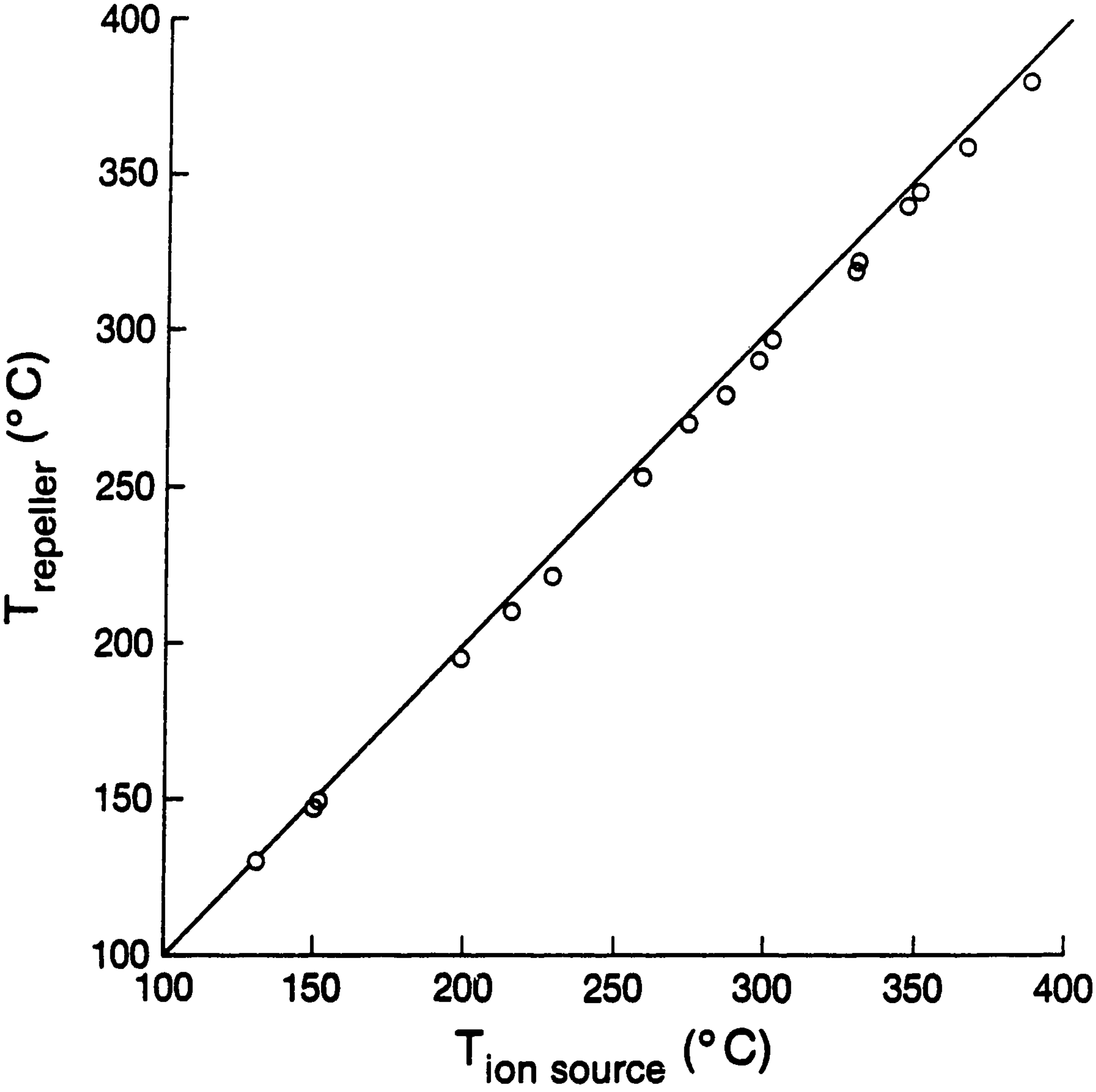

Figure 6.2 Ion source temperatures measured by thermocouples: Tc 2 in position 8 and Tc 3 in position 12. See Figure 6.1.

developing over a 300 °C range has only a minimal effect on the van't Hoff plots obtained, as shown in Figures 6.8 and 6.9 of Results and Discussion. The van't Hoff plots with the temperatures from thermocouples Tc 1, Tc 2 and Tc 3 were found to be very close (see Figures 6.8 and 6.9), and this was taken as proof that the measured temperatures are of adequate accuracy.

6.2b Experimental Conditions Used in Equilibrium Measurements

The gas mixtures, passed in slow flow through the ion source, consisted of methane carrier gas at 1.5-3.5 torr pressures containing D_2O at pressures in the 100-1000 mtorr range for equilibria (6.1) or CH_3OH in the 1-100 mtorr range for equilibria (6.2). D_2O instead of H_2O was used in order to avoid interference of $^{35}Cl^-$ from the chloride ion present as small impurity with $HO^-{\cdot}HOH$, also of mass 35. The thermodynamic values obtained for reaction (6.1b) should be practically the same as that for the protonated species [1]. Higher pressures of water had to be used in order to speed up the establishment of equilibrium (6.1) since the forward rate constants for this equilibrium are appreciably smaller than those for equilibrium (6.2) [23].

The gas mixtures were prepared in the 5 l thermostated glass bulb by injecting the liquid reagents (D_2O and CH_3OH) with a calibrated syringe into a known pressure (~1 atm) of methane. A constant flow of the gas mixture through the ion source was obtained by means of a control valve and the pressure in the ion source was measured with a capacitance manometer; see Chapter 1.

In order to produce DO^- and CH_3O^-, nitrous oxide (3-100 mtorr) was added to the reaction mixture. The main reactions that occur are

$$e^- + N_2O = N_2 + O^- \quad (6.7)$$

$$O^- + D_2O = DO^- + DO \quad (6.8)$$

$$O^- + CH_3OH = CH_3O^- + HO \quad (6.9)$$

These are then followed by the equilibria (6.1) and (6.2).

The electron pulses were 10-50 μs wide and the electron energy was 2700 eV.

A typical time dependence, showing the raw ion counts observed in measurements of equilibrium (6.1) is shown in Figure 6.3. The reactant ions, DO^- and $DO^-{\cdot}DOD$ and the DO^- adduct to N_2O represented, in practically all measurements, over 95% of the total ions observed. Equilibrium (6.1) is seen to establish rapidly, within ~0.3 ms. The formation of the N_2O adduct is slower than the equilibrium (6.1). At long reaction times, the intensities of the equilibrated DO^- and $DO^-{\cdot}DOD$ are seen to decrease somewhat faster with time than the N_2O adduct intensity. The diffusion rates of DO^- and $DO^-{\cdot}DOD$ at equilibrium and $DO^-{\cdot}N_2O$ are expected to be very similar as the diffusion coefficient of the ions are assumed [24] to be inversely proportional to the reduced mass of the ion and the bath gas, CH_4. Therefore, the more rapid decrease of DO^- and $DO^-{\cdot}DOD$ has to be caused by a reaction of either DO^- or $DO^-{\cdot}DOD$ with N_2O to form the adduct ion, as shown in (6.10).

$$DO^- \text{ (or } DO^-{\cdot}DOD) + N_2O = DO^-{\cdot}N_2O \text{ (+DOD)} \quad (6.10)$$

$$CH_3O^- \text{ (or } CH_3O^-{\cdot}HOCH_3) + N_2O = CH_3O^-{\cdot}N_2O \text{ (+ } CH_3OH) \quad (6.11)$$

Since reaction (6.10) and the analogous (6.11) could be affecting equilibria (6.1) and (6.2), a study of the N_2O adduct forming reactions was made [23]. Unfortunately, the mechanism could not be established since the reactions

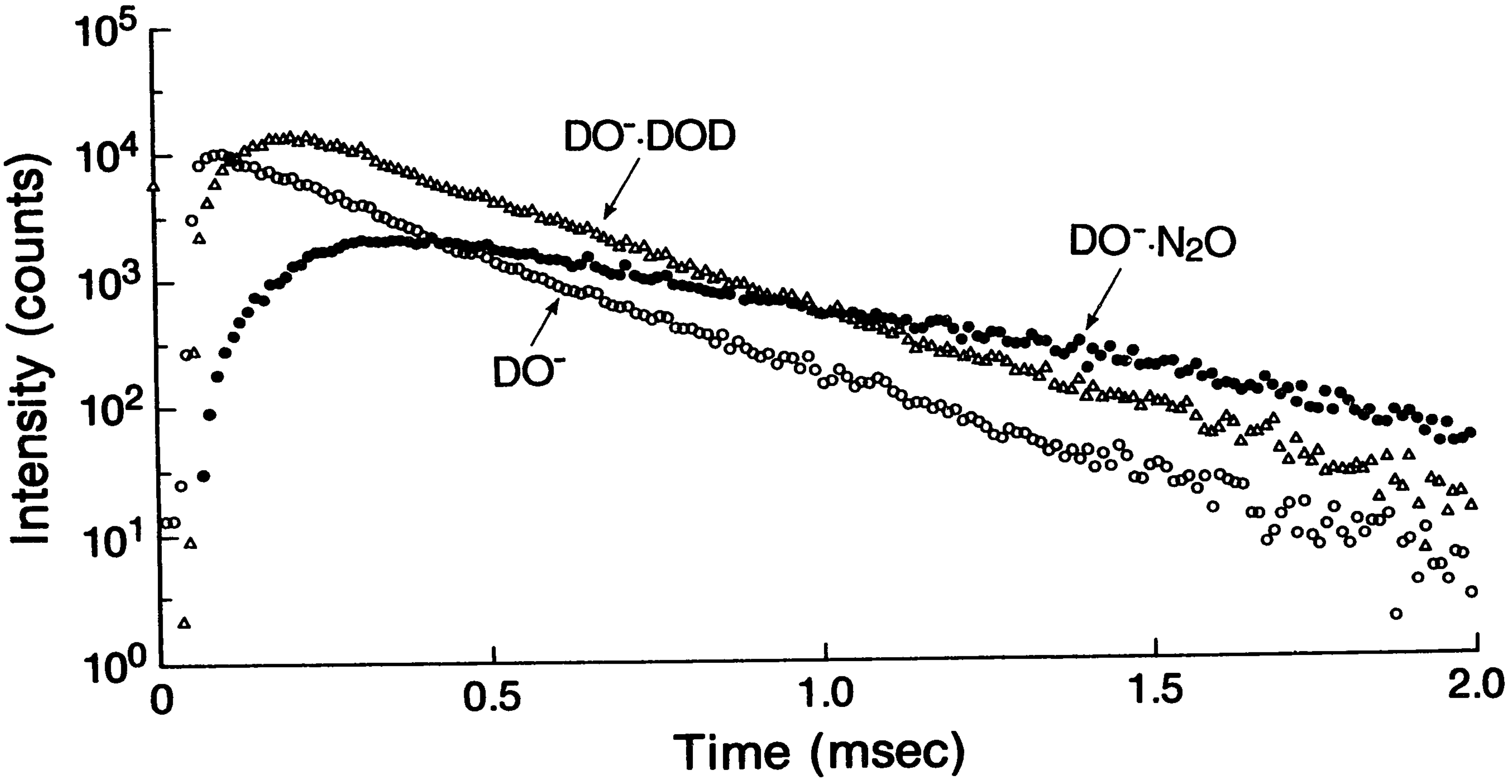

Figure 6.3 Raw ion counts, as a function of time after electron pulse, collected with multiscaler. Ion intensity changes reflect achievement of equilibrium (6.1): $DO^- + DOD = DO^- \cdot DOD$. A side reaction, the formation of $DO^- \cdot N_2O$, is observed also. Ion source temperature 345°C; $p(CH_4) = 2.8$ torr; $p(D_2O) = 0.45$ torr; $p(N_2O) = 0.039$ torr.

were not simple. For example the rate of (6.11) was found to be very weakly dependent on the N_2O concentration. An increase of the N_2O concentration by a factor of 100 led to an increase of the rate by only a factor of ~3. Conditions of measurement: CH_4 pressure, 3 torr; CH_3OH pressure, 60 mtorr; N_2O pressure, from 1 to 100 mtorr; temperature, 325 °C.

Meot-Ner et al. [13], McMahon et al. [25] and Bierbaum et al. [26] have also used N_2O as a route [13, 25] to OH^- and CH_3O^-, and studied the N_2O adduct formation [26]. Unfortunately these authors have not provided a characterization of reactions (6.10) and (6.11).

Since an understanding of reactions (6.10) and (6.11) was not achieved, the equilibria (6.1) and (6.2) were determined at a wide range of N_2O pressures and found to be independent of the N_2O pressure. These data are summarized in Figures 6.4 and 6.5.

The N_2O electron capture cross section is large only for electrons with ~2 eV kinetic energy [27]. The secondary electrons in the present system are rapidly thermalized by the carrier gas, so that sufficient O^- yield was obtained only with relatively high N_2O pressures, $p(N_2O) > 3$ mtorr. However, the D_2O and CH_3OH concentrations were always chosen high enough so as to lead to observed rates of formation of the N_2O adduct which were appreciably slower than the establishment of equilibria (6.1) and (6.2). The independence of the equilibria (6.1) and (6.2) of the N_2O pressure, demonstrated in Figures 6.4 and 6.5, is a consequence of such a choice of conditions.

The higher clusters, $DO^-(DOD)_2$ and $CH_3O^-(CH_3OH)_2$, were also observed particularly at lower temperatures. They were found to be in equilibrium with $DO^-{\cdot}DOD$ and $CH_3O^-{\cdot}HOCH_3$, respectively. The experimental conditions were always so chosen as to lead to intensities of the higher clusters that were less than ~20% of the ions involved in the equilibria (6.1) and (6.2).

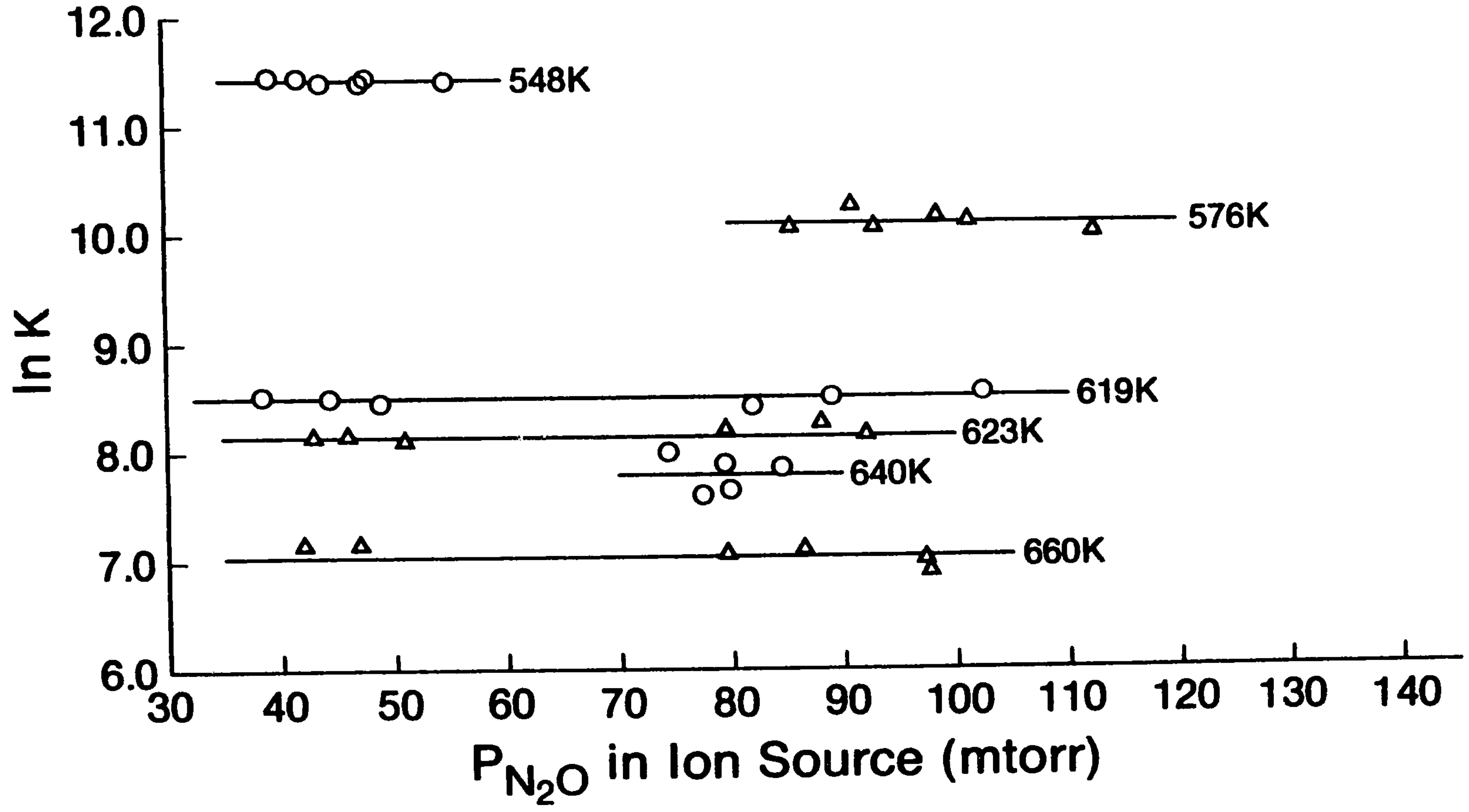

Figure 6.4 Independence of equilibrium constant K_1 of N_2O pressure. At each temperature, experiments involved 2-3 different D_2O pressures.

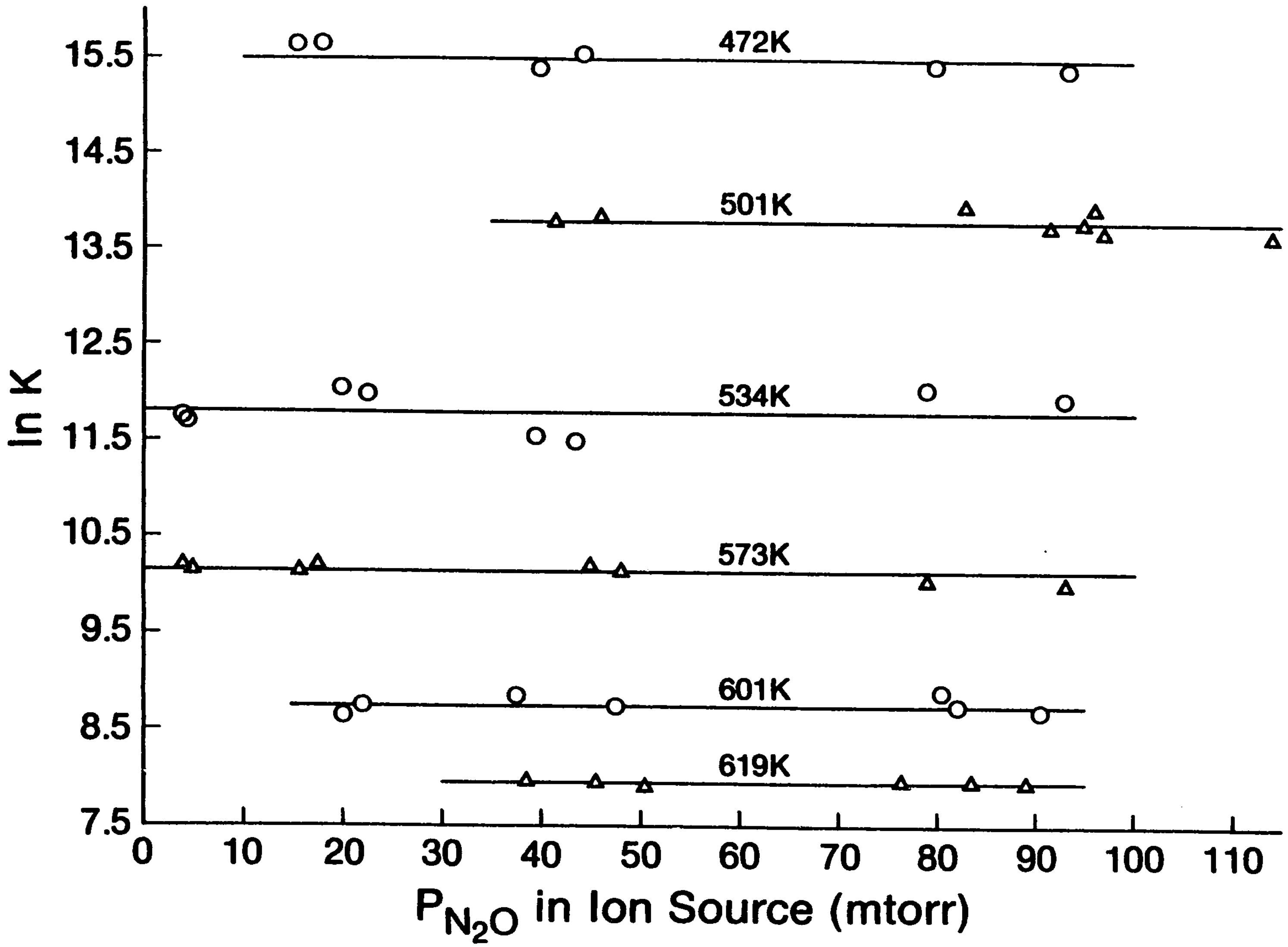

Figure 6.5 Independence of equilibrium constant K_2 of N_2O pressure. Both N_2O and CH_3OH pressures changed in different runs.

6.3 Results and Discussion

6.3a Experimental Results from Ion Equilibrium Measurements

The equilibrium constants of reactions (6.1) and (6.2) determined at different temperatures and different partial pressures of the clustering gas, D_2O and CH_3OH, respectively, are shown in Figures 6.6 and 6.7 and the van't Hoff plots obtained with these data are shown in Figures 6.8 and 6.9. The ΔH^o and the ΔS^o values resulting from the various plots from this laboratory are also given in the figures. Since it is believed that the measurements with the thermocouples Tc 2 and Tc 3 are the most reliable, see Experimental, the average ΔH^o and ΔS^o values from these two determinations, which are very close in any case, was used in Table 6.1.

It is evident from Figures 6.8 and 6.9, which show also the Meot-Ner data [13], that the slopes of the van't Hoff plots from both laboratories are very close. This leads to very good agreement for the ΔH_1^o = -27.6 kcal/mol, present work, versus ΔH_1^o = -26.8 kcal/mol, Meot-Ner et al. [13], and ΔH_2^o = -29.3 kcal/mol, present work, versus ΔH_2^o = -29.3 kcal/mol, Meot-Ner et al. [13]; see Table 6.1. Unfortunately, the agreement for the intercepts is not very good. Meot-Ner's lines are displaced upwards, i.e., they predict at any given temperature, equilibrium constants higher by a factor of ~8 for reaction (6.1) and ~7 for reaction (6.2). This leads to a difference in the evaluated entropies: ΔS_1^o = -28.1 cal/(deg mol), present work, versus ΔS_1^o = -22.8 cal/(deg mol), Meot-Ner et al. [13], and ΔS_2^o = -31.8 cal/(deg mol), present work, versus ΔS_2^o = -27.6 cal/(deg mol), Meot-Ner et al. [13]; see Table 6.1. The difference by a factor of ~8 in the equilibrium constants is larger than may be expected for ion-molecule equilibrium measurements from different laboratories. Also unusual is the fact that the difference remains essentially constant at all temperatures. More

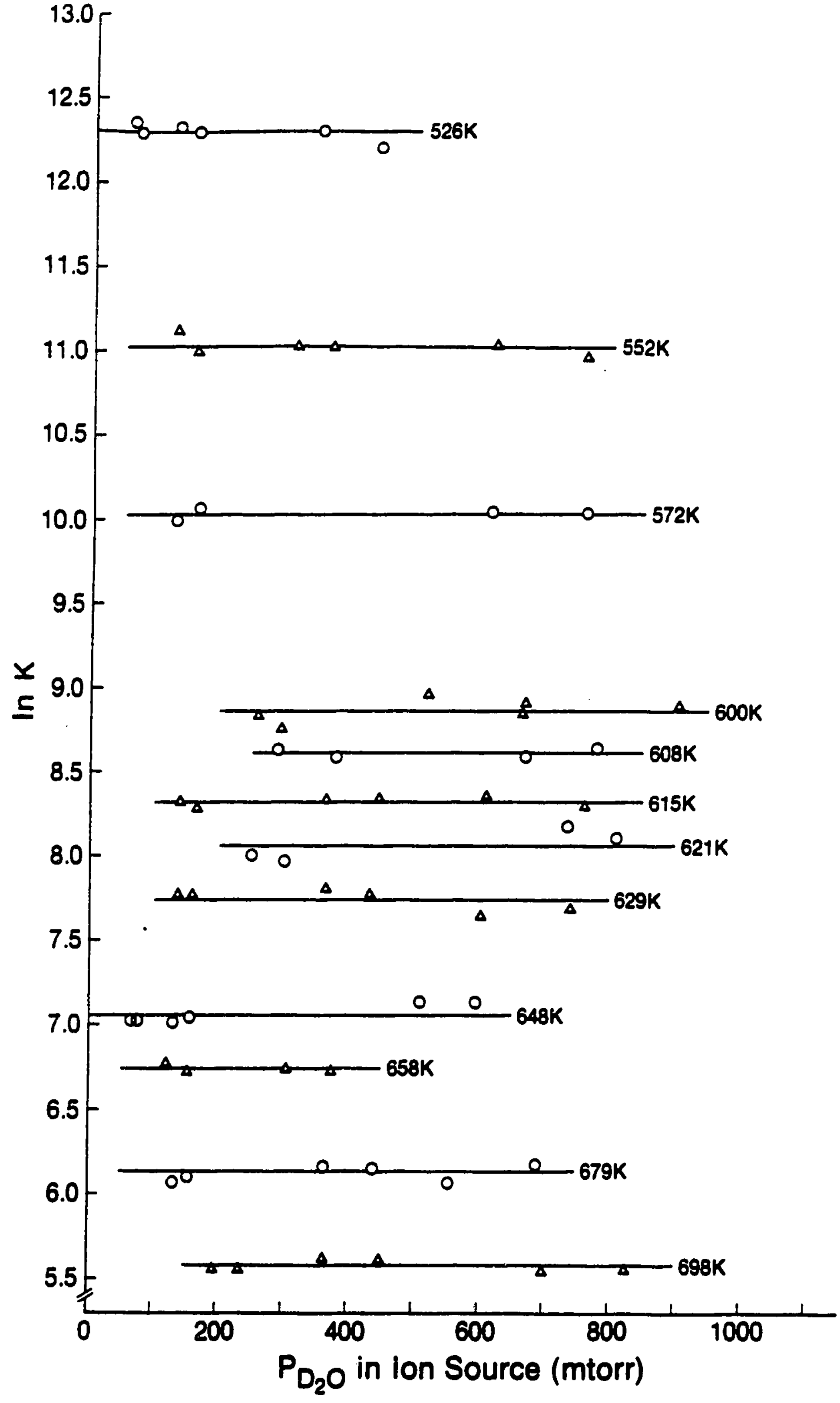

Figure 6.6 Independence of K_1 of D_2O pressure.

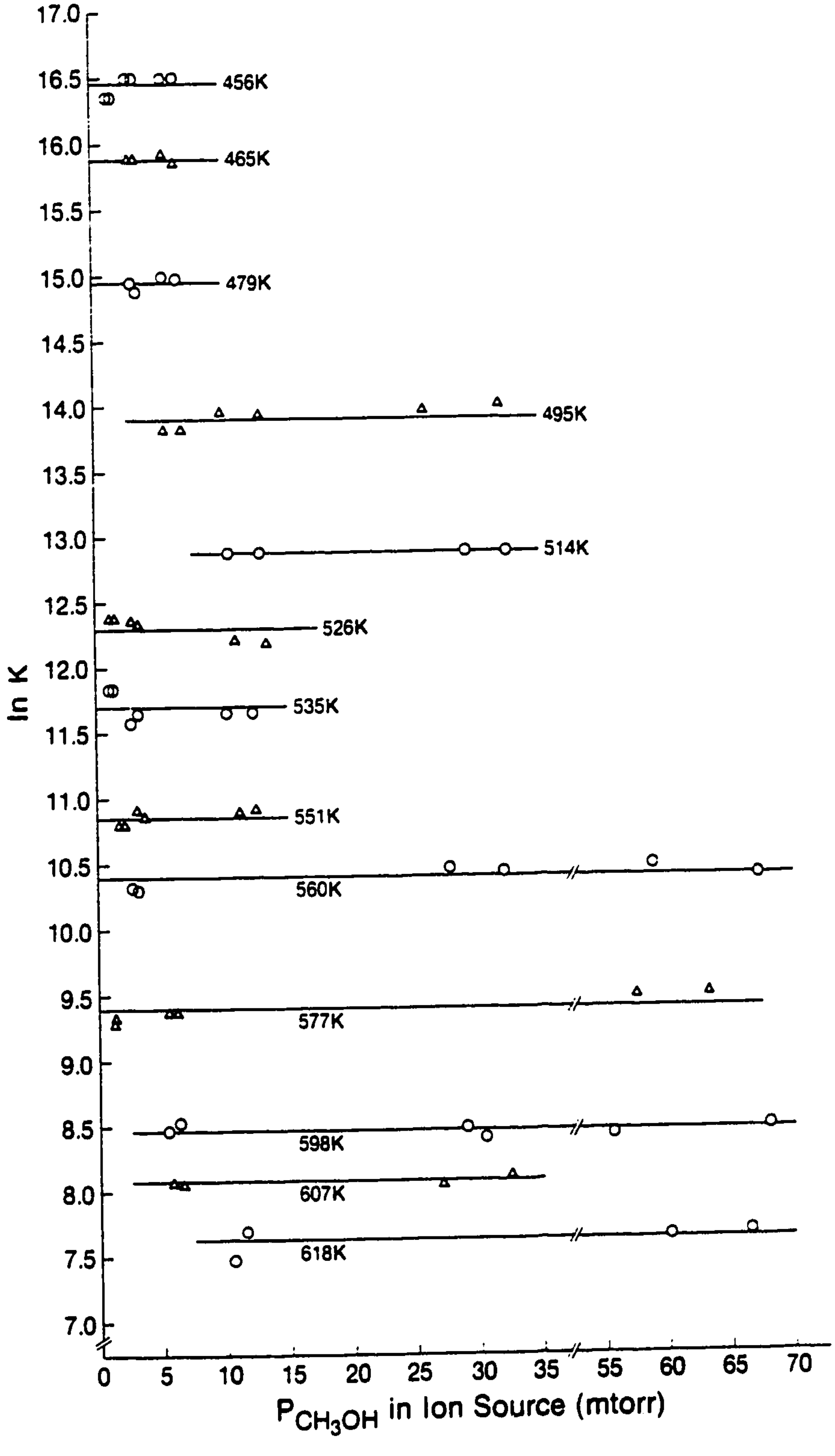

Figure 6.7 Independence of K_2 of CH_3OH pressure.

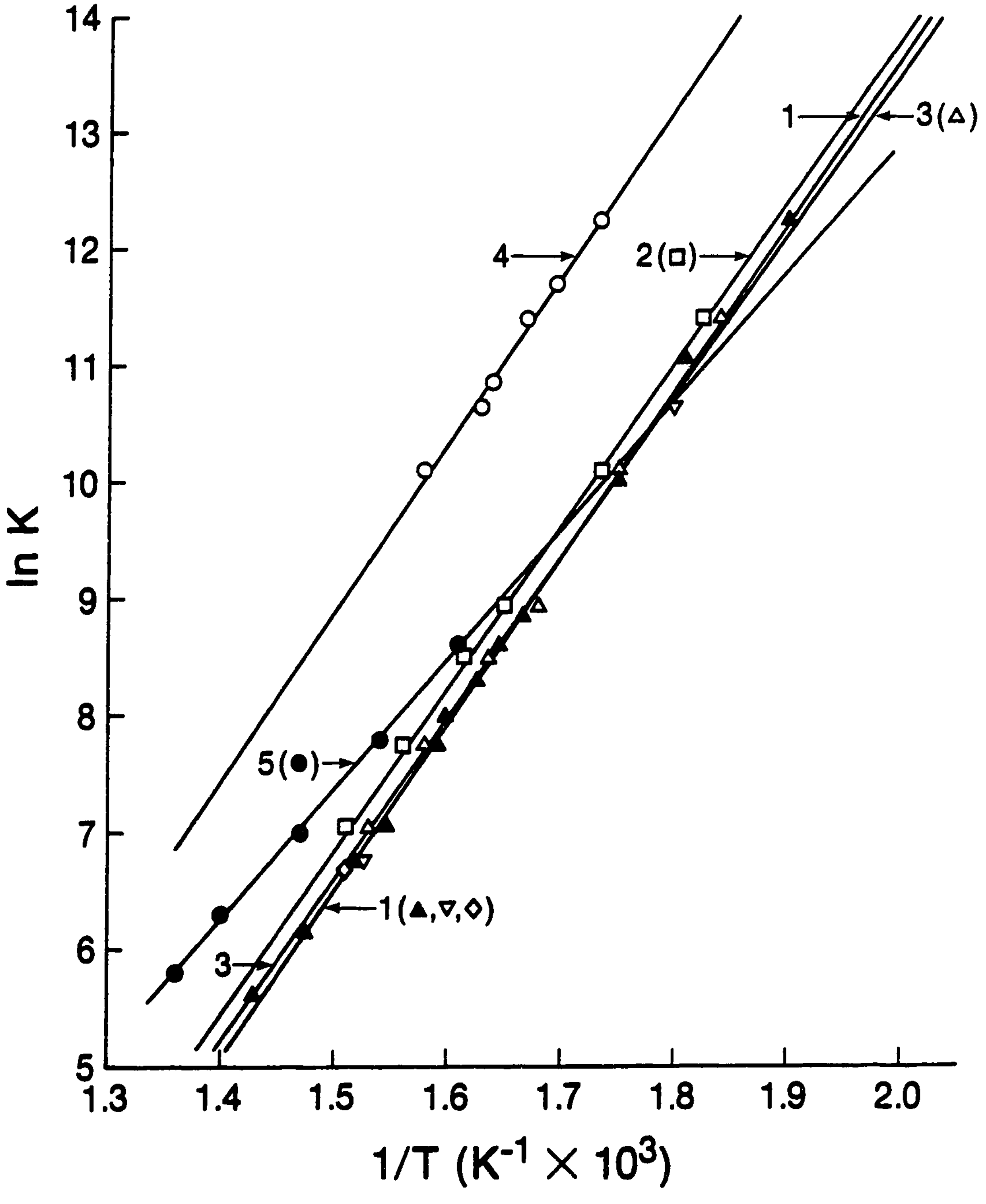

Figure 6.8 van't Hoff plots of K_1 for reaction (6.1): $DO^- + DOD = DO^- \cdot DOD$. Numbers identify different sources of data. Plots 1, 2 and 3 correspond to data obtained with thermocouples 1, 2 and 3 and lead to $-\Delta H_1^\circ$ (28.5, 27.5, 27.7 kcal/mol), $-\Delta S_1^\circ$ (29.9, 27.7, 28.5 cal/(deg mol)). Plot 4, Meot-Ner [13]: $-\Delta H_1^\circ$ = 26.8 kcal/mol, $-\Delta S_1^\circ$ = 24.2 cal/(deg mol). Plot 5, early PHPMS results [1]: $-\Delta H_1^\circ$ = 22.5 kcal/mol, $-\Delta S_1^\circ$ = 19.1 cal/(deg mol).

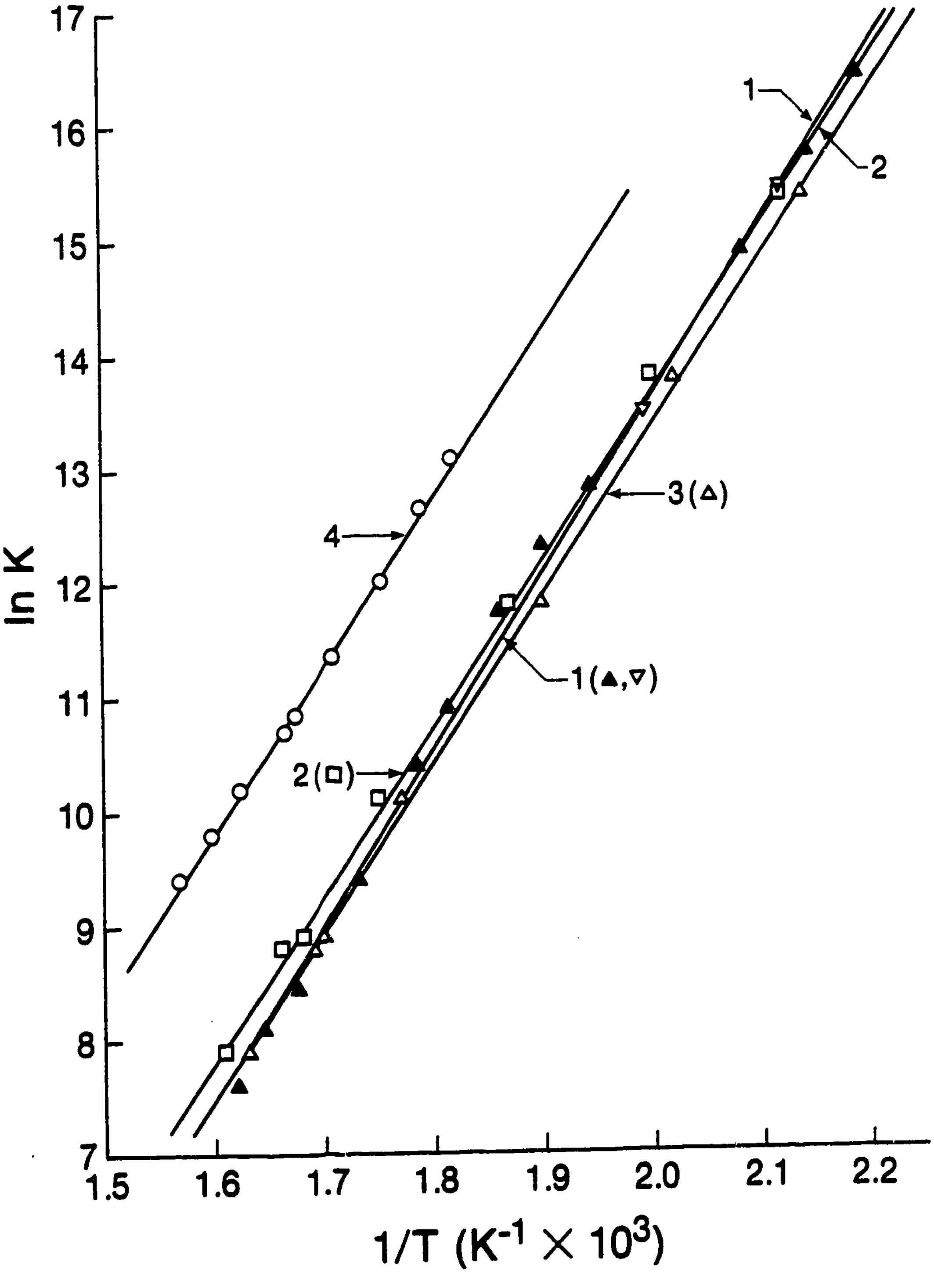

Figure 6.9 van't Hoff plots of K_2 for reaction (6.2): $CH_3O^- + CH_3OH = CH_3O^- \cdot HOCH_3$. Plots 1, 2 and 3 correspond to data with thermocouples 1, 2 and 3 and lead to $-\Delta H_2^o$ (30.7, 29.3, 29.4 kcal/mol) and $-\Delta S_2^o$ (34.2, 31.3, 32.3 cal/(deg mol)). Plot 4, Meot-Ner [13]: $-\Delta H_2^o = 29.3$ kcal/mol, $-\Delta S_2^o = 27.6$ cal/(deg mol).

Table 6.1

a. Energy data in kcal/mol, entropies in cal/(deg mol). Standard state, 1 atm.

b. Average temperature of van't Hoff plot.

c. Average of values given by Meot-Ner [13].

d. Level of calculation beyond Hartree-Fock given in brackets after author's name. ΔE_e^o is the electronic energy. ΔH^o is the enthalpy change at 298 K, unless otherwise noted, where zero point energies and thermal energies of reactants as well as $\Delta(pV)$ term is included. ΔS^o for 298 K.

e. Estimate obtained by adding change from ΔE_e^o to ΔH^o equal to +0.9 kcal/mol, evaluated by Jorgensen et al. [8].

f. Evaluated on the basis of geometries and normal frequencies, see Table 6.2, of reactants obtained by Jorgensen et al. [8, 33].

g. No diffuse s and p functions in basis set and no correction for electron correlation.

h. Estimate of ΔH^o from ΔE_e^o(DZ+P), due to Dixon et al. [39].

k. Evaluated in present work on the basis of geometries and normal vibrations due to Dixon et al. [39], see Table 6.3.

l. ΔS_1^o due to Meot-Ner and Sieck [13] with correction for mass dependent discrimination [29].

m. ΔH_1^o and ΔS_1^o calculated for 600 K.

Table 6.1 Thermochemical and theoretical data[a] for reactions (6.1) and (6.2)

$HO^- + HOH = HO^- \cdot HOH$

Experimental data

	T^b	$-\Delta H^o$	$-\Delta S^o$
(1990) Present work	600	27.6	28.1
(1986) Meot-Ner [13]	600	26.8[c]	(22.8)[c]
			(24.2)[l]
(1970) Arshadi [1]	660	22.5	19.1
(1971) Payzant [2]	~600	24.0	20.8

Theoretical calculations[d]

	$-\Delta E_e^o$	$-\Delta H^o$	$-\Delta S^o$
(1976) Diercksen [5] (CI)	28.2	~27.3[e]	-
(1974) Ikuta [6] (MP3)	28.0	~27.1[e]	-
(1974) Ikuta [6] (CI)	27.1	~26.2[e]	-
(1986) Jorgensen [8] (MP2)	27.5	26.6	24.6[f]
	(26.5)[m]	(24.6)[f,m]	

$CH_3O^- + CH_3OH = CH_3O^- \cdot HOCH_3$

Experimental data

	T	$-\Delta H^o$	$-\Delta S^o$
present work	550	29.3	31.8
Meot-Ner [13]	590	29.3[c]	27.6[c]

Theoretical calculations

	$-\Delta E_e^o$	$-\Delta H^o_{298}$	$-\Delta S^o_{298}$
Dixon [39]	25.9[g]	~25.6[h]	~27.9[k]
Jorgensen [40]	25.7[g]	~25.4[h]	

common is a difference in the temperature trends of the data where larger ΔH^o values are compensated by larger ΔS^o values; see, for example, the plot from earlier determinations for reaction (6.1) from this laboratory [1] and present determinations in Figure 6.8. This kind of difference may be attributed to errors of temperature measurement at high temperatures. Thus, in the earlier measurement [1], the actual temperature of the sampled reaction system at high temperatures might have been lower than the assumed temperature based on the thermocouple reading. An error of ~30 K at the highest temperature of the measurement, 740 K, would be required to bring the previous [1] and present results to agreement. Measurements of the temperature of the reacting gases is difficult at the high temperatures required when strongly bonded complexes are involved [22, 28].

The divergence of the present results and Meot-Ner's [13] determination should not be due to temperature errors but some other instrumental artefact. A possible cause would be a faulty correction for mass dependent ion transmission of the quadrupole mass spectrometer [13]. Such a correction is not required for the magnetic instrument used in the present work. A recent re-examination of the mass dependent transmission of the Sieck/Meot-Ner apparatus leads [29] to a transmission correction for the pair $HO^-/HO^-\cdot HOH$ which decreases K_1 by a factor of approximately 2. This corresponds to a decrease of ΔS_1^o by 1.4 cal/(deg mol) and an improved ΔS_1^o = -24.2 cal/(deg mol) which is also given in Table 6.1. The re-examination of the transmission of the pair $CH_3O^-/CH_3O^-\cdot HOCH_3$ showed that essentially no correction is required for this pair [29]. No correction was made [29] for the response of the ion detector to ions of different mass and different chemical composition. Since the detector was a conversion dynode electron multiplier operated in the analogue (i.e., current detection) mode [30], such a correction is required. However, previous experience with this device indicates that the corrections needed are small, i.e., less than by a factor of two [30]. In the present instrument, which uses ion counting detection, a correction for the response of the electron multiplier is not required.

It is possible that collisional dissociation of the adducts such as $HO^-\cdot HOH + CH_4 \rightarrow HO^- + HOH + CH_4$, occurring in the ion acceleration and mass analysis region of the present apparatus, could be reducing the observed ion ratios and thus also the measured equilibrium constants; see Chapter 3. In order to examine whether such a process occurs in the acceleration region, the total acceleration voltage was changed by a factor of two. In other experiments the potential between the ion source and the first ion acceleration electrode, see Figure 6.1, was decreased by a factor of 10. The ion ratios measured under these new conditions were found to be essentially invariant. Mass dependent discrimination, due to deflection of the electron beam by stray magnetic fields from the mass analysis magnet, see Chapter 1, was also shown not to be present, since x, y refocusing of the electron beam at different ion masses produced less than 5% change of the ion intensities. Therefore, the reasons for the remaining discrepancy between the present and the Meot-Ner [13] results are not known at this time.

6.3b Comparison of $\Delta H°$ Values with Other Work

The present $\Delta H_1°$ values are in good agreement with the theoretically evaluated $\Delta H_1°$ (see Table 6.1). The evaluation of $\Delta H_T°$ at a given temperature T from the electronic energies $\Delta E_e°$ obtained from the MO calculation involves [8, 31] the terms shown in equation (6.12), where $\Delta E_v°$ is the difference in the

$$\Delta H_T^o = \Delta E_e^o + \Delta E_v^o + \Delta\Delta E^o_{v,T} + \Delta E^o_{rot,T} + \Delta E^o_{trans,T} + \Delta(pV) \quad (6.12a)$$

$$\Delta H_T^o = \Delta E_e^o + \Delta E_v^o + \Delta\Delta E^o_{v,T} - 7/2\ RT \quad (6.12b)$$

vibrational zero point energies, while the remaining ΔE^o terms are the vibrational, rotational and translational energy differences at temperature T. Since rotation and translation are classical at the temperature of interest, the equation for reaction (6.1) reduces to the form shown in (6.12b). Therefore only the frequencies of the normal vibrations are required to evaluate $\Delta H^o_{1,T}$ from ΔE_e^o. Using computed frequencies, Jorgensen et al. [8] obtained ΔE_v^o = +2.1 kcal/mol and $\Delta\Delta E^o_{v,298}$ = +0.9 kcal/mol and these led via equation (6.12b) to $\Delta H^o_{1,298}$ = -26.6 kcal/mol. The value $\Delta H^o_{1,600}$ = -26.5 kcal/mol is obtained in the present work in an analogous manner [31, 32] using Jorgensen's computed frequencies [33]. It should be noted that the van't Hoff plots were interpreted under the assumption that the slope, i.e., the ΔH^o, is constant. Therefore, the ΔH^o deduced from the plots corresponds to a ΔH^o near the average temperature used in the plot and this is ~600 K, and the comparison with the theoretically evaluated ΔH^o and ΔS^o values should be made at this temperature. As it turns out, due to cancellations, both ΔH_1^o and ΔS_1^o are essentially temperature independent between 300 and 600 K; see Table 6.1. Jorgensen's [8] results show that the change from the electronic energy ΔE_e^o, evaluated with electron correlation correction, to the $\Delta H^o_{1,298}$ corresponds to +0.9 kcal/mol. One can assume that a similar change would occur between ΔE_e^o and $\Delta H^o_{1,298}$ for the values calculated by Diercksen et al. [5] and Ikuta [6], and the $\Delta H^o_{1,298}$ obtained with this correction are also shown in Table 6.1. All these theoretical ΔH_1^o values are seen to be within less than 1 kcal/mol of Jorgensen's value: ΔH_1^o = -26.6 kcal/mol which is close to the -27.6 kcal/mol present experimental result and -26.8 kcal/mol result of Meot-Ner and Sieck

[13]. The probable error in the experimental ΔH_1° can be estimated to be ±2 kcal/mol. This error is an estimate based on comparison of results from van't Hoff plots obtained at different conditions; see, for example, Figure 6.8. The standard deviation in a given plot is generally much smaller, ~0.5 kcal/mol.

The error in the theoretical calculations for ΔH_1° is also difficult to estimate but may be assumed at ±2 kcal/mol for the ΔE_e° evaluations [5, 6, 8] and probably another 0.5 kcal/mol in the conversion from ΔE_e° to ΔH_1° due to errors in the normal frequencies [8] and neglect of anharmonicity [34-37]. Particularly large anharmonicities occur for the symmetric and antisymmetric O-H-O stretch, and these vibrations are also strongly coupled [36, 37]. Considering the above uncertainties, the agreement between the two most recent experimental ΔH_1° values and the theoretical ΔH_1° results in Table 6.1 is very good.

Golub and Steiner [38] measured, some time ago, the efficiency of electron photodetachment from $HO^-{\cdot}HOH$. They observed a very gradual onset with increasing photon energy and assumed that this is due to a dissociative transition: $HO^-{\cdot}HOH \rightarrow OH + HOH + e$. Combining the threshold (2.95 eV) with the electron affinity of OH (1.828 eV), a bond energy of 25.8 kcal/mol for HO^--HOH is obtained. However, Brauman et al. [14] have pointed out that the equilibrium geometry of the neutral $HO{\cdot}HOH$, whose bond energy can be estimated at ~4 kcal/mol, is close to the geometry of the negative ion $HO^-{\cdot}HOH$ and therefore, due to more favorable Frank-Condon factors, the photodetachment threshold might be due to the transition $HO^-{\cdot}HOH \rightarrow HO{\cdot}HOH + e$. If this is the case, the HO^--HOH bond energy predicted by the threshold would be: 25.8 kcal/mol + 4 kcal/mol = 29.8 kcal/mol. This value, in the absence of internal energy in $HO^-{\cdot}HOH$ (hot bands), represents an upper limit to the bond energy. Furthermore, the onset [38] is very gradual and could easily be 0.1 to

0.2 eV lower on the basis of Steiner's data. Therefore, Steiner's results with the Brauman interpretation are consistent with the value of ~27 kcal/mol indicated by the recent experimental and theoretical results of Table 6.1. Obviously modern experimental photodetachment data for $HO^-{\cdot}HOH$ would be of great interest.

The agreement between the present experimental ΔH_2^o value for the association of the methoxide anion with methanol, ΔH_2^o = -29.3 kcal/mol, and Sieck and Meot-Ner's result, -29.3 kcal/mol, is very good (Table 6.1). Again a probable error of ±2 kcal/mol can be assumed. Unfortunately, for this system, only two theoretical calculations, due to Weil and Dixon [39] and Jorgensen et al. [40], are available and both of these involve basis sets, DZ+P and $6\text{-}31G^*$, respectively, which are without diffuse basis functions. Electron correlation and ΔH^o evaluation were also not included. From comparisons with more accurate calculations of related systems [8], the expected changes at the various levels of calculation can be estimated and the authors [39] deduce an approximate value of $\Delta H_2^o \approx -25.6$ kcal/mol (Table 6.1). A similar value, $\Delta H_2^o \approx -25.4$ kcal/mol, can be deduced from the ΔE_e^o for reaction (6.2) of Jorgensen et al. [40]. This result is lower but still compatible with the present experimental results considering the larger error expected for the theoretical estimate.

The present experimental value, $\Delta H_2^o \approx -29$ kcal/mol, is very much larger than the -19.3 ± 3 kcal/mol result obtained by Brauman [14] from the electron photodetachment threshold of $CH_3O^-{\cdot}HOCH_3$.

6.3c The Entropy Changes ΔS_1^o and ΔS_2^o

The geometries and the normal vibrations of HO^-, HOH and $HO^-{\cdot}HOH$ obtained in the theoretical calculations by Jorgensen et al. [8, 33] can be used to evaluate the third law entropies of the above reactants [32, 41] and thus also

ΔS_1^o. Shown in Table 6.2 are the translational, rotational and vibrational entropy terms calculated in this work from these data [8, 33]. Only the lower frequencies for $HO^-{\cdot}HOH$ are shown since it is only these that make significant contributions to the vibrational entropies. The resulting entropy changes at 298 and 600 K are essentially identical due to cancellations between the entropies of the products and the reactants. The value ΔS_1^o = -24.6 cal/(deg mol) is very close to the transmission corrected value of Meot-Ner [13, 29] of -24.2 cal/(deg mol) and somewhat smaller than the present result of -28.1 cal/(deg mol). The error in the theoretical ΔS_1^o is difficult to estimate. Of greatest importance are the low frequency vibrations which make the major contributions to the vibrational entropy of $HO^-{\cdot}HOH$. The lowest vibrational frequency (164.2 cm^{-1}) corresponds to the torsional oscillation of the two OH groups around the O-H-O axis. The entropy due to this motion can be evaluated also on the basis of a hindered rotation [32] using a barrier of 1.4 kcal/mol which corresponds to the difference between cis and trans configurations [8] of $HO^-{\cdot}HOH$ and also as a free rotation. The S^o terms obtained at 298 K are not significantly different: 2.5 (vib), 3.25 (h.rot) and 3.8 (f.rot) cal/(deg mol). The present experimental $-\Delta S_1^o$ is ~3 cal/(deg mol) higher than the theoretical result. While this could be due to experimental error, there might be also problems with the theoretical results. Thus the magnitudes of the three to four softest frequencies in $HO^-{\cdot}HOH$ might be too low. Also the assumed harmonicity of these vibrations in the ab initio and entropy calculation is not justified.

Theoretically evaluated ΔS_2^o based on the geometry and frequencies calculated by Dixon et al. [39] are shown in Table 6.3. The entropy changes in cal/(deg mol) calculated in the present work are -27.9 (298 K) and -26.6 (600 K). These values are very close to Meot-Ner's result of -27.6 cal/degree mol [13] and some 3 cal/(deg mol) lower than the present value of -31.8 cal/(deg mol).

Table 6.2 Theoretical[a] ΔS° for reaction: $OH^- + HOH = OH^-\cdot HOH$

	S°_{Trans}	S°_{Rot}	S°_{Vib}	S°_{Total}
HO^-	34.5	6.7	~ 0	41.2 [41.2][i]
	(37.9)	(8.1)	(~ 0)	(46.0) [46.1][i]
HOH	34.6	10.4	~ 0	45.0 [45.0][j]
	(38.1)	(12.5)	(0.1)[b]	(50.7) [50.8][j]
$OH^-\cdot HOH$	36.6	20.1	2.5[c], 1.2[d], 0.7[e], 0.5[f]	61.6
	(40.1)	(22.1)	(3.9)[c], (2.4)[d], (1.8)[e], (1.4)[f], (0.3)[g], (0.1)[h]	(72.1)

$$\Delta S_1^\circ\ (300\ K) = S^\circ\ (OH^-\cdot HOH,\ 300\ K) - S^\circ\ (HOH,\ 300\ K) - S^\circ\ (HO^-,\ 300\ K)$$

$$= -24.6\ cal/(deg\ mol)$$

$$\Delta S_1^\circ\ (600\ K) = -24.6\ cal/(deg\ mol)$$

---

a. Values for entropy at 298 K without parentheses and 600 K with parentheses in cal/(deg mol) for standard state, 1 atm, based on geometries of reactants and vibrational frequencies (cm^{-1}): HO^- (3739.0); HOH (1826.6[b], 4070.7, 4189.0); $OH^-\cdot HOH$ (164.2[c], 342.8[d], 486.6[e], 604.0[f], 1390.4[g], 1899.3[h], 2373.1, 3941.5, 4086.4). From Jorgensen et al. [8, 33].

i. JANAF tables.

j. Calculated by Meot-Ner [13].

Table 6.3 Theoretical[a] ΔS° for reaction: $CH_3O^- + CH_3OH = CH_3O^- \cdot HOCH_3$

	S°_{Trans}	S°_{Rot}	S°_{Vib}	S°_{Total}
CH_3O^-	36.3	16.3	0.2	52.8 [55.6][b]
	(39.7)	(18.4)	(2.0)	(60.1) [60.6][b]
CH_3OH	36.4	18.9	1.4	56.7 [57.2][b]
	(39.8)	(21.0)	(4.8)	(65.6) [66.7][b]
$CH_3O^- \cdot HOCH_3$	38.4	24.7	18.5	81.6
	(41.8)	(26.8)	(30.5)	(99.1)

ΔS_2° (300 K) = -27.9 cal/(deg mol)

ΔS_2° (600 K) = -26.6 cal/(deg mol)

---

a. Values in cal/(deg mol), standard state, 1 atm, based on geometries of reactants and vibrational frequencies in the paper by Weil and Dixon [39]. Values without parentheses 298 K, values with parentheses 600 K.

b. Calculated by Meot-Ner [13].

The calculations of Dixon et al. [39] are of lower accuracy, and it is difficult to assess the error expected for the entropy evaluation.

REFERENCES

1. M. Arshadi and P. Kebarle, J. Phys. Chem., 74, 1483 (1970).
2. J. D. Payzant, R. Yamdagni and P. Kebarle, Can. J. Chem., 49, 3308 (1971).
3. W. P. Kraemer and G. H. F. Diercksen, Theor. Chim. Acta, 23, 398 (1972).
4. M. D. Newton and S. Ehrenson, J. Am. Chem. Soc., 93, 4971 (1971).
5. B. O. Roos, W. P. Kraemer and G. H. F. Diercksen, Theor. Chim. Acta, 42, 77 (1976).
6. S. Ikuta, J. Comput. Chem., 5, 374 (1984).
7. C. M. Rohlfing, L. C. Allen, C. M. Cook and H. B. Schlegel, J. Chem. Phys., 78, 2498 (1983).
8. J. Gao, D. S. Garner and W. L. Jorgensen, J. Am. Chem. Soc., 108, 4784 (1986).
9. G. Caldwell, M. D. Rozeboom, J. P. Kiplinger and J. E. Bartmess, J. Am. Chem. Soc., 106, 4660 (1984).
10. S. G. Lias, J. E. Bartmess, J. F. Liebman, J. L. Holmes, R. D. Levin and W. G. Mallard, J. Phys. Chem. Ref. Data, 17, Suppl. No. 1 (1988).
11. G. Caldwell and P. Kebarle, unpublished work.
12. H. van der Wel and N. M. M. Nibbering, Recl. Trav. Chim. Pays-Bas, 107, 491 (1988).
13. M. Meot-Ner and L. W. Sieck, J. Phys. Chem., 90, 6687 (1986).
14. C. R. Moylan, J. A. Dodd, H. Chan-Chung and J. I. Brauman, J. Chem. Phys., 86, 5350 (1987).
15. P. Kebarle, G. W. Dillow and G. J. C. Paul, Adv. Mass Spectrom., 11, 506 (1988).
16. L. S. Crocker, G. J. C. Paul and P. Kebarle, in preparation.

17. S. D. Tanner, G. I. Mackay and D. K. Bohme, Can. J. Chem., 59, 1615 (1981).
18. G. I. Mackay, A. B. Rakshit and D. K. Bohme, Can. J. Chem., 60, 2594 (1982).
19. P. Kebarle, W. R. Davidson, M. A. French, J. B. Cummings and T. B. McMahon, Faraday Discuss. Chem. Soc., 64, 220 (1978).
20. G. I. Mackay and D. K. Bohme, J. Am. Chem. Soc., 100, 327 (1978).
21. P. M. Hierl, A. F. Ahrens, M. J. Henchman, A. A. Viggiano, J. F. Paulson and D. C. Clary, Faraday Discuss. Chem. Soc., 85, 37 (1988).
22. P. Kebarle, "Techniques of Chemistry: Techniques for the Study of Ion-Molecule Reactions". Editors J. M. Farrar and W. H. Saunders, Jr. Wiley-Interscience. New York (1988). Chapter 5.
23. G. J. C. Paul and P. Kebarle, in preparation.
24. W. Lindinger and D. L. Albritton, J. Chem. Phys., 62, 3517 (1975).
25. T. B. McMahon, private communication.
26. V. M. Bierbaum, J. J. Grabowski, and C. H. DePuy, J. Phys. Chem., 88, 1389 (1984).
27. L. G. Christophorou, "Atomic and Molecular Radiation Physics". Wiley-Interscience. New York (1971).
28. K. Hiraoka, H. Takimoto and S. Yamabe, J. Phys. Chem., 90, 5910 (1986).
29 L. W. Sieck, private communication.
30. L. W. Sieck, J. Phys. Chem., 89, 5552 (1985).
31. J. E. Del Bene, H. D. Mettee, M. J. Frisch, B. T. Luke and J. A. Pople, J. Phys. Chem., 87, 3279 (1983).
32. K. S. Pitzer, "Quantum Chemistry". Prentice-Hall. Englewood Cliffs, New Jersey (1961).

33. W. L. Jorgensen, private communication.

34. J. A. Pople, R. Krishnan, H. B. Schlegel and J. S. Binkley, Int. J. Quantum Chem., 13, 225 (1979).

35. J. A. Pople, H. B. Schlegel, R. Krishnan, D. J. Defrees, J. S. Binkley, M. J. Frisch, R. A. Whiteside, R. F. Hout and W. J. Hehre, Int. J. Quantum Chem., 15, 269 (1981).

36. G. V. Yukhnevich, E. G. Kokhanova, A. I. Pavlyuchko and V. V. Volkov, J. Mol. Struct. (Theochem), 122, 1 (1985).

37. V. Spirko, W. P. Kraemer and A. Cejchan, J. Mol. Spectrosc., 136, 340 (1989).

38. S. Golub and B. Steiner, J. Chem. Phys., 49, 5191 (1968).

39. D. A. Weil and D. A. Dixon, J. Am. Chem. Soc., 107, 6859 (1985).

40. W. L. Jorgensen and M. Ibrahim, J. Comput. Chem., 2, 7 (1981).

41. M. A. Paul, "Principles of Chemical Thermodynamics". McGraw-Hill Book Co. New York (1951).

CHAPTER 7

ELECTRON AFFINITIES OF CYCLIC UNSATURATED DICARBONYLS: MALEIC ANHYDRIDES, MALEIMIDES AND CYCLOPENTENEDIONE

7.1 Introduction

It has been known for some time that the cyclic unsaturated dicarbonyl compounds of structure I and II can capture electrons and form stable radical anions [1-4].

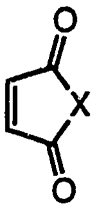

I

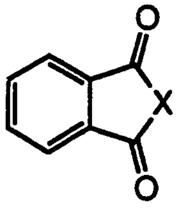

II

X = (O, NH, CH_2)

In particular the maleic anhydride (I, X = O), phthalic anhydride (II, X = O), maleimide (I, X = NH) and phthalimide (II, X = NH) radical anions are known to form by one electron reductions of the neutral parent compounds in solution [1,2]. Also in the gas phase, long lived negative ions have been observed [4], and some electron affinities have been determined. Compounds I and II resemble the benzoquinones and naphthaquinones with regard to electron capture. Thus, they also act as similar electron acceptors in charge transfer complexes and also, but to a much lesser extent, have biological significance as electron carriers [5-7].

1. A version of this chapter has been published: G. J. C. Paul and P. Kebarle, J Am. Chem. Soc., 111, 464 (1989).

A large number of electron affinities have been reported by Kebarle [8, 9] which were obtained by measuring electron transfer (et) equilibria (reaction (7.1)) in the gas phase with the PHPMS.

$$A^- + B = A + B^- \quad \text{(et)} \qquad (7.1)$$

$$e + B = B^- \quad \text{(a)} \qquad (7.2)$$

$$\Delta G^o = -RT \ln K \qquad (7.3)$$

$$-\Delta H_a^o(B) \approx EA(B) \qquad (7.4)$$

The ΔG_1^o and ΔH_1^o values obtained by making measurements with a number of compounds can be combined into a scale of relative electron attachment free energies ΔG_a^o and ΔH_a^o; see equation (7.2). By calibrating the scale to the literature value for ΔG_a^o and ΔH_a^o of one compound (SO_2, primary standard), the rest of the absolute values are obtained [8]. In general, the structures and internal motions of B and B^- are very similar, which leads to very similar heat capacities $c_p(B)$ and $c_p(B^-)$. As a consequence, the electron affinity, which relates to electron attachment at 0 K, and the enthalpy change ΔH_a^o, at 298 K, are numerically very similar such that $EA \approx -\Delta H_a^o$ within 1-2 kcal/mol. Thus, not only ΔG_a^o and ΔH_a^o values are obtained but also fairly accurate EA. The ΔG_a^o and the ΔH_a^o are of interest in their own right, since in many actual experimental situations (thermal energies) it is these quantities and not the EA that are relevant.

After the determination of ΔG_a^o, ΔH_a^o and EA for the quinones [9], it was natural to extend the measurements to the cyclic dicarbonyls and these determinations are reported and discussed in this chapter.

7.2 Experimental

The measurements of the electron transfer equilibria (7.1) were performed with the pulsed electron high pressure mass spectrometer, PHPMS. The apparatus and general methodology are described in Chapters 1-3. The concentrations in the ion source were chosen to be sufficiently high so the kinetic stage, i.e., the approach to equilibrium, was short (less than ~0.2 ms). This generally occurred for concentrations of A and B in the millitorr range. Methane at pressures in the 2-4 torr range was used as the bath gas. In constant temperature runs the ratio of partial pressures of A and B were changed within a factor of 5-10 to establish that K was invariant. K values for the van't Hoff plots were determined both at static temperatures and as the temperature was slowly decreased (dynamic run).

In the majority of measurements A^- and B^- were the dominant ions. In all cases it was checked that side reactions, if any, were much slower than equilibrium rates (7.1).

All the compounds used were obtained from commercial sources.

7.3 Results and Discussion

7.3a Thermochemical Data for Electron Attachment

The equilibrium constants K_{et} of the electron transfer reactions (7.1) determined at 423 K were used to evaluate $\Delta G_{et}^{o} = -RT\ln K_{et}$. The resulting ΔG_{et}^{o} values are shown in Figure 7.1, combined in a scale of gradually increasing electron attachment free energies, ΔG_a^o. The scale contains a number of reference compounds, mostly substituted quinones and nitrobenzenes, whose ΔG_a^o (equation (7.2)) were determined in previous work [8, 9], and the present relative values, i.e., the ΔG_{et}^{o}, were used to obtain absolute values, ΔG_a^o, for the new compounds by calibrating to the reference

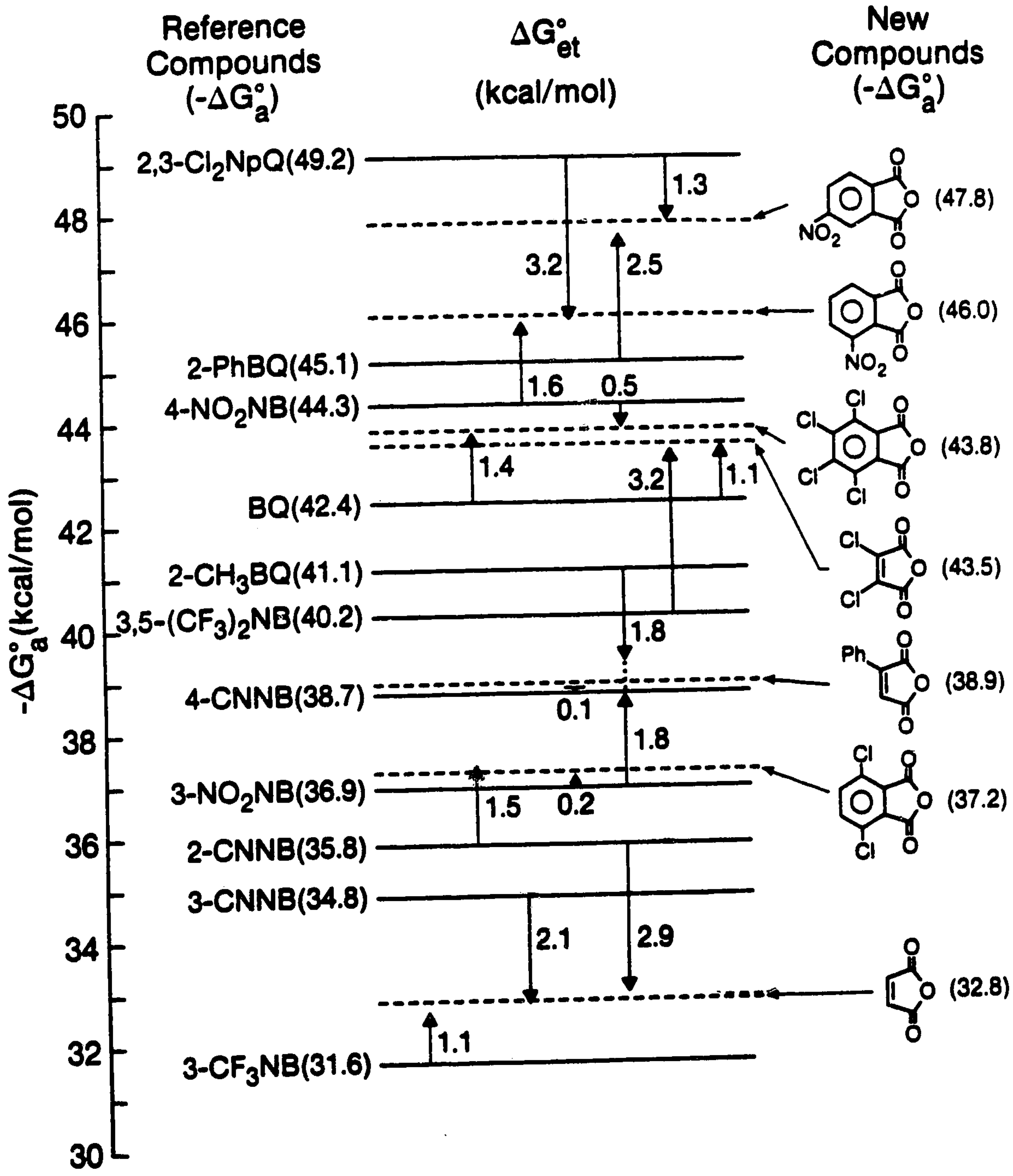
Reference Compounds (-ΔG°a)
ΔG°et (kcal/mol)
New Compounds (-ΔG°a)
50
48
46
44
42
40
38
36
34
32
30
-ΔG°a (kcal/mol)
2,3-Cl2NpQ(49.2)
2-PhBQ(45.1)
4-NO2NB(44.3)
BQ(42.4)
2-CH3BQ(41.1)
3,5-(CF3)2NB(40.2)
4-CNNB(38.7)
3-NO2NB(36.9)
2-CNNB(35.8)
3-CNNB(34.8)
3-CF3NB(31.6)
1.3
3.2
2.5
1.6
0.5
1.4
3.2
1.1
1.8
0.1
1.8
1.5
0.2
2.1
2.9
1.1
(47.8)
(46.0)
(43.8)
(43.5)
(38.9)
(37.2)
(32.8)
O
NO2
Cl
Ph

Figure 7.1 Values for electron transfer free energies ΔG_{et}° measured at 423 K. On the left side are reference compounds whose electron attachment free energies ΔG_a° for the process $e + B = B^-$ were determined in earlier work [8, 9]. Lengths of arrows correspond to given ΔG_{et}°. ΔG_a° deduced for new compounds are given in parentheses in right column.

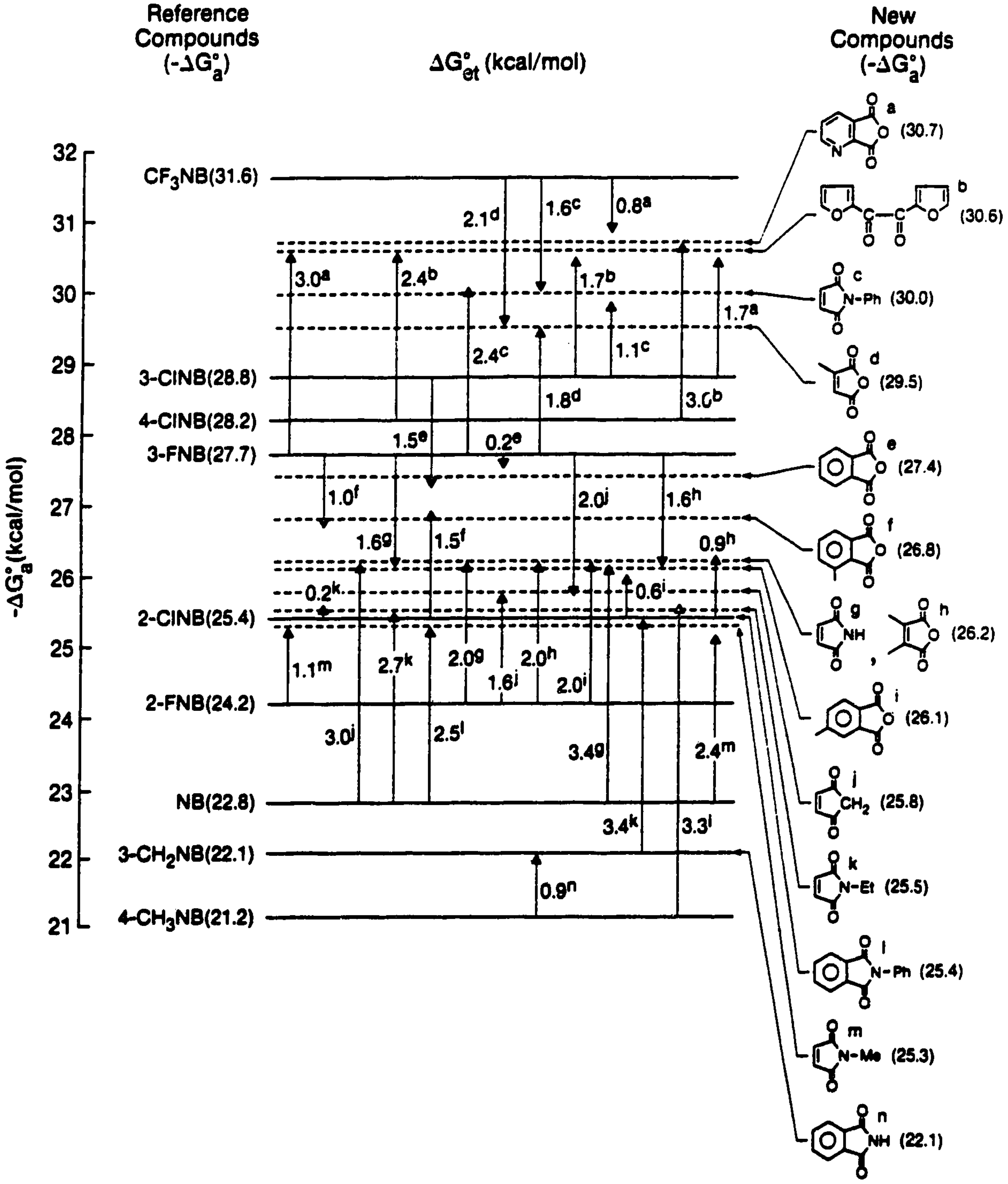
Reference Compounds ($-\Delta G^\circ_a$)
ΔG°_{et} (kcal/mol)
New Compounds ($-\Delta G^\circ_a$)
$-\Delta G^\circ_a$(kcal/mol)
32
31
30
29
28
27
26
25
24
23
22
21
CF_3NB(31.6)
3-ClNB(28.8)
4-ClNB(28.2)
3-FNB(27.7)
2-ClNB(25.4)
2-FNB(24.2)
NB(22.8)
$3\text{-}CH_3NB$(22.1)
$4\text{-}CH_3NB$(21.2)
2.1^d
1.6^c
0.8^a
3.0^a
2.4^b
1.7^b
1.7^a
1.1^c
2.4^c
1.8^d
3.0^b
1.5^e
0.2^e
1.0^f
2.0^j
1.6^h
1.6^g
1.5^f
0.9^h
0.2^k
0.6^i
1.1^m
2.7^k
2.0^g
2.0^h
1.6^j
2.0^i
3.0^j
2.5^l
3.4^g
2.4^m
3.4^k
3.3^l
0.9^n
a (30.7)
b (30.6)
c N-Ph (30.0)
d (29.5)
e (27.4)
f (26.8)
g NH
h (26.2)
i (26.1)
j CH_2 (25.8)
k N-Et (25.5)
l N-Ph (25.4)
m N-Me (25.3)
n NH (22.1)

Figure 7.1 continued

compounds; see Figure 7.1. For most of the new compounds, electron transfer equilibria with two or more reference compounds were measured and the resulting multiple thermodynamic cycles are seen to be consistent within less than 0.3 kcal/mol; see Figure 7.1.

The ΔG_a^o at 423 K for the 21 compounds of structures I and II obtained from Figure 7.1 are given in Table 7.1. For a more limited number of compounds determinations of the equilibrium constants K_{et} at different temperatures were performed also. The resulting van't Hoff plots are shown in Figure 7.2. Plots of a similar nature were obtained for K values determined by static and dynamic methods; see Plots 1a, 1b in Figure 7.2. The ΔH_{et}^o and ΔS_{et}^o obtained from the slopes and the intercepts of the plots were used to construct the ΔH_{et}^o and ΔS_{et}^o scales shown in Figures 7.3 and 7.4. The consistency in the multiple ΔH_{et}^o determinations is somewhat less satisfactory (~0.5 kcal/mol) than that observed in the ΔG_{et}^o scale (Figure 7.1). The largest relative inconsistencies, ~2 cal/(deg mol), are seen in the ΔS_{et}^o scale (Figure 7.4). It should be noted that the ΔH_a^o and ΔS_a^o of the reference compounds are also uncertain to 1-2 kcal/mol and to ~2 cal/(deg mol) [8-10] so that an error of ±2 kcal/mol should be assumed for the ΔH_a^o values and ±3 cal/(deg mol) for the ΔS_a^o values.

The ΔS_a^o of the compounds for which van't Hoff plots were not obtained were estimated on the basis of ΔS_a^o determined for compounds of similar structure. For these compounds the errors in ΔH_a^o and ΔS_a^o are even larger and if one is interested in consistent comparisons between the compounds, the ΔG_a^o at 423 K are to be preferred by far.

The electron attachment enthalpies ΔH_a^o, given in Table 7.1, originate from the ΔH_a^o scale in Figure 7.3 for the compounds for which van't Hoff plots

Table 7.1 Thermochemical Data for Electron Attachment: $e + B = B^-$

B	$-\Delta G^\circ_a$[a]		$-\Delta S^\circ_a$[b]	$-\Delta H^\circ_a$[c]	EA[d] lit.	B	$-\Delta G^\circ_a$[a]		$-\Delta S^\circ_a$[b]	$-\Delta H^\circ_a$[c]	EA[d] lit.
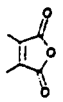	26.2	1.14	2	26.8	1.16	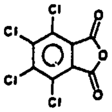	43.8	1.90	(3)	45.1	1.95, 1.7[g] 1.6[h]
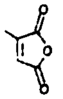	29.5	1.28	(1)	29.9	1.29	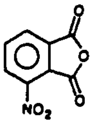	46.0	1.99	(3)	47.3	2.05
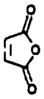	32.8 (32.7)[f]	1.42	1	33.2	1.44, 1.4[e] 1.4,[f] 1.3,[g] 1.6[h]	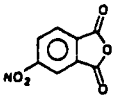	47.8	2.07	(3)	49.1	2.13
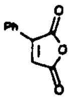	38.9	1.69	(3)	40.2	1.78	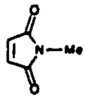	25.3	1.10	(1)	25.7	1.12
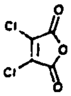	43.5	1.89	(1)	43.9	1.90	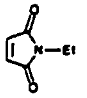	25.5	1.11	(1)	25.9	1.12
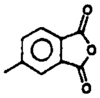	26.1	1.13	(3)	27.4	1.19	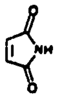	26.2	1.14	1	26.6	1.16
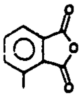	26.8	1.16	(3)	28.1	1.22	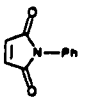	30.0	1.30	3	31.4	1.36
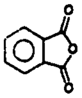	27.4 (27.4)[f]	1.19	3	28.7	1.24, 1.20[f] 1.3,[g] 1.2[h]	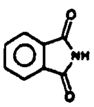	22.1	0.96	(3)	23.4	1.01
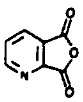	30.7	1.33	(3)	32.0	1.39, 1.3[g]	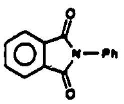	25.4	1.10	(3)	26.6	1.16
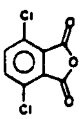	37.2	1.61	(3)	38.5	1.67	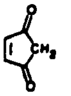	25.8	1.12	(1)	26.2	1.14
						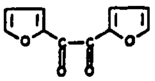	30.6	1.33	(1)	31.0	1.34

a. ΔG_a° at 423 K in kcal/mol. Estimated error ±1 kcal/mol, values in eV also given, from Figure 7.1. b. ΔS_a° in cal/(deg mol). From van't Hoff plots, Figures 7.2 and 7.4. Estimated values in parentheses. Estimated error ±3 cal/(deg mol). c. ΔH_a° in kcal/mol. From van't Hoff plots, Figures 7.2 and 7.3, or from estimated ΔS_a°, see ΔS_a° in parentheses. Estimated error ±2 kcal/mol. d. EA in eV from assumption $-\Delta H_a^\circ$ = EA. e. Compton et al. [3], from endothermic charge transfer threshold. f. Fukuda and McIver (ICR) [11]. g. Chen and Wentworth [12] charge transfer spectra in solution, E_{CT}. h. Chen and Wentworth [12] reduction potential in solution, $E_{1/2}$.

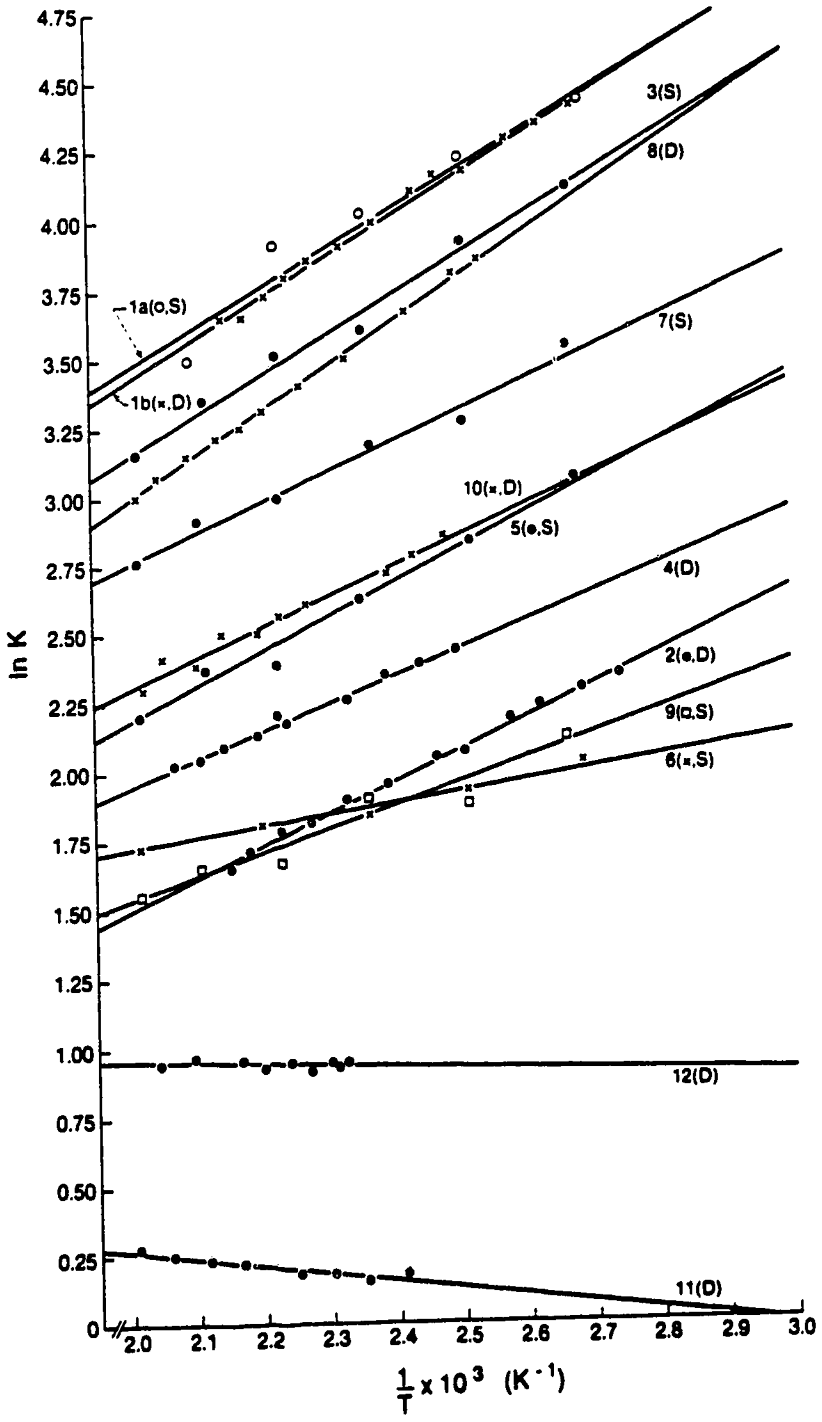

Figure 7.2 van't Hoff plots of electron transfer equilibrium constants K_{et}. Numbers identify reactions given in Figure 7.3. In some of the individual measurements (S) static temperatures were used. In others, measurements were made as the temperature decreased slowly (D).

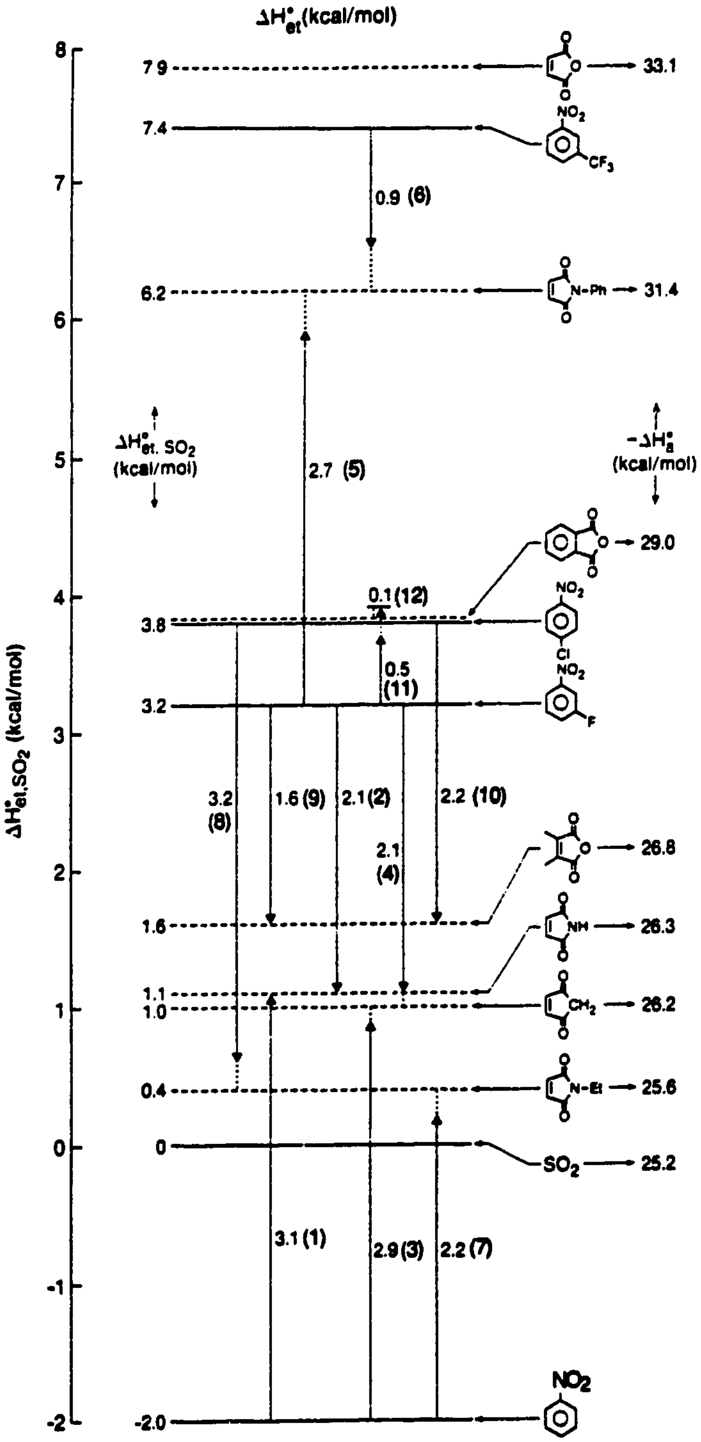

ΔH°et (kcal/mol)
ΔH°et,SO2 (kcal/mol)
ΔH°et. SO2 (kcal/mol)
-ΔH°a (kcal/mol)
8
7
6
5
4
3
2
1
0
-1
-2
7.9
7.4
6.2
3.8
3.2
1.6
1.1
1.0
0.4
0
-2.0
0.9 (6)
2.7 (5)
0.1 (12)
0.5 (11)
3.2 (8)
1.6 (9)
2.1 (2)
2.1 (4)
2.2 (10)
3.1 (1)
2.9 (3)
2.2 (7)
33.1
31.4
29.0
26.8
26.3
26.2
25.6
25.2
NO2
CF3
N-Ph
Cl
F
NH
CH2
N-Et
SO2

Figure 7.3 Scale of electron transfer enthalpies, ΔH_{et}^{o}, based on van't Hoff plots shown in Figure 7.2. ΔH_{et}^{o} given in numbers beside arrows with decimal point. Number in brackets identifies plot in Figure 7.2. $-\Delta H_a^{o}$ for: $e + B = B^{-}$, given in the right column.

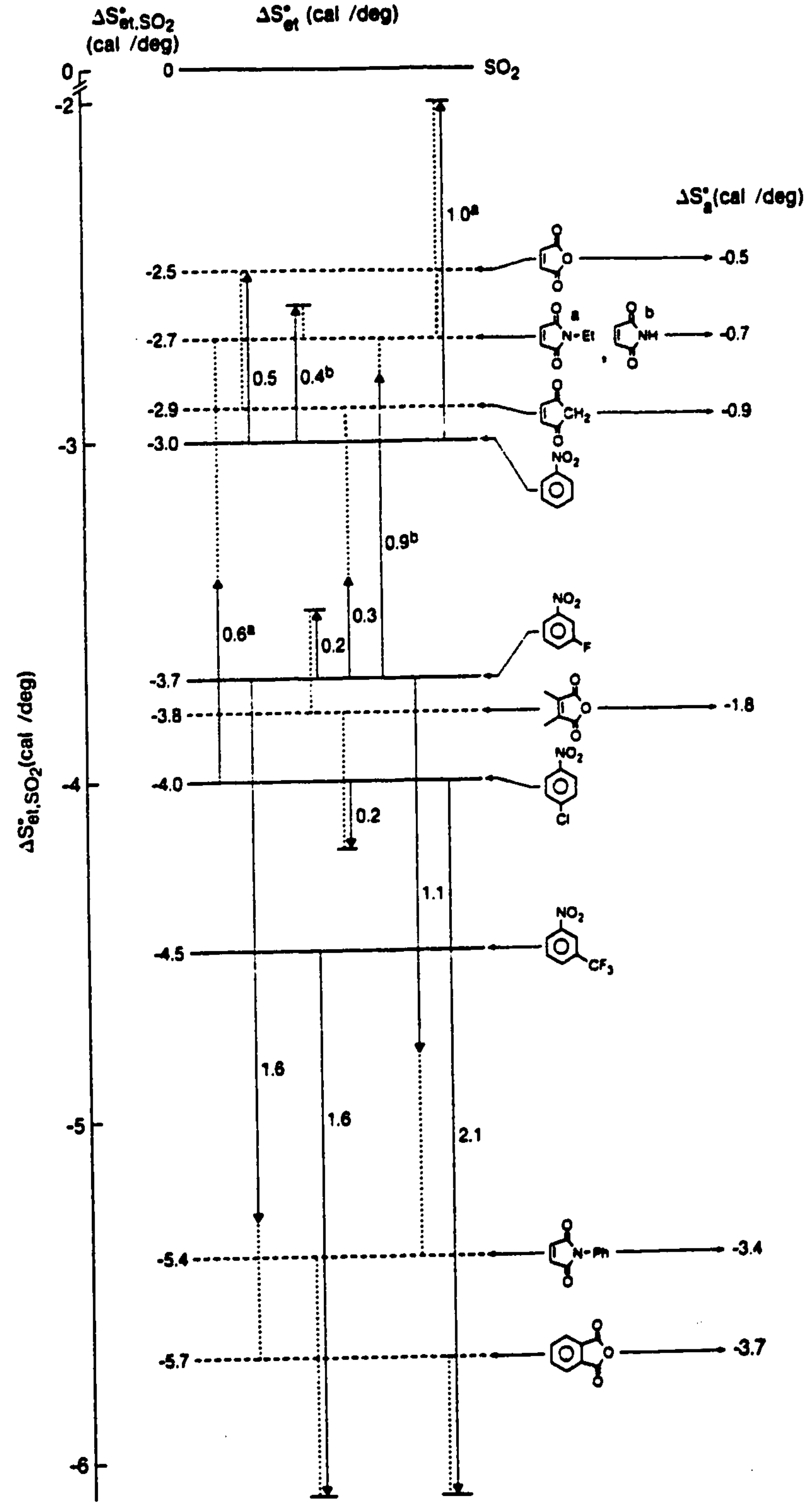
ΔS°et,SO2 (cal /deg)
ΔS°et (cal /deg)
0
SO2
ΔS°a(cal /deg)
ΔS°et,SO2(cal /deg)
0
-2
-3
-4
-5
-6
-2.5
-2.7
-2.9
-3.0
-3.7
-3.8
-4.0
-4.5
-5.4
-5.7
-0.5
-0.7
-0.9
-1.8
-3.4
-3.7
1.0a
0.5
0.4b
0.9b
0.6a
0.2
0.3
0.2
1.1
1.6
1.6
2.1
a
b
N-Et
NH
CH2
NO2
F
Cl
CF3
N-Ph

Figure 7.4 Entropy changes, ΔS_{et}^{o}, for electron transfer reactions from van't Hoff plots in Figure 7.2. Solid lines, actual measurements. Dotted lines connect actual measurements to compound involved.

were obtained. For the remaining compounds the ΔH_a^o were evaluated from equation (7.5),

$$\Delta G^o = \Delta H^o - T\Delta S^o \tag{7.5}$$

the ΔG_a^o from Figure 7.1 and the estimated ΔS_a^o given in Table 7.1.

The electron affinities shown in Table 7.1 are the ΔH_a^o values of Table 7.1 with inverted sign and [illegible] to electron volt, i.e., the approximation $EA = -\Delta H_a^o$ was made. It should [illegible] noted that the stationary electron convention [9] was used for the evaluation of ΔG_a^o and ΔS_a^o.

There are several determinations in the literature with which the present data can be compared. Experimental gas phase determinations of the threshold for the endothermic charge transfer: $Cs + B = Cs^+ + B^-$, by Compton et al. [3], led to EA = 1.4 ±0.2 eV for maleic anhydride, in good agreement with the present 1.44 eV result.

Fukuda and McIver [11] have determined relative electron attachment free energies, i.e., a scale of ΔG_{et}^o, which when calibrated to the present scale [8] lead to ΔG_a^o values for ~380 K. The values obtained for maleic and phthalic anhydride are essentially identical to the present results; see Table 7.1.

The values of Chen and Wentworth [12] based on electron transfer charge spectra in solution E_{CT} and polarographic reduction potentials $E_{1/2}$ are also in fair agreement. The largest deviation is observed for tetrachlorophthalic anhydride: 1.95 eV, present results, versus 1.7 eV from E_{CT} and 1.6 eV from $E_{1/2}$; see Table 7.1. The lower E_{CT} and $E_{1/2}$ values are probably due to the neglect of the change of coulombic and solvation interactions that occur for charge delocalized ions [9]; see Section 7.3c.

7.3b Effects of Substituents on the Electron Affinities

The electron affinities of the substituted maleic and phthalic anhydrides are compared with those of similarly substituted benzo and naphthoquinones [9] (data in brackets) in Figure 7.5. The extra electron in both types of systems enters the LUMO, which is a π^* orbital resulting from a combination of $\pi^*_{C=C}$ and two $\pi^*_{C=O}$ [13]. As expected, from the smaller extent of conjugation in the anhydrides, their LUMO energies are higher, which leads to lower EA for these compounds relative to the quinones. Thus, the EA of maleic anhydride is ~10 kcal/mol lower than that for benzoquinone; see Figure 7.5. Substitution by the electron donating methyl destabilizes the LUMO's of the quinones [9] and the anhydrides. The destabilizing effect is larger for the anhydrides whose π systems are somewhat more localized. Thus, two methyls decrease the EA of benzoquinone by only 3.1 kcal/mol, while the decrease is 6.6 kcal/mol for maleic anhydride; see Figure 7.5. The stabilizing effects of electron withdrawing substituents like phenyl or chlorine are also larger for the anhydrides. Thus, Ph increases the EA of benzoquinone by 2.7 kcal/mol and that of maleic anhydride by 6 kcal/mol; see Figure 7.5. The change from benzoquinone to anthraquinone leads to a decrease of the electron affinity by 2.2 kcal/mol [9], while the analogous change from maleic to phthalic anhydride leads to the larger decrease of 5.4 kcal/mol. Extension of the π system is also observed to cause a decrease in electron affinity (3.2 kcal/mol) from maleimide to phthalimide; see Table 7.1.

The more remote substitution by electron withdrawing substituents on the benzene group of the phthalic anhydride also leads to significant increases of the electron affinity. Thus, substitution with two Cl atoms in positions 3,6 leads to an increase of 9.8 kcal/mol; see Figure 7.5. This effect is almost as large as the Cl substituent effect in 1,2-dichloromaleic anhydride, which is 10.7 kcal/mol.

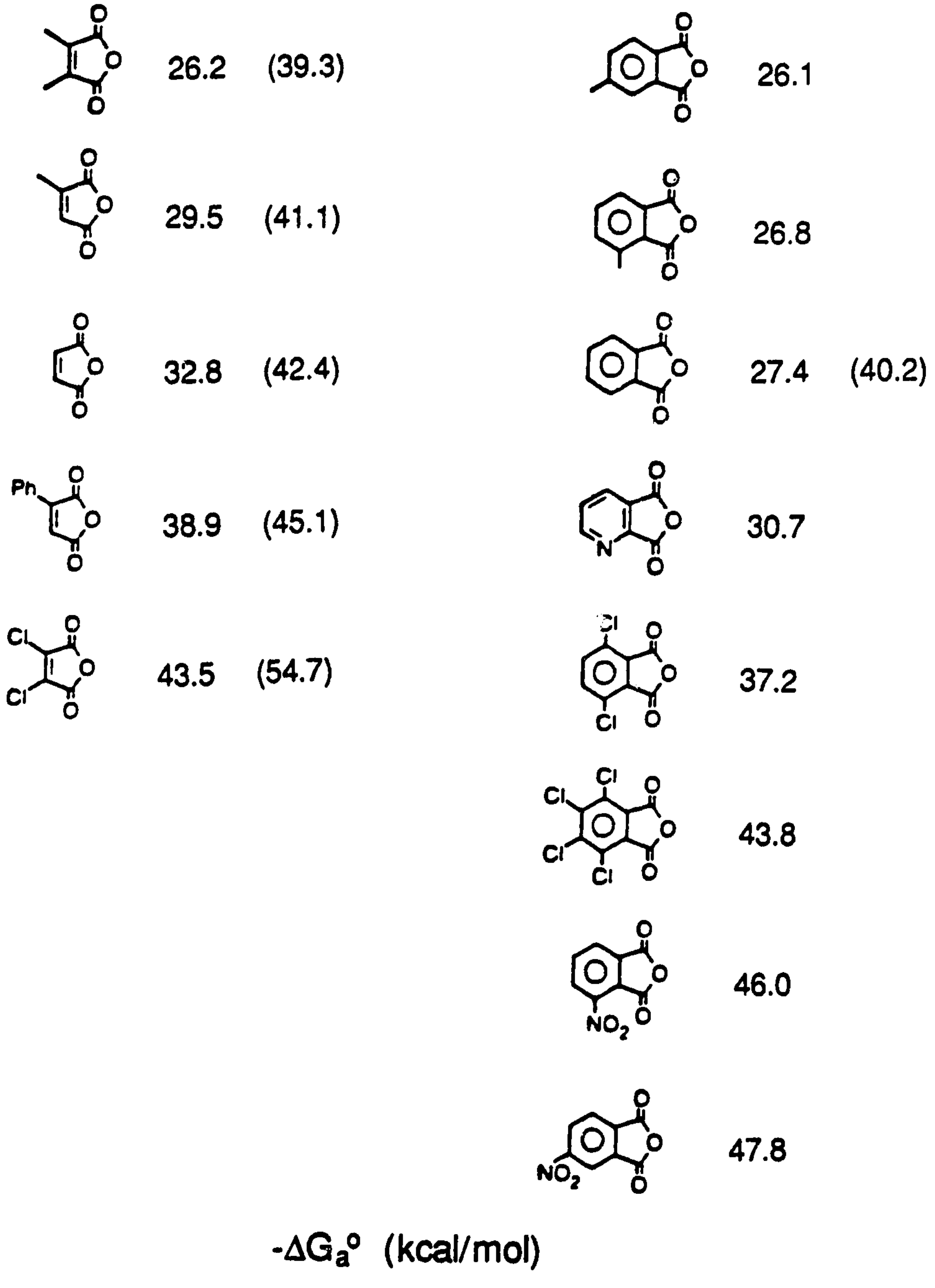
26.2 (39.3)
29.5 (41.1)
32.8 (42.4)
38.9 (45.1)
43.5 (54.7)
26.1
26.8
27.4 (40.2)
30.7
37.2
43.8
46.0
47.8
Ph
Cl
N
NO_2
-ΔGa° (kcal/mol)

Figure 7.5 Electron attachment free energies, $-\Delta G_a^o$, for the maleic and phthalic anhydrides. Values given in brackets are the $-\Delta G_a^o$ for the corresponding quinones [9].

One would have expected a considerably smaller increase for the more remote substitution in phthalic anhydride because the stabilization is largely due to σ withdrawal by Cl and the polarizability of Cl. The relatively large effect is probably due to the lesser destablization due to π donation by the Cl atoms (-R) when they are on the benzene ring when compared to the 1,2 positions in maleic anhydride.

Nitro substitution in phthalic anhydride has a very large effect on the electron affinity which is increased by ~20 kcal/mol. This can be compared to the ~22 kcal/mol change from nitrobenzene EA (22.8 kcal/mol) to para-dinitrobenzene EA (44.3 kcal/mol) [8]. The EA of the 4-NO_2 substituted phthalic anhydride is ~2 kcal/mol higher than that for the 3-NO_2 isomer; see Figure 7.5. This is probably due to the larger coulombic repulsion between the negative charge on the adjacent COO and NO_2 groups in the 3-NO_2 substituted phthalic anhydride radical anion. It may noted that the nitro substituted phthalic anhydrides also can be considered as doubly COO substituted nitrobenzenes. The 4-NO_2 substituted phthalic anhydride becomes the m,p-diCOO substituted isomer which is expected [8, 14] to have a higher EA than the o,m-diCOO compound, i.e., the 3-NO_2 phthalic anhydride. As expected, the electron donating methyl group is observed to have a stronger destabilizing effect when in the 4-position of phthalic anhydride as opposed to the 3-position; see Figure 7.5.

It is interesting to note that the electron affinity of the pyridine analogue of phthalic anhydride (EA = 30.7 kcal/mol) is somewhat larger than that of phthalic anhydride (EA = 27.4 kcal/mol); see Figure 7.5. This probably reflects a lowering of the π^* LUMO by the higher electronegativity of the N atom relative to the C atom. Recent measurements [15] which gave a higher EA for pentafluoropyridine relative to hexafluorobenzene should be due to the same effect. Electron transmission spectroscopy studies of the temporary negative ion states of benzene and pyridine by Burrow et al. [16] have shown that EA(pyridine) is about 12 kcal/mol higher than EA(benzene). This difference can also be attributed to the higher electronegativity of N relative to C. The presence of more electronegative N causes a splitting of the degenerate e_{2u} LUMO of benzene into two orbitals, where the lower one $b_1(\pi^*)$ becomes the LUMO in pyridine [16].

The electron attachment energies for the cyclic dicarbonyls with bridging O, NH and CH_2, from Table 7.1, are given below.

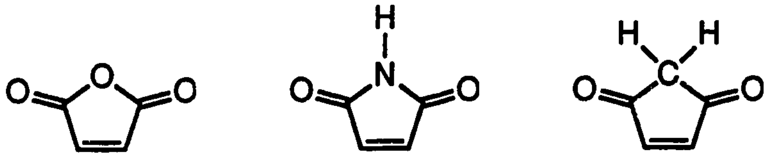

32.8 26.2 25.8

$-\Delta G_a^o$ (kcal/mol)

The electron affinity of the oxy compound is 6.5 kcal/mol larger than that of the NH and CH_2 bridged structures. Methoxy substitution of benzoquinone was found to lead to a small decrease of the electron affinity. This was assumed to be due to the destabilizing effect of π donation by the oxygen. A similar destabilization can be expected also in maleic anhydride. This however is counteracted by σ withdrawal due to the large electronegativity of the oxygen so that a net stabilization of the π^* LUMO results. For nitrogen, in maleimide, the π destabilization should be similar and since the electronegativity is lower and further lowered by the presence of H, the π destabilization is barely overbalanced and the electron affinity ends up to be similar to that for the CH_2 bridged cyclodione where there is essentially no destabilization by π donation and no stabilization by σ withdrawal.

For maleimide the data in Table 7.1 provide some information for substitution on the N atom. Thus Me or Et substitution decrease the electron affinity by less than 1 kcal/mol, an effect much smaller than the 3 kcal/mol decrease for Me substitution on sp^2 carbon in maleic anhydride. Similarly Ph substitution on N in maleimide increases the electron affinity by 3.8 kcal/mol, while in maleic anhydride the increase is by 6 kcal/mol. The smaller effects for maleimide are expected, since with regard to the $\pi^*_{C=O}$ and $\pi^*_{C=C}$ system which determines the electron affinity, the substitution on N in maleimide is relatively remote.

Unfortunately, recent theoretical calculations concerning the LUMO's and the electron affinities of the cyclic dicarbonyls I and II have not been reported; however, results from earlier work are available. This work was stimulated by interest in correlations of the occupied orbital energies with the ionization potentials and unoccupied orbitals with electron affinities [13, 17-19] within the context of Koopman's theorem. Of primary interest are the HOMO and LUMO which are also of importance in lowest energy electronic spectra [20, 21] and Frontier molecular orbital theory which relates chemical reactivity to these orbitals, as for example, for nucleophilic and cycloadditions to quinones [22] and to the anhydrides, I and II.

Kunii and Kuroda [17], using the Pariser-Parr-Pople approximation to the Hartree-Fock equation with an adjusted core parameter β, obtained IP and EA for 30 heteroaromatic compounds including the EA for maleic anhydride (1.43 eV) and phthalic anhydride (0.99 eV). These results are fairly close to the present values of 1.4 and 1.2 eV; see Table 7.1. Later work by Compton et al. [18, 19] with the same formalism but an adjustable β and γ provided IP and EA for some 100 heteroaromatic compounds including the EA for maleic anhydride

(1.0 eV) and maleimide (0.94 eV) which are in fair agreement with the present results in Table 7.1.

7.3c Comparison with Reduction Potentials in Solution. Solvation Energy of the Radical Anions

Several determinations of the polarographic halfwave reduction potential, $E_{1/2}$, relating to the reaction (7.2): $B + e = B^{-}$, in solution, where B is the substituted cyclodiones I and II, have been reported [23-27]. On the basis of these data and the present determinations of the gas phase reduction (electron attachment) energies one can examine how well the gas phase data correlate with those in solution and also obtain approximate solvation energies for the radical anions B^{-}. Comparisons of this type for other systems were reported in previous work from Kebarle [8, 9, 28]. The equation (7.6) used [9] is based on a Born type cycle for the reduction reaction (7.2) in the gas phase and solution [9, 29]. The ΔG_a^{o} (B) is the electron attachment free energy

$$EA(B) \approx -\Delta G_a^{o}(B) = +23.06E_{1/2}(B) + (\Delta G_{sol}^{o}(B^{-}) - \Delta G_{sol}^{o}(B)) + 108.6 \qquad (7.6)$$

$$B_{(g)} \rightarrow B_{(sol)} \qquad (7.7a)$$

$$B^{-}_{(g)} \rightarrow B^{-}_{(sol)} \qquad (7.7b)$$

($-\Delta G_a^{o}(B) \approx EA(B)$), see Table 7.1, in kcal/mol, $E_{1/2}(B)$ is the polarographic reduction potential in volts versus the calomel electrode, and the solvation energies $\Delta G_{sol}^{o}(B)$, $\Delta G_{sol}^{o}(B^{-})$ are defined in (7.7). The numerical constant, 108.6 (kcal/mol), leads to these quantities being in kcal/mol units.

A plot of $E_{1/2}(B)$, obtained by Peover [23] and Nagy [26, 27] in dimethylformamide, DMF, versus the SCE, are shown in Figure 7.6 plotted versus $EA \approx -\Delta G_a^{o}$. It is evident that for this group of compounds the correlation

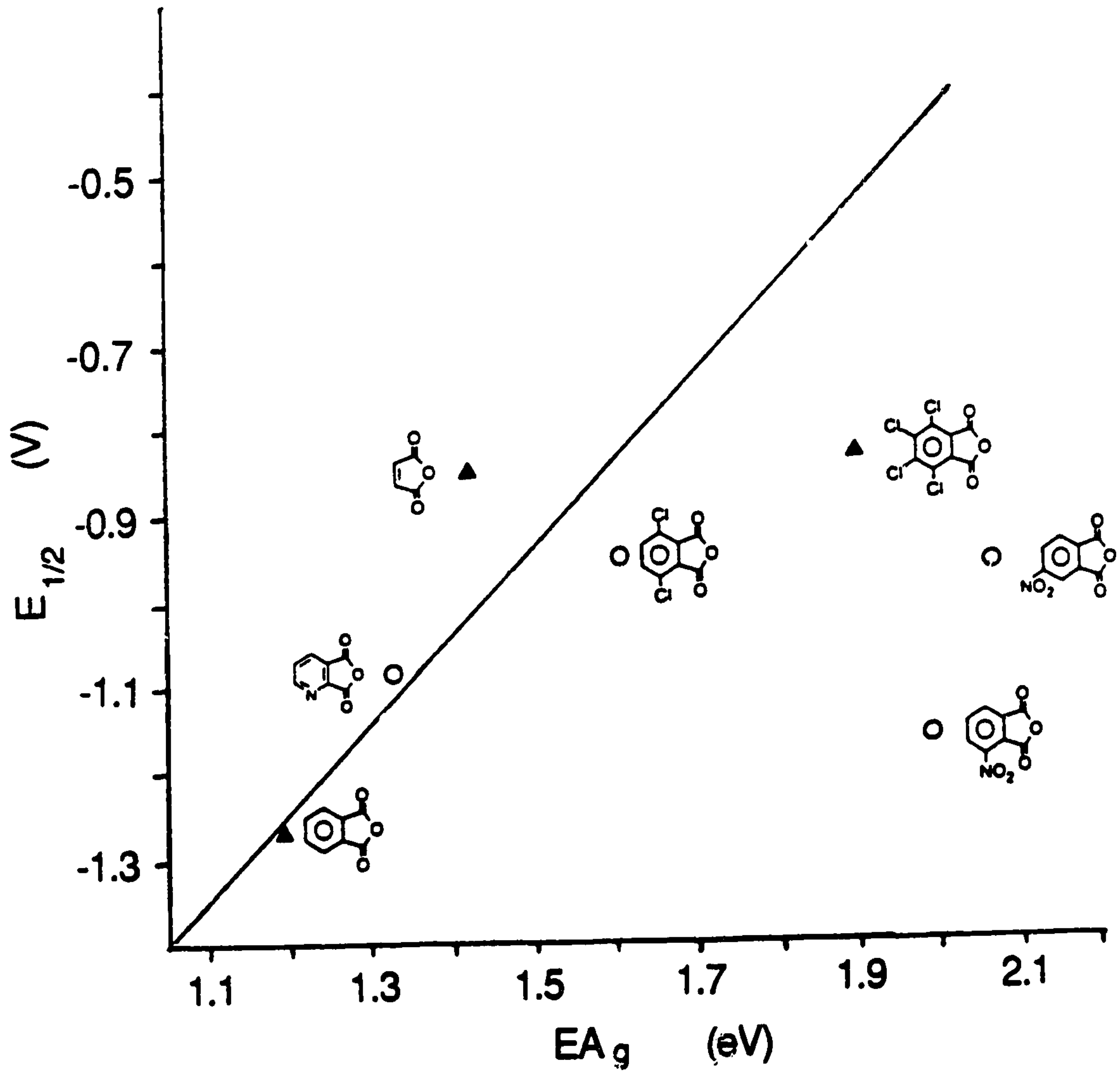

Figure 7.6 Polarographic halfwave potentials in dimethylformamide (DMF) versus gas phase electron attachment free energies ($-\Delta G_a^{\circ}$). Solid line corresponds to slope = 1 expected if assumption is made that the solvation energies in DMF are constant, see equation (7.6) in text. Lack of correlation for present compounds demonstrates importance of changing solvation energies: (▲) $E_{1/2}$ from Peover [23]; (o) $E_{1/2}$ from Nagy [26, 27].

between $E_{1/2}$ and EA is poor. $E_{1/2}$ data from different laboratories are taken under somewhat different conditions and may be displaced by a constant value. Therefore, it is significant in Figure 7.6 that the $E_{1/2}$ data originating from the same laboratory show no significantly better correlation with the EA values. Furthermore, it is the high EA compounds that have EA values that are relatively much higher than the corresponding $E_{1/2}$ data, i.e., these compounds are found far to the right of the unit slope line in Figure 7.6. This suggests that the trends observed are real and that significant changes in $\Delta G_{sol}^{o}(B^{-}) - \Delta G_{sol}^{o}(B)$ occur within this series of compounds.

The solvation energy difference $\Delta\Delta G_{sol}^{o} = \Delta G_{sol}^{o}(B^{-}) - \Delta G_{sol}^{o}(B)$, evaluated with equation (7.6) from the data in Figure 7.6, is shown in Figure 7.7. These results show that the solvation exothermicity, $-\Delta\Delta G_{sol}^{o}$, is smallest for the highest EA compounds. Significantly these are the compounds substituted with the strongest electron withdrawing groups: NO_2 or multiply substituted by Cl, i.e., the radical anions with the largest charge delocalization for which the lowest $-\Delta G_{sol}^{o}(B^{-})$ are expected since it is known that charge delocalization leads to a decrease of solvation. It should be noted that the solvation exothermicity of B^{-} is very much larger than that of B and therefore $\Delta\Delta G_{sol}^{o}$ is dominated by the $\Delta G_{sol}^{o}(B^{-})$ term. A rough estimate of $\Delta G_{sol}^{o}(B)$ can be obtained from equation (7.8).

$$\Delta G_{sol}{}^{o}(B) = RT\ln\frac{P_B}{C_B} \qquad (7.8)$$

The vapor pressures P_B over the pure liquid or solid were obtained from Stull [30]: MaAn = 3.7 x 10^{-4} atm; PhAn = 5 x 10^{-6} atm, and the solubilities C_B in DMF were measured in the present work: MaAn = 22.8 mol/L; PhAn = 2.8 mol/L. The $\Delta G_{sol}^{o}(B)$ values at 298 K for maleic and phthalic anhydride are

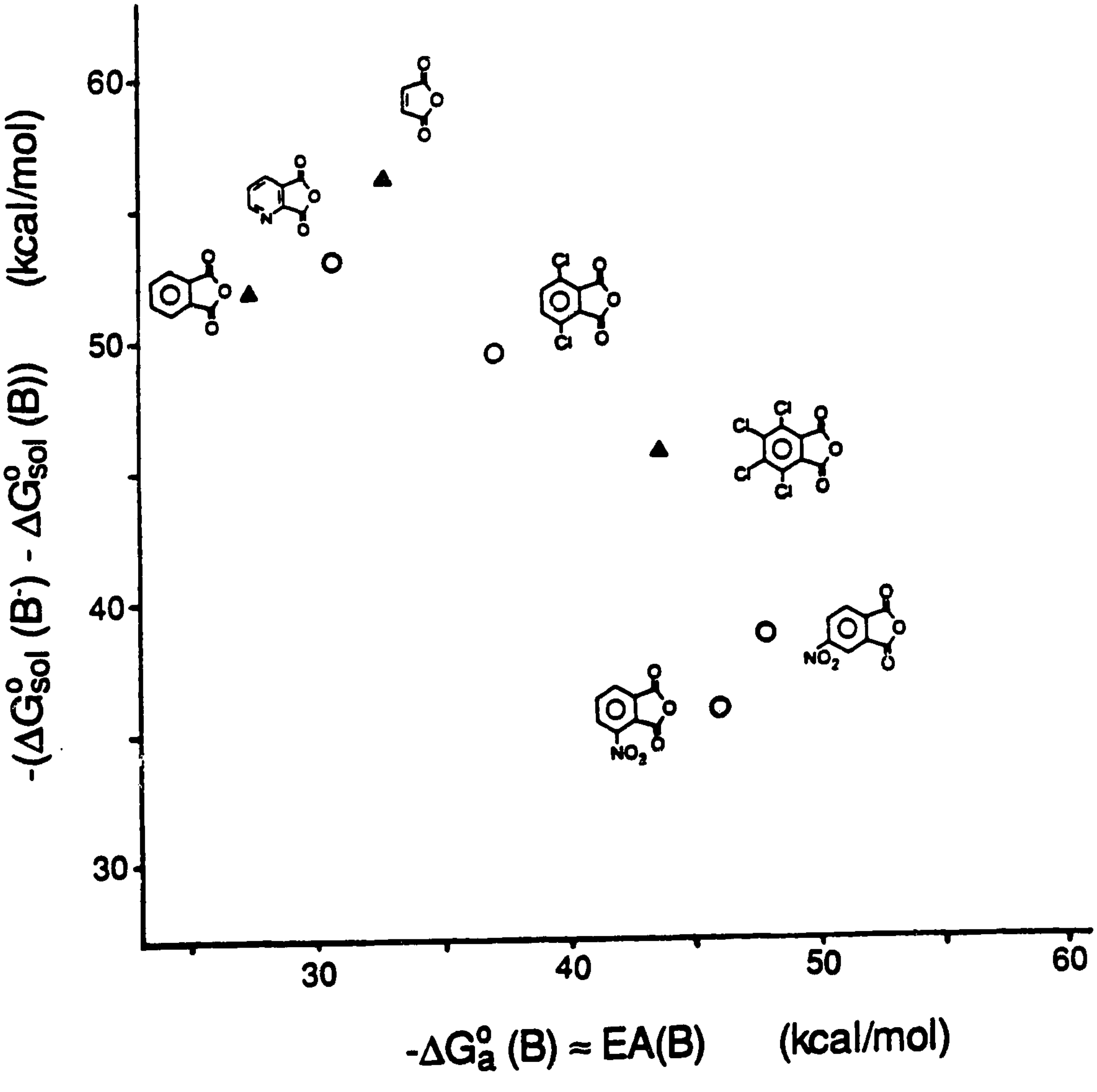

Figure 7.7 Solvation energies $\Delta\Delta G_{sol}{}^o = \Delta G_{sol}{}^o(B^-) - \Delta G_{sol}{}^o(B)$ deduced with equation (7.6) from $E_{1/2}$ shown in Figure 7.6 and present $\Delta G_a{}^o$ results. $\Delta\Delta G_{sol}{}^o$ is dominated by $\Delta G_{sol}{}^o(B^-)$, see text. Large decreases of solvation exothermicity for B^- with increasing electron affinity ($-\Delta G_a{}^o(B)$) are due to increasing charge delocalization in B^-.

approximately -6.5 and -7.8 kcal/mol which is close to 1/10 of the value for $\Delta G_{sol}^{o}(B^{-})$; see Figure 7.7.

Similar $\Delta G_{sol}^{o}(B^{-})$ trends were found in earlier comparisons of EA with $E_{1/2}$ values [8, 9, 28]. However, for the present series of compounds the effects are very large. The scatter and deviation from unit slope in Figure 7.6 is very pronounced and correspondingly the differences in $\Delta\Delta G_{sol}^{o}$ in Figure 7.7 are amongst the largest. A large difference was observed in earlier work [28] for NO_2 substitutions: $-\Delta\Delta G_{sol}^{o}$ (nitrobenzene) ≈ 58 kcal/mol and $-\Delta\Delta G_{sol}^{o}$(1,4-dinitrobenzene) ≈ 48 kcal/mol in DMF. These values and the difference are similar to the data in Figure 7.7 for phthalic anhydride and the nitrophthalic anhydrides, although the change in the latter group is ~5 kcal/mol larger. This larger difference may be due to a true effect or experimental discrepancies caused by the different origin of the $E_{1/2}$ data.

Prior to the availability of the abundant gas-phase electron transfer equilibria data [8], electron affinities were often obtained [1, 2, 12] from available $E_{1/2}$ values via equation (7.6) and the assumption that $\Delta\Delta G_{sol}^{o}$ is constant, particularly in dipolar aprotic solvents like DMF. The results in Figure 7.6 and 7.7 show that for some groups of compounds this assumption breaks down and can lead to relative errors of 10 kcal/mol or more. Now that EA data are available, it is appropriate to concentrate on the solvation energies of the ions and their relative magnitudes. The availability of abundant data will lead to a much needed improved understanding of ion solvation of diverse systems. Also required are extensive modern determinations of reduction potentials and their temperature dependence under standardized conditions. Some work of this nature has been performed; see Parker et al. and references therein [31].

REFERENCES

1. G. Briegleb, Angew. Chem., Int. Ed. Engl., 3, 617 (1964).
2. M. Batley and L. E. Lyons, Nature, 196, 573 (1962).
3. R. N. Compton, P. W. Reinhardt and C. D. Cooper, J. Chem. Phys., 60, 2953 (1974).
4. L. G. Christophorou, Adv. Electronics Electron Phys., 56, 55 (1978).
5. R. E. McCarty, P. R. Pittman and Y. Tsuchiya, J. Biol. Chem., 247, 3048 (1972).
6. F. Di Virgilio, M. Pozzan, and G. F. Azzone, Biochim. Biophys. Acta, 589, 223 (1981).
7. R. Barr and F. Crane, Biochim. Biophys. Acta, 681, 139 (1982).
8. S. Chowdhury and P. Kebarle, Chem. Rev., 87, 513 (1987).
9. T. Heinis, S. Chowdhury, S. L. Scott and P. Kebarle, J. Am. Chem. Soc., 110, 400 (1988).
10. S. Chowdhury, T. Heinis, E. P. Grimsrud and P. Kebarle, J. Phys. Chem., 90, 2747 (1986).
11. E. K. Fukuda and R. T. McIver Jr., J. Am. Chem. Soc., 107, 2291 (1985).
12. E. C. M. Chen and W. E. Wentworth, J. Chem. Phys., 63, 3183 (1975).
13. A. Modelli, G. Distefano and D. Jones, Chem. Phys., 73, 395 (1982).
14. S. Chowdhury, H. Kishi, G. W. Dillow and P. Kebarle, Can. J. Chem., 67, 603 (1989).
15. G. W. Dillow and P. Kebarle, J. Am. Chem. Soc., 110, 4877 (1988).
16. P. D. Burrow, A. J. Ashe III, D. J. Bellville and K. D. Jordan, J. Am. Chem. Soc., 104, 425 (1982).
17. T. L. Kunii and H. Kuroda, Theor. Chim. Acta, 97, 106 (1968).

18. J. M. Younkin, L. J. Smith and R. N. Compton, Theor. Chim. Acta, 41, 157 (1976).

19. R. N. Compton, Y. Yoshioka and K. D. Jordan, Theor. Chim. Acta (Berlin), 54, 261 (1980).

20. H. D. Scharf and H. Leismann, Z. Naturforsch., 286, 662 (1973).

21. Von M. Augustin, M. Kohler and S. Hartling, J. Prakt. Chem., 315, 717 (1973).

22. M. D. Rozeboom, I.-M. Tegmo Larsson and K. N. Houk, J. Org. Chem., 46, 2338 (1981).

23. M. E. Peover, Trans. Faraday Soc., 58, 2370 (1962).

24. A. Nemeckova, M. Maturova, M. Pergal and F. Santavy, Collect. Czech. Chem. Commun., 26, 2749 (1961).

25. A. Ryvolova-Kejharova and P. Zuman, Collect. Czech. Chem. Commun., 36, 1019 (1971).

26. J. B. Nagy, O. B. Nagy and A. Bruylants, J. Phys. Chem., 78, 980 (1974).

27. O. B. Nagy, H. Lion and J. B. Nagy, Bull. Soc. Chim. Belg., 84, 1053 (1975).

28. P. Kebarle, G. W. Dillow, K. Hirao and S. Chowdhury, Faraday Discuss. Chem. Soc., 85, 1 (1988).

29. F. A. Matsen, J. Chem. Phys., 24, 602 (1956).

30. D. R. Stull, In. Eng. Chem., 34, 517 (1947).

31. M. Svaan and V. O. Parker, Acta Chem. Scand., B38, 767 (1984).

CHAPTER 8

CONCLUDING SUMMARY

The work presented in this thesis describes research in two different areas of gas phase negative ion-molecule chemistry. The first part of the study involves an investigation of the chemical bonding in selected negative ion-molecule complexes. This was accomplished using bond strength determinations obtained directly and indirectly through measurements of ion-molecule association and transfer equilibria with the pulsed electron high pressure mass spectrometer (PHPMS). This work is of fundamental interest and provides a platform for the understanding of solvent effects on chemical reactions. The second part of the study involves electron affinity determinations for a group of organic compounds, the cyclic unsaturated dicarbonyls. These determinations were achieved through measurements of electron transfer equilibria using the PHPMS. The cyclic unsaturated diones are known to act as electron acceptors in charge transfer complexes and have biological significance as electron carriers [1-3].

In Chapter 2 it was found that the hydrogen bond energies in YPhOH·X^- (X^- = Cl^-, Br^- and I^-) increase approximately linearly with the gas phase acidities of the phenols, YPhOH. This is in agreement with earlier observations which showed the bond energies in MH·B^-, where MH were oxygen and nitrogen acids and B^- closed shell anions, increase with increasing acidity of MH [4, 5]. A detailed analysis of the substituent effects, which is possible for YPhOH·X^-, shows that the relationship with the acidity of MH can be divided into two parts. One is the increasing extent of actual proton transfer from MH on formation of the hydrogen bonded complex. Such proton transfer occurs in YPhOH·X^- only for the series X^- = Cl^-. The second effect, which occurs for Cl^- and is dominant for Br^- and I^-, is not directly related to the acidity of the phenols (or MH in general) but depends on a similarity of the substituent effects on the acidity and on the stabilization of $YPhOH{\cdot}X^-$ (or $MH{\cdot}B^-$ in general). The dominant contribution to $YPhOH{\cdot}X^-$ stabilization in this case is due to the field effects of the substituents with π delocalization only playing a small part. Therefore, the correlation with the acidity of YPhOH, where π delocalization is important, is not very close. The findings for the $YPhOH{\cdot}X^-$ system are useful because they can be generalized to $MH{\cdot}B^-$ hydrogen bonded complexes.

In Chapters 3-5 analysis of experimentally determined bond free energies ($-\Delta G^{o}_{XA}$) and quantum mechanical calculations indicate the ion-molecule complexes $SB{\cdot}X^-$, $SQ{\cdot}X^-$ and $SE{\cdot}X^-$ (SB, SQ and SE = substituted benzenes, quinones and ethylenes and $X^- = F^-$, Cl^-, Br^- and I^-) have a variety of structures. Substituents with protic hydrogens such as CO_2H, OH and NH_2, which involve in strong hydrogen bonding, were excluded from analysis.

In Chapter 3 Taft substituent analysis [6] of bond free energies suggests that Cl^- and Br^- form aromatic C-H bonded complexes with all singly substituted benzenes, C_6H_5Y. The field effects of the substituents provide the dominant contribution to bonding in these complexes. Theoretical calculations predict that the halide ion hydrogen bonds to the proton meta to the substituent when Y is a σ acceptor, π donor and to the proton para to the substituent when Y is a σ acceptor, π acceptor [7, 8]. Analysis of the bond free energies for singly substituted nitrobenzenes with Br^- also indicates the formation of hydrogen bonded complexes. A clear cut analysis of the bonding of Br^- to triply substituted benzenes with strongly electron withdrawing substituents like CF_3, CN and NO_2 could not be obtained. In this case a σ bonded Meisenheimer complex where Br^- bonds to an unsaturated carbon atom in the benzene ring or an electrostatic complex where Br^- lies on the axis perpendicular to the benzene plane may have similar stability to the hydrogen bonded complex.

In Chapter 4 substituent effect analysis of experimentally determined bond free energies indicates F^- forms σ bonded complexes with the perfluorobenzenes, C_6F_5Y, where Y is a σ acceptor, π acceptor. π delocalization (+R effect) is determined to make an important contribution to stabilization in these complexes. σ bonding is also predicted in the complex $C_6F_6{\cdot}F^-$ from ab initio MO calculations [9]. Analysis of the products from nucleophilic aromatic substitution reactions in solution [10] indicate F^- inserts preferentially in the para position relative to the electron withdrawing substituent. Information on the stability and structure of σ bonded Meisenheimer complexes is of interest as these complexes are proposed to be intermediates in nucleophilic aromatic substitution reactions [11]. Substituent effects on bond free energies in the complexes $C_6F_5Y{\cdot}X^-$ (X^- = Cl^- and Br^-) are observed to be much weaker than those for $C_6F_5Y{\cdot}F^-$. The small resonance (R) and field (F) contributions to stabilization are consistent with an electrostatic complex geometry where X^- is on an axis perpendicular to the benzene plane. This structure was predicted for the complexes $C_6F_6{\cdot}X^-$ (X^- = Cl^-, Br^- and I^-) from ab initio MO calculations [12].

In Chapter 5 ab initio MO calculations by Hirao et al. [8] provide structural information on the complexes $TCNE{\cdot}X^-$ (TCNE = tetracyanoethylene and X^- = F^-, Cl^- and Br^-) and $F_4BQ{\cdot}X^-$ (F_4BQ = tetrafluoro-para-benzoquinone and X^- = Cl^- and Br^-). Covalent bonding is predicted in $TCNE{\cdot}F^-$ where F^- σ bonds to one of the ethylene carbons. Partial charge transfer complexes are predicted most stable for the complexes $F_4BQ{\cdot}X^-$ (X^- = Cl^- and Br^-) where X^- is on an axis perpendicular to the benzene plane, although electrostatic complexes of similar geometry are found to be only slightly less stable (~1-2 kcal/mol). For $TCNE{\cdot}X^-$

(X^- = Cl^- and Br^-) an electrostatic interaction is favored. Interestingly, stable σ bond formation is also predicted for the complexes $F_4BQ{\cdot}Br^-$ and $TCNE{\cdot}X^-$ (X^- = Cl^- and Br^-), which is due to the presence of strong electron withdrawing substituents. Varying degrees of agreement are observed between experimentally determined bond strengths, $-\Delta H^{o}_{XA}$, for these complexes and those $-\Delta E^{o}_{XA}$ values calculated by Hirao et al. [8].

In Chapter 7 the electron affinities (EA) of 20 cyclic diones, mostly substituted maleic and phthalic anhydrides and maleimides and phthalimides, are reported. The substituent effects on the electron affinities for the anhydrides are similar to those observed earlier for the benzoquinones and the naphthoquinones [13] but somewhat larger because the π systems are somewhat more localized. Comparison of the electron affinities with reduction potentials in dimethylformamide ($E_{1/2}$) [14-16] permits the evaluation of the solvation energies of the radical anions in dimethylformamide ($\Delta G^{o}_{sol}(B^-)$). Significant decreases of solvation exothermicity with increasing electron affinities of the precursor neutral compounds are observed. Similar $\Delta G^{o}_{sol}(B^-)$ trends were found in earlier comparisons of EA with $E_{1/2}$ values [13, 17].

REFERENCES

1. R. E. McCarty, P. R. Pittman and Y. Tsuchiya, J. Biol. Chem., 247, 3048 (1972).
2. F. Di Virgilio, M. Pozzan and G. F. Azzone, Biochim. Biophys. Acta, 589, 223 (1981).
3. R. Barr and F. Crane, Biochim. Biophys. Acta, 681, 139 (1982).
4. R. Yamdagni and P. Kebarle, J. Am. Chem. Soc., 93, 7139 (1971).
5. J. W. Larson and T. B. McMahon, J. Am. Chem. Soc., 105, 2944 (1983).
6. R. W. Taft and R. D. Topsom, Prog. Phys. Org. Chem., 16, 1 (1987).
7. M. A. French, S. Ikuta and P. Kebarle, Can. J. Chem., 60, 1907 (1982).
8. G. Paul, K. Hirao, S. Obata and P. Kebarle, in preparation.
9. K. Hiraoka, S. Misuze and S. Yamabe, J. Chem. Phys., 86, 4102 (1987).
10. K. C. Ho and J. Miller, Aust. J. Chem., 19, 423 (1966).
11. J. F. Bunnett and R. E. Zahler, Chem Rev., 49, 273 (1951).
12. K. Hiraoka, S. Misuze and S. Yamabe, J. Phys. Chem., 91, 5294 (1987).
13. T. Heinis, S. Chowdhury, S. L. Scott and P. Kebarle, J. Am. Chem. Soc., 110, 400 (1988).
14. M. E. Peover, Trans. Faraday Soc., 58, 2370 (1962).
15. J. B. Nagy, O. B. Nagy and A. Bruylants, J. Phys. Chem., 78, 980 (1974).
16. O. B. Nagy, H. Lion and J. B. Nagy, Bull. Soc. Chim. Belg., 84, 1053 (1975).
17. S. Chowdhury and P. Kebarle, Chem. Rev., 87, 513 (1987).